Prediction and Analysis of Stochastic Convergence in the Standard and Extrapolated Power Methods Applied to Monte Carlo Fission Source Iterations

by

Bryan Elmer Toth

A dissertation submitted in partial fulfillment
of the requirements for the degree of
Doctor of Philosophy
(Nuclear Engineering and Radiological Sciences)
in the University of Michigan
2018

Doctoral Committee:

Professor William R. Martin, Chair
Dr. David P. Griesheimer, Bettis Atomic Power Laboratory
Professor James Paul Holloway
Professor Edward W. Larsen
Professor Divakar Viswanath

Bryan Elmer Toth

betoth@umich.edu

ORCID iD: 0000-0003-4219-5531

Dedication

This dissertation is dedicated to the “best family ever” (A. Toth, personal communication, 2014).

Acknowledgements

The author would like to acknowledge that portions of this research were performed under appointment to the Rickover Graduate Fellowship Program sponsored by the Naval Reactors Division of the U.S. Department of Energy and the Nuclear Regulatory Commission Fellowship Program.

Table of Contents

List of Tables

List of Figures

List of Appendices

Abstract

In Monte Carlo (MC) eigenvalue calculations, numerous cycles of the fission source iterative procedure may need to be discarded to sufficiently converge an initial guess toward the steady-state fission distribution in a system. Reducing the number of discarded cycles is desirable to save computer time, and knowing when one may stop discarding is important to avoid introducing a bias in desired quantities from simulations. In this work, approximate prescriptions are derived for the evolution of eigenmode components of the fission source at each cycle using the standard and extrapolated power methods adapted to MC neutron transport. The approximate prescriptions may be used to diagnose and predict convergence of the standard and extrapolated fission source iterations. Despite the lack of success by previous researchers, the approximate prescriptions reveal that the extrapolated power method can reduce the number of discarded cycles compared with the standard power method for some cases.

The probability density functions (PDFs) of eigenmode components are shown to be approximately normally distributed and thus may be wholly described by their means and variances. Two methods for approximating the mean of single-cycle variances of eigenmode components are constructed and validated. The mean of single-cycle variances of eigenmode components may be used to predict the variance of eigenmode components after multiple cycles.

A novel convergence diagnostic that focuses on convergence of the probability density functions (PDFs) of eigenmode components of the fission source distribution is developed. The Bhattacharyya coefficient and relative entropy are examined as measures of similarity between eigenmode component PDFs, and relative entropy is shown to be

preferable. A predictive convergence diagnostic is constructed using a threshold maximum value for the relative entropy between eigenmode PDFs at each cycle and their steady-state PDFs. Prescriptions for the optimal numbers of extrapolated and standard cycles to discard are derived using the new diagnostic such that the number of discarded cycles is minimized for a chosen relative entropy threshold. The new diagnostic is significant because it may be applied before or during a running simulation, and it provides the user with tangible confidence intervals for the eigenmode components when given appropriate input.

Chapter 1. Introduction

Criticality calculations are an important tool in fission system design and safety analysis. Monte Carlo (MC) neutron transport is one method for such calculations. The MC method is especially well-suited for working with complex geometries because no discretization of the particle phase space is necessary as with deterministic techniques like Sn [1], [2]. However, MC transport can be computationally expensive, especially for systems with large dominance ratios, the ratio of the second largest eigenvalue to the fundamental, largest, eigenvalue [3]. This situation is common in problems that are many mean free paths thick, and/or have regions which exchange few neutrons per generation, such as the Whitesides' problem [3].

In MC criticality calculations, an iterative technique known as the method of successive generations [4], which is analogous to the power method from linear algebra [5], attempts to force the higher harmonics out of the fission neutron distribution estimate at each iteration. The true fission neutron distribution is approximated at each iteration by a randomly sampled set of fission neutron source locations (points). After a sufficient number of iteration cycles, the distribution of source points becomes stationary and fluctuates about the fundamental mode, the eigenfunction with the largest eigenvalue. The initial guess for the fission distribution and the eigenvalues of the problem are the primary factors determining the number of cycles required to converge to the stationary fission distribution [6].

Theoretically, an acceleration technique from linear algebra should be able to reduce the number of cycles required to reach a converged state [7]. The most elementary acceleration technique is linear extrapolation. Previous attempts to apply linear extrapolation for accelerating the convergence of the MC neutron source iteration were unsuccessful [7], [8]. The researchers did not recognize any gain from the use of linear

extrapolation, and the researchers conjectured that noise in the MC procedure was to blame. Their attempts were deemed unsuccessful because their convergence metric was flawed, which is demonstrated in Section 1.4. In Sections 2.1-2.3 equations are derived to describe the evolution of eigenmode components in the standard and extrapolated MC eigenfunction iterations, which account for the stochastic noise and provide insight into the nature of MC source convergence. Implementation concerns regarding extrapolation in MC iterations along with validation of the extrapolated model are presented in Section 2.4. Using the derivations, the theoretical convergence properties of the standard and extrapolated power methods are compared in Section 2.5 along with empirical evidence to support the proposed theory. The comparison and empirical evidence demonstrate that linear extrapolation can be applied successfully in some cases to significantly reduce the number of cycles that are required to sufficiently converge the fission source. Techniques for estimating initial eigenmode components under various circumstances are discussed in Section 2.6.

The derived model makes some simplifying assumptions regarding the noise introduced by the MC procedure at each cycle. Theoretical justification for the assumption that eigenmode decomposition coefficients are normally distributed is provided in Section 3.1, and empirical evidence to support the normality assumption is presented in Section 3.2. The noise is also assumed to be uncorrelated with previous cycles. That assumption is examined in the context of validating the model for the variance of eigenmode components in Section 3.3. The practical matter of estimating the variance introduced into eigenmode components after each cycle is explored in Section 3.4.

A novel convergence diagnostic that focuses on convergence of the probability density functions (PDFs) of eigenmode components of the fission source distribution is developed in Sections 4.1-4.2. The new diagnostic can predict or guarantee a reasonable level of convergence and independence from the initial starting distribution after a certain number of iteration cycles with appropriate input variables. As an additional use case, the diagnostic is applied in Section 4.3 to determine the optimal number of extrapolated

cycles for a MC source iteration using linear extrapolation.

1.1 Neutron Transport

In the field of neutron transport, a sought after piece of information is the angular neutron flux $\psi(\vec{r},E,\hat{\Omega},t)$, which is the distance traversed by neutrons per unit time, volume, energy, and solid angle at position $\vec{r}$ traveling in direction $\hat{\Omega}$ with energy *E* at time *t*. From the angular neutron flux, many desired quantities such as power distribution, fuel burnup, and radiation dose can be determined. This dissertation will only focus on neutron transport, so the terms flux and neutron flux are equivalent, and the discussion is also restricted to steady-state, so the dependence on time can be dropped. The angular flux is governed by the steady-state neutron transport equation, which can be expressed as [9]

$$M\left[\psi(\vec{r},\hat{\Omega},E)\right]=Q(\vec{r},E,\hat{\Omega}). \tag{1.1.1}$$

Where *M* is the net loss operator defined by

$$\begin{aligned} M\left[\psi(\vec{r},\hat{\Omega},E)\right] &\equiv \hat{\Omega}\cdot\nabla\psi(\vec{r},\hat{\Omega},E)+\Sigma_t(\vec{r},E)\psi(\vec{r},\hat{\Omega},E) \\ &-\int_0^\infty dE'\int_{4\pi} d\hat{\Omega}'\Sigma_s(\vec{r},\hat{\Omega}'\rightarrow\hat{\Omega},E'\rightarrow E)\psi(\vec{r},\hat{\Omega}',E'), \end{aligned} \tag{1.1.2}$$

$Q(\vec{r},E,\hat{\Omega})$ represents the neutron source density per unit time, volume, energy, and solid angle, and Σ_s, $\nu\Sigma_f$, Σ_a and Σ_t are the scattering, fission production, absorption, and total cross sections, respectively. For a source arising only from fission events, which are assumed to be emitted isotropically, the source can be written as

$$Q(\vec{r}',\Omega',E')=\frac{1}{\lambda}\frac{1}{4\pi}\int_0^\infty dE_0\int_{4\pi} d\Omega_0\chi(E_0\rightarrow E')\nu\Sigma_f(\vec{r}',E_0)\psi(\vec{r}',\Omega_0,E_0) \tag{1.1.3}$$

Where $\chi(E_0\rightarrow E')$ is the energy spectrum of fissions that are induced by a neutron with incident energy E_0, and λ is a constant that balances the left and right sides of (1.1.1). For simplicity, the energy spectrum of emitted neutrons is assumed to be independent of the incident neutron energy that induced fission, i.e., $\chi(E_0\rightarrow E')=\chi(E')$, which is a common assumption [9]. This assumption simplifies (1.1.3) to

$$Q(\vec{r}',\Omega',E')=\frac{1}{\lambda}\frac{1}{4\pi}\chi(E')s(r') \tag{1.1.4}$$

where

$$s(\vec{r}\,') \equiv \int_0^\infty dE_0 \int_{4\pi} d\Omega_0 \nu\Sigma_f(\vec{r}\,', E_0)\psi(\vec{r}\,', \Omega_0, E_0), \tag{1.1.5}$$

which is the number of neutrons emitted at $\vec{r}\,'$ per unit volume and time.

The Green's function, *G*, associated with this transport problem is a solution of [10]

$$M\left[G(\vec{r}\,' \to \vec{r}, \hat{\Omega}' \to \hat{\Omega}, E' \to E)\right] = \delta(\vec{r} - \vec{r}\,')\delta(\hat{\Omega} - \hat{\Omega}')\delta(E - E'). \tag{1.1.6}$$

Multiplying (1.1.6) by $Q(\vec{r}\,', E', \hat{\Omega}')$ and integrating over all $\vec{r}\,', E', \hat{\Omega}'$ in the problem space yields

$$\int_V d^3r' \int_{4\pi} d\hat{\Omega}' \int_0^\infty dE' M\left[G(\vec{r}\,' \to \vec{r}, \hat{\Omega}' \to \hat{\Omega}, E' \to E)\right] Q(\vec{r}\,', \hat{\Omega}', E') = Q(\vec{r}, \hat{\Omega}, E). \tag{1.1.7}$$

The net loss operator is linear and does not act on an initial source point location, $\vec{r}\,', E', \hat{\Omega}'$; therefore, the net loss operator can be brought outside of the integration, i.e.,

$$M\left[\int_V d^3r' \int_{4\pi} d\hat{\Omega}' \int_0^\infty dE' G(\vec{r}\,' \to \vec{r}, \hat{\Omega}' \to \hat{\Omega}, E' \to E) Q(\vec{r}\,', \hat{\Omega}', E')\right] = Q(\vec{r}, \hat{\Omega}, E). \tag{1.1.8}$$

From the problem statement in (1.1.1), (1.1.8) can be expressed as

$$M\left[\int_V d^3r' \int_{4\pi} d\hat{\Omega}' \int_0^\infty dE' G(\vec{r}\,' \to \vec{r}, \hat{\Omega}' \to \hat{\Omega}, E' \to E) Q(\vec{r}\,', \hat{\Omega}', E')\right] = M\left[\psi(\vec{r}, \hat{\Omega}, E)\right]. \tag{1.1.9}$$

From the parallelism with respect to the net loss operator that is observable in (1.1.9), the angular flux can be formulated as

$$\psi(\vec{r}, \hat{\Omega}, E) = \int_V d^3r' \int_{4\pi} d\hat{\Omega}' \int_0^\infty dE' G(\vec{r}\,' \to \vec{r}, \hat{\Omega}' \to \hat{\Omega}, E' \to E) Q(\vec{r}\,', \hat{\Omega}', E'). \tag{1.1.10}$$

Inserting the fission source described by (1.1.4) into (1.1.10) yields

$$\psi(\vec{r}, \hat{\Omega}, E) = \frac{1}{\lambda} \int_V d^3r' \int_{4\pi} d\hat{\Omega}' \int_0^\infty dE' G(\vec{r}\,' \to \vec{r}, \hat{\Omega}' \to \hat{\Omega}, E' \to E) \frac{\chi(E')}{4\pi} s(\vec{r}\,'). \tag{1.1.11}$$

Multiplying both sides of (1.1.11) by $\nu\Sigma_f(\vec{r}, E)$ and then integrating over all *E* and $\hat{\Omega}$ yields

$$\int_0^\infty dE \int_{4\pi} d\hat{\Omega} \nu\Sigma_f(\vec{r}, E)\psi(\vec{r}, \hat{\Omega}, E) = \frac{1}{\lambda} \int_0^\infty dE \int_{4\pi} d\hat{\Omega} \nu\Sigma_f(\vec{r}, E) \cdot \int_V d^3r' \int_{4\pi} d\hat{\Omega}' \int_0^\infty dE' G(\vec{r}\,' \to \vec{r}, \hat{\Omega}' \to \hat{\Omega}, E' \to E) \frac{\chi(E')}{4\pi} s(\vec{r}\,'), \tag{1.1.12}$$

Which can be simplified using the definition in (1.1.5) to produce

$$s(\vec{r}) = \frac{1}{\lambda} \int_V d^3 r' s(\vec{r}') A(\vec{r}' \to \vec{r}) \tag{1.1.13}$$

Where the energy-angle averaged Green's function is

$$A(\vec{r}' \to \vec{r}) \equiv \int_0^\infty dE \int_{4\pi} d\hat{\Omega} \nu \Sigma_f(\vec{r}, E) \int_{4\pi} d\hat{\Omega}' \int_0^\infty dE' \frac{\chi(E')}{4\pi} G(\vec{r}' \to \vec{r}, \hat{\Omega}' \to \hat{\Omega}, E' \to E). \tag{1.1.14}$$

The integral in the right hand side of (1.1.13) shall be defined as the fission (neutron) production operator, H where

$$H[s(\vec{r})] \equiv \int_V d^3 r' s(\vec{r}') A(\vec{r}' \to \vec{r}). \tag{1.1.15}$$

This definition of the fission production operator casts the integral transport equation into a classic eigenvalue problem, i.e.,

$$H[b_n(\vec{r})] = \lambda_n b_n(\vec{r}) \quad \forall n \in \mathbb{Z} > 0 \tag{1.1.16}$$

where λ_n is the eigenvalue of the n^{th} mode, and $b_n(\vec{r})$ is the right eigenfunction that corresponds with the eigenvalue λ_n. In this dissertation, the indices are set such that the eigenvalues are ordered from largest to smallest, i.e., $\lambda_1 > |\lambda_2| \geq \ldots \geq |\lambda_n| \geq 0$. The operator H is always non-negative because neutrons can only escape, be captured, or cause fission, and the operator is linear [9]. The operator is generally not symmetric for multi-group or continuous energy problems [10]. From the Perron-Frobenius theorem, the first eigenvalue and eigenfunction are guaranteed to be non-negative [11]–[13].

In this work, casting the continuous space into a discrete one is frequently helpful for understanding and implementation purposes. This is achieved through the fission matrix formalism [14]. The fission matrix F can be obtained by integrating a fission density function over a set of *N* subdivisions of the physical problem space where each region is denoted by its volume V_j, i.e.,

$$S(i) = \int_{r \in V_i} s(\vec{r}) d\vec{r} \quad \forall i \in \{1..N\}, \tag{1.1.17}$$

and integrating (1.1.13) over the subdivision V_i, which yields

$$\begin{aligned}
\int_{\vec{r}\in V_i} d^3r\, s(\vec{r}) &= \frac{1}{\lambda_n}\int_{\vec{r}\in V_i} d^3r \int_V d^3r'\, s(\vec{r}\,')A(\vec{r}\,'\to\vec{r}) \\
S(i) &= \frac{1}{\lambda_n}\int_V d^3r' \int_{\vec{r}\in V_i} d^3r\, s(\vec{r}\,')A(\vec{r}\,'\to\vec{r}) \\
S(i) &= \frac{1}{\lambda_n}\sum_{j=1}^{N}\int_{\vec{r}'\in V_j} d^3r' \int_{\vec{r}\in V_i} d^3r\, s(\vec{r}\,')A(\vec{r}\,'\to\vec{r}) \\
S(i) &= \frac{1}{\lambda_n}\sum_{j=1}^{N} F(i,j)S(j)
\end{aligned} \tag{1.1.18}$$

where $S(i)$ is the number of fissions per generation inside subdivision V_i, and the row i and column j entry of the fission matrix is

$$F(i,j) = \int_{\vec{r}'\in V_j} d^3r' \int_{\vec{r}\in V_i} d^3r \frac{s(\vec{r}\,')}{S(j)} A(\vec{r}\,'\to\vec{r}). \tag{1.1.19}$$

The fission matrix element $F(i,j)$ is equal to the average number of fission neutrons born in region V_i from one average fission neutron born in region V_j. The fission matrix has associated eigenvalues $\Lambda_1 > |\Lambda_2| \geq \ldots \geq 0$ and right eigenvectors $\{B_1, B_{2,}\ldots\}$. The fundamental mode eigenvalue of F is equivalent to that of H because all that has been done is casting the source as a vector with no approximation. There is no basis for assuming that the multiplicity of any eigenvalue is 1 other than for the fundamental, nor that the geometric multiplicity of an eigenvalue is equal to the algebraic multiplicity; therefore, the eigenvectors may not necessarily comprise a basis for the problem space. For a small enough region size, $S(i)/V_i$ is a discrete approximation to the actual continuous source distribution $s(\vec{r})$ [10]. Empirical evidence obtained from refining the mesh used to generate a fission matrix indicates that higher modes do exist and that the fission matrix eigenvalues can be accurate representations of the continuous fission production operator eigenvalues [10].

To discern properties of convergence for an iterative solving technique, decomposing a source function into its eigenfunction components is often useful. The left $\{b_1^\dagger, b_2^\dagger, \ldots\}$ and right $\{b_1, b_2, \ldots\}$ eigenfunctions of a linear operator are orthogonal according to the relationships,

$$(\lambda_i - \lambda_j) b_i^\dagger \cdot b_j = 0. \tag{1.1.20}$$

These orthogonality relations allow one to calculate a decomposition of a function into eigenfunction components. Any function $f(\vec{r})$ in the span of $\{b_1, b_2, ...\}$ can be expressed as a functional expansion in terms of the eigenbasis, i.e.,

$$f(\vec{r}) = \sum_n \beta_n b_n(\vec{r}) \tag{1.1.21}$$

where β_n is the decomposition coefficient (DC) of the n^{th} mode (eigenfunction). For convenience, the eigenfunctions are normalized such that

$$\int b_n^2(\vec{r})\, d^3 r = 1\,, \tag{1.1.22}$$

And the left eigenfunctions are normalized such that

$$\int b_n^\dagger(\vec{r}) b_n(\vec{r})\, d^3 r = 1\,. \tag{1.1.23}$$

With these chosen normalizations and the orthogonality relation in (1.1.20), the DCs are calculated according to

$$\beta_n = \int b_n^\dagger(\vec{r}) f(\vec{r})\, d^3 r\,. \tag{1.1.24}$$

A similar set of definitions and relations applies to the discrete eigenvectors. From linear algebra, the sets of left $\{B_1^\dagger, B_2^\dagger, ...\}$ and right $\{B_1, B_2, ...\}$ eigenvectors for a matrix follow the orthogonality relationship,

$$(\Lambda_i - \Lambda_j) B_i^\dagger \cdot B_j = 0. \tag{1.1.25}$$

Any vector V in the span of $\{B_1, B_2, ...\}$ can be expressed as a combination of eigenvectors, i.e.,

$$V = \sum_n \beta_n B_n. \tag{1.1.26}$$

For convenience, the eigenvectors are normalized such that the dot product is

$$B_n \cdot B_n = 1\,, \tag{1.1.27}$$

And the left eigenvectors are normalized such that

$$B_n^\dagger \cdot B_n = 1\,. \tag{1.1.28}$$

With these chosen normalizations and the orthogonality relation in (1.1.25), the DCs are calculated according to

$$\beta_n = B_n^\dagger \cdot V\,. \tag{1.1.29}$$

For this work, all initial source distributions will be in the span of *H* and the eigenspace will be assumed to span the same subspace as *H* such that naturally valid source distributions can be reconstructed from their eigenfunction decomposition. For codes which allow the initial source to be non-zero in non-fissile regions, the source distribution is not in the span of *H*. In such cases at least one discarded cycle would be required to avoid erroneous fission matrix entries. The eigenspace for a problem is generally not known in advance, but can be estimated from eigenvector solutions of the fission matrix. The power method is another technique, which can find the first eigenvalue and eigenfunction.

1.2 Power Method

The power method is an iterative numerical technique from linear algebra, which powers out the presence of non-fundamental eigenmodes from an initial guess for the fundamental mode [9]. The iteration can be expressed as

$$u^{(m+1)}(\vec{r}) = k^{(m+1)} H[u^{(m)}(\vec{r})] \quad \forall\, m \geq 0 \tag{1.2.1}$$

where $u^{(m)}(\vec{r})$, which shall be called the source bank, is the spatial distribution of fission neutrons after *m* applications of the fission operator, and $k^{(m)}$ is the normalization constant used after the m^{th} application of the fission operator. One can decompose the initial guess $u^{(0)}$ as

$$u^{(0)}(\vec{r}) \equiv \sum_{n=1}^{\infty} \beta_n b_n(\vec{r}) \tag{1.2.2}$$

where β_n is defined as the initial source bank decomposition coefficient (SBDC) corresponding to mode *n*, which may also be referenced as $u_n^{(0)}$. Furthermore, all iterates have eigenmode decompositions

$$u^{(m)}(\vec{r}) \equiv \sum_{n=1}^{\infty} u_n^{(m)} b_n(\vec{r}) \quad \forall m \geq 0 \tag{1.2.3}$$

where $u_n^{(m)}$ is the SBDC of $u^{(m)}(\vec{r})$ for the n^{th}-mode after *m* applications of the fission operator with normalization. Using (1.1.16) and the linearity of the fission operator, (1.2.1) becomes

$$u^{(m+1)}(\vec{r}) = k^{(m+1)} \sum_{n=1}^{\infty} \lambda_n u_n^{(m)} b_n(\vec{r}). \tag{1.2.4}$$

By recursion, (1.2.4) can be generalized into

$$u^{(m+M)}(\vec{r}) = \sum_{n=1}^{\infty} \left[\left(\prod_{l=1}^{M} k^{(m+l)} \right) \lambda_n^M u_n^{(m)} b_n(\vec{r}) \right] \quad \forall M \geq 1 . \tag{1.2.5}$$

The recursion in (1.2.5) can be carried through to the initial guess, which yields

$$u^{(m)}(\vec{r}) = \sum_{n=1}^{\infty} \left[\left(\prod_{l=1}^{m} k^{(l)} \right) \lambda_n^m \beta_n b_n(\vec{r}) \right] \quad \forall m \geq 1 . \tag{1.2.6}$$

The normalization coefficients must be prescribed in such a way that the eigenfunction estimates converge to a scalar multiple of the fundamental mode as the number of cycles approaches infinity. For ease of demonstration, the inverse of the largest eigenvalue is used as the normalization coefficient for all cycles of the deterministic power method. In practice, the eigenfunction estimate is normalized to satisfy a particular norm, typically the one or two-norm, and the Rayleigh quotient is the estimate for the fundamental eigenvalue [15]. By inserting this idealized normalization constant, (1.2.6) becomes

$$u^{(m)}(\vec{r}) = \sum_{n=1}^{\infty} \left(\frac{\lambda_n}{\lambda_1} \right)^m \beta_n b_n(\vec{r}) \ . \tag{1.2.7}$$

Under this normalization, the SBDCs at cycle *m* are

$$u_n^{(m)} = \left(\frac{\lambda_n}{\lambda_1} \right)^m \beta_n \ . \tag{1.2.8}$$

As evidenced by (1.2.8), the presence of each non-fundamental mode will decay after every cycle by the ratio of its eigenvalue to the largest eigenvalue. By definition, the decay coefficient of mode *n* is λ_n / λ_1. A higher decay coefficient indicates that the presence of a mode will diminish slower than a mode with a lower decay coefficient. The deterministic power method iteration is terminated when some specified criteria is met. The criteria are typically related to the ratio of the current eigenfunction or eigenvalue estimate to the estimate calculated by the previous cycle [16].

1.3 Extrapolation

For certain problems, the rate of convergence (rate of decay) of a non-fundamental mode

may be prohibitively slow because the eigenvalue is very close to the fundamental mode eigenvalue [16]. The change observed in an eigenfunction estimate from a single application of the neutron production operator is typically much less than what would be needed to eliminate the non-fundamental mode; therefore, one could conceivably arrive at a better estimate by pushing the eigenfunction estimate further in the direction of the observed change. This notion is extrapolation, a subset of relaxation iterative techniques in linear algebra [17]. The most basic form of extrapolation is constant single-parameter linear extrapolation, which modifies the iteration defined in (1.2.1) to

$$v^{(m+1)}(\vec{r}) = k^{(m+1)} H\left[v^{(m)}(\vec{r})\right] + \alpha\left(k^{(m+1)} H\left[v^{(m)}(\vec{r})\right] - v^{(m)}(\vec{r})\right) \text{ for } m \geq 0 \tag{1.3.1}$$

where α is the extrapolation parameter, $v^{(m)}(\vec{r})$ is the eigenfunction estimate after completing cycle m, and the initial guess is

$$v^{(0)}(\vec{r}) = u^{(0)}(\vec{r}) \equiv \sum_{n=1}^{\infty} \beta_n b_n(\vec{r}). \tag{1.3.2}$$

Each of the other iterates have the decompositions

$$v^{(m)}(\vec{r}) \equiv \sum_{n=1}^{\infty} v_n^{(m)} b_n(\vec{r}) \tag{1.3.3}$$

where $v_n^{(m)}$ is the n^{th}-mode SBDC of the extrapolated eigenfunction estimate, $v^{(m)}(\vec{r})$, upon completing cycle m. The change of symbol from u to v differentiates the extrapolated algorithm from the standard power method in this text.

Using (1.1.16) and the linearity of the fission operator, (1.3.1) becomes

$$v^{(m+1)}(\vec{r}) = k^{(m+1)} \sum_{n=1}^{\infty} \lambda_n v_n^{(m)}(\vec{r}) + \alpha \sum_{n=1}^{\infty} \left[k^{(m+1)} \lambda_n v_n^{(m)}(\vec{r}) - v_n^{(m)}(\vec{r})\right]. \tag{1.3.4}$$

The summations in (1.3.4) can be grouped together yielding

$$v^{(m+1)}(\vec{r}) = \sum_{n=1}^{\infty} \left[(1+\alpha) k^{(m+1)} \lambda_n - 1\right] v_n^{(m)}(\vec{r}). \tag{1.3.5}$$

By recursion, (1.3.5) can be used to prescribe the fundamental eigenfunction estimate after M cycles from a given starting cycle m, i.e.,

$$v^{(m+M)}(\vec{r}) = \sum_{n=1}^{\infty} \left\{ \prod_{i=1}^{M} \left[(1+\alpha) k^{(m+i)} \lambda_n - 1\right] v_n^{(m)}(\vec{r}) \right\}. \tag{1.3.6}$$

The recursion of (1.3.5) can also be executed back to the initial guess to predict the fundamental eigenfunction estimate after completing a total of m cycles, i.e.,

$$v^{(m)}(\vec{r})=\sum_{n=1}^{\infty}\left\{\prod_{i=1}^{m}\left[(1+\alpha)k^{(i)}\lambda_n-1\right]\beta_n b_n(\vec{r})\right\}. \tag{1.3.7}$$

For demonstrative purposes, the inverse of the largest eigenvalue is used as the normalization coefficient for all cycles of the deterministic extrapolated power method. Inserting this normalization coefficient into (1.3.7) yields

$$v^{(m)}(\vec{r})=\sum_{n=1}^{\infty}\left((1+\alpha)\frac{\lambda_n}{\lambda_1}-\alpha\right)^m\beta_n b_n(\vec{r}). \tag{1.3.8}$$

Therefore at cycle *m*, the SBDCs of the extrapolated algorithm are

$$v_n^{(m)}=\left((1+\alpha)\frac{\lambda_n}{\lambda_1}-\alpha\right)^m\beta_n. \tag{1.3.9}$$

And the corresponding decay coefficients are

$$\eta_n=(1+\alpha)\frac{\lambda_n}{\lambda_1}-\alpha. \tag{1.3.10}$$

A positive extrapolation parameter shifts all the decay coefficients of non-fundamental modes lower because the eigenvalue ratios with the fundamental mode are less than unity. This makes the second harmonic component of the eigenfunction estimate converge faster until $\alpha=\lambda_2/(\lambda_1-\lambda_2)$. Increasing α beyond that value pushes the decay coefficient away from zero in the negative direction, which causes oscillations in the DC. The convergence rate (CR) shall be defined as one minus the absolute value of the decay coefficient, i.e.,

$$CR=1-|\eta_n|. \tag{1.3.11}$$

The convergence rate is dictated only by the magnitude of the decay coefficient with a higher convergence rate being preferred over a lower one. Figure 1.3.1 shows the relationship between the eigenvalue ratio and the decay coefficient and the convergence rate for several different choices of the extrapolation parameter. As evidenced by the figure, extrapolation shifts the convergence rates of the slowest converging modes toward those modes with lower eigenvalue ratios while the modes with the lowest eigenvalue ratios will converge slower than they would have under the standard power method algorithm [18]. When the extrapolation parameter is too large, the convergence rate

becomes negative, which indicates a divergent sequence for those modes with the negative rate. For the extrapolated algorithm to converge, the magnitude of all non-fundamental mode decay coefficients must be less than one. Therefore, the modes with the lowest eigenvalues limit the gain in the convergence rate that can be achieved for the slowest converging modes. The magnitude of all non-fundamental decay coefficients are less than 1 when

$$-1<\alpha<\frac{1+\lambda_n/\lambda_1}{1-\lambda_n/\lambda_1} \tag{1.3.12}$$

for all modes [18]. Assuming that the smallest eigenvalue is equal to 0, convergence is only guaranteed for $|\alpha|<1.0$. The optimum value of α, which maximizes the convergence rate of all modes under this condition is [18]

$$\alpha=\frac{\lambda_2}{2\lambda_1-\lambda_2}. \tag{1.3.13}$$

All of the analysis up to this point applies to a deterministic linear operator. The remainder of this document will turn its focus toward stochastic operators encountered in MC transport.

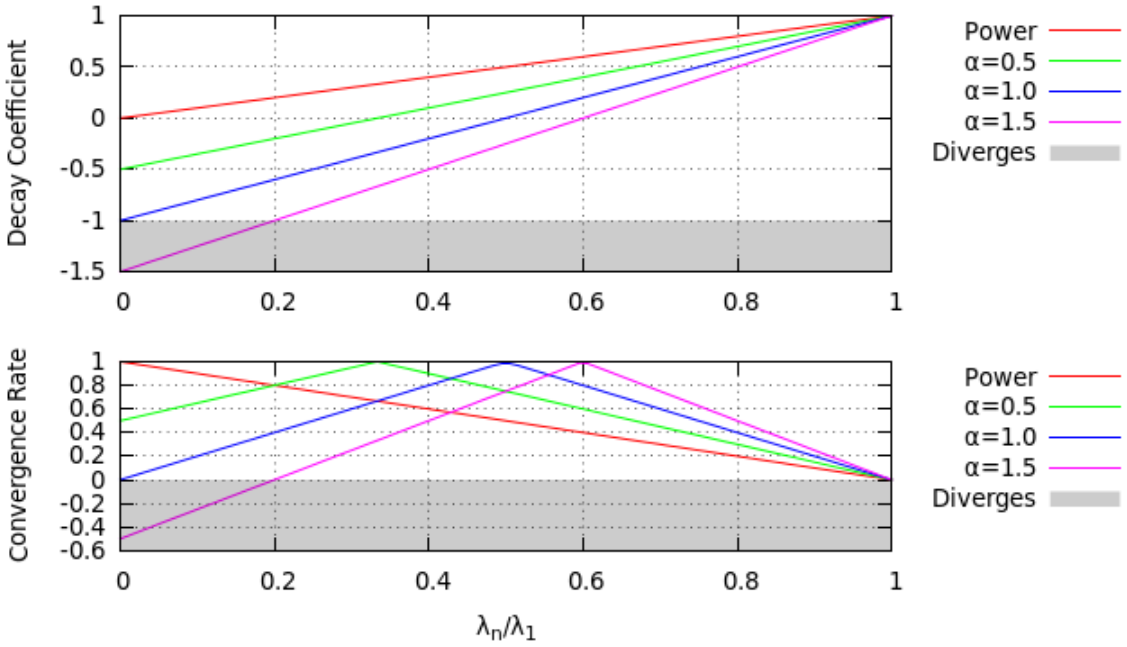

Figure 1.3.1 The decay coefficient (1.3.10) and convergence rate (1.3.11) versus eigenvalue ratio for several different levels of extrapolation and the standard power method.

1.4 Prior MC Extrapolation Research

Several researchers have investigated the use of extrapolation for accelerating the convergence of MC neutron source iterations. Gast and Candelore show that linear extrapolation is a “fair game” strategy when the number of histories per cycle approaches infinity in the limit of infinitely many cycles, which is the same for the power method [8]. However, Gast and Candelore reported no improvement in convergence rate from their implementation of linear extrapolation. Gast and Candelore did not publish any data or measures for convergence to support their conclusion [8]. Additionally, an implementation of Chebyshev polynomial extrapolation, which uses the previous 2 cycles to improve the next source estimate did not produce an improvement in convergence rates [7]. Swaja cited private communications with Gast and Candelore in his dissertation and used similar terminology [7]; therefore, the author assumes that Gast and Candelore used a measure of convergence that is similar to the one reported by Swaja. Swaja measured source convergence by combining how much each mesh bin differed from the reference solution relative to the uncertainty in each bin from a reference power method simulation [7]. Such a measure is inadequate for recognizing the benefit from extrapolation because extrapolation amplifies the variance in each bin, which obscures its ability to hasten convergence of the mean.

Gast and Candelore define a fair game for MC source convergence as

$$\lim_{M\to\infty}\left[P\left|\frac{1}{M}\sum_{m=1}^{M}\left(u^{(m)}(\vec{r})-u_1(\vec{r})\right)\right|<\epsilon\right]=1 \quad \forall\vec{r}\in V,\ \epsilon>0 \tag{1.4.1}$$

Where P denotes the probability that the normalized sum is less than some arbitrarily set criterion ϵ, and M is the total number of cycles [8]. This is a desirable property for an iteration to possess because it ensures that the normalized summation of all eigenfunction estimates will tend toward the fundamental mode. An extrapolated power method algorithm yields an unbiased estimate for the shape of the fundamental mode under the same conditions as the power method [8]. However, Gast and Candelore did not observe acceleration of convergence rate from use of extrapolation, which they attributed to noise

in the source distribution difference calculation [8]. They claimed to have used as many as 2000 histories per cycle [8], which is relatively low for modern computers. The test problem was not described, nor proof of the assertion published.

Swaja implemented a Chebyshev polynomial extrapolation method, which extrapolates using two prior eigenfunction estimates, i.e.

$$v^{(m+1)} = v^{(m)} + \alpha^{(m)}\left(k^{(m)} H\left[v^{(m)}\right] - v^{(m)}\right) + \beta^{(m)}\left(v^{(m)} - v^{(m-1)}\right) \tag{1.4.2}$$

Where $\alpha^{(m)}$ and $\beta^{(m)}$ are extrapolation parameters [7]. The parameters are determined from

$$\alpha^{(0)} = 2\left(2 - \frac{\lambda_2}{\lambda_1}\right)^{-1}, \quad \alpha^{(m)} = 4\frac{\lambda_0}{\lambda_1}\frac{\cosh m\gamma}{\cosh(m+1)\gamma} \quad \forall m \geq 1, \tag{1.4.3}$$

and

$$\beta^{(0)} = 0, \quad \beta^{(m)} = \frac{\cosh(m-1)\gamma}{\cosh(m+1)\gamma} \quad \forall m \geq 1, \tag{1.4.4}$$

where

$$\gamma = \cosh^{-1} 2\left(\frac{\lambda_2}{\lambda_1} - 1\right)^{-1}. \tag{1.4.5}$$

Swaja created a new diagnostic for assessing convergence [7]. He defined $PE(i)$, the probable error of the i^{th} bin of a discretized source distribution, as the variance of the fraction of fissions occurring in the i^{th} bin multiplied by the constant 0.6745, such that 50% of samples should lie within 1 probable error of the mean fission fraction [7]. The fission fraction is the ratio of the total weight or number of progeny produced in the i^{th} bin to the total weight or number of progeny in all bins. However, he did not describe exactly how the probable error was calculated for his reference calculations, but a different probable error appears to be used for each test problem and each bin within a problem. He additionally describes the number of probable errors that the discretized source distribution deviates from the converged value as

$$NPE^{(m)}(i) = \left|\frac{\widetilde{V}^{(m)}(i) - B_1(i)}{PE(i)}\right| \tag{1.4.6}$$

where $\widetilde{V}^{(m)}$ is the discretized MC eigenfunction estimate in the m^{th} cycle, and B_1 is the

discretized fundamental mode [7]. Furthermore, he defined the performance coefficient,

$$PC^{(m)} = \sum_{r=1}^{R^{(m)}} \left[\text{number of bins with } NPE^{(m)}(i) > r \right], \tag{1.4.7}$$

where $R^{(m)}$ is the smallest integer greater than or equal to the maximum value of $NPE^{(m)}(i)$ for all bins [7]. He recommends that a performance coefficient greater than twice the number of bins indicates that the fission fractions of bins are not well converged, while a performance coefficient of 0 shows that all bins are perfectly converged, and one can expect an average of 7.5 from infinitely many cycles [7]. He reasoned that an iterative scheme with a lower performance coefficient after a certain number of cycles than the reference, a power method iteration, would indicate an improvement in convergence [7].

Swaja tested Chebyshev on 10 region slabs with 1-group macroscopic cross sections $\nu\Sigma_f = \Sigma_t = 1$ and widths of 2, 10, 20, and 40 mean free paths to collision [7]. The test calculations of Swaja began with 500 particles per cycle with that number increasing by 10 at each cycle, and the initial source point distribution had each bin within 2 probable errors of the fundamental mode. [7] According to Swaja, these test problems are similar to those used by Gast and Candelore [7], [8]. For all calculations performed by Swaja, the performance coefficient in nearly all cycles of the Chebyshev extrapolated cycles were higher than performance coefficients of their respective power method analogs, which Swaja attributed to statistical noise [7].

The failures observed by Swaja for Chebyshev extrapolation are attributable to noise because his performance coefficient is highly sensitive to amplification of noise. Extrapolation increases the noise in the eigenfunction estimates [7], [8], [19]. For a source estimate that approaches the fundamental mode, the number of probable errors that a fission fraction deviates from the fundamental mode becomes highly correlated with the variance of the fission fraction. The variance of a bin is

$$Var[\tilde{V}^{(m)}(i)] = E\left[\left|\tilde{V}^{(m)}(i) - E\left[\tilde{V}^{(m)}(i)\right]\right|^2\right], \tag{1.4.8}$$

which in the limit of many cycle becomes

$$\lim_{m\to\infty} Var[\widetilde{V}^{(m)}(i)] = E\left[\left|\widetilde{V}^{(m)}(i) - B_n(i)\right|^2\right] \tag{1.4.9}$$

because extrapolation is a fair game. Comparing (1.4.6) with (1.4.9), one can see that the variance is the expected value of the number of probable errors squared when scaled by the inverse of the probable error, i.e.,

$$\frac{\lim_{m\to\infty} Var[\widetilde{V}^{(m)}(i)]}{(PE(i))^2} = E\left[\left|\frac{\widetilde{V}^{(m)}(i) - U_B(i)}{PE(i)}\right|^2\right] = E\left[(NPE(i))^2\right]. \tag{1.4.10}$$

Therefore, for the sources used by Swaja [7] and Gast and Candelore [8], which were selected to be within 2 probable errors of the fundamental mode, the expected number of probable errors and the performance coefficient was assured to be greater when using extrapolation because extrapolation increases the variance. If the researchers had turned off the extrapolation method prior to convergence of the reference power method, then they may have observed an improvement in the performance coefficient by allowing the noise to decay, which Chapter 4 shows. In Chapter 4, a different diagnostic is proposed that measures convergence in the mean and variance of the eigenvector components of the fission source distribution to better determine convergence acceleration.

Chapter 2. Spectral Analysis of Standard and Extrapolated Monte Carlo

In the physical world, neutron transport is a sequence of stochastic events. A neutron is born from some radiation source at a random position with a direction and energy also determined randomly. The particle travels randomly sampled distances from collision to collision until eventually being absorbed or leaving the region of interest. At each collision, the neutron has a probability of being absorbed into the nucleus or scattering. A scattering event changes the direction and energy of the neutron. Absorption terminates the particle, but for certain materials there exists a probability that the nucleus will produce progeny, which can continue a chain reaction. MC neutron transport algorithms embrace a methodology that mimics the natural behavior of neutrons. Rather than attempt to solve linear systems of equations derived from the Boltzmann transport equation, MC methods estimate desired quantities by aggregating results from a multitude of simulated events that are sampled randomly from the probability density functions (PDFs) associated with fundamental particle interactions in matter [1], [4]. To obtain the correct result with a reasonable uncertainty band, an adequate number of events must be sampled from the correct source distribution, which is the fundamental mode [3], [4], [20].

To find the effective multiplication factor and fundamental mode of fissile systems with MC, the method of successive generations is applied, which is the MC analog to the standard power method of linear algebra [4], [21]. The expected behavior of the eigenfunction components of the fundamental mode estimates at each cycle are presented. The expectations are useful when determining how many cycles are sufficient to obtain a reasonable approximation of the fundamental mode. The number of cycles that are sufficient to estimate the fundamental mode may be large, hindering the ability to

use MC as a solution technique for some problems [22]. The number of cycles needed to obtain a reasonable approximation of the fundamental mode can be reduced by applying extrapolation to the fission eigenvalue problem, which this chapter addresses. However, extrapolation amplifies the noise inherent in the MC process, which leads to increased uncertainty in the fundamental mode estimates as this chapter shows. Therefore, a detailed noise analysis is provided and used to better characterize what is meant by a "reasonable approximation," which may also be referred to as a converged fission source.

2.1 Monte Carlo Eigenvalue Calculations

The Boltzmann transport equation fully describes the expectation of the neutron angular flux; however, the equation can be difficult to solve without introducing errors from discretization of the physical geometry and/or particle interaction probabilities (cross-sections) [9]. MC transport algorithms attempt to arrive at the same results as would be obtained from solving the Boltzmann transport equation by performing random transport of many pseudo-particles and averaging the results [1]. MC methods do not need to introduce discretization of the geometry, and MC methods can use the best available cross-section data, but all MC results have an associated uncertainty because of the stochastic nature of the algorithm [23].

The life of a particle from birth to absorption or escape is known as a particle history [4]. MC eigenvalue calculations begin with a bank of $L^{(0)}$ neutron birth positions where $L^{(0)}$ is a positive integer. Those initial positions may be sampled from a distribution provided by the user; the positions can come from a previous MC calculation, or they could all be located at the same or multiple specified points, such as the problem center. This first bank of neutron source sites is the initial guess for the fundamental mode. The source bank can be represented in functional form as

$$\tilde{u}^{(0)}(\vec{r}) = \sum_{l=1}^{L^{(0)}} q_l^{(0)} \delta(\vec{r} - \vec{r}_l^{(0)}) \tag{2.1.1}$$

Where δ is the Dirac delta function, $q_l^{(0)}$ is the tally weight of the l^{th} source point, and $\vec{r}_l^{(0)}$ is the position of the l^{th} source point in the initial guess, cycle 0, bank.

Then, the MC simulation randomly samples the neutron starting directions and energies from known distributions corresponding to the material at the birth position [1]. Afterwards, the neutron is transported through the problem space by sampling a distance to collision [23]. At a collision, the location is stored in a new bank $\hat{u}^{(1)}$, which will be referred to as the intermediate bank, with an associated fission production weight w that depends on the location $\vec{r}$ of the collision according to

$$w(\vec{r}) = q\, p_a(\vec{r}) \frac{\nu \Sigma_f(\vec{r})}{\Sigma_a(\vec{r})} \tag{2.1.2}$$

where q is the tally weight of the particle entering the collision, and $p_a(\vec{r})$ is the probability of absorption. The probability of absorption may be the physical probability of absorption, i.e. $\Sigma_a(\vec{r})/\Sigma_t(\vec{r})$, or the probability can be adjusted by sampling done to determine the event or set the fission production weight to an integer. If a sampled distance to collision reaches outside the specified problem geometry, then the particle is considered to be absorbed just outside the problem geometry with zero production weight. In analog MC, histories are terminated when an absorption event is sampled or a particle escapes [1]. Since only one absorption is possible under analog MC, the intermediate bank can contain at most $L^{(0)}$ locations with non-zero fission production weights. In contrast, implicit capture MC treats a fraction of the particle as absorbed at each collision, and the remainder continues to move through the problem as though it scattered. The particle exits each collision with a reduced tally weight according to the fraction absorbed. Whenever the tally weight drops below a cutoff value, the particle undergoes a Russian roulette procedure [1]. Histories will eventually be killed by roulette or escape from the region of interest. Either of these procedures, implicit capture or analog capture, can be viewed as the MC fission production operator $\widetilde{H}$, which is the MC representation of the fission production operator defined in (1.1.15). In essence, $\widetilde{H}$ transfers a source point to one or more collision positions and gives each collision location an associated neutron production weight. In implementations, sites with zero production weight are not actually stored because they are not used in the following cycle.

After tracking $L^{(0)}$ neutrons from birth to death, the intermediate bank contains a set of collision positions which provide a new fission distribution estimate when combined with their production weights,

$$\hat{u}^{(1)}(\vec{r}) = \sum_{l=1}^{L^{(0)}} \sum_{c=0}^{C_l} w\left(\vec{r}_{l,c}^{(1)}\right) \delta\left(\vec{r} - \vec{r}_{l,c}^{(1)}\right) = \widetilde{H}\left[\widetilde{u}^{(0)}(\vec{r})\right] \tag{2.1.3}$$

where C_l is the number of collisions in history *l*, and $\vec{r}_{l,c}^{(1)}$ is the location of the c^{th} collision in history *l*. With the standard power method, the intermediate bank is normalized by the operator $\widetilde{k}^{(1)}$ to yield the fission source bank for use in the next cycle;

$$\widetilde{u}^{(1)}(\vec{r}) = \widetilde{k}^{(1)} \hat{u}^{(1)}(\vec{r}) = \widetilde{k}^{(1)} \widetilde{H}[\widetilde{u}^{(0)}(\vec{r})] . \tag{2.1.4}$$

Another cycle is begun using $\tilde{u}^{(1)}(\vec{r})$ and the iterative procedure continues until a specified *M* cycles complete. The resulting source point distribution at cycle *m* is

$$\widetilde{u}^{(m)}(\vec{r}) = \widetilde{k}^{(m)} \widetilde{H}[\widetilde{u}^{(m-1)}] = \left(\prod_{i=1}^{m} \widetilde{k}^{(i)} \right) \widetilde{H}^m[\widetilde{u}^0(\vec{r})] \tag{2.1.5}$$

where $\tilde{k}^{(m)}$ is the normalization procedure applied to the set of fission source points that result from the m^{th} application of the MC fission operator. The normalization by $\widetilde{k}^{(m)}$ has a variety of possible implementations, but it can be thought of as a scalar that keeps the total starting tally weight constant and equal to 1 between cycles, thus it approaches in probability to the inverse of the effective multiplication factor as the source distribution converges. The normalization in (2.1.5) helps ensure that the iteration will converge to a finite eigenfunction estimate. The algorithm must restart source points if there are ever no fission sites generated by a particular cycle [8]. For algorithms used in this work, the normalization sets each source bank to have a constant *L* points with uniform tally weights equal to L^{-1}, but this is not a requirement. One could easily start a variable number of neutrons in each cycle with or without different weights in any fashion where the total starting weight at each cycle is kept constant. The details of the normalization procedure will affect the amount of noise in each cycle, but the behavior described in the derivations to follow are not expected to change. Normalization by a stochastic quantity introduces a bias in the eigenfunction estimate [4], [24], [25]; however, adequate numbers of histories can mitigate the bias, and thus, the bias will generally be ignored in this

dissertation.

2.2 Expectations from the Stochastic Power Method

Consider a MC fission operator $\tilde{H}$, which is an unbiased estimator of the true fission operator *H*, such that

$$E[\tilde{H}[\tilde{u}(\vec{r})]]=H[\tilde{u}(\vec{r})] \tag{2.2.1}$$

Where *E*[*] denotes the expected value of *, and $\tilde{u}(\vec{r})$ is some distribution of fission source points. This implies that

$$\widetilde{H}[\widetilde{u}(\vec{r})]=H[\widetilde{u}(\vec{r})]+\zeta(\vec{r}) \tag{2.2.2}$$

Where $\zeta(\vec{r})$ is a random function with zero mean, i.e.,

$$E[\zeta(\vec{r})]=0\ . \tag{2.2.3}$$

A typical MC code implements the power method [26] to construct an iterative scheme that can solve for the fundamental eigenmode $b_1(\vec{r})$ as follows

$$\widetilde{u}^{(m+1)}(\vec{r})=\widetilde{k}^{(m+1)}\widetilde{H}[\widetilde{u}^{(m)}(\vec{r})]=\widetilde{k}^{(m+1)}H[\widetilde{u}^{(m)}(\vec{r})]+\xi^{(m+1)}(\vec{r}) \quad \forall m\geq 0 \tag{2.2.4}$$

where $\xi^{(m)}(\vec{r})$ is the deviation from the expected result of applying the MC fission operator to the source bank of the m^{th} transport cycle after absorbing the normalization coefficient, i.e.,

$$\xi^{(m)}(\vec{r})=\widetilde{k}^{(m)}\zeta^{(m)}(\vec{r}) \quad \forall m\geq 1\ . \tag{2.2.5}$$

Henceforth, $\xi^{(m)}(\vec{r})$ shall be referred to as the deviation function of cycle *m*, and $\zeta^{(m)}(\vec{r})$ will be called the unnormalized deviation function of cycle *m*.

The eigenfunction estimate in (2.2.4) can be expressed as a decomposition in the eigenbasis

$$\widetilde{u}^{(m+1)}(\vec{r})\equiv\sum_{n=1}^{\infty}\widetilde{u}_n^{(m+1)}b_n(\vec{r})=\widetilde{k}^{(m+1)}H\left[\sum_{n=1}^{\infty}\widetilde{u}_n^{(m)}b_n(\vec{r})\right]+\sum_{n=1}^{\infty}\xi_n^{(m+1)}b_n(\vec{r}) \tag{2.2.6}$$

where $\xi_n^{(m)}$ is the deviation function decomposition coefficient (DFDC) of the n^{th} mode at cycle *m*. Using the linearity of the fission operator, (2.2.6) becomes

$$\widetilde{u}^{(m+1)}(\vec{r})=\widetilde{k}^{(m+1)}\sum_{n=1}^{\infty}\widetilde{u}_n^{(m)}H\left[b_n(\vec{r})\right]+\sum_{n=1}^{\infty}\xi_n^{(m+1)}b_n(\vec{r}). \tag{2.2.7}$$

From the definition of eigenvalues and eigenfunctions, which appears in (1.1.16), the fission operator applied to an eigenfunction can be simplified to the eigenfunction

multiplied by the corresponding eigenvalue, which reduces (2.2.7) to

$$\widetilde{u}^{(m+1)}(\vec{r}) = \widetilde{k}^{(m+1)} \sum_{n=1}^{\infty} \lambda_n \widetilde{u}_n^{(m)} b_n(\vec{r}) + \sum_{n=1}^{\infty} \xi_n^{(m+1)} b_n(\vec{r}). \tag{2.2.8}$$

Therefore, the SBDCs from the MC power method are

$$\widetilde{u}_n^{(m+1)} = \widetilde{k}^{(m+1)} \lambda_n \widetilde{u}_n^{(m)} + \xi_n^{(m+1)}. \tag{2.2.9}$$

Equation (2.2.9) describes a recursive relationship. The recursion executed back to the initial guess yields

$$\widetilde{u}_n^{(m)} = \beta_n \lambda_n^m \prod_{i=1}^{m} \widetilde{k}^{(i)} + \xi_n^{(m)} + \sum_{i=1}^{m-1} \lambda_n^i \xi_n^{(m-i)} \prod_{j=0}^{i-1} \widetilde{k}^{(m-j)} \quad \forall\, m \in \mathbb{Z} \geq 2\,. \tag{2.2.10}$$

The SBDCs of (2.2.10) can also be expressed in terms of the unnormalized DFDCs, $\zeta_n^{(m)}$, i.e.,

$$\widetilde{u}_n^{(m)} = \beta_n \lambda_n^m \prod_{i=1}^{m} \widetilde{k}^{(i)} + \sum_{i=0}^{m-1} \lambda_n^i \zeta_n^{(m-i)} \prod_{j=0}^{i} \widetilde{k}^{(m-j)}\,. \tag{2.2.11}$$

These eigenfunction decompositions of the source bank distributions are not particularly enlightening in their present form but with a few assumptions, some useful information may be ascertained.

For comparison with the deterministic power method, selecting all the normalization constants to be the inverse of the fundamental eigenvalue simplifies (2.2.10) further to

$$\tilde{u}_n^{(m)} = \beta_n \left(\frac{\lambda_n}{\lambda_1}\right)^m + \sum_{i=0}^{m-1} \left(\frac{\lambda_n}{\lambda_1}\right)^i \xi_n^{(m-i)}. \tag{2.2.12}$$

Comparing (2.2.12) with (1.2.8), one can see that the introduction of noise from the stochastic operator adds an additional term to the SBDCs. That term is a summation of all the prior deviation coefficients where the contribution of each deviation is dampened by the eigenvalue ratio successively for each cycle after the introduction of that particular deviation coefficient. Equation (2.2.12) demonstrates that no mode can ever be completely forced out of the fundamental mode estimate by MC transport if the SBDC of that mode has non-zero variance, which is assumed true for all modes except those interrupted by artificial conditions such as reflecting boundaries. Even if a mode is forced out in one cycle, the mode could spontaneously reappear in a later cycle.

In practice, the normalization coefficients are not constant and do not equal λ_1^{-1}. The normalization constants are calculated from the inverse of the integral of the source iterates, i.e.,

$$\frac{1}{\widetilde{k}^{(m)}}=\int_V \hat{u}^{(m)}(\vec{r})\,d^3r=\int_V \sum_{n=1}^{\infty}\hat{u}_n^{(m)}b_n(\vec{r})\,d^3r=\sum_{n=1}^{\infty}\hat{u}_n^{(m)}\int_V b_n(\vec{r})\,d^3r. \tag{2.2.13}$$

The normalization constant will vary according to a combination of the noise in each intermediate bank decomposition coefficient (IBDC) such that

$$\frac{1}{\widetilde{k}^{(m)}}=\sum_{n=1}^{\infty}\left(\lambda_n\widetilde{u}_n^{(m-1)}+\zeta_n^{(m)}\right)\int_V b_n(\vec{r})\,d^3r. \tag{2.2.14}$$

From (2.2.13) or (2.2.14), one can see that the presence of antisymmetric modes has no effect on the normalization because the volume integral of the eigenfunction is zero. For other modes, the normalization constant will be dependent on the noise introduced into each mode; however, the noise associated with the normalization constant is from a combination of noise from many modes; therefore, as an approximation, $\zeta_n^{(m)}$ and $\widetilde{k}^{(m)}$ will be assumed to be uncorrelated random variables. If $\zeta_n^{(m)}$ and $\widetilde{k}^{(m)}$ are uncorrelated, the DFDCs $\xi_n^{(m)}$, which are the products of $\zeta_n^{(m)}$ and $\widetilde{k}^{(m)}$, must have expected values of zero because of (2.2.3).

With the aforementioned assumptions, one can determine the accumulated effect of normalization on the expected value of SBDCs in the limit of infinitely many cycles. For an unbiased MC iteration, the expected source distribution must converge to a multiple of the fundamental mode in the limit of infinitely many cycles, i.e.,

$$\lim_{m\to\infty} E\left[\widetilde{u}^{(m)}(\vec{r})\right]=Y\,b_1(\vec{r}) \tag{2.2.15}$$

Where Y is a constant that satisfies the chosen normalization, i.e.,

$$Y=\frac{1}{\int_V b_1(\vec{r})\,d^3r}. \tag{2.2.16}$$

The expected value of the SBDCs must also converge accordingly, i.e.,

$$\lim_{m\to\infty} E\left[\widetilde{u}_n^{(m)}\right]=\begin{cases}0 & \forall\, n>1\\ Y & n=1\end{cases}. \tag{2.2.17}$$

The expected value in (2.2.17) can be expanded using (2.2.10) to yield

$$E\left[\tilde{u}_n^{(m)}\right]=E\left[\beta_n\lambda_n^m\prod_{i=1}^{m}\tilde{k}^{(i)}+\xi_n^{(m)}+\sum_{i=1}^{m-1}\lambda_n^i\xi_n^{(m-i)}\prod_{j=0}^{i-1}\tilde{k}^{(m-j)}\right]$$
$$=E\left[\beta_n\lambda_n^m\prod_{i=1}^{m}\tilde{k}^{(i)}\right]+E\left[\xi_n^{(m)}\right]+\sum_{i=1}^{m-1}E\left[\lambda_n^i\xi_n^{(m-i)}\prod_{j=0}^{i-1}\tilde{k}^{(m-j)}\right]. \quad (2.2.18)$$

With the assumption that

$$E\left[\xi_n^{(m)}\right]=0\,, \quad (2.2.19)$$

and that normalizations are uncorrelated with noise introduced in prior cycles, i.e.,

$$\sum_{i=1}^{m-1}E\left[\lambda_n^i\xi_n^{(m-i)}\prod_{j=0}^{i-1}\tilde{k}^{(m-j)}\right]=\sum_{i=1}^{m-1}E\left[\lambda_n^i\xi_n^{(m-i)}\right]E\left[\prod_{j=0}^{i-1}\tilde{k}^{(m-j)}\right]=0\,, \quad (2.2.20)$$

the expectations for SBDCs are

$$E\left[\tilde{u}_n^{(m)}\right]=\beta_n\lambda_n^m E\left[\prod_{i=1}^{m}\tilde{k}^{(i)}\right]. \quad (2.2.21)$$

The expectations in (2.2.21) can readily be estimated for a test problem with known eigenfunctions, namely a highly scattering one-group uniform slab reactor. Figure 2.2.1 contains examples of such data for the uniform slab problem with a far from converged initial source described in Appendix A. The empirical observations for the problem are means from 1000 independent simulations with different random number seeds where each simulation started with 4000 identical source points in the first cycle. From Figure 2.2.1, one can see that for each mode presented, the mean of SBDCs, which is the left-hand side (LHS) of (2.2.21), is in close proximity to the scaled mean of the multiplication of normalization coefficients, which is the right-hand side (RHS) of (2.2.21), and the two often overlap. The scaling factors are those that precede the expectation term on the RHS of (2.2.21). Several other calculations were performed using different initial source distributions, and all yielded similar agreement. These results show that the aforementioned assumptions can be valid, but the results should not be taken as proof of general applicability.

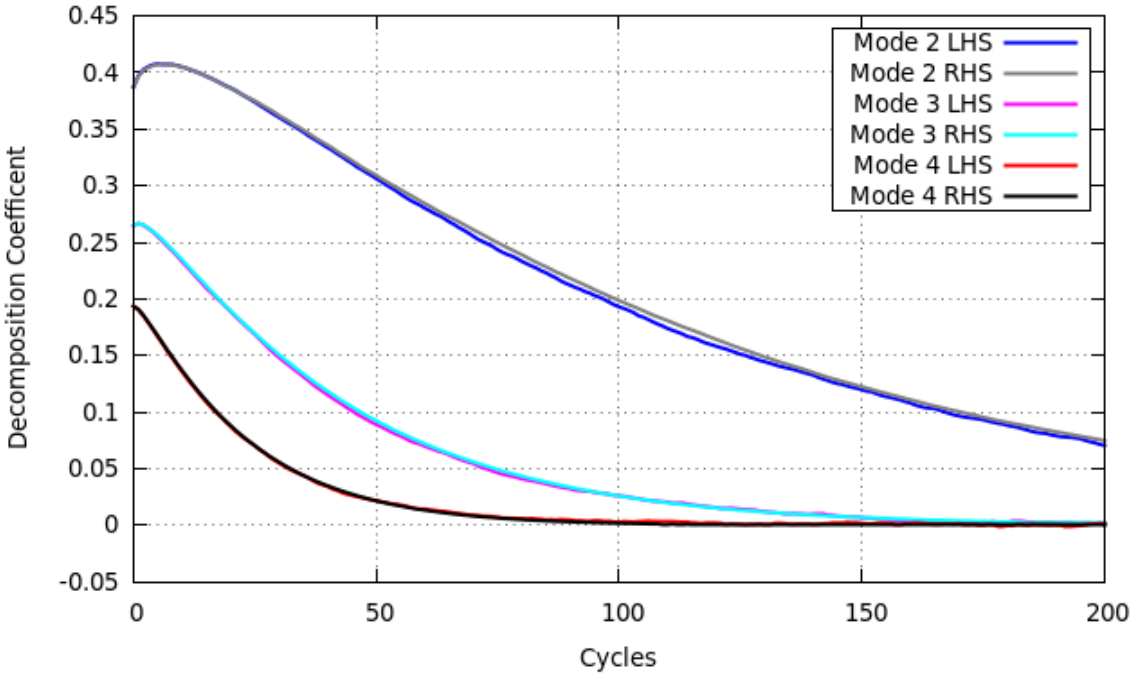

Figure 2.2.1. Empirical data collected from a highly scattering uniform slab for the LHS and RHS of (2.2.21) for several non-fundamental modes.

By observing the implications of these assumptions on the fundamental mode SBDC, one can see that the expected multiplication of normalization coefficients has the limit,

$$\lim_{m\to\infty} \beta_1 \lambda_1^m E\left[\prod_{i=1}^{m} \tilde{k}^{(i)}\right] = Y$$
$$\lim_{m\to\infty} E\left[\prod_{i=1}^{m} \lambda_1 \tilde{k}^{(i)}\right] = \frac{Y}{\beta_1} = \frac{1}{\beta_1 \int_V b_1(\vec{r})\, d^3 r}. \tag{2.2.22}$$

Therefore, one must conclude that for sufficiently many cycles,

$$E\left[\prod_{i=1}^{m} \tilde{k}^{(i)}\right] = \frac{Y}{\beta_1 \lambda_1^m} \forall\, m \gg 1. \tag{2.2.23}$$

Substituting the expectation for the multiplication of normalization factors from (2.2.23) into (2.2.21) yields an easier to evaluate expression for the expectation of SBDCs, which is

$$E\left[\tilde{u}_n^{(m)}\right] = \beta_n \frac{Y}{\beta_1}\left(\frac{\lambda_n}{\lambda_1}\right)^m \forall\, m \gg 1. \tag{2.2.24}$$

The expectation from (2.2.24) shall be referred to as the adjusted constant multiplier approximation, which can be contrasted with the expectation from the constant multiplier approximation derived from (2.2.12), i.e.,

$$E\left[\tilde{u}_n^{(m)}\right] = \beta_n \left(\frac{\lambda_n}{\lambda_1}\right)^m. \tag{2.2.25}$$

As one can see from (2.2.24) and (2.2.25), the only difference between the constant multiplier approximation and the adjusted constant multiplier approximation is the factor Y/β_1, which means that the two approximations converge at the same rate. The constant multiplier approximation preserves the SBDCs of the initial source, i.e., for *m*=0, (2.2.25) is exact, while the adjusted approximation may be highly erroneous for early cycles depending on the initial source and the shape of the fundamental mode. However, the expectations from the adjusted constant multiplier are more accurate than the constant multiplier for large numbers of cycles because the accumulated effect of drift in the normalization factor is taken into account. The net result is that the two approximations will tend to sandwich the theoretical expected values of SBDCs. This can be observed

for the second and third modes in Figures 2.2.2 and 2.2.3, respectively, which each contain SBDC expectations determined empirically and expectations from (2.2.24) and (2.2.25) for the same slab test problem that was used earlier in this section. The initial value of the adjusted constant multiplier curve, which is the intersection of the curve with the y-axis in Figures 2.2.2 and 2.2.3, has no particular physical interpretation and is only an artifact of matching the adjusted constant multiplier approximation with the expectation of SBDCs after many cycles.

If one looks to estimate the expectation of SBDCs during a running simulation, then the normalizations from cycles that have been run can be used to improve the estimate. If M transport operators have been applied, then the expected value of accumulated normalizations can be calculated by removing the known normalization constants, $\widetilde{k}^{(j)} \forall\ j \in [1, M]$, from the expectation, i.e.,

$$E\left[\prod_{i=1}^{m} \widetilde{k}^{(i)}\right] = E\left[\prod_{i=M+1}^{m} \widetilde{k}^{(i)}\right] \prod_{j=1}^{M} \widetilde{k}^{(j)}. \tag{2.2.26}$$

If m is close to M, then one may approximate the expected multiplication of future normalization constants to be the value of the most recent normalization constant to the power m-M; however, in general, one should revert to the adjusted constant normalization approximation to yield the expected PDFs near convergence. When utilizing the known normalization coefficients in (2.2.21), the expected SBDCs under the constant normalization approximation become

$$E\left[\widetilde{u}_n^{(m)}\right] = \beta_n \prod_{i=1}^{M} \lambda_n \widetilde{k}^{(i)} \left(\frac{\lambda_n}{\lambda_1}\right)^{m-M}. \tag{2.2.27}$$

However, the expectations of SBDCs from the adjusted constant normalization approximation do not change because the normalization constants are assumed to be converged. Having generated these estimators for the expected values of SBDCs from the stochastic power method, similar estimators for the stochastic extrapolated power method are needed to make comparisons between the two iteration schemes.

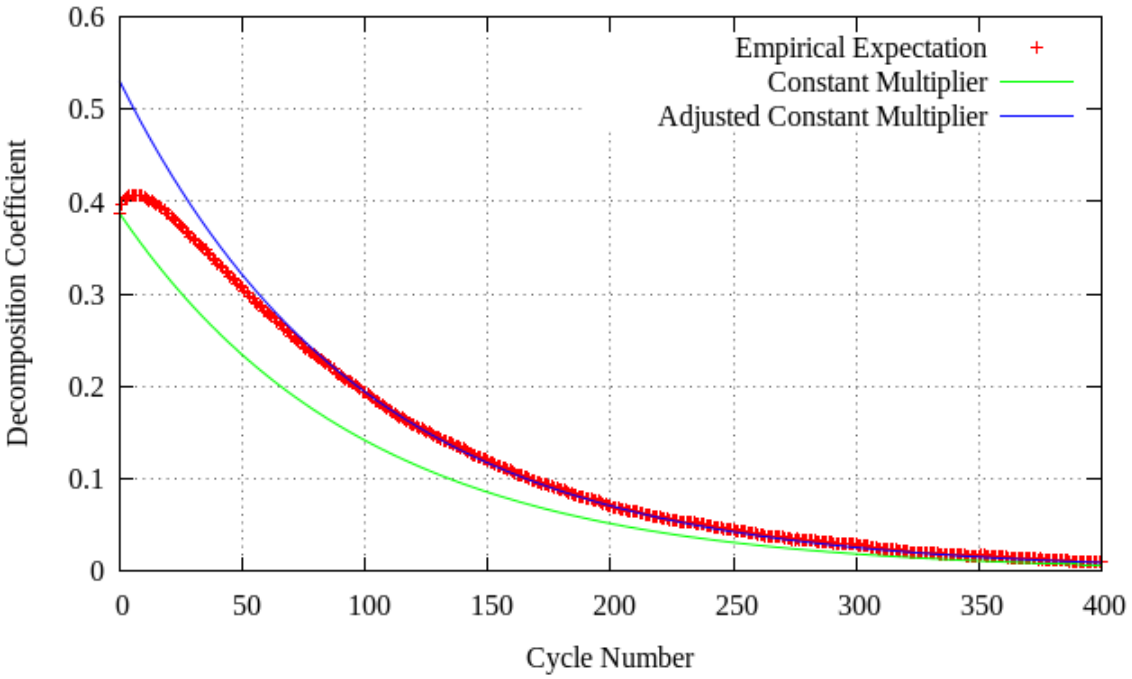

Figure 2.2.2. Uniform slab second mode expected DC versus cycle as estimated with empirical data, with constant normalization, and with adjusted constant normalization.

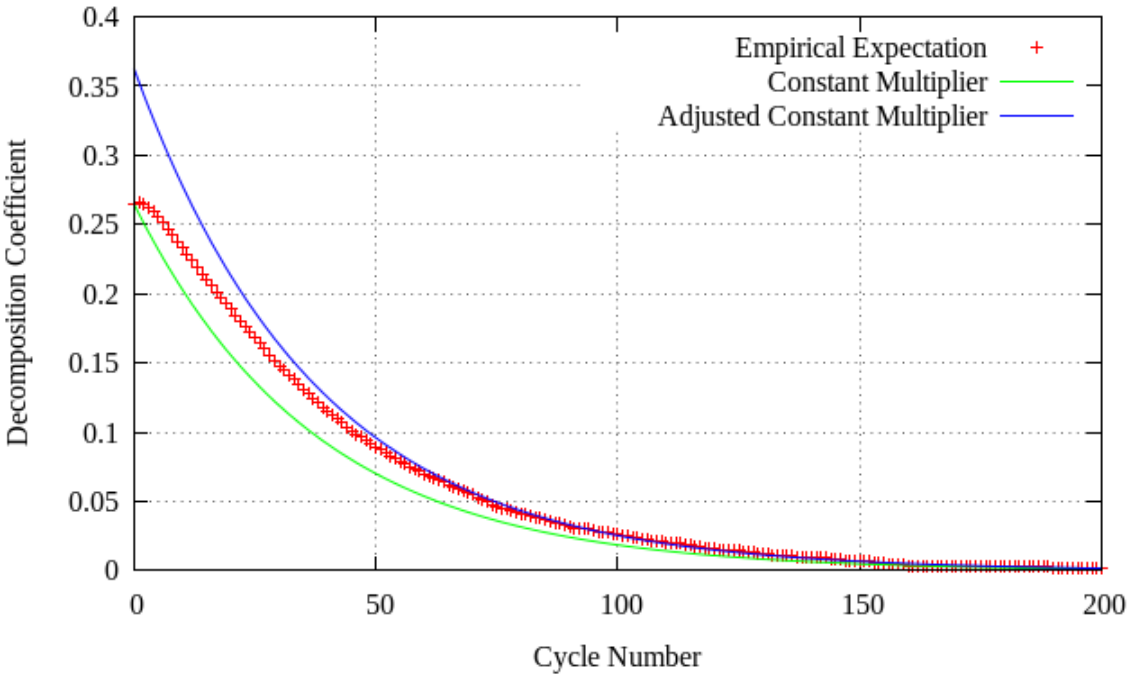

Figure 2.2.3. Uniform slab third mode expected DC versus cycle as estimated with empirical data, with constant normalization, and with adjusted constant normalization.

2.3 Expectations from Stochastic Extrapolation

Introducing the stochastic fission operator into the extrapolated power method iteration from (1.3.1) yields

$$\widetilde{\nu}^{(m+1)}(\vec{r})=(1+\alpha)\,\widetilde{k}^{(m)}\,\widetilde{H}[\,\widetilde{\nu}^{(m)}(\vec{r})]-\alpha\,\widetilde{\nu}^{(m)}(\vec{r})\quad\forall\, m\geq 0\,. \tag{2.3.1}$$

Applying (2.2.2) to (2.3.1) expresses the iteration in terms of the true fission operator as follows

$$\widetilde{\nu}^{(m+1)}(\vec{r})=(1+\alpha)\,\widetilde{k}^{(m+1)}\left(H[\,\widetilde{\nu}^{(m)}(\vec{r})]+\zeta^{(m+1)}(\vec{r})\right)-\alpha\,\widetilde{\nu}^{(m)}(\vec{r})\,. \tag{2.3.2}$$

To mimic (2.2.4) the deviation function absorbs the normalization coefficient to produce

$$\widetilde{\nu}^{(m+1)}(\vec{r})=(1+\alpha)\,\widetilde{k}^{(m+1)}H[\,\widetilde{\nu}^{(m)}(\vec{r})]+(1+\alpha)\,\xi^{(m+1)}(\vec{r})-\alpha\,\widetilde{\nu}^{(m)}(\vec{r})\,, \tag{2.3.3}$$

which can be expressed in an eigenbasis decomposition as

$$\widetilde{\nu}^{(m)}(\vec{r})\equiv\sum_{n=1}^{\infty}\widetilde{\nu}_n^{(m)}\,b_n(\vec{r}) \tag{2.3.4}$$

$$\widetilde{\nu}^{(m+1)}(\vec{r})=(1+\alpha)\,\widetilde{k}^{(m+1)}\,H\left[\sum_{n=1}^{\infty}\widetilde{\nu}_n^{(m)}\,b_n(\vec{r})\right]+(1+\alpha)\sum_{n=1}^{\infty}\xi_n^{(m+1)}\,b_n(\vec{r})-\alpha\sum_{n=1}^{\infty}\widetilde{\nu}_n^{(m)}\,b_n(\vec{r}). \tag{2.3.5}$$

Using linearity of the fission operator, (2.3.5) becomes

$$\widetilde{\nu}^{(m+1)}(\vec{r})=(1+\alpha)\,\widetilde{k}^{(m+1)}\sum_{n=1}^{\infty}H\left[\widetilde{\nu}_n^{(m)}\,b_n(\vec{r})\right]+(1+\alpha)\sum_{n=1}^{\infty}\xi_n^{(m+1)}\,b_n(\vec{r})-\alpha\sum_{n=1}^{\infty}\widetilde{\nu}_n^{(m)}\,b_n(\vec{r}). \tag{2.3.6}$$

Applying the definition of eigenvalues and eigenfunctions in (1.1.16), the operator can be removed from (2.3.6) to produce

$$\widetilde{\nu}^{(m+1)}(\vec{r})=(1+\alpha)\,\widetilde{k}^{(m+1)}\sum_{n=1}^{\infty}\lambda_n\,\widetilde{\nu}_n^{(m)}\,b_n(\vec{r})+(1+\alpha)\sum_{n=1}^{\infty}\xi_n^{(m+1)}\,b_n(\vec{r})-\alpha\sum_{n=1}^{\infty}\widetilde{\nu}_n^{(m)}\,b_n(\vec{r})\,, \tag{2.3.7}$$

which simplifies to

$$\widetilde{\nu}^{(m+1)}(\vec{r})=\sum_{n=1}^{\infty}\left\{\left[(1+\alpha)\,\lambda_n\,\widetilde{k}^{(m+1)}-\alpha\right]\widetilde{\nu}_n^{(m)}+(1+\alpha)\,\xi_n^{(m+1)}\right\}b_n(\vec{r})\,. \tag{2.3.8}$$

From (2.3.8), the SBDCs of the extrapolated iteration are

$$\widetilde{\nu}_n^{(m+1)}=\left[(1+\alpha)\,\lambda_n\,\widetilde{k}^{(m+1)}-\alpha\right]\widetilde{\nu}_n^{(m)}+(1+\alpha)\,\xi_n^{(m+1)}\,. \tag{2.3.9}$$

As specified by (2.3.9), carrying out the recursion to the initial guess produces

$$\tilde{v}_n^{(m)} = \beta_n \prod_{i=1}^{m} \left[(1+\alpha)\lambda_n \tilde{k}^{(i)} - \alpha \right] + (1+\alpha)\xi_n^{(m)} + (1+\alpha) \sum_{i=1}^{m-1} \left\{ \prod_{j=i+1}^{m} \left[(1+\alpha)\lambda_n \tilde{k}^{(j)} - \alpha \right] \right\} \xi_n^{(i)} \quad \forall\, m \in \mathbb{Z} \geq 2 . \tag{2.3.10}$$

For comparison purposes, selecting all the normalization coefficients to be the inverse of the fundamental eigenvalue simplifies (2.3.10) further to the extrapolated constant multiplier approximation,

$$\tilde{v}_n^{(m)} = \beta_n \left[(1+\alpha)\frac{\lambda_n}{\lambda_1} - \alpha \right]^m + (1+\alpha) \sum_{i=1}^{m} \left[(1+\alpha)\frac{\lambda_n}{\lambda_1} - \alpha \right]^{(m-i)} \xi_n^{(i)} \quad \forall\, m \in \mathbb{Z} \geq 1 . \tag{2.3.11}$$

Similar to the result derived in (2.2.12), (2.3.11) has an additional summation term that is not present in the deterministic coefficients in (1.3.9). Each term inside the summation in (2.3.11) is the deviation from the expected result of the fission operator at a previous cycle attenuated repeatedly by the decay coefficient η_n, defined in (1.3.10), for every cycle after the deviation was introduced by the stochastic fission operator. In addition to shifting the decay coefficient, the extrapolation amplifies each deviation by the factor $(1+\alpha)$ in the cycle where the deviation is introduced. This initial amplification persists throughout the remaining cycles as will be shown in section 2.5.

With the uncorrelatedness assumption of (2.2.19), the expectations of extrapolated SBDCs under the constant normalization approximation of (2.3.11) are

$$E\left[\tilde{v}_n^{(m)}\right] = \beta_n \left[(1+\alpha)\frac{\lambda_n}{\lambda_1} - \alpha \right]^m . \tag{2.3.12}$$

However, as previously mentioned in Section 2.2, the normalization coefficients are not constant in real simulations. From (2.3.10), the expectations of extrapolated SBDCs are

$$E\left[\tilde{v}_n^{(m)}\right] = \beta_n E\left[\prod_{i=1}^{m} \left[(1+\alpha)\lambda_n \tilde{k}^{(i)} - \alpha \right] \right] + (1+\alpha) E\left[\xi_n^{(m)}\right] + (1+\alpha) \sum_{i=1}^{m-1} E\left[\left\{ \prod_{j=i+1}^{m} \left[(1+\alpha)\lambda_n \tilde{k}^{(j)} - \alpha \right] \right\} \xi_n^{(i)} \right]. \tag{2.3.13}$$

With the uncorrelatedness assumptions of (2.2.19) and (2.2.20) applied to (2.3.13), the expectations of extrapolated SBDCs are

$$E\left[\widetilde{\nu}_n^{(m)}\right]=\beta_n E\left[\prod_{i=1}^{m}\left\{(1+\alpha)\lambda_n\widetilde{k}^{(i)}-\alpha\right\}\right]. \tag{2.3.14}$$

If the extrapolated power method is an unbiased estimator for the fundamental mode, then in the limit of infinitely many cycles, the expectations of non-fundamental mode SBDCs must approach zero, and the expectation of the fundamental mode SBDC must approach *Y* as expressed in (2.2.17). Observing this fact for the infinite cycle limit of (2.3.14) for the fundamental mode, i.e.,

$$\lim_{m\to\infty} E\left[\widetilde{\nu}_1^{(m)}\right]=Y=\lim_{m\to\infty}\beta_1 E\left[\prod_{i=1}^{m}\left\{(1+\alpha)\lambda_1\widetilde{k}^{(i)}-\alpha\right\}\right], \tag{2.3.15}$$

indicates that

$$\lim_{m\to\infty} E\left[\prod_{i=1}^{m}\left\{(1+\alpha)\lambda_1\widetilde{k}^{(i)}-\alpha\right\}\right]=\frac{Y}{\beta_1}. \tag{2.3.16}$$

As the source distribution estimates converge, the normalization constants $\widetilde{k}^{(m)}$ will as well. Thus after many cycles the normalization may be approximated as a constant that is equal to the inverse of the fundamental eigenvalue. If one makes a constant normalization assumption throughout a simulation, then for the limit on the fundamental mode SBDC in (2.3.15) to hold, the right hand side of (2.3.16) must be used to adjust the extrapolated constant multiplier expectation estimator of (2.3.12) to yield the adjusted extrapolated constant multiplier approximation, which is

$$E\left[\widetilde{\nu}_n^{(m)}\right]=\beta_n\frac{Y}{\beta_1}\left[(1+\alpha)\frac{\lambda_n}{\lambda_1}-\alpha\right]^m \forall\, m\in\mathbb{Z}\gg 1. \tag{2.3.17}$$

This is analogous to the derivations of (2.2.24) for the power method with slightly less rigor. The expectations in (2.3.12) and (2.3.17) should sandwich the true expectation because the constant normalization in (2.3.12) is more accurate for early cycles, and the true expectation should transition toward the adjusted normalization approximation of (2.3.17) as more cycles complete.

As with the standard power method, if one looks to estimate the expectation of extrapolated SBDCs during a running simulation, then the normalizations from cycles that have been run can be used to improve the estimate. If *M* transport operators have been applied, removing the terms containing known normalization constants,

$\widetilde{k}^{(j)} \forall\, j \in [1, M]$, from the expectation of multiplied decay coefficients yields

$$E\left[\prod_{i=1}^{m}\left\{(1+\alpha)\lambda_n \widetilde{k}^{(i)} - \alpha\right\}\right] = \prod_{i=1}^{M}\left\{(1+\alpha)\lambda_n \widetilde{k}^{(i)} - \alpha\right\} E\left[\prod_{i=M+1}^{m}\left\{(1+\alpha)\lambda_n \widetilde{k}^{(i)} - \alpha\right\}\right]. \quad (2.3.18)$$

If *m* is close to *M*, then one may approximate the expected multiplication of future decay coefficients to be the value of the most recent decay coefficient to the power *m-M*; however, in general, one should use a better estimate for the stationary normalization factor for predicting the expectation after numerous cycles. Applying the constant normalization approximation to (2.3.14) while including known normalizations produces the following estimates for the mean of SBDCs,

$$E\left[\widetilde{v}_n^{(m)}\right] = \beta_n \prod_{i=1}^{M}\left\{(1+\alpha)\lambda_n \widetilde{k}^{(i)} - \alpha\right\} \prod_{i=M+1}^{m}\left\{(1+\alpha)\frac{\lambda_n}{\lambda_1} - \alpha\right\}. \quad (2.3.19)$$

As with the power method, including observed normalizations into the adjusted extrapolated constant multiplier approximation has no effect because the decay coefficients are assumed to be converged. However, the two approximations will no longer sandwich the true expectation because the extrapolated constant multiplier approximation will vary with the normalizations observed in each cycle. To assess the accuracy of (2.3.12) and (2.3.17) and as a corollary (2.3.19), one must define an implementation of the extrapolated power method.

2.4 Implementation of Extrapolation

The first step in extrapolating a MC source bank is determining how the subtraction operation in (2.3.1) should be handled. One solution would be to combine the intermediate and source banks together such that all of the points from each bank would be in the source bank of the next cycle with tally weights scaled by $1+\alpha$ or $-\alpha$ for points taken from the intermediate or source banks, respectively. This approach was not used because some MC codes choose to not allow negative weight particles [1], and particle cancellation is a non-trivial computation [27]. Instead, the MC source banks are converted into smoother functions, which can easily be added, subtracted, and scaled. The first attempt used a moving average to estimate the source density at each point in the bank [28]. This required finding the number of neighboring points, which fit inside

the counting window. The algorithm for finding nearest neighbors is of the order L^2 operations where *L* is the number of points in the bank [28]. This was particularly expensive for large window sizes. Therefore, a much simpler implementation which converted the source banks into discrete vectors was selected because counting the number of points in each bin requires order *L* operations.

As in (2.1.1), a MC fission source bank consists of *L* points at locations $\vec{r}_l$ with tally weights q_l, which can be expressed as

$$\tilde{u}(\vec{r}) = \sum_{l=1}^{L} q_l \delta(\vec{r} - \vec{r}_l). \tag{2.4.1}$$

The points are in a continuous space V_∞, which can be discretized into a vector space V_N. The discretized fission source bank is defined by

$$\tilde{U}(i) = \int_{V_N(i)} \sum_{l=1}^{L} q_l \delta(\vec{r} - \vec{r}_l) \forall\, 1 \le i \le N \tag{2.4.2}$$

where the source is integrated over each spatial bin i with volume $V_N(i)$. In a similar fashion but starting from (2.1.3), the intermediate bank is discretized according to

$$\hat{U}(i) = \int_{V_N(i)} \sum_{l=1}^{L^{(0)}} \sum_{c=1}^{C_l} w_{l,c} \delta(\vec{r} - \vec{r}_{l,c}) \forall\, 1 \le i \le N. \tag{2.4.3}$$

Once in vector form, a discretized form of (2.3.1) determines the desired fraction of source sites in each vector bin to start in the subsequent cycle. If a bin contains a negative value for the source density, then the bin is set to 0, and no sites will be started in that bin for the next generation. This clipping can distort the extrapolation procedure, so care was taken for the majority of simulations in this dissertation to make bins or particle numbers large enough that clipping was not often encountered. In practice at least one source point should be in every fissile region if the problem is not undersampled [29], but the experimental code used in this investigation did not make any such accommodations to avoid any interference with assessing the performance of the extrapolation technique.

After determining the desired fraction of source sites that will start in each bin, a

stratified sampling routine calculates precisely how many source sites will be in each bin for the source bank used in the next cycle. The stratified sampling routine ensures that the number of source sites placed in each bin is as close to the desired fraction as possible given the finite number of source sites desired for the next generation. Then stratified sampling picks the actual source points to start inside a bin from the points in the intermediate bank that are inside the same bin. The selection of sites within a bin is stratified in the sense that all points of equal fission production weight inside the bin are placed in the new source bank *n* times before any point from the intermediate bank could have *n*+1 replicas placed in the new source bank. The procedure for each bin is described in the following pseudo-code for fission sites with equal fission production weights:

```
probability = #neededInSourceBin/#inBinOfIntermediateBank
accumulator = 0
#inSourceBin = 0
for i=1 to #inBinOfIntermediateBank
        accumulator = accumulator + probability
        #toAddToSource = floor(probability)
        test = accumulator - ( #inSourceBin + #toAddToSource )
        if( randomNumber0_1 <= test ) then
                #toAddToSource = #toAddToSource + 1
        endif
        for n = 1 to #toAddToSource
                #inSourceBin = #inSourceBin + 1
                place  i^th  particle into source bank
        end
end.
```

This two tiered sampling algorithm reduces the variance in the number of points that appear in each bin compared to a similar algorithm which modifies selection weights of each point in the intermediate bank and only performs one round of sampling. This algorithm was chosen because it is consistent with the source point selection scheme in MC21 [30]; however, the sampling can be avoided altogether in a code that allows

histories to start with different tally weights.

Having defined an implementation for the extrapolated power method, the uncorrelatedness assumptions that were used to generate (2.3.14) can be shown to be reasonable approximations. For this assessment, the same uniform slab and 4000 point starting source that was used in Section 2.2 was simulated 1000 times with extrapolation. The optimal extrapolation parameter of 0.98 as determined from (1.3.13) was used along with 16 equal width spatial bins for performing extrapolation. Figure 2.4.1 shows reasonable agreement between the empirically observed expectations for the left and right sides of (2.3.14) for several non-fundamental modes, which indicates that the uncorrelatedness assumptions are reasonable for this problem setup. However, for mode number 2, the expectations from the standard power method in Figure 2.2.1 showed better agreement than the expectations from the extrapolated power method. This is expected because extrapolation combines information from the previous cycle to formulate a new estimate for the fundamental mode, which should amplify correlations.

Having shown that the uncorrelatedness assumptions can be applied to this uniform slab test problem, application of the extrapolated constant multiplier model of (2.3.12) and the adjusted extrapolated constant multiplier model of (2.3.17) can be performed. The two models are plotted with the empirically determined expected values in Figures 2.4.2 and 2.4.3 for the second and third modes, respectively. As can be seen in Figures 2.4.2 and 2.4.3, the extrapolated constant multiplier models sandwich the theoretical expected values with both models converging to the same expected value of zero. As expected, the extrapolated constant multiplier model is more accurate than the adjusted extrapolated constant multiplier model for earlier cycles, but eventually the expected SBDC curve moves toward the adjusted extrapolated constant multiplier model after multiple cycles.

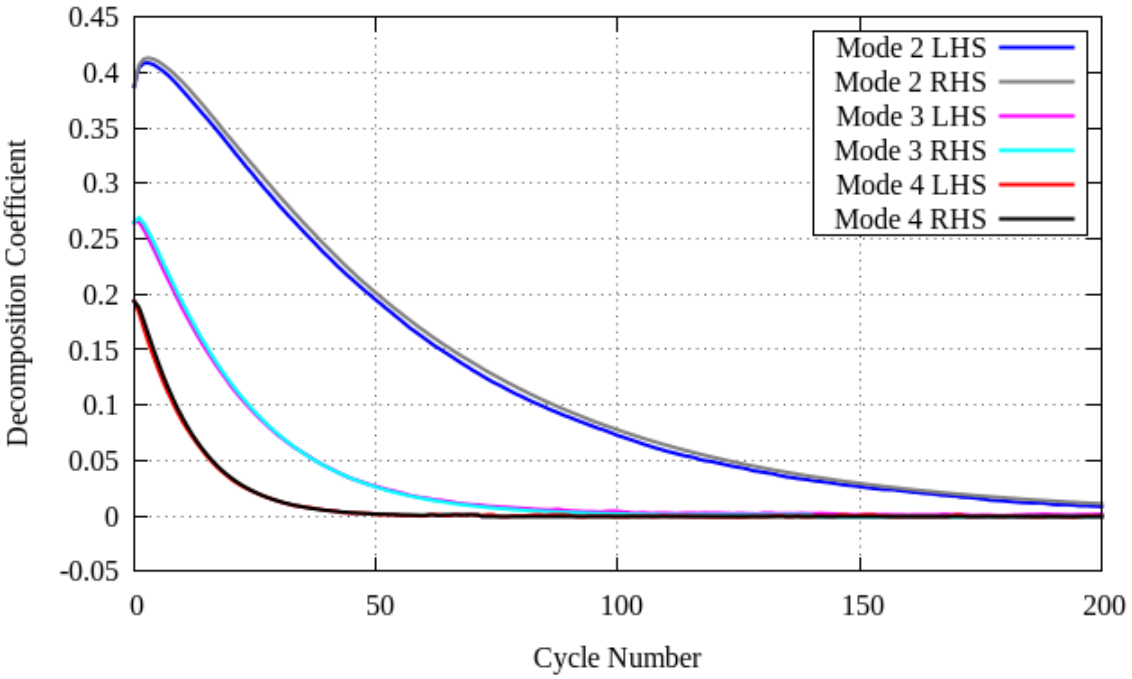

Figure 2.4.1. Empirical data collected from a highly scattering uniform slab for the LHS and RHS of (2.3.14) for several non-fundamental modes.

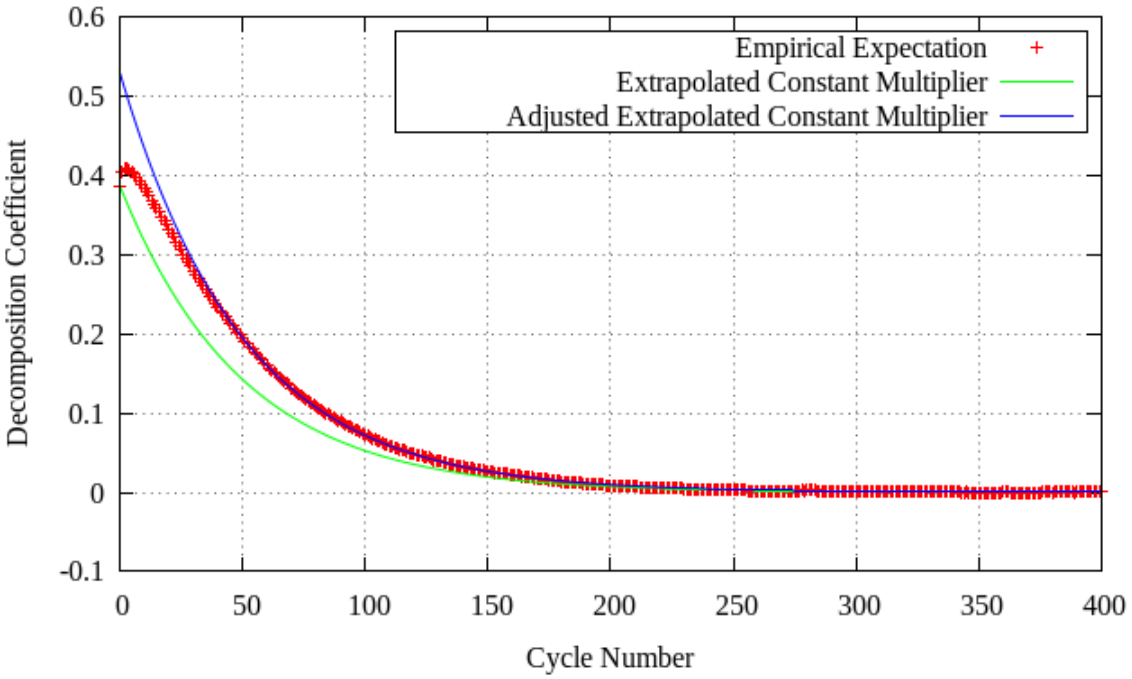

Figure 2.4.2. Uniform slab second mode expected SBDC versus cycle as estimated with empirical data, with constant normalization, and with adjusted constant normalization.

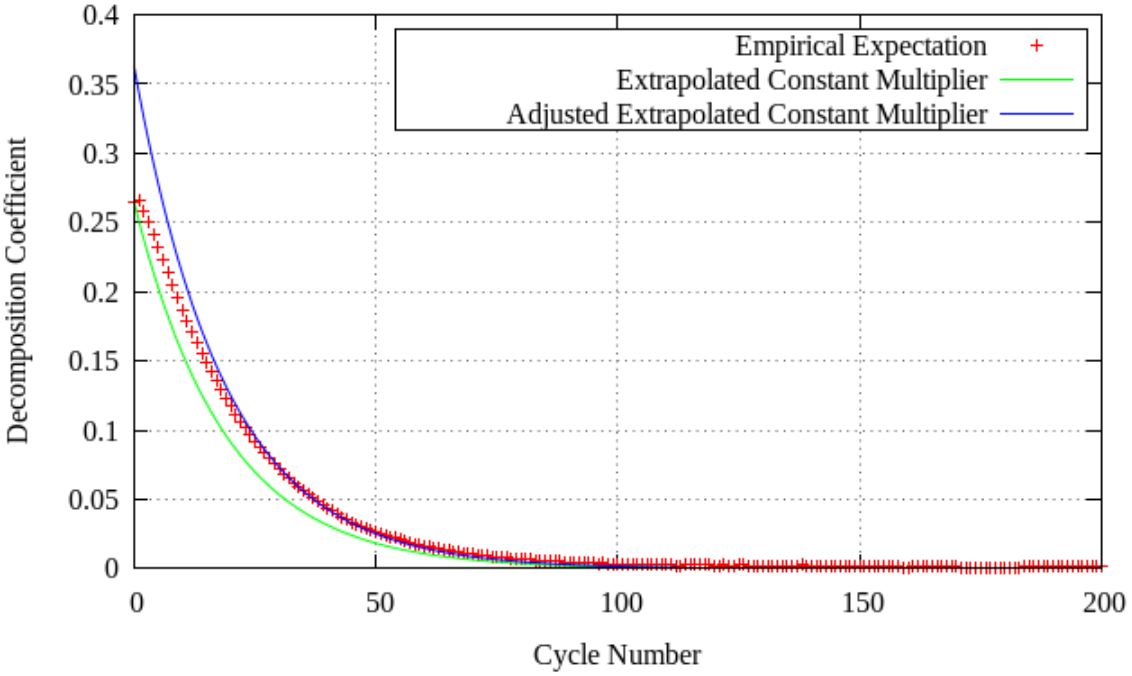

Figure 2.4.3. Uniform slab third mode expected SBDC versus cycle as estimated with empirical data, with constant normalization, and with adjusted constant normalization.

The choice of using 16 bins for the previous test problem was deliberate. If the extrapolation mesh is too fine for the number of histories, the clipping of negative density regions that is performed for this extrapolation implementation induces a bias in the fission source distribution. This can be observed in Figure 2.4.4, which contains expected SBDCs that were obtained empirically for the third mode of the uniform slab problem that was used earlier with 16, 64, and 256 mesh bins. Figure 2.4.4 also contains the empirically determined expected SBDCs of the finest mesh, 256 bins, with 4.0E5 source sites per cycle, which is greater than the 4.0E3 sites per cycle that was used to generate the other curves. As one can see from Figure 2.4.4, increasing the refinement without changing the number of histories per cycle caused an increasing bias in the expected SBDCs, such that those simulations would not converge to the fundamental mode if extrapolation were enabled throughout the simulations. This behavior is not universal across the eigenvalue spectrum; increasing the refinement of the extrapolation mesh improved the convergence rate of many anti-symmetric modes for this problem; for example, the second mode, which Figure 2.4.5 shows, decayed fastest with the finest mesh of the cases run for the smaller number of histories per cycle. The clipping of negative regions had the effect of increasing the extrapolation parameter applied to the anti-symmetric modes. Using too fine of a mesh leads to a source distribution that looks similar to a picket fence because the regions have very few fission sites, which causes them to be pushed by large percentages relative to the source distribution, and bins which are pushed negative are clipped, which distorts the procedure. Figure 2.4.6 demonstrates this using 256 mesh bins for extrapolation with 4.0E3 source sites per cycle as the “Less Histories” curve and 4.0E5 source sites per cycle as the “More Histories” curve. The “fence posts” move in subsequent cycles as neutrons leak out of the “posts” and cause fissions in the suppressed regions, which is then amplified by extrapolation. The task of finding a prescription for the appropriate number of mesh bins is potential future research.

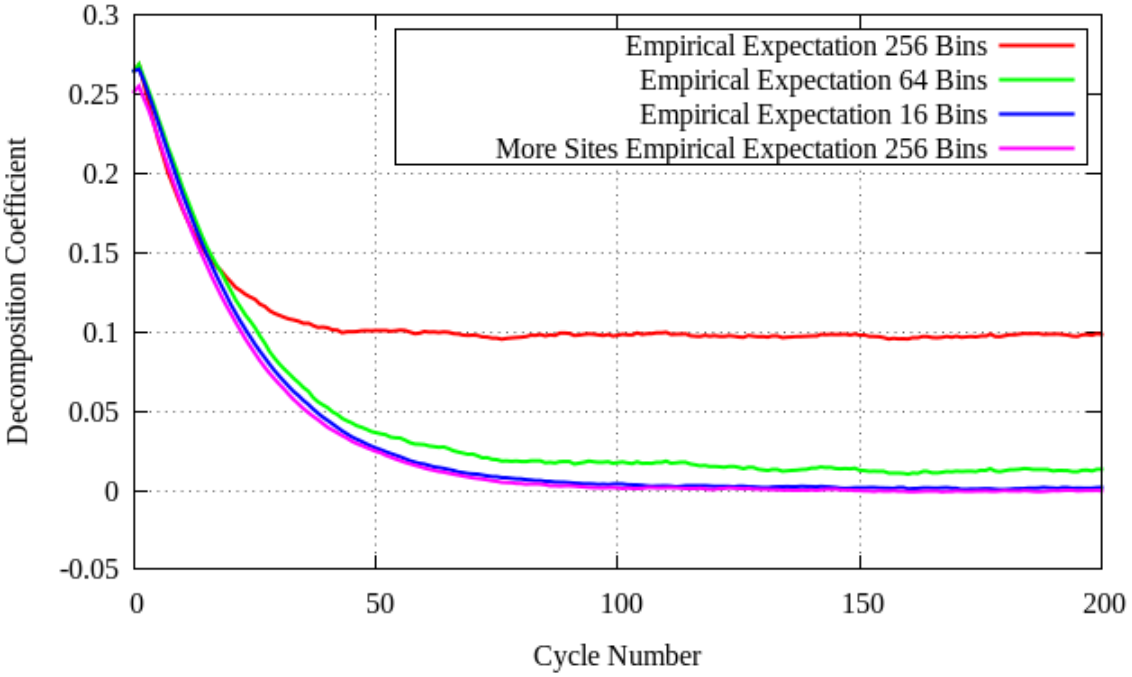

Figure 2.4.4. Uniform slab third mode expected SBDC versus cycle for extrapolation with various mesh configurations, which are indicated in the legend.

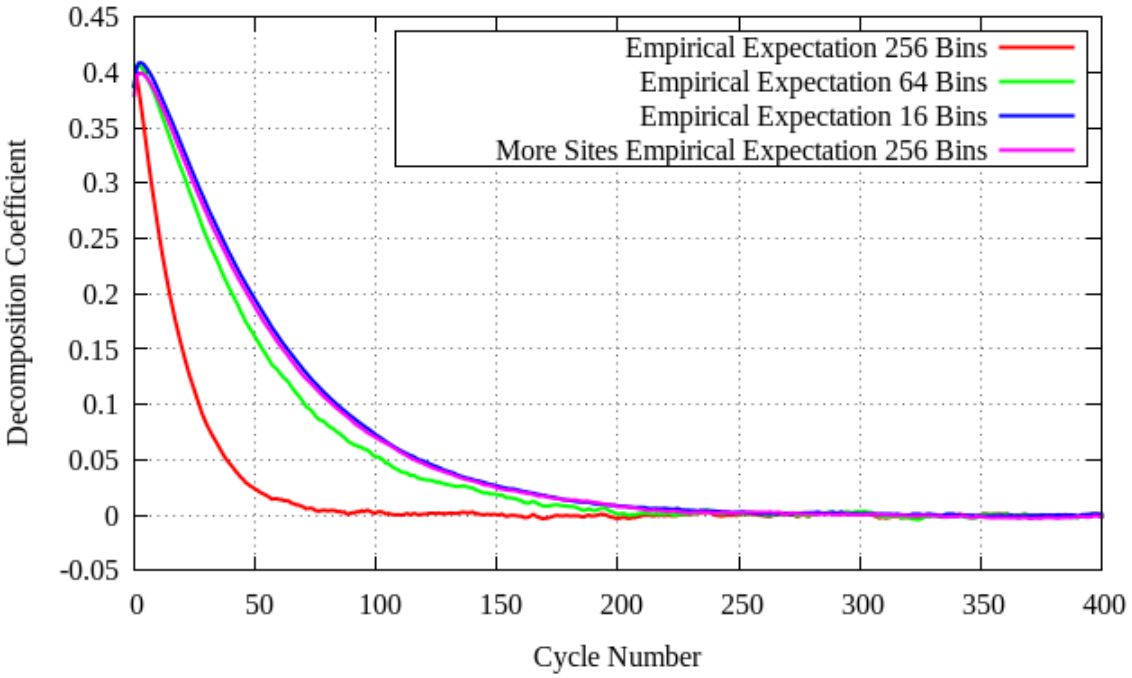

Figure 2.4.5. Uniform slab second mode expected SBDC versus cycle for extrapolation with various mesh configurations, which are indicated in the legend.

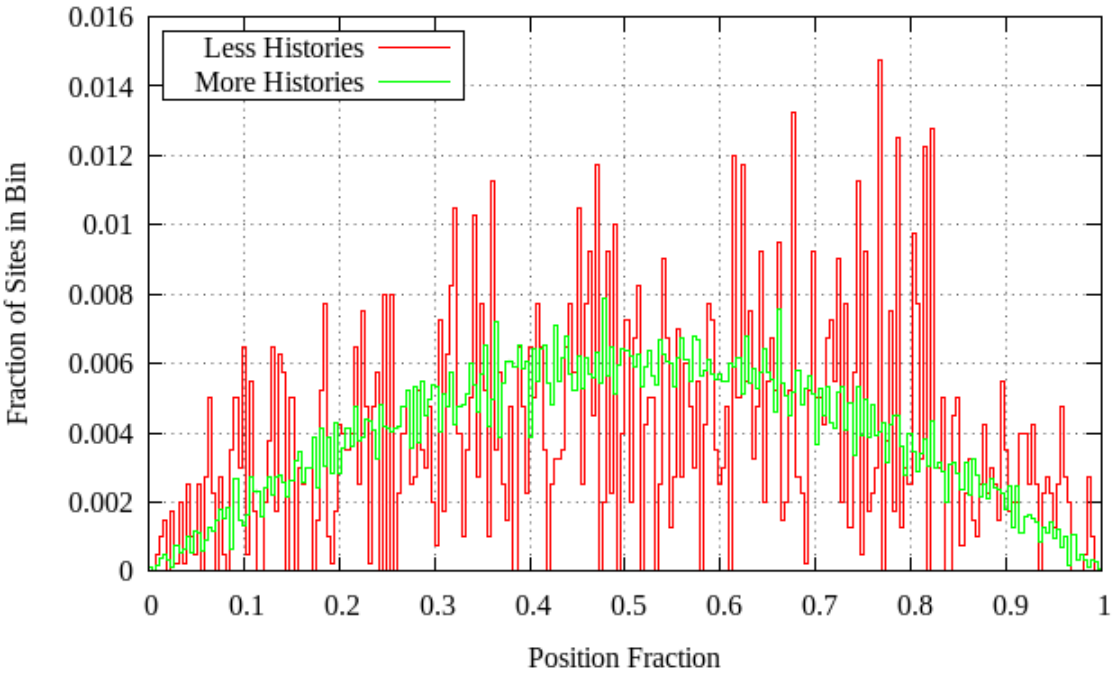

Figure 2.4.6. Uniform slab source site distribution at cycle 420 using extrapolation with 256 mesh bins for 1000 simulations with 4.0E3 and 4.0E5 source sites per cycle.

Having developed reasonable models for the expected behavior of SBDCs from the standard and extrapolated power methods, one can compare the two and investigate the noise associated with those expectations with the goal of understanding convergence and converging source site distributions with fewer cycles.

2.5 Convergence Comparison

Having derived and shown the evolution of SBDCs that one can expect using the standard and extrapolated power methods, the two iterations can be compared with respect to rate and reliability of convergence. From the perspective of a MC user, the fission source has converged after some number of discarded cycles when the source site distribution of a particular cycle is expected to be reasonably close to the fundamental mode. This section will show that extrapolation can be used to reach a reasonable source site distribution with fewer cycles than the standard power method. To justify this claim, the uncertainty in the SBDCs will be investigated to better understand what is meant by the term reasonable with respect to proximity of a source site distribution to the fundamental mode.

When choosing the number of discarded cycles, one should consider the bias that may be introduced by the choice. The expected values of SBDCs of non-fundamental modes are the eigenfunction components of the bias in the distribution from which a source bank is sampled at a particular cycle. The distributions are biased in the sense that they are not the fundamental mode. As the MC source iterations approach convergence, the expected values of SBDCs from the standard power method follow the adjusted constant multiplier approximation as in (2.2.24),

$$E\left[\tilde{u}_n^{(m)}\right]=\beta_n\frac{Y}{\beta_1}\left(\frac{\lambda_n}{\lambda_1}\right)^m, \tag{2.5.1}$$

and the expected values of SBDCs from the extrapolated power method follow the adjusted extrapolated constant multiplier approximation as in (2.3.17),

$$E\left[\tilde{\nu}_n^{(m)}\right] = \beta_n \frac{Y}{\beta_1}\left[(1+\alpha)\frac{\lambda_n}{\lambda_1} - \alpha\right]^m . \qquad (2.5.2)$$

The only difference between the two models is in the decay coefficient, which is the part of each equation that is exponentiated. The relationship between the extrapolation parameter α and the extrapolated decay coefficient appears in Section 1.3. Combining results from the standard and extrapolated power methods for the diffuse uniform slab problem, which were presented earlier in this chapter, demonstrates the potential for improvement in the expected SBDCs when extrapolating with a parameter of 0.98. The SBDCs of the second mode appear in Figure 2.5.1 with their approximate models for both iteration techniques, and the SBDCs of the third mode appear similarly in Figure 2.5.2. Figures 2.5.1 and 2.5.2 clearly show that the extrapolated power method with an appropriate mesh and extrapolation parameter can diminish the bias in the source distribution faster than the standard power method. For example, in the third mode component, the standard power method iteration falls below a bias of 5.0E-02 after 73 cycles, and the extrapolated power iteration falls below the same level after only 38 cycles, which is a 52% reduction in the number of cycles. Additionally, after 300 cycles, the expected SBDC of the second mode is 2.9E-02±2.2E-03 which is 26 times larger than the expected SBDC from extrapolation, which is 1.1E-03±3.1E-03. From this fact, a user might decide that if 300 cycles were to be discarded, then extrapolation should be used to generate the source for the first actively tallied cycle.

However, observation of the expected absolute value (ABS) of the SBDC of the second mode in Figure 2.5.3 should convince the user to choose the standard power method over extrapolation. From Figure 2.5.3, one can see that the expected ABS of the SBDC converges to a stationary level that is greater when using extrapolation than when using the standard power method. After 300 cycles, the expected ABS of the SBDC from the standard power method is 6.1E-02±1.3E-03, and the expected ABS of the SBDC from extrapolation is 7.9E-02±1.9E-03. This indicates that one should expect a sampled source distribution at cycle 300 to be 30% further from the fundamental mode along the second mode component when using extrapolation versus the standard power method. In

general, a user should strive to choose the first tallied cycle such that the source will be as close to the fundamental mode as reasonably possible. Therefore, after 300 cycles, one should use the source estimate from the standard power method rather than the extrapolated power method because of the lower expected ABS of the SBDC. Despite the greater bias in the second mode component of the source distribution, the standard power method is expected to yield an estimate for the fundamental mode at cycle 300 that is closer in shape to the fundamental mode than that from the extrapolated power method. Therefore, the standard power method provides a more reliable estimate for the fundamental mode than the extrapolated power method when the two are close to their respective stationary levels, e.g., after 300 discarded cycles. The stationary source distribution from the extrapolated power method is a less reliable estimate for the fundamental mode than the stationary source distribution from the standard power method because extrapolation amplifies the variance of SBDCs.

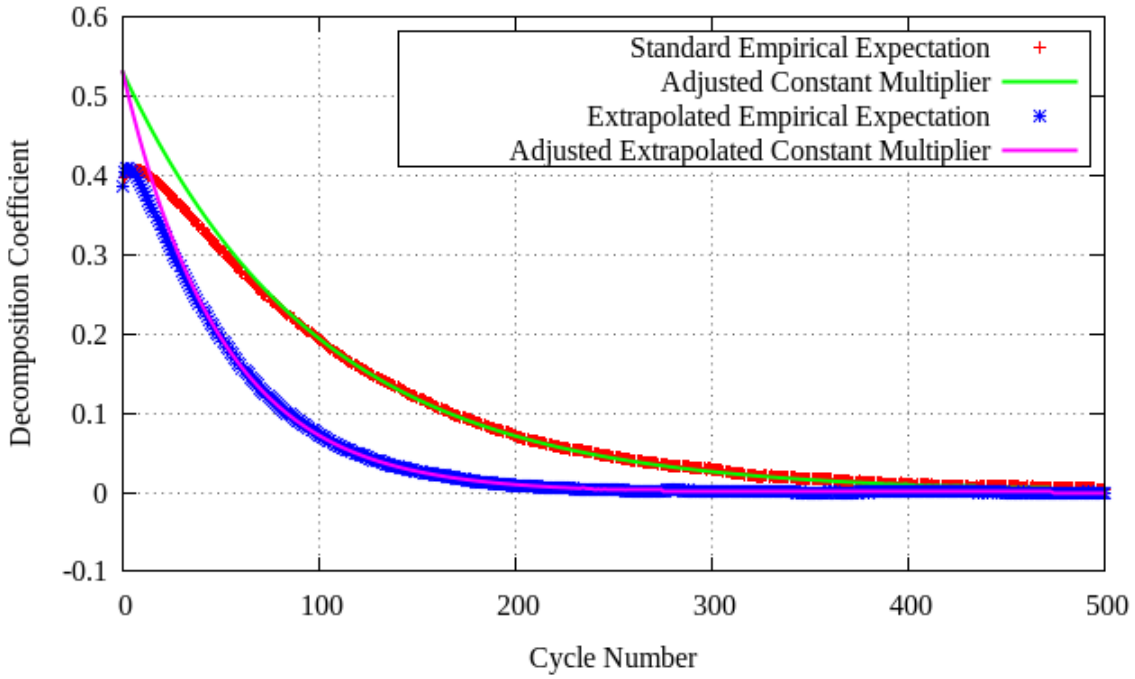

Figure 2.5.1. Uniform slab second mode empirically-determined expected SBDC versus cycle for the standard and extrapolated power methods with their adjusted constant multiplier predictions.

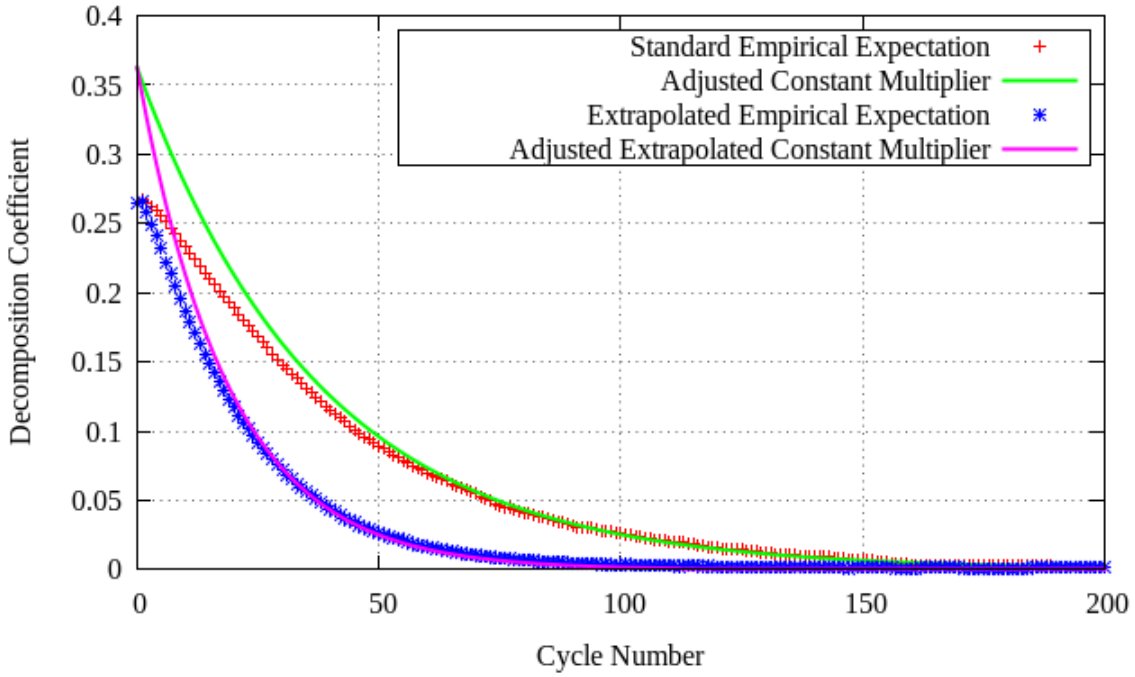

Figure 2.5.2. Uniform slab third mode empirically-determined expected SBDC versus cycle for the standard and extrapolated power methods with their adjusted constant multiplier predictions.

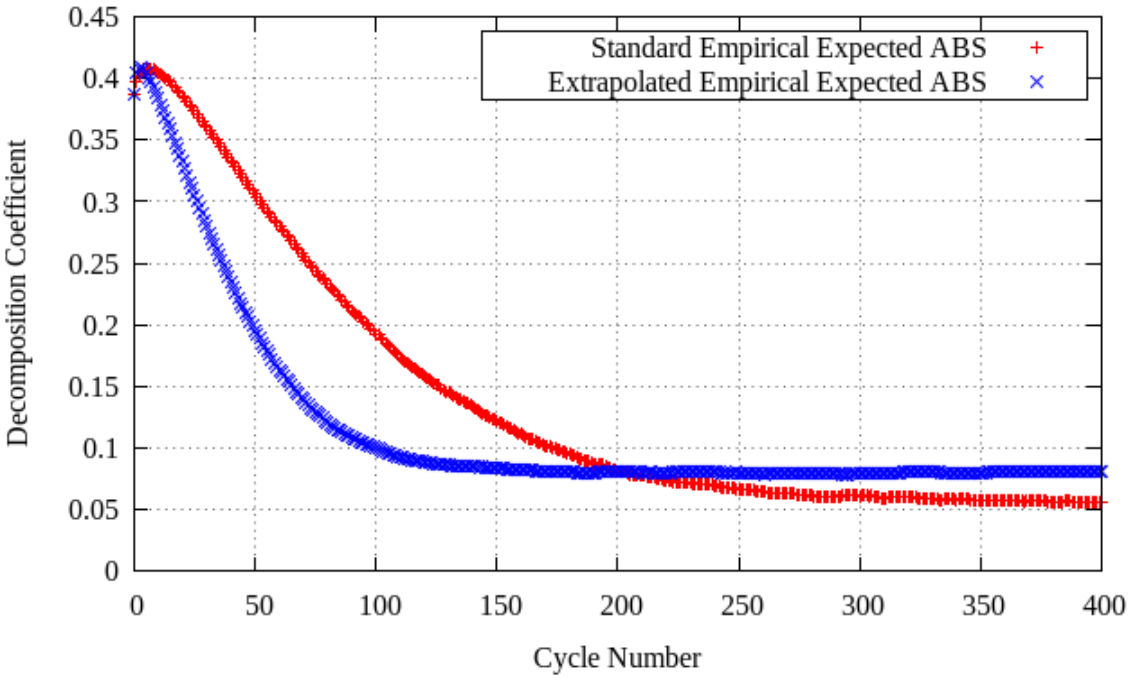

Figure 2.5.3. Uniform slab empirically-determined expected ABS of SBDC of second mode versus cycle for the standard and extrapolated power methods.

The amplification of variance by extrapolation can be demonstrated by looking at the equations that govern the SBDCs, namely (2.2.10),

$$\widetilde{u}_n^{(m)} = \beta_n \lambda_n^m \prod_{i=1}^{m} \widetilde{k}^{(i)} + \xi_n^{(m)} + \sum_{i=1}^{m-1} \lambda_n^i \xi_n^{(m-i)} \prod_{j=0}^{i-1} \widetilde{k}^{(m-j)}, \tag{2.5.3}$$

and (2.3.10),

$$\begin{aligned} \widetilde{v}_n^{(m)} = \beta_n \prod_{i=1}^{m} \left[(1+\alpha)\lambda_n \widetilde{k}^{(i)} - \alpha \right] + (1+\alpha)\xi_n^{(m)} \\ + (1+\alpha) \sum_{i=1}^{m-1} \left\{ \prod_{j=i+1}^{m} \left[(1+\alpha)\lambda_n \widetilde{k}^{(j)} - \alpha \right] \right\} \xi_n^{(i)}, \end{aligned} \tag{2.5.4}$$

and making some assumptions about the characteristics of the noise in each cycle. The goal of this investigation will be to have equations that can be used to estimate the variances of non-fundamental mode SBDCs at or near their stationary distributions where the normalization procedure is reasonably converged. Using an assumption of constant normalization with adjustment to preserve the expected value limit converts (2.5.3) into

$$\widetilde{u}_n^{(m)} = \beta_n \frac{Y}{\beta_1} \left(\frac{\lambda_n}{\lambda_1} \right)^m + \sum_{i=1}^{m} \left(\frac{\lambda_n}{\lambda_1} \right)^{m-i} \xi_n^{(i)} \quad \forall\, m \in \mathbb{Z} \gg 1, \tag{2.5.5}$$

and (2.5.4) into

$$\widetilde{v}_n^{(m)} = \beta_n \frac{Y}{\beta_1} \left[(1+\alpha)\frac{\lambda_n}{\lambda_1} - \alpha \right]^m + (1+\alpha) \sum_{i=1}^{m} \left[(1+\alpha)\frac{\lambda_n}{\lambda_1} - \alpha \right]^{m-i} \xi_n^{(i)} \quad \forall\, m \in \mathbb{Z} \gg 1\,. \tag{2.5.6}$$

Under this approximation, the deviation function decomposition coefficients (DFDCs), $\xi_n^{(m)}$, absorb the noise from stochastic normalization in the terms containing β_n of (2.5.3) and (2.5.4). With (2.2.19) and the additional assumption that the random variables $\xi_n^{(m)}$ are uncorrelated with other cycles, the covariances are

$$COV\left[\xi_n^{(m)} \xi_n^{(m-i)}\right] = E\left[\xi_n^{(m)} \xi_n^{(m-i)}\right] - E\left[\xi_n^{(m)}\right] E\left[\xi_n^{(m-i)}\right] = \begin{cases} 0, & \forall\, i \neq 0 \\ Var\left[\xi_n^{(m)}\right] \equiv \left(\sigma_n^{(m)}\right)^2, & i = 0. \end{cases} \tag{2.5.7}$$

Since the DFDC terms represent all the noise from a single-cycle, the variance of DFDCs, $\left(\sigma_n^{(m)}\right)^2$, shall be referred to as the single-cycle variance. With the covariances from (2.5.7), the variances of SBDCs can be readily estimated.

Under the adjusted constant normalization approximation, the variances of the standard

power method SBDCs are

$$Var[\tilde{u}_n^{(m)}] = Var\left[\beta_n \frac{Y}{\beta_1}\left(\frac{\lambda_n}{\lambda_1}\right)^m + \sum_{i=1}^{m}\left(\frac{\lambda_n}{\lambda_1}\right)^{m-i}\xi_n^{(i)}\right]. \tag{2.5.8}$$

The β_n term in (2.5.8) is constant; therefore, it does not contribute to the variance and can be removed from (2.5.8) to yield

$$Var[\tilde{u}_n^{(m)}] = Var\left[\sum_{i=1}^{m}\left(\frac{\lambda_n}{\lambda_1}\right)^{m-i}\xi_n^{(i)}\right]. \tag{2.5.9}$$

The variance of the sum of uncorrelated random variables is the sum of their variances [13]; therefore, with the uncorrelatedness assumption of (2.5.7), the variances of standard power method SBDCs are

$$Var[\tilde{u}_n^{(m)}] = \sum_{i=1}^{m}\left(\frac{\lambda_n}{\lambda_1}\right)^{2(m-i)} Var\left[\xi_n^{(i)}\right]. \tag{2.5.10}$$

Additionally, under the same assumptions, the variances of the extrapolated power method SBDCs are

$$Var\left[\tilde{v}_n^{(m)}\right] = Var\left[\beta_n \frac{Y}{\beta_1}\left[(1+\alpha)\frac{\lambda_n}{\lambda_1} - \alpha\right] + (1+\alpha)\sum_{i=1}^{m}\left[(1+\alpha)\frac{\lambda_n}{\lambda_1} - \alpha\right]^{m-i}\xi_n^{(i)}\right]. \tag{2.5.11}$$

The β_n term in (2.5.11) is not random and does not contribute to the variance; therefore, the β_n term can be removed from the variance calculation, which reduces (2.5.11) to

$$Var\left[\tilde{v}_n^{(m)}\right] = Var\left[(1+\alpha)\sum_{i=1}^{m}\left[(1+\alpha)\frac{\lambda_n}{\lambda_1} - \alpha\right]^{m-i}\xi_n^{(i)}\right]. \tag{2.5.12}$$

According to the uncorrelatedness assumption in (2.5.7), (2.5.12) contains a sum of uncorrelated random variables $\xi_n^{(m)}$; thus, (2.5.12) may be expressed as

$$Var\left[\tilde{v}_n^{(m)}\right] = (1+\alpha)^2\sum_{i=1}^{m}\left[(1+\alpha)\frac{\lambda_n}{\lambda_1} - \alpha\right]^{2(m-i)} Var\left[\xi_n^{(i)}\right]. \tag{2.5.13}$$

For estimating variances while a simulation is running, the actual normalization factors used should replace the constant normalization factors, $1/\lambda_1$, where applicable for the first *M* cycles that have been completed. This yields a variance estimate of

$$Var[\tilde{u}_n^{(m)}]=\sum_{i=1}^{m} Var\left[\xi_n^{(i)}\right]\cdot\begin{cases}\left(\dfrac{\lambda_n}{\lambda_1}\right)^{2(m-i)} & \forall\, i\geq M\\ \left(\dfrac{\lambda_n}{\lambda_1}\right)^{2(m-M)}\cdot\displaystyle\prod_{j=i+1}^{M}\left(\lambda_n\tilde{k}^{(j)}\right)^2 & \forall\, i<M\leq m\end{cases} \tag{2.5.14}$$

for the standard power method and an estimate of

$$Var[\tilde{v}_n^{(m)}]= \sum_{i=1}^{m} Var\left[\xi_n^{(i)}\right]\cdot\begin{cases}\left[(1+\alpha)\dfrac{\lambda_n}{\lambda_1}-\alpha\right]^{2(m-i)} & \forall\, i\geq M\\ \left[(1+\alpha)\dfrac{\lambda_n}{\lambda_1}-\alpha\right]^{2(m-M)}\cdot\displaystyle\prod_{j=i+1}^{M}\left[(1+\alpha)\lambda_n\tilde{k}^{(j)}-\alpha\right]^2 & \forall\, i<M\leq m\end{cases} \tag{2.5.15}$$

for the extrapolated power method.

As the source site distribution approaches stationarity, the single-cycle deviations are assumed to also approach steady state probability distributions with variances

$$\lim_{m\to\infty} Var\left[\xi_n^{(m)}\right]=\sigma_n^2. \tag{2.5.16}$$

For estimating the SBDC variances, the non-fundamental mode DFDCs are approximated by their steady state distributions. Under this approximation, the variances of the standard power method SBDCs from (2.5.10) are

$$Var[\tilde{u}_n^{(m)}]=\sum_{i=0}^{m-1}\left(\frac{\lambda_n}{\lambda_1}\right)^{2i}\sigma_n^2\cdot \tag{2.5.17}$$

Equation (2.5.17) contains a geometric series with common ratio λ_n^2/λ_1^2, which reduces to

$$Var\left[\tilde{u}_n^{(m)}\right]=\sigma_n^2\frac{1-(\lambda_n/\lambda_1)^{2m}}{1-(\lambda_n/\lambda_1)^2}\quad \forall\, n>1\,. \tag{2.5.18}$$

The variances converge in the limit of many cycles to

$$\lim_{m\to\infty} Var\left[\tilde{u}_n^{(m)}\right]=\sigma_n^2\frac{1}{1-(\lambda_n/\lambda_1)^2}\quad \forall\, n>1\,. \tag{2.5.19}$$

Similarly, for the extrapolated power method, the variances of SBDCs from (2.5.13) are

$$Var\left[\tilde{v}_n^{(m)}\right]=(1+\alpha)^2\sum_{i=0}^{m-1}\left[(1+\alpha)\frac{\lambda_n}{\lambda_1}-\alpha\right]^{2i}\sigma_n^2.. \tag{2.5.20}$$

Equation (2.5.20) contains a geometric series with common ratio $\left[(1+\alpha)\lambda_n/\lambda_1-\alpha\right]^2$. For all modes where the magnitude of the common ratio is not equal to one, the variances are

$$Var\left[\tilde{v}_n^{(m)}\right]=\frac{1-\left[(1+\alpha)\dfrac{\lambda_n}{\lambda_1}-\alpha\right]^{2m}}{1-\left[(1+\alpha)\dfrac{\lambda_n}{\lambda_1}-\alpha\right]^{2}}(1+\alpha)^2\sigma_n^2, \tag{2.5.21}$$

which simplify to

$$Var\left[\tilde{v}_n^{(m)}\right]=\frac{1-\left[(1+\alpha)\lambda_n/\lambda_1-\alpha\right]^{2m}}{1-\left(\dfrac{\lambda_n}{\lambda_1}\right)^2-\dfrac{2\alpha}{1+\alpha}\left(1-\dfrac{\lambda_n}{\lambda_1}\right)}\sigma_n^2. \tag{2.5.22}$$

Equation (2.5.22) describes the variances of all non-fundamental SBDCs with common ratios that are not equal to 1. For modes with common ratios whose magnitudes are less than one, the variances of the extrapolated SBDCs converge to

$$\lim_{m\to\infty} Var\left[\tilde{v}_n^{(m)}\right]=\frac{1}{1-\left(\dfrac{\lambda_n}{\lambda_1}\right)^2-\dfrac{2\alpha}{1+\alpha}\left(1-\dfrac{\lambda_n}{\lambda_1}\right)}\sigma_n^2. \tag{2.5.23}$$

If the common ratio has a magnitude greater than 1 for a mode, then the series diverges for that mode, and the source distribution as a whole does not converge.

Figure 2.5.4 contains an example of the variance approximations plotted with variances calculated from 10,000 empirical observations of the SBDCs for the second mode of the same uniform slab problem as presented earlier in this chapter. The single cycle variance was estimated by approximating the limit of the variance in (2.5.19) with the average of variances from 400 converged standard power method cycles and solving (2.5.19) for σ_n^2 using the diffusion theory eigenvalue ratio of 0.99. The stationary variance of the extrapolated simulations agrees well with the theory as can be seen in Figure 2.5.4 after about 150 cycles; however, prior to reaching stationarity the approximations overestimate their respective variances for both the standard and extrapolated power methods. This overestimation during the converging cycles was not observed for other modes, such as the third mode, which can be seen in Figure 2.5.5. This difference in behavior is

attributable to differences between the stationary single cycle variances σ_n^2 and their respective non-stationary single cycle variances, $\left(\sigma_n^{(m)}\right)^2$, because the overestimation was not observed when starting with a converged source, which is discussed in Section 3.3.

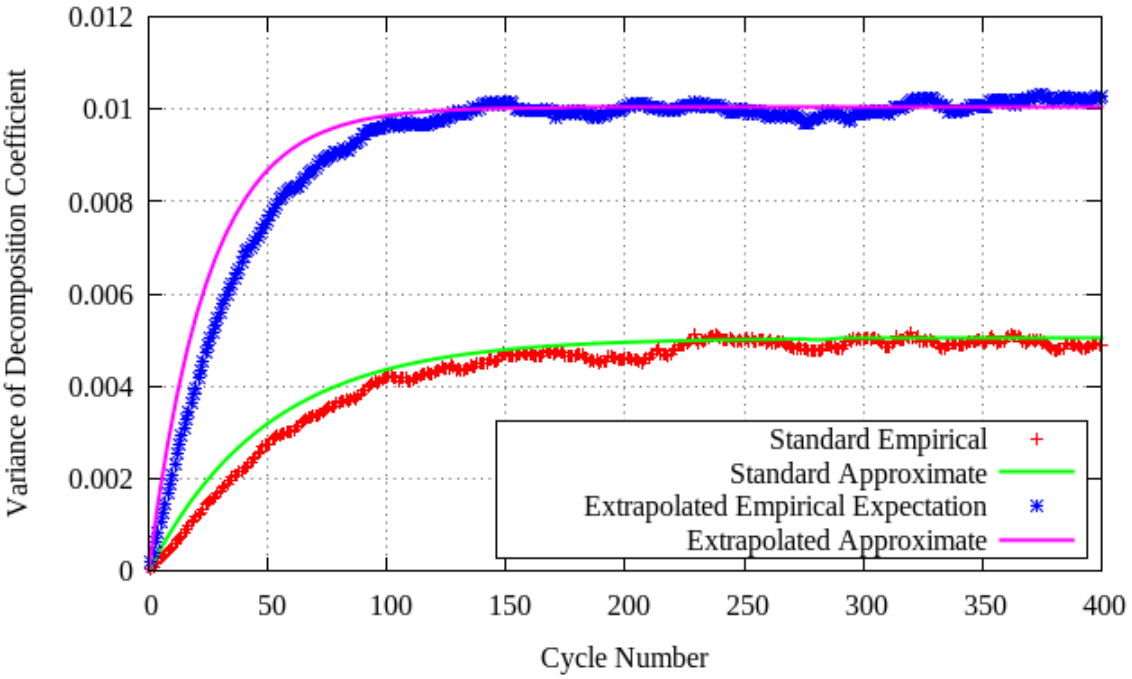

Figure 2.5.4. Uniform slab second mode SBDC variance versus cycle for the standard and extrapolated power methods with their approximations.

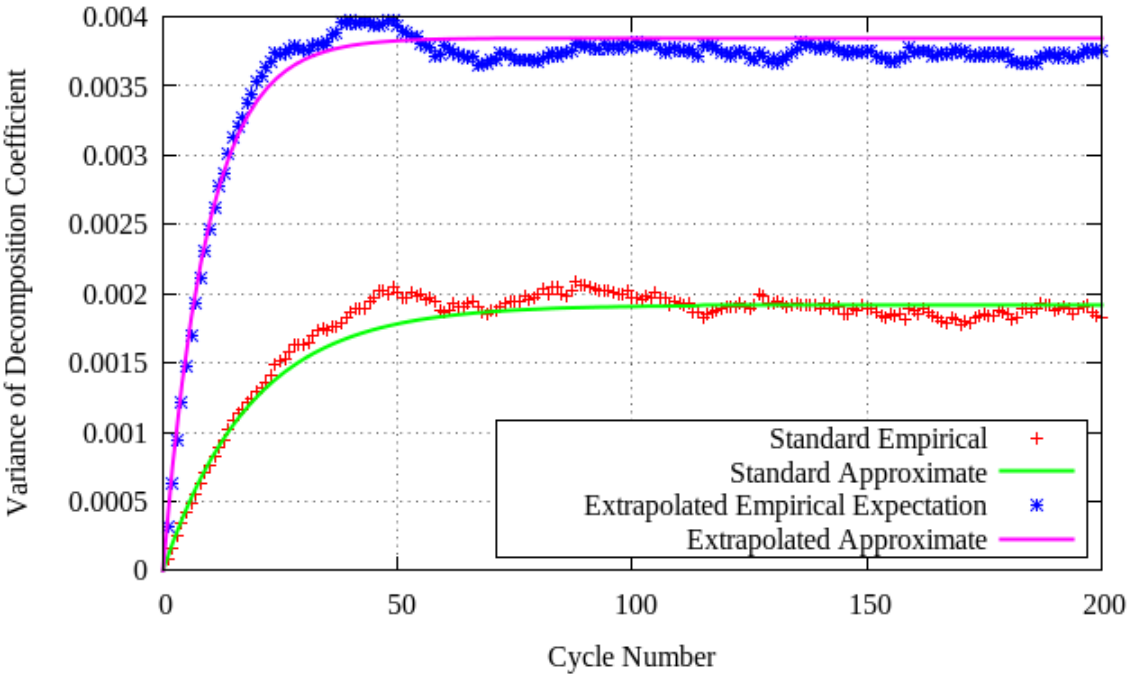

Figure 2.5.5. Uniform slab third mode SBDC variance versus cycle for the standard and extrapolated power methods with their approximations.

This attribution can be inferred from the relative variance, which is defined here as the ratio of the extrapolated variance to the standard variance. From the approximate variances in (2.5.18) and (2.5.22) for the standard and extrapolated power methods, respectively, the approximate relative variances of non-fundamental modes are

$$\frac{Var\left[\widetilde{v}_n^{(m)}\right]}{Var\left[\widetilde{u}_n^{(m)}\right]}=\frac{1-\left[(1+\alpha)\lambda_n/\lambda_1-\alpha\right]^{2m}}{1-\left(\frac{\lambda_n}{\lambda_1}\right)^2-\frac{2\alpha}{1+\alpha}\left(1-\frac{\lambda_n}{\lambda_1}\right)}\cdot\frac{1-\left(\lambda_n/\lambda_1\right)^2}{1-\left(\frac{\lambda_n}{\lambda_1}\right)^{2m}}. \tag{2.5.24}$$

In the limit of infinitely many cycles, the relative variances should converge to

$$\lim_{m\to\infty}\frac{Var\left[\widetilde{v}_n^{(m)}\right]}{Var\left[\widetilde{u}_n^{(m)}\right]}=\frac{1-\left(\lambda_n/\lambda_1\right)^2}{1-\left(\frac{\lambda_n}{\lambda_1}\right)^2-\frac{2\alpha}{1+\alpha}\left(1-\frac{\lambda_n}{\lambda_1}\right)}=\frac{1+\lambda_n/\lambda_1}{1+\frac{\lambda_n}{\lambda_1}-\frac{2\alpha}{1+\alpha}}. \tag{2.5.25}$$

In Figure 2.5.6, the relative variances from the approximation equations follow the empirical data better than the non-relative variances in Figures 2.5.4 and 2.5.5 because the differences between the approximate and actual single cycle variances cancel each other to some extent when calculating the ratio.

The relative variance approximations can be inaccurate because of the imperfect implementation of extrapolation. For example, the accuracy of converged relative variances from (2.5.25) tended to diminish for increasing mode numbers for the 16 bin extrapolation mesh with 4.0E3 histories per cycle as Figure 2.5.7 shows. The approximate equations make poor predictions for the higher order modes because the extrapolation is performed on a relatively coarse mesh that does not capture the spatial detail of those higher order modes. Refining the extrapolation mesh increases the accuracy of the variance approximations when coupled with an appropriate increase in the number of histories as Figure 2.5.7 also demonstrates for a 256 bin extrapolation mesh with 4.0E5 histories per cycle. The shape of mode 16 is likely responsible for the outlier in the stationary relative variances of the 16 bin extrapolation mesh, which is observable in Figure 2.5.7. Mode 16 has 8 peaks and 8 troughs, which each line up with a mesh-bin midpoint, such that the main features of this mode are reasonably well represented by the coarse mesh; therefore, mode 16 is extrapolated more effectively than

neighboring modes in the eigenvalue spectrum, which are not represented as accurately on the coarse mesh. For the periodic eigenmodes of the uniform slab in Appendix A, higher order modes are mapped to lower order modes on the 16-bin mesh in a phenomenon referred to as aliasing [31]. More effective extrapolation yields a higher relative variance because extrapolation amplifies noise introduced at each cycle. Less effective extrapolation of higher order modes is not necessarily undesirable, but the user should be aware of this potential for inaccuracy when estimating variances.

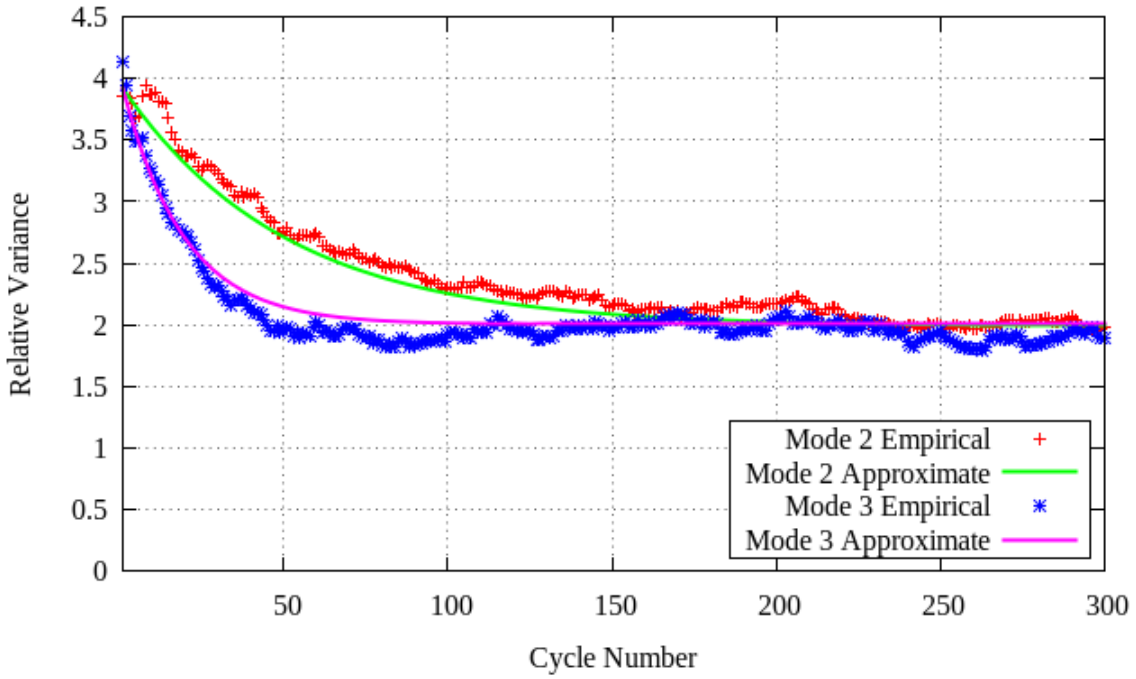

Figure 2.5.6. Uniform slab relative variances of second and third mode SBDCs calculated empirically and approximated.

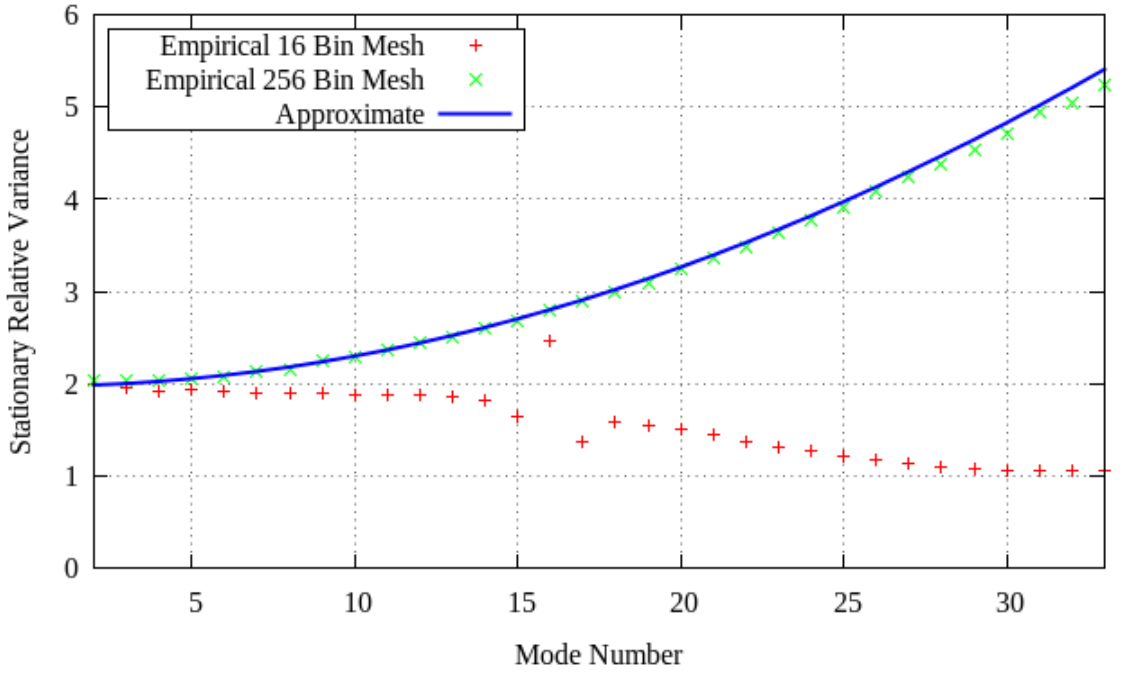

Figure 2.5.7. Uniform slab stationary relative variances of SBDCs calculated empirically for two different extrapolation meshes and approximated using constant normalization.

For modes which are well represented by the extrapolation mesh, one can apply the aforementioned approximate model for the variances of SBDCs to estimate the expected ABSs of SBDCs. However, to make the estimation, one must know or assume a distribution for the PDFs of SBDCs. For the following derivation, the SBDCs are assumed to be normally distributed; evidence in Chapter 3 supports this assumption.

For a normally distributed random variable X with mean μ and standard deviation σ, the PDF of a random variable κ, which is equal to the ABS of X, is the normal distribution folded over to the positive side of the x-axis with the following PDF,

$$f_\kappa(x)=\begin{cases}\frac{1}{\sigma\sqrt{2}}\left[e^{-\frac{(x-\mu)^2}{2\sigma^2}}+e^{-\frac{(x+\mu)^2}{2\sigma^2}}\right] & \forall\, x\geq 0\\ 0 & \forall\, x<0.\end{cases} \tag{2.5.26}$$

Thus, the CDF of κ is

$$F_\kappa(x)=1/2\left[\operatorname{erf}\left(\frac{x+\mu}{\sigma\sqrt{2}}\right)+\operatorname{erf}\left(\frac{x-\mu}{\sigma\sqrt{2}}\right)\right] \tag{2.5.27}$$

Where the error function (erf) is defined as

$$\operatorname{erf}(x)=\frac{2}{\sqrt{\pi}}\int_0^x e^{-t^2}dt\,. \tag{2.5.28}$$

From (2.5.26), the expected value of κ is

$$\begin{aligned}E[\kappa]&=\int_0^\infty x f_\kappa(x)\,dx\\ &=\sigma\sqrt{\frac{2}{\pi}}e^{\frac{-\mu^2}{2\sigma^2}}-\mu\operatorname{erf}\left(\frac{-\mu}{\sqrt{2}\sigma}\right).\end{aligned} \tag{2.5.29}$$

For an unbiased iteration, the stationary mean μ of non-fundamental mode SBDCs is zero, which simplifies (2.5.29) to

$$E[\kappa]=\sigma\sqrt{\frac{2}{\pi}}. \tag{2.5.30}$$

Inserting the standard deviation estimates from (2.5.18) and (2.5.22) into (2.5.29) yields the approximate expected ABSs of SBDCs for the standard and extrapolated power methods, respectively. For example, Figure 2.5.8 displays the the ABSs of SBDCs for the second mode of the uniform slab with a 16 bin extrapolation mesh and 4.0E3 histories per cycle. As Figure 2.5.8 shows, the ABSs from the adjusted constant multiplier

approximations follow the empirical observations closely as the second mode approaches convergence. This agreement suggests that the normalized SBDCs are indeed normally distributed random variables, which Chapter 3 demonstrates along with additional information about the single-cycle variances of SBDCs.

As the theoretical approximations and example data show, extrapolation increases the variances of SBDCs, which can adversely affect the reliability of selecting a source site distribution from the extrapolated algorithm. However, if extrapolation is only performed for some cycles and turned off at some point in a simulation, then the potential exists to reach a sufficiently converged source with fewer cycles. A maximum ABS of a SBDC can be used as a convergence criterion, such that if the ABS of a SBDC falls below that maximum value, then the source distribution is considered sufficiently converged with respect to that mode. As an example, when extrapolation was stopped after the first 100 cycles for the uniform slab problem in Appendix A with 4.0E3 source sites per cycle, the expected ABS of the second mode SBDC reached a value within 10% of the converged ABS of the SBDC after 218 cycles, which is 20.4% fewer than the 274 cycles that the standard power method required to reach a similar expected ABS of the second mode SBDC. For a less restrictive condition of within 50% of the converged ABS of the SBDC, extrapolation was expected to reach that ABS of the SBDC for the second mode after 128 cycles while the standard power method was expected to require 196 cycles, which is 34.7% fewer cycles. As the convergence condition increases, which is relaxing the criterion, the variance becomes a less significant factor in calculating the expected ABS of a SBDC because of the decaying exponential in (2.5.29); therefore, the performance of extrapolation relative to the standard power method improves as the restriction on the ABS of SBDCs increases. While the crossing of ABS of SBDCs within some range of their expected ABSs can be a useful criterion, it does not address underestimation of uncertainty that can result from collecting data across multiple independent simulations; thus, Section 4.2 presents a new convergence diagnostic that can apply universally to all run strategies that involve some form of stochastic convergence. These results demonstrate that extrapolation can provide advantages over

the standard power method when a proper number of extrapolated cycles is used. A technique for selecting the number of extrapolated cycles given a particular choice for the extrapolation parameter appears in Section 4.3.

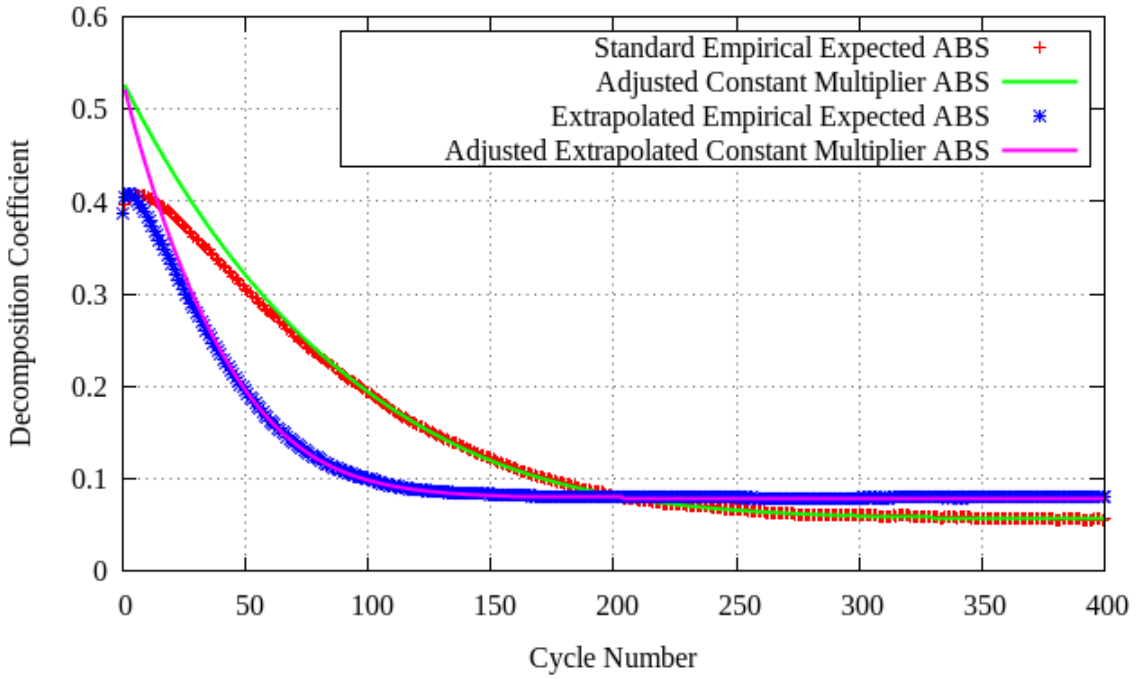

Figure 2.5.8. Uniform slab expected absolute value of SBDCs of the second mode calculated empirically and via the constant multiplier approximation for both the standard and extrapolated power methods.

2.6 Estimating the Initial Source Bank Decomposition Coefficients

The proximity of the initial fission source distribution to the fundamental mode affects the number of cycles needed to sufficiently converge a sequence of source distribution estimates. To determine the expected number of cycles required to sufficiently converge a fission iteration from the adjusted multiplier approximation that Section 2.2 describes, SBDCs of the initial distribution, i.e., β_n, and the shape of the fundamental mode, which determines *Y*, must be known or estimated. For an accurate estimate, the eigenfunctions or at least approximate eigenvectors must be known. Continuous eigenfunctions are generally unknown; however, eigenvectors may be estimated during a simulation via the fission matrix [6], [32], [33]. With estimates for the eigenvectors, the aforementioned variables are trivial to calculate. However, without any knowledge of eigenvectors, one may choose to make reasonable estimates for the variables of interest to determine an upper-bound for the number of discarded cycles. This section presents an algorithm to estimate a maximum bound for the initial SBDCs. An estimator for the ratio Y/β_1 is derived and examined. Additionally, the details of making an informed estimate for β_n and *Y* are presented for use when starting from a reasonably converged source from a prior simulation.

Using the normalization of the source bank with the definition and properties of the *p*-norms, the initial SBDCs may be approximately bounded. The source banks are all normalized such that their 1-norm is unity, and from the definition of the *p*-norms [16], the 2-norm of any distribution must be less than or equal to its 1-norm, which yields the relation

$$\left\|U^{(0)}\right\|_2 \le \left\|U^{(0)}\right\|_1 = 1. \tag{2.6.1}$$

The 2-norm will equal the 1-norm only if $U^{(0)}$ is a standard basis vector, i.e., one vector element is 1 and all other elements are zero. The vector $U^{(0)}$ when decomposed into eigenvectors has SBDCs β_n, which can be calculated from (1.1.29),

$$\beta_n = B_n^{\dagger} \cdot U^{(0)}. \tag{2.6.2}$$

If $U^{(0)}$ is parallel or anti-parallel to $B_n^{\dagger}$ of a particular mode, the magnitude of the SBDC

is maximized for that mode, and the vector may be expressed as

$$U^{(0)}=\pm\left\|U^{(0)}\right\|_2\frac{B_n^\dagger}{\left\|B_n^\dagger\right\|_2}. \tag{2.6.3}$$

Therefore, by inserting (2.6.3) into (2.6.2), one can see that the magnitude of a SBDC of a 1-norm normalized vector $U^{(0)}$ is bounded by

$$|\beta_n|\le\left\|U^{(0)}\right\|_2\left\|B_n^\dagger\right\|_2\le\left\|U^{(0)}\right\|_1\left\|B_n^\dagger\right\|_2=\left\|B_n^\dagger\right\|_2. \tag{2.6.4}$$

Despite the normalization conditions of (1.1.27),

$$B_n\cdot B_n=1, \tag{2.6.5}$$

and (1.1.28),

$$B_n^\dagger\cdot B_n=1, \tag{2.6.6}$$

the Cauchy-Schwartz inequality,

$$\left|B_n^\dagger\cdot B_n\right|\le\left\|B_n^\dagger\right\|_2\left\|B_n\right\|_2, \tag{2.6.7}$$

reveals that the 2-norm of the adjoint eigenvector may not have an upper bound but the 2-norm is always greater than or equal to one. However, for distinct eigenvalues, one may assume that the adjoint eigenvector is close in shape to the right eigenvector [34]; for such an assumption, $\left\|B_n^\dagger\right\|_2\approx1$. With this assumption inserted into (2.6.4), the maximum absolute values for SBDCs of an initial source distribution are approximately $\left\|U^{(0)}\right\|_2$, which is less than or equal to one as (2.6.1) shows.

In addition to a bound for β_n, an estimate for the ratio Y/β_1 is necessary to calculate expected values with the adjusted constant multiplier approximation as in (2.2.24) and (2.3.17). From (2.2.22), the ratio Y/β_1 is

$$\frac{Y}{\beta_1}=\lim_{m\to\infty}E\left[\prod_{i=1}^{m}\lambda_1\widetilde{k}^{(i)}\right]. \tag{2.6.8}$$

An iterative approximation of Y/β_1 is obtained by truncating the product in (2.6.8) to include only the number of cycles that have been simulated, i.e.,

$$\prod_{i=1}^{m}\lambda_1\widetilde{k}^{(i)}\approx\frac{Y}{\beta_1}. \tag{2.6.9}$$

As an estimate for the fundamental eigenvalue in (2.6.9), one may use the mean of the

inverses of normalization factors from the second half of cycles, which is

$$\lambda_1 \approx \frac{2}{m} \sum_{i=m/2}^{m} \frac{1}{\widetilde{k}^{(i)}}. \tag{2.6.10}$$

This may not be an optimal estimator for the fundamental eigenvalue, but it was used as a proof of concept for the estimator. As an example, Table 2.6.1 summarizes the parameters associated with the uniform slab problem in Appendix A with a 256-bin mesh and an initial source in the left-most bin.

β_1	$\|B_1\|_1$	Y	Y/β_1
1.169E-3	14.44	6.926E-2	59.23

Table 2.6.1: Parameters of 256-bin uniform slab with initial source in left-most bin.

Figure 2.6.1 shows the expected evolution of the iterative estimates for Y/β_1 over the first 600 cycles when using 4E+4 histories as approximated by averaging the results from 774 independent simulations. The expected estimate for Y/β_1 crossed the true value after approximately 301 cycles, which was approximately when the fundamental eigenvalue estimate approached its converged value. The eigenvalue estimate became reasonably converged approximately 100 cycles after the normalization factors approached their converged mean because the eigenvalue estimator is a moving average, which necessitates some delay in calculating an accurate estimate [35]. The expected estimate for Y/β_1 was within a factor of ten of the true value after only 5 cycles, which may be sufficient depending on the use case of the approximate model. The estimator produced a positively biased result that slowly increased with more cycles; this behavior is attributable to the well-documented bias induced by stochastic normalization [4], [25], [36], [37]. This increasing behavior was more notable when using 4E+3 histories per cycle as Figure 2.6.2 demonstrates from averaging 1000 simulations, and the bias was less notable when using 4E+5 histories as Figure 2.6.2 shows from the average of 446 simulations. Therefore, this estimation technique for Y/β_1 is sensitive to under-sampling.

While this iterative technique can yield reasonable estimates for Y/β_1, the variance of

those estimates grows exponentially. If one assumes that the normalization factors are nearly independent, that their PDFs are square integrable, and that the fundamental eigenvalue estimate approaches a constant, then the left-hand side of (2.6.9) approaches a log-normally distributed random variable [38]. The variance of a log-normal random variable *C* may be expressed as

$$Var[C] = e^{2\mu+2\sigma^2} - e^{2\mu+\sigma^2} \tag{2.6.11}$$

Where μ and σ are the location and scale parameters, respectively, of the PDF, which is

$$p(c) = \frac{1}{c\sigma\sqrt{2\pi}} e^{\frac{-(\ln c-\mu)^2}{2\sigma^2}}. \tag{2.6.12}$$

For a log-normal random variable produced by the multiplication of *m* random variables, i.e.,

$$C = X_1 X_2 \cdots X_m \tag{2.6.13}$$

where X_i is a random variable that is independent from X_j if $i \neq j$, the location parameter is

$$\mu = \sum_{i=1}^{n} E[\ln X_i], \tag{2.6.14}$$

And the scale parameter is

$$\sigma^2 = \sum_{i=1}^{m} Var[\ln X_i]. \tag{2.6.15}$$

For (2.6.9), the random variables are

$$X_i = \lambda_1 \tilde{k}^{(i)}. \tag{2.6.16}$$

Assuming that the normalization factors approach a stationary distribution, then both (2.6.14) and (2.6.15) increase linearly with respect to the number of cycles after sufficiently many cycles are simulated. Therefore, the exponents in (2.6.11) increase linearly with respect to cycle number, which indicates that the variance of the estimation technique should increase exponentially with respect to the number of cycles simulated. The variances from the uniform slab problem support this approximation as Figure 2.6.3 shows. A linear fit of variances from cycles 401 to 1000 on a log plot yielded the exponents and Pearson correlation coefficients that Table 2.6.2 shows. The correlation

coefficients for all three exponential fit lines exceeded 0.99, which supports the approximate analysis of the properties of the variance in the estimator for Y/β_1. This increasing variance behavior may be combated somewhat by averaging the estimates over an increasing number of cycles as a simulation runs in a similar fashion to the estimator for the fundamental eigenvalue; however, this was not tested.

Histories	**Exponent**	**Correlation Coefficient**
4E+3	0.002024	0.9907
4E+4	0.001214	0.9932
4E+5	0.001682	0.9927

Table 2.6.2: Properties of exponential fit to variances of Y/β_1 estimates from cycles 401 to 1000 of uniform slab simulations with various numbers of histories per cycle.

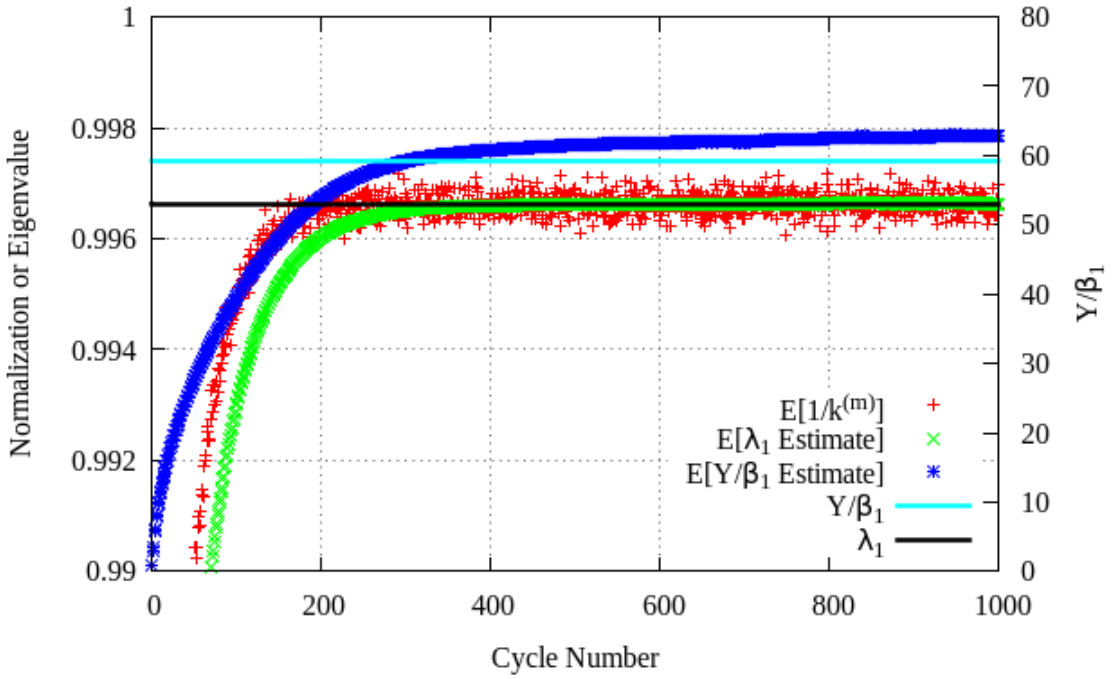

Figure 2.6.1 Plot of expected value of Y/β_1 estimate with its composing elements for the uniform slab problem with 4E+4 histories per cycle.

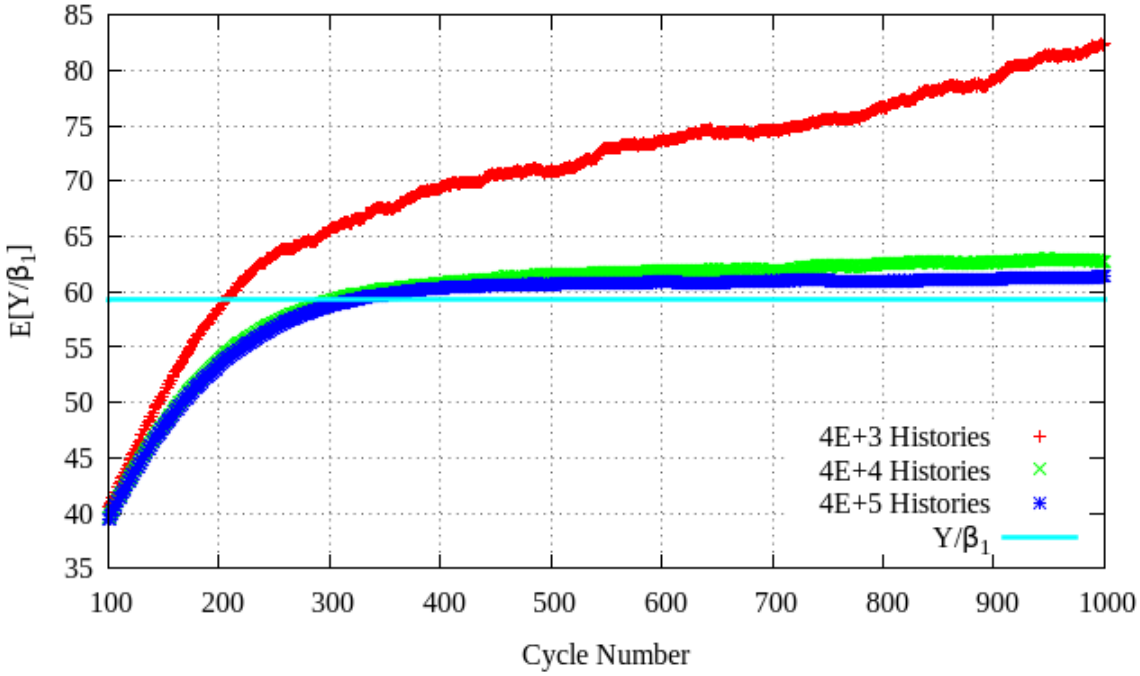

Figure 2.6.2 Plot of expected value of Y/β_1 estimate for various numbers of histories per cycle for the uniform slab problem.

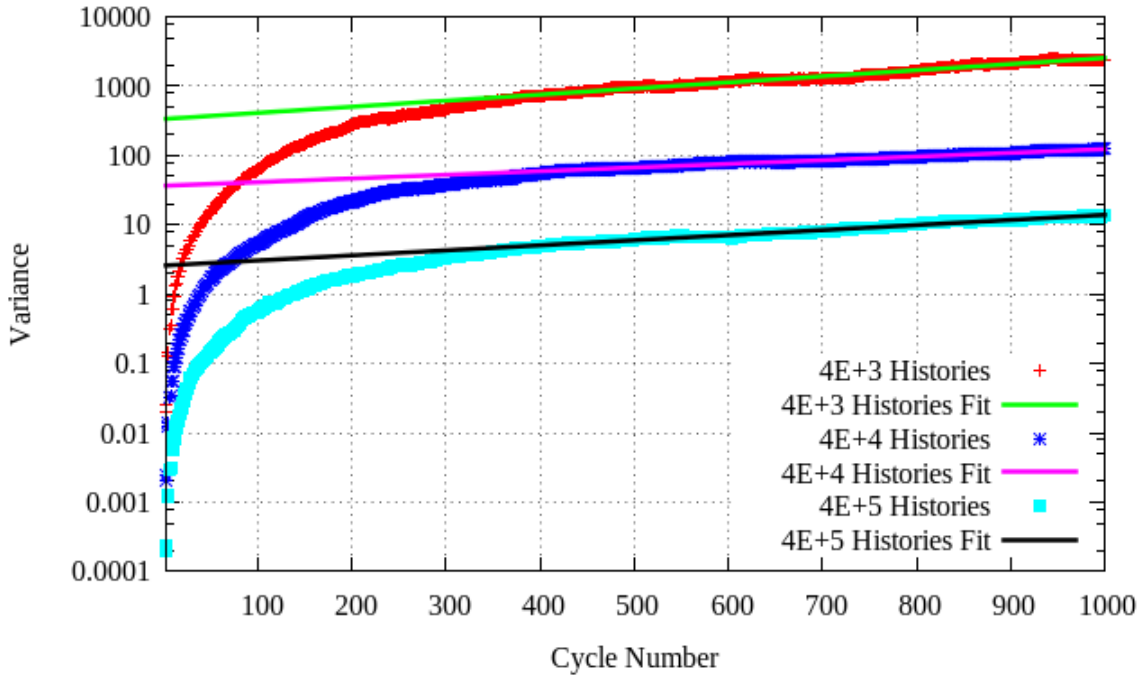

Figure 2.6.3 Plot of variances of Y/β_1 estimates for the uniform slab problem with various numbers of histories per cycle along with their respective exponential fit lines from data in cycles 401 through 1000.

2.6.1 Decomposition Coefficients of Initial Starting Source from Prior Simulation

If the initial source estimate is created from a prior simulation, then the properties of the SBDC PDFs of that prior simulation can be used to estimate β_n for a new simulation. For example, if the prior simulation used a sufficiently large number of power method cycles, then the PDFs of all non-fundamental modes would have nearly zero means and variances that are calculable from (2.3.7),

$$\lim_{m\to\infty} Var\left[\tilde{u}_n^{(m)}\right] = \sigma_n^2 \frac{1}{1-\left(\lambda_n/\lambda_1\right)^2} \quad \forall\, n>1\,. \tag{2.6.1.1}$$

A user could then estimate the initial SBDCs from the boundary of a chosen confidence interval for the normal distribution because the SBDCs are assumed to be normally distributed. For example, in 99.9% of the source banks selected from sufficiently converged simulations, the initial non-fundamental SBDCs will follow

$$\beta_n \le \frac{3.291\,\sigma_n}{\sqrt{1-\left(\lambda_n/\lambda_1\right)^2}} \quad \forall\, n>1\,. \tag{2.6.1.2}$$

Additionally, with a 2-norm normalized estimate for the fundamental mode from the prior simulation, Y may be approximated by the 1-norm of the fundamental mode estimate. The initial decomposition coefficient β_1 for the new simulation is calculable from the dot product of the 2-norm normalized fundamental mode estimate with the initial source for the new simulation. The ratio Y/β_1 will be similar to one but not necessarily equal because the source points are a finite sample from the stationary distribution of the prior simulation.

The best choice for the maximum bound on β_n should ultimately depend on how accurate one views an initial guess and how that guess is being applied, such as for determining an extrapolation cutoff or calculating the appropriate number of discard cycles. Having described how to estimate β_n and Y/β_1, the new modal convergence diagnostic may be applied to selecting an extrapolation cutoff cycle and predicting a minimum number of cycles that should be discarded becomes possible.

Chapter 3. Monte Carlo Noise

An understanding of the noise inherent in the MC fission operator is central to assessing convergence of a neutron source iteration and the feasibility and expected performance of linear extrapolation as a source convergence acceleration technique. In Section 2.5, two key assumptions allowed for a meaningful understanding of the convergence properties of the MC operator with and without extrapolation. Griesheimer and Nease investigated these assumptions [39] after being postulated by Toth and Martin [19]. The first of those assumptions, that the noise in the functional SBDCs is Gaussian, was agreed with by Griesheimer and Nease [39] under analog transport, but they did not prove it. The first section of this chapter will provide proof of the Gaussian nature of the functional SBDCs under analog and implicit capture, and the following section presents numerical tests to support the claim.

In (2.5.7) the noise components introduced at each cycle are assumed to be uncorrelated with respect to noise components from other cycles. As for the second assumption regarding independence of the deviation coefficients, Griesheimer and Nease show that the variances of SBDCs depend on the initial source points [39], which disproves the assumption. The extent of that dependence is not readily calculable for an arbitrary problem, but the dependence will be shown empirically to be negligible for the non-fundamental modes of a nearly stationary fission distribution, which is of primary interest. Griesheimer and Nease also show for a 1-D uniform slab that the variance per mode converges as the mode order increases, and the difference in the variances from the fundamental mode and a high order mode is approximately one order of magnitude for their test problem using analog MC. This chapter presents data that indicates a smaller range of variances arises when using implicit capture. Given the similarity in mode variances, the use of an alternate set of basis functions is proposed as a mechanism for

estimating the variance of DCs, and numerical results demonstrate the feasibility of the approach.

3.1 Normality of the Decomposition Coefficients

In Section 2.5, the eigenfunction DCs of a MC neutron transport algorithm are assumed to be normally distributed random variables. In this section, this assumption is proven for the intermediate bank decomposition coefficients (IBDCs) after a single cycle and the assumption of normality for the SBDCs is further justified. The proof applies to both analog and implicit capture MC. This proof relies on demonstrating that an IBDC is a summation of independent random variables and that the properties of these random variables meet the necessary criteria for application of the central limit theorem (CLT) to the distribution of their summation. Thus, for a sufficient number of these independent random variables, their summation, which is a DC, approaches a normal distribution.

The normality of the IBDCs can be shown by starting from the definition of an inner product over the domain *V*, i.e.,

$$\langle f, g \rangle = \int_V f(\vec{r}) g(\vec{r}) \, d\vec{r} \, . \tag{3.1.1}$$

If $g(\vec{r})$ is bounded, such that

$$g \in L^2(V) = \left\{ g : \int_V |g(\vec{r})|^2 \, d\vec{r} \le 1 \right\}, \tag{3.1.2}$$

and $f(\vec{r})$ is finite integrable over the domain, then the inner product is defined. For a normalized bi-orthogonal basis *b*, the DCs f_n of a function $f(\vec{r})$ are determined from an inner product as in (1.1.24), i.e.,

$$f_n = \int_V f(\vec{r}) b_n^{\dagger}(\vec{r}) \, d\vec{r} \, . \tag{3.1.3}$$

Copying (2.1.3), the intermediate fission bank is

$$\hat{u}^{(m)}(\vec{r}) = \tilde{H}\left[\tilde{u}^{(m-1)}\right] = \sum_{l=1}^{L} \sum_{c=1}^{C_l} w\left(\vec{r}_{l,c}^{(m)}\right) \delta\left(\vec{r} - \vec{r}_{l,c}^{(m)}\right) \tag{3.1.4}$$

where $\tilde{H}$ is the stochastic transport operator, *L* is the number of source sites in the source bank $\tilde{u}^{(m-1)}$, C_l is the number of collisions in history *l*, $\vec{r}_{l,c}^{(m)}$ is the location of the c^{th}

collision in history l of the m^{th} transport cycle, and $w\left(\vec{r}_{l,c}^{(m)}\right)$ is the fission production weight at each collision site. Inserting (3.1.4) into (3.1.3) yields the IBDCs, which are

$$\hat{u}_n^{(m)} = \sum_{l=1}^{L} \sum_{c=1}^{C_l} \int_V d\vec{r}\, w(\vec{r}_{l,c}^{(m)}) \delta(\vec{r} - \vec{r}_{l,c}^{(m)}) b_n^*(\vec{r}) = \sum_{l=1}^{L} \sum_{c=1}^{C_l} w(\vec{r}_{l,c}^{(m)}) b_n^*(\vec{r}_{l,c}^{(m)}). \quad (3.1.5)$$

The inner summation, which is from a single history, can be treated as a realization $\hat{x}_{n,l}$ of a random variable $\boldsymbol{X}_{n,l}$. Hence, the IBDCs are the random variable,

$$\hat{\boldsymbol{u}}_n^{(m)} = \sum_{l=1}^{L} \boldsymbol{X}_{n,l} \quad \forall n \in \mathbb{N}. \quad (3.1.6)$$

The starting point location, $\vec{r}_l^{(m-1)}$, determines the distribution of the random variable $\boldsymbol{X}_{n,l}$, and the random variable does not depend on the outcome of any other history; therefore, $\{\boldsymbol{X}_{n,l} : l \in \mathbb{N}, l \le L\}$ is a set of independent random variables. In addition to independence, other conditions must be satisfied to apply the CLT [13]. The distributions of $\boldsymbol{X}_{n,l}$ differ between analog transport and implicit capture facilitating different sufficient conditions for the CLT; therefore, they are treated separately in Sections 3.1.1 and 3.1.2.

3.1.1 Normality Under Analog Transport

Under analog MC, no histories can contribute an infinite tally score, and the basis functions are bounded; hence, $0 \le |\boldsymbol{X}_{n,l}| < \infty \; \forall l \in \mathbb{N}, l \le L$ for analog MC. The bounded nature of $\boldsymbol{X}_{n,l}$ implies that the PDF is 0 outside of some interval. If $b_n^*(\vec{r})$ is non-zero over a finite fissile region, then the variance of $\boldsymbol{X}_{n,l}$ will be non-zero because any isotropic source point inside the geometry can contribute a zero or non-zero value to the DC, each with finite non-zero probability. Having a finite interval over which the PDF is non-zero and a non-zero variance for $\{\boldsymbol{X}_{n,l} : l \in \mathbb{N}, l \le L\}$ are sufficient conditions to apply the CLT to the summation in (3.1.6) [13]; therefore, the IBDCs approach a normal distribution with many histories per cycle under analog transport.

3.1.2 Normality Under Implicit Capture

The normality assertion can also be extended to implicit capture schemes. The fission production weight at each collision from (2.1.2) is

$$w(\vec{r}_{l,c}^{(m)}) = q_{l,c}^{(m)} p_a(\vec{r}_{l,c}^{(m)}) \frac{\nu \Sigma_f(\vec{r}_{l,c}^{(m)})}{\Sigma_a(\vec{r}_{l,c}^{(m)})} . \tag{3.1.2.1}$$

Because neutrons are survival biased in implicit capture, the tally weights are reduced after each sampled collision according to

$$q_{l,c}^{(m)} = q_{l,c-1}^{(m)} (1 - p_a(\vec{r}_{l,c-1}^{(m)})) , \tag{3.1.2.2}$$

which maintains a fair game [1]. When the tally weight drops below a cutoff q_{cut}, roulette kills the particle or sets the weight to some higher value q_s in such a manner that the expectation of the tally weight follows (3.1.2.2). Because particles are terminated by a stochastic roulette procedure under implicit capture, the event chain may approach infinity; therefore, the PDF of $\boldsymbol{X}_{n,l}$ is not zero outside of a finite domain. Subsequently, the conditions, which were satisfied for analog MC in the previous paragraph, are no longer met by an implicit capture algorithm. The Berry-Esseén theorem states that if

$$E[\boldsymbol{X}_{n,l}^3] \leq C \sigma_{n,l}^2 \tag{3.1.2.3}$$

where $\boldsymbol{X}_{n,l}$ is a random variable with variance $\sigma_{n,l}^2$ and *C* is some constant, then the distribution of the sum of independent random variables,

$$\hat{\boldsymbol{u}}_n^{(m)} = \sum_{l=1}^{L} \boldsymbol{X}_{n,l} , \tag{3.1.2.4}$$

approaches the normal distribution [13]. This theorem also gives a bound of the error in the approximation, but the bound is not needed for this work. For notational simplicity, the cycle superscript and the history subscript along with the explicit dependence on position are dropped from the fission production weights, such that $w(\vec{r}_{l,c}^{(m)}) \equiv w_c$ in the following derivation of the bound on the third moment of the random variable $\boldsymbol{X}_{n,l}$. Stationary-state MC particle transport is a Markov process [21]; therefore, w_c, is a random variable with conditional PDF

$$P(w_c | w_{c-1}, w_{c-2}, \ldots, w_1) = P(w_c | w_{c-1}) \; \forall \; c > 1 \tag{3.1.2.5}$$

The expectation in (3.1.2.3) can be calculated as

$$E\left[\left|\boldsymbol{X}_{n,l}\right|^3\right]=\int_{\boldsymbol{W}}\left|\sum_{c=1}^{\infty}w_c b_n^*(\vec{r}_c)\right|^3 P(w_1)dw_1\prod_{c=2}^{\infty}P(w_c|w_{c-1})dw_c \qquad (3.1.2.6)$$

Where $\boldsymbol{W}$ is the space of all w_c where $w_c>0$. The $w_c=0$ regions can be excluded because they do not contribute to the expectation. The individual fission weight contributions inside $\boldsymbol{W}$ are bounded, such that

$$0<w_c=q_c p_a(\vec{r}_c)\frac{\nu\Sigma_f(\vec{r}_c)}{\Sigma_a(\vec{r}_c)}\le q_c T\ . \qquad (3.1.2.7)$$

where T is some finite constant. Thus, the more complicated problem geometry can now be simplified to a uniform infinite medium problem whose third moment bounds that of the original problem. Additionally, the magnitude of the left eigenfunctions are bounded by a constant U as a result of the normalization condition. Therefore, (3.1.2.6) can be bounded by a calculable integral

$$E\left[\left|\boldsymbol{X}_{n,l}\right|^3\right]\le\int T^3U^3\left(\sum_{c=1}^{\infty}q_c\right)^3 P(q_1)dq_1\prod_{c=2}^{\infty}P(q_c|q_{c-1})dq_c=T^3U^3E\left[\left(\sum_{c=1}^{\infty}q_c\right)^3\right]. \qquad (3.1.2.8)$$

To evaluate the integral in (3.1.2.8), the PDFs of the tally weights need to be determined. The starting tally weight q_1 is some constant Q; therefore, the PDF is

$$P(q_1)=\delta(q_1-Q)\ . \qquad (3.1.2.9)$$

In the bounding uniform infinite medium problem, the absorption probability is constant and greater than zero, i.e., $p_a(\vec{r}_{l,c}^{(m)})\equiv p_a>0$ because $T > 0$; therefore, the sequence of tally weights is deterministic above the cutoff, and the PDF is

$$P(q_c|q_{c-1})=\delta(q_c-(1-p_a)q_{c-1})\forall c\ge 2, q_{c-1}> q_{cut}/(1-p_a)\ . \qquad (3.1.2.10)$$

When the outgoing tally weight of a particle would fall below the cutoff weight q_{cut}, the outgoing tally weight is set to q_s with probability $p_{s,c}=(1-p_a)q_c/q_s$, or the tally weight is instead set to 0 with probability $1-p_{s,c}$. The PDF representing this transformation is

$$P(q_c|q_{c-1})=p_{s,c-1}\delta(q_c-q_s)+(1-p_{s,c-1})\delta(q_c)\forall c\ge 2, q_{c-1}< q_{cut}/(1-p_a)\ . \qquad (3.1.2.11)$$

From these PDFs, (3.1.2.8) can be sandwiched by the two extremes of implicit capture, which are $q_{cut}=0$, and $q_{cut}=q_s\ge Q$. With $q_{cut}=0$, the integral in (3.1.2.8) can be

evaluated using the PDF equations (3.1.2.9) and (3.1.2.10), such that

$$\int T^3U^3\left(\sum_{c=1}^{\infty} q_c\right)^3 P(q_1)dq_1\prod_{c=2}^{\infty} P(q_c|q_{c-1})dq_c = T^3U^3\left(Q+\sum_{c=2}^{\infty}(1-p_a)q_{c-1}\right)^3 . \quad (3.1.2.12)$$

Observing (3.1.2.2), the summation term in the right hand side of (3.1.2.12) is a series with common ratio $(1-p_a)<1$; therefore, the series must converge, and the series converges to $T^3U^3Q(1+1/p_a)$.

In the opposite extreme where $q_{cut}=q_s\geq Q$, roulette is played after every collision in the infinite medium. At collision number *j*, the particle will either be killed, making $q_c=0$ for all $c>j$, or the particle will leave the collision with tally weight q_s . The expectation for the cube of the sum of tally weights appearing in (3.1.2.8) can be calculated by placing the probabilities described by (3.1.2.9) and (3.1.2.11) into the integrand of (3.1.2.8) and carrying out the integration. Another approach begins by observing the possible events which compose the expectation and their respective probabilities, which are summarized in Table 3.1.2.1.

$\sum_{c=1}^{\infty} q_c$	**Probability**
Q	$1-(1-p_a)Q/q_s$
$Q+q_s$	$(1-p_a)Q/q_s(1-(1-p_a)q_s/q_s)$
$Q+q_s+q_s$	$(1-p_a)Q/q_s\left[(1-p_a)q_s/q_s\right]\left[1-(1-p_a)q_s/q_s\right]$
$Q+q_s+q_s+q_s$	$(1-p_a)Q/q_s\left[(1-p_a)q_s/q_s\right]\left[(1-p_a)q_s/q_s\right]\left[1-(1-p_a)q_s/q_s\right]$
$\vdots$	$\vdots$
$Q+C_lq_s$	$\frac{Q}{q_s}p_a\prod_{c=1}^{C_l}(1-p_a)$

Table 3.1.2.1: Events contributing to the moment expectation value.

Then, using the entries of Table 3.1.2.1, the expectation of the cube of the sum of tally weights is calculated by multiplying the possible realization values by their probability of occurrence and summing all of the results for each possible realization [13], i.e.,

$$E\left[\left(\sum_{c=1}^{\infty} q_c\right)^3\right] = Q^3\left(1-(1-p_a)\frac{Q}{q_s}\right)+(Q+q_s)^3\frac{Q}{q_s}p_a(1-p_a) +(Q+2q_s)^3\frac{Q}{q_s}p_a(1-p_a)^2+\ldots \quad (3.1.2.13)$$
$$= Q^3\left(1-(1-p_a)\frac{Q}{q_s}\right)+\frac{Q}{q_s}p_a\sum_{c=1}^{\infty}(Q+cq_s)^3(1-p_a)^c.$$

Placing (3.1.2.13) into (3.1.2.8) provides a bound on the third moment of a high cutoff, infinite medium simulation such that

$$E[X_{n,l}^3]\le T^3U^3Q^3\left[1-(1-p_a)\frac{Q}{q_s}\right]+T^3U^3\frac{Q}{q_s}p_a\sum_{c=1}^{\infty}\left[(Q+cq_s)^3(1-p_a)^c\right]. \quad (3.1.2.14)$$

For a purely absorbing infinite medium, the probability of absorption p_a is unity; therefore, the third moment is bounded by $T^3U^3Q^3$. Purely void or scattering systems $p_a=0$ have no fissions; therefore, all moments are zero. For all other configurations, the absorption probability is bounded such that $0<p_a<1$. The summation in (3.1.2.14) can be viewed as a power series $f(z)$ in the complex variable *z*, such that

$$f(z)=\sum_{c=1}^{\infty}\gamma_c(z-1)^c \quad (3.1.2.15)$$

where $\gamma_c=(Q+cq_s)^3(-1)^c$. The Cauchy-Hadamard theorem [40] states that the radius of convergence *R* of $f(z)$ about 1 is given by

$$\frac{1}{R}=\limsup_{c\to\infty}\left(|\gamma_c|^{(1/c)}\right). \quad (3.1.2.16)$$

The limit superior of the c^{th} root of the sequence coefficients is

$$\limsup_{c\to\infty}\left(|\gamma_c|^{(1/c)}\right)=\limsup_{c\to\infty}\left((Q+cq_s)^3\right)^{1/c}=1; \quad (3.1.2.17)$$

therefore, the radius of convergence is 1, which includes all values of the absorption probability, $0<p_a<1$, which have not yet been assigned a bound for their third moment. Therefore, the third moment is finite for the case of a high cutoff tally weight. All implicit capture simulations can be sandwiched by the two schemes, $q_{cut}=0$ and $q_{cut}=q_s\ge Q$, which were shown to have finite third moments. Therefore, all implicit capture schemes have finite third moments, and according to the Berry-Esseén theorem, finite third moments imply that the PDFs of the variables approach normal distributions. Therefore, the IBDCs, determined using either implicit or analog capture MC, are

normally distributed random variables in the limit of large numbers of histories.

3.1.3 Normality of the Source Bank Decomposition Coefficients

Having shown that the IBDCs are normally distributed, the author proposes that the SBDC may be assumed to be approximately normally distributed. This assumption is reasonable if the normalization may be approximated by a finite non-zero constant. Multiplication by a constant allows application of the CLT to the SBDCs under analog and implicit capture using the same arguments that apply to the IBDCs. The author speculates that if the single-cycle variance of $\widetilde{k}^{(m)}$ is sufficiently small, then the SBDCs are approximately normally distributed with possibly different variances being sufficiently small for different modes. Section 3.2 presents empirical evidence to support the assumption of normality for SBDCs.

3.2 Verifying Gaussian Nature of Decomposition Coefficients

This section presents empirical evidence to support the assumptions of normality for the intermediate and normalized source banks. Data was collected from simulations of the uniform slab from Appendix A and the two-dimensional heterogeneous reactor in Appendix C. Normal probability plots visually demonstrate normality of the IBDCs and SBDCs. In addition to visual examination, the null hypothesis of normality was repeatedly tested by comparing the Pearson correlation coefficient (PCC) of the probability plots against a table of critical values. If the number of failures was greater than that expected for a normally distributed random variable at the 0.1% significance level, then the DC of the mode under investigation was considered to not be normally distributed. The 0.1% significance level for the test was chosen to minimize the risk of falsely rejecting the null hypothesis that the DCs are normally distributed because the author is only concerned if the DC distributions consistently differ from the normal distribution. The majority of the test cases yielded the expected agreement; however, for particularly “bad” initial source distributions or low numbers of histories per cycle, the

tests failed for some modes, which tended to be associated with the higher eigenvalues.

The normal probability plots of this section were generated by first calculating the sample mean $\bar{x}$ and the unbiased sample variance s^2, which is synonymous with sample variance in this document, from

$$\bar{x}=\sum_{i=1}^{n} x_i \tag{3.2.1}$$

and

$$s^2=\frac{1}{n-1}\sum_{i=1}^{n}\left(x_i-\bar{x}\right)^2, \tag{3.2.2}$$

respectively, where n is the number of samples, x_i is the i^{th} sample, and s is the sample standard deviation [13]. Then the data was converted to Z-values by

$$Z_i=\frac{x_i-\bar{x}}{s}. \tag{3.2.3}$$

After sorting the Z-values from most negative to most positive, the Z-values were plotted versus the approximate normal order statistic medians, N_i, of the normal distribution [41], [42]. The sample PCCs were calculated using the *pearsonr* function of the SciPy library [43], which reports using the equation,

$$r=\frac{\sum_{i=1}^{n}\left(x_i-\bar{x}\right)\left(N_i-\bar{N}\right)}{\left[\sum_{i=1}^{n}\left(x_i-\bar{x}\right)^2\right]\left[\sum_{i=1}^{n}\left(N_i-\bar{N}\right)^2\right]}, \tag{3.2.4}$$

where r is the PCC, and $\bar{N}$ is the mean of the normal order statistic medians, which is zero. To test the null hypothesis, the probability plot correlation coefficients (PPCCs) were compared to their 5% significance level, which was taken from a table published in the *Engineering Statistics Handbook* as tabulated from studies by Filliben and Devaney [41], [42], [44]. Each particular combination of source distribution and geometry was simulated repeatedly using different random number streams, and the number of failures was compared with that expected for the 5% significance level, which should reject the null hypothesis in approximately 5% of tests if the variable is normally distributed. The test may be viewed as a Bernoulli trial with expected probability of failure p equal to 0.05

for a normally distributed random variable. The total number of failures from a set of *n* trials is a binomial experiment with expected value *np* and variance *np(1-p)* [13]. The 5% significance level was chosen over the 1% level for the PPCC test to produce more false positives, which yields a lower relative standard deviation for the total number of failures from *n* trials, which is

$$\sigma_{relative} = \frac{\sqrt{np(1-p)}}{np}. \tag{3.2.5}$$

When a set of tests has more failures than would be expected in 99.9% of similar experiments, i.e., a 0.1% significance level, then the result was considered to be significant.

The first test problem investigated was the uniform slab problem in Appendix A. A variety of initial source distributions were simulated; results for three of those initial distributions appear in Figures 3.2.1-3.2.3 where each figure contains results from 5000 tests of 100 implicit capture simulations of 1.0E5 histories for the first 60 modes. The expected number of failures for each 5000 tests is 250 with a 0.1% significance level of 299. Figure 3.2.1 shows the observed number of failures from initial source points sampled from the fundamental mode. None of the DCs from the fundamental mode source in Figure 3.2.1 approach or exceed the 0.1% significance level; therefore, the normality assumption cannot be refuted. Failures from tests of source points sampled from a far from converged source containing the first 33-modes were also below the significance threshold as Figure 3.2.2 shows. However, failures from PPCC normality tests of DCs exceeded the 0.1% significance threshold of 299 for some of the modes when the initial source distribution was confined to the left-most bin of 256 spatial subdivisions of the uniform slab, which Figure 3.2.3 displays. The modes that exceeded the significance level of 299 for the intermediate bank were the first through fourth modes, which had failures of 335, 327, 308, and 301, respectively. After normalization, the first and 19th modes exceeded the significance threshold of 299 with 310 and 301 failures, respectively. This demonstrates that the distribution of source bank sites may affect the validity of the normality assumption. Figure 3.2.4 shows a similar test for the left-sided source with the number of histories increased to 1.0E6. As can be seen in

Figure 3.2.4, increasing the number of histories reduces the number of failures, such that the normality assumption may not be refuted.

The normality assumption was also tested for the continuous energy 2-D reactor problem in Appendix C with a 20x20 grid applied for the purpose of estimating eigenvectors from a fission matrix solution, which was used to estimate eigenvector DCs. The infinite dimension was that parallel to the rods. The results from those tests supported the normality assumption when an adequate number of source points was used. For example, Figure 3.2.5 reports that the number of failures in normality tests of the first 50 modes were all beneath the 0.1% significance threshold of 67 for 1000 tests of 99 implicit capture simulations. The starting source used in the tests contained 1.0E5 source points from a far from converged source distribution containing large components of the first ten modes. Using an extrapolation parameter α of 0.965 yielded the test results in Figure 3.2.6, which were below the 0.1% significance threshold and that supports the assumption that extrapolated DCs may also be considered normally distributed.

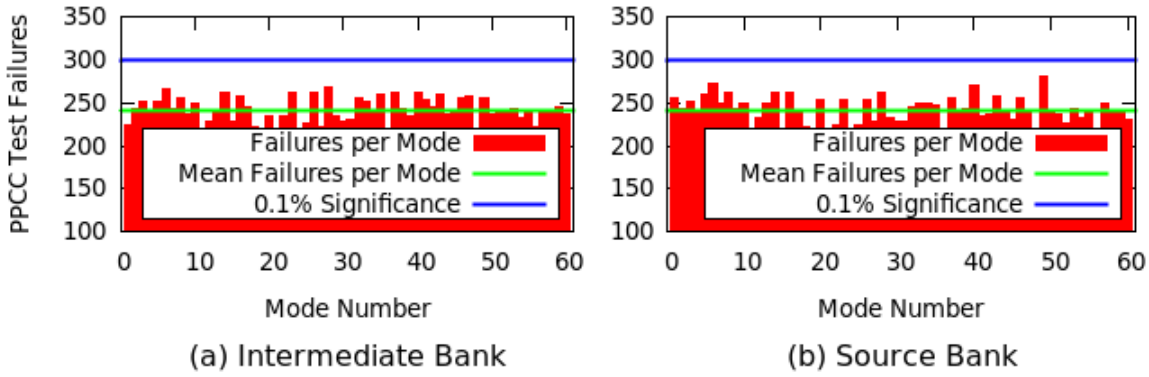

Figure 3.2.1 Hypothesis test results for DCs from 5000 implicit capture simulations of a thick sub-critical uniform slab with fundamental mode starting source.

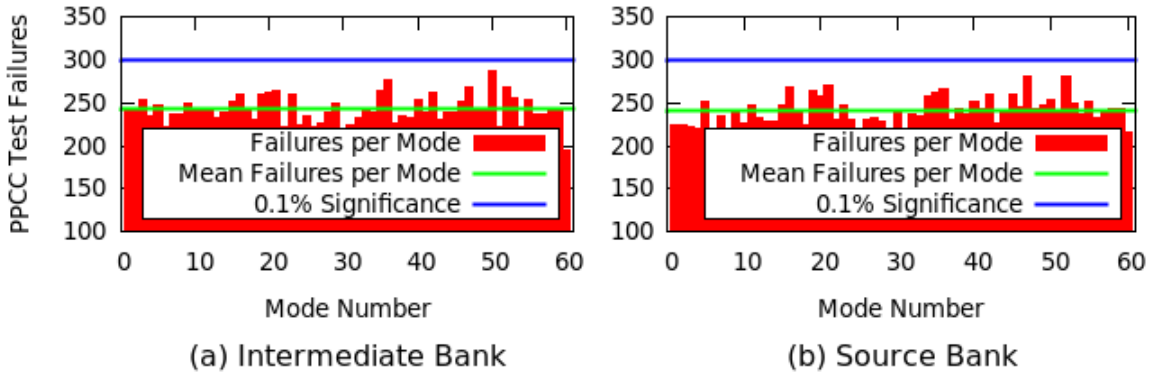

Figure 3.2.2 Hypothesis test results for DCs from 5000 implicit capture simulations of a thick sub-critical uniform slab with starting source composed of the first 33 modes.

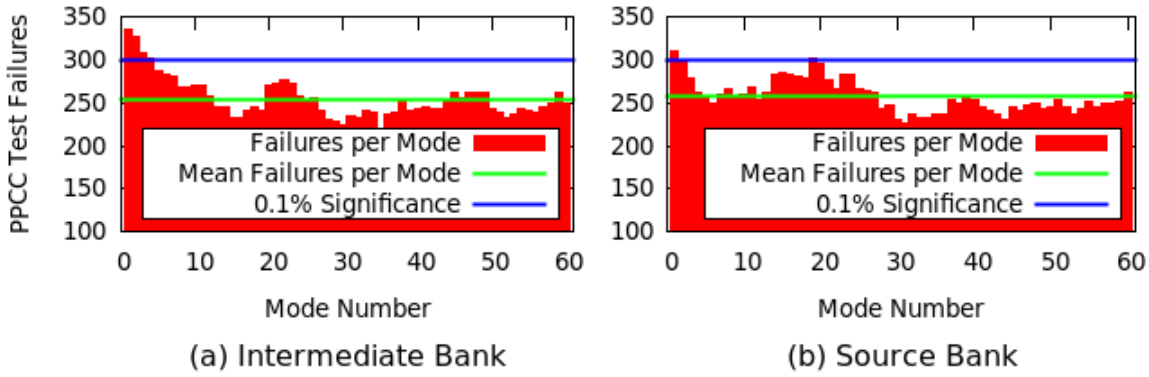

Figure 3.2.3 Hypothesis test results for DCs from 5000 implicit capture simulations of a thick sub-critical uniform slab with 1.0E4 starting source points on the left-side.

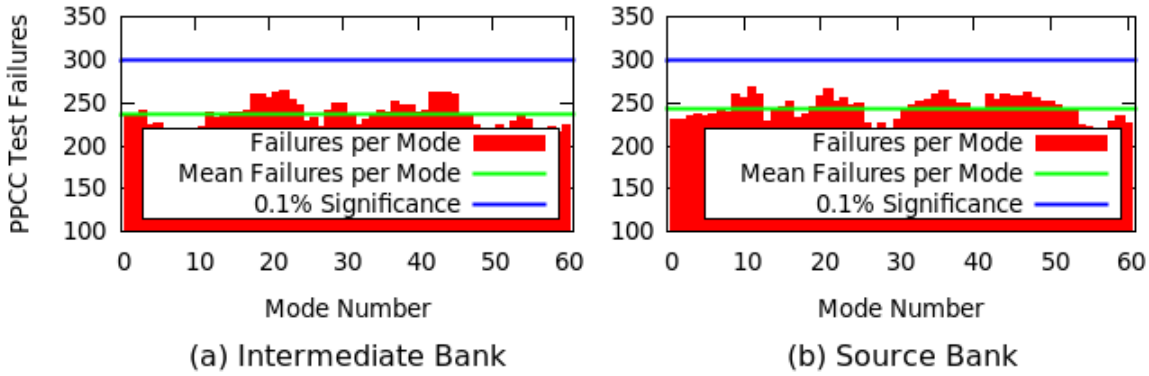

Figure 3.2.4 Hypothesis test results for DCs from 5000 implicit capture simulations of a thick sub-critical uniform slab with 1.0E5 starting source points on the left-side.

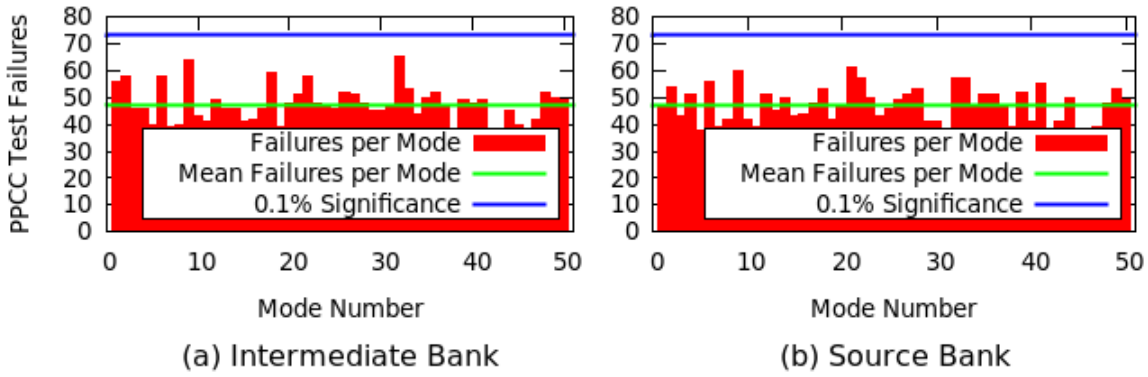

Figure 3.2.5 Hypothesis test results for DCs from 1000 standard simulations of a 2-D reactor with a 10-mode starting source of 1.0E5 points.

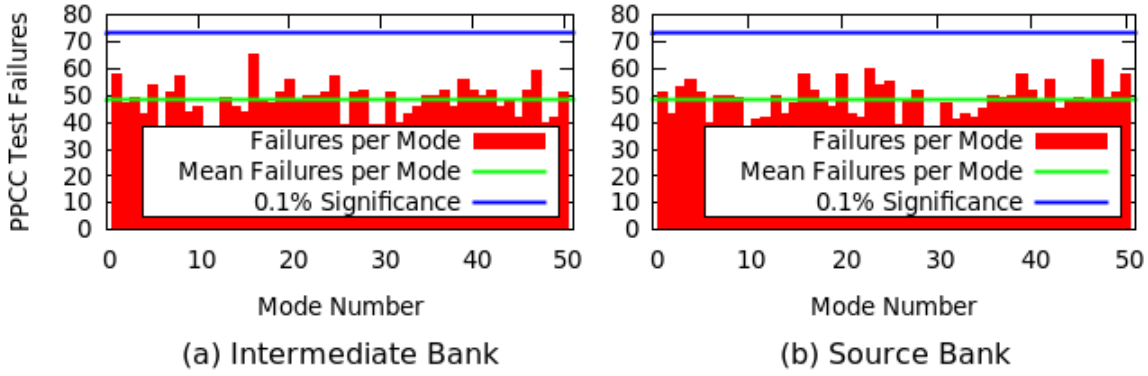

Figure 3.2.6 Hypothesis test results for DCs from 1000 extrapolated simulations of a 2-D reactor with a 10-mode starting source of 1.0E5 points.

With the assumption that DCs are normally distributed after a single cycle, the constant multiplier approximation predicts that the DCs are normally distributed after executing multiple cycles when the source distribution is sufficiently converged. To demonstrate this empirically, multiple independent simulations were performed with different random number streams that began with an identical set of source sites. Those source sites were allowed to change over the course of a simulation by selecting source sites for the next cycle from the fission sites in the previous transport cycle. Then, the PPCCs for each mode were calculated at each cycle and compared with the table of critical values. If the

DCs of a mode are normally distributed, then a 5% test failure rate was expected for the critical value used. The total number of failures for a mode may be viewed as a binomial experiment; however, unlike tests earlier in this section, the Bernoulli trials may not be independent; however, they were assumed to be independent to facilitate this analysis. As an example, the uniform slab problem was simulated 215 times with 500 standard power method cycles using analog capture and 1.0E4 histories per cycle with a starting source that was sampled from the fundamental mode. The PCC was calculated for each cycle. Testing of this analog capture setup showed no excessive failures beyond the 0.1% significance level for the first 60 modes after 5000 tests of 100 repetitions of the first cycle, which one can see in Figure 3.2.7; however, the excessive number of failures from tests without a fixed source, which can be seen in Figure 3.2.8, indicates that the normality assumption does not necessarily hold after multiple cycles. Fortunately, results from 253 simulations where the number of histories was increased by a factor of 10 do not exceed the 0.1% significance level, which can be observed in Figure 3.2.9. Therefore, the sufficient number of histories needed to consider a DC normally distributed after multiple cycles may be greater than that for a single cycle, which was expected because the fluctuating nature of normalizations accumulates over multiple cycles as can be seen in the equations of Chapter 2, which govern the DCs.

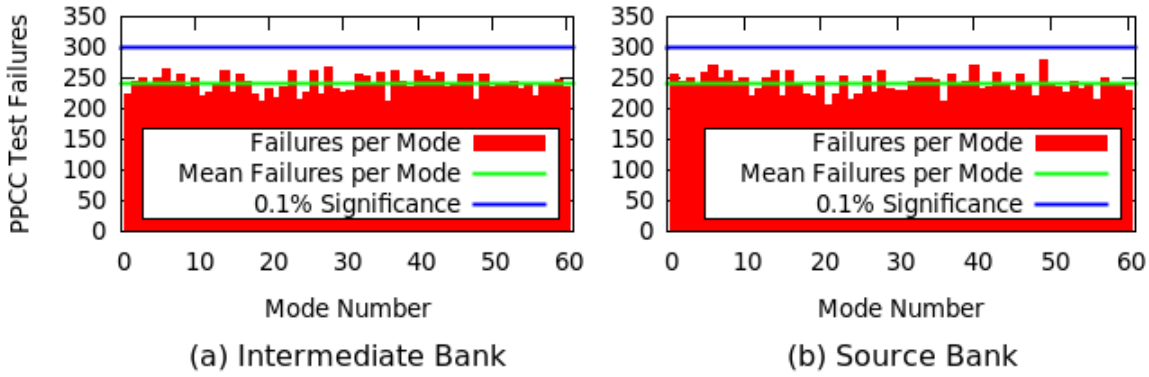

Figure 3.2.7 Hypothesis test results for DCs from 5000 analog capture simulations of 500 fixed source cycles of a thick sub-critical uniform slab with 1.0E4 starting source points from the fundamental mode.

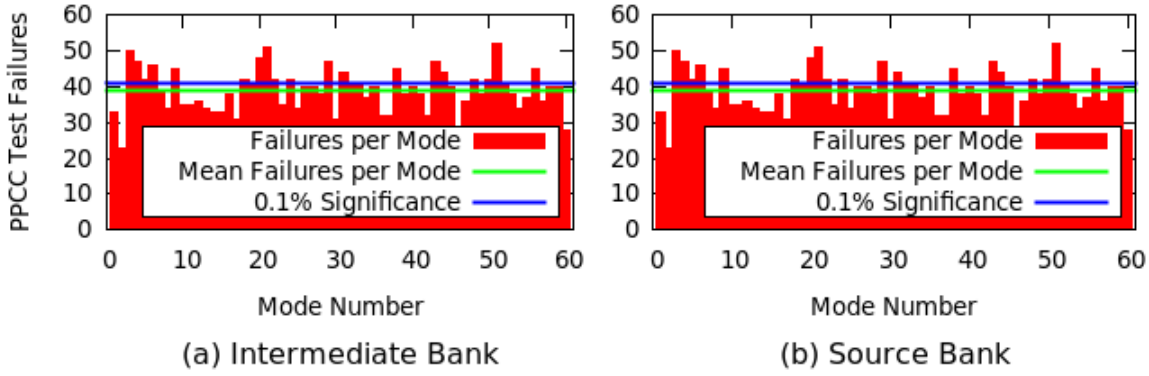

Figure 3.2.8 Hypothesis test results for DCs from 215 analog capture simulations of 500 cycles of a thick sub-critical uniform slab with 1.0E4 starting source points from the fundamental mode.

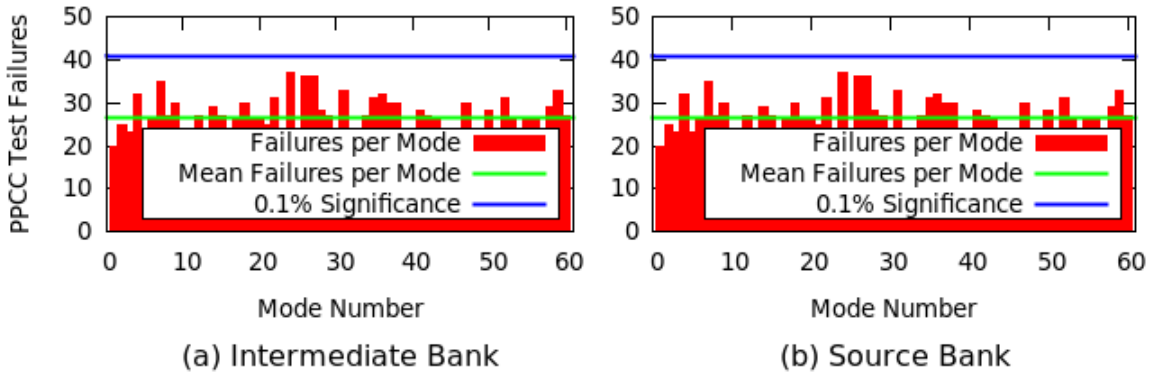

Figure 3.2.9 Hypothesis test results for DCs from 253 analog capture simulations of 500 cycles of a thick sub-critical uniform slab with 1.0E5 starting source points from the fundamental mode.

3.3 Validation of Variance from Constant Multiplier Model

As Section 2.5 discusses, knowing the variance of SBDCs is useful for setting convergence criteria and comparing different source algorithms. The constant multiplier equations from Section 2.5 provide a method for approximating the variances of SBDCs for reasonably converged simulations. In the process of simplifying the model for the purpose of generating the adjusted constant multiplier equations, one value, σ_n^2, is assumed to represent the single-cycle variances of mode *n*, and the DFDCs of mode *n* are assumed to be uncorrelated with respect to cycle for all non-fundamental modes. The means of single-cycle sample variances, $\left[s_n^{(m)}\right]^2$, over numerous cycles, i.e., values of *m*, are proposed as a mechanism for determining the representative variances σ_n^2. Section 3.1.1 presents and examines thusly determined representative variances for several test problems. Sections 3.3.2 and 3.3.3 provide empirical evidence that validates the variance estimation of the constant multiplier model for standard and extrapolated power methods, respectively. Agreement between the model and observations supports the use of the mean of single-cycle sample variances as the representative variance.

3.3.1 Calculating the Representative Variances

If the single-cycle deviations approach steady state probability distributions, which is assumed in Section 2.5, then the representative variance may be calculated from the mean of unbiased single-cycle variance estimates. A method for calculating the unbiased sample variance from independent and identically distributed temporary source bank decomposition coefficients (TSBDCs) is presented. The single-cycle variances are shown to converge while the fission source distribution converges, but the single-cycle variances require fewer cycles to sufficiently converge than their corresponding SBDCs. Analog capture is shown to yield smaller single-cycle variances than implicit capture, which is attributed to the additional variation associated with filling the intermediate bank in a non-analog fashion.

To obtain unbiased estimates for single-cycle variances in this section, each cycle consisted of numerous repetitions of three steps applied to a single set of source sites where the repetitions differed only by their random number streams. The first step was transporting the source bank to sample fission sites for populating a temporary intermediate bank. The second step was sampling a temporary source bank from the temporary intermediate bank. The third step was calculating the temporary source bank decomposition coefficients (TSBDCs). Only eigenvector decompositions were performed because the continuous eigenfunctions were unknown for some of the test problems. For a particular mode, each TSBDC is a sample; therefore, the unbiased sample variances of the TSBDCs from (3.2.2) is an estimate for the population variance of the SBDCs [13]. The temporary source bank from a single repetition was used as the source bank for the next cycle, such that the distribution of source sites would be identical in distribution with the source sites from a simulation that did not feature the use of repetitions. These identical repetitions are only used for estimating $\left[\sigma_n^{(m)}\right]^2$ and not for the purpose of reaching a stationary distribution.

To obtain a reasonable value for σ_n^2 that can predict the stationary variance of a SBDC, the single-cycle variances, $\left[\sigma_n^{(m)}\right]^2$, must be reasonably converged. The single-cycle variances are in general not constant with respect to cycle number *m*; this is most notable for simulations which begin with spatial distributions of source sites that are not similar in shape to the fundamental mode. As an example, when using a far from converged initial starting source containing large components of the first 33 modes for the uniform slab problem of Appendix A, the sampled single-cycle variances for the second and third modes of the source bank started low and converged to their stationary values as the source bank distribution approached its stationary state, which Figure 3.3.1.1 shows. The sample single-cycle variances and SBDCs in Figure 3.3.1.1 are the means from 400 independent implicit capture simulations with 1000 bank repetitions of 1.0E4 histories per cycle. The mean sample single-cycle variances of the second mode ranged between [2.68E-7, 4.99E-7], and the mean sample single-cycle variances of the third mode ranged

between [4.10E-7, 4.89E-7], which shows that a poor choice for σ_n^2 determined from empirical observations could yield a variance estimate that is up to 46% or 16% lower than the actual converged single-cycle variance for the second or third modes, respectively. For both modes, which Figure 3.3.1.1 presents, the sample single-cycle variance curves converged prior to the SBDC curves. This behavior was observed for other configurations tested; however, for brevity, this document does not include those results. The remaining examples of this section use starting sources sampled from their fundamental modes to avoid notable bias from convergence of the source estimates except where specified.

For the uniform slab problem in Appendix A, the reference single-cycle variances were calculated with the test code from sample means of single-cycle sample variances of the first 60 modes from multiple simulations of 400 stationary cycles with 1000 temporary bank repetitions of 1.0E4 histories in each temporary bank. The results from the test code were verified by comparing them with results using MCNP to transport neutrons and fill the intermediate banks. The results from MCNP and a hybrid version of the test code are from 400 stationary cycles with 100 temporary bank repetitions of 1.0E4 histories, each. The hybrid test code mimics MCNP with analog capture, which adds fission sites to the intermediate bank at each collision whether using analog or implicit capture [1]; therefore, when using analog capture with MCNP, the scheme is a hybrid between analog and implicit capture. The mean single-cycle SBDC variances from 400 analog capture simulations, 333 implicit capture simulations, 1000 hybrid simulations, 190 MCNP analog capture simulations, and 144 MCNP implicit capture simulations appear in Figure 3.3.1.2. The standard deviations of the mean single-cycle variances were all less than 0.1% of their respective mean single-cycle variance. The uncertainties are not plotted because they are too small to notice. From Figure 3.3.1.2, one can see that the results from the hybrid test code overlap with MCNP using analog capture, and the results from the test code with implicit capture match those from MCNP with implicit capture, which verifies the implementation of 1-D 1-group transport in the test code.

From Figure 3.3.1.2, one can also see that filling the intermediate bank in a non-analog fashion increases the single-cycle variances when compared with analog capture, which the hybrid and MCNP analog capture curves reflect. The author postulates that filling the intermediate bank in a non-analog fashion increases the single-cycle variances by allowing histories to score a greater variety of numbers of fissions and in a greater variety of locations. The variances of lower order modes are increased in greater proportion than higher-order modes. For higher order modes, a history does not have to move far between collisions to reach regions with eigenvector values that differ significantly from the previous collision; therefore, the differences between single-cycle variances under implicit and analog capture are expected to be less for higher order modes because the additional variation in fission location has a limited effect for higher order modes. The use of implicit capture transport reduces the single-cycle variances relative to the hybrid method, which can be seen when comparing the hybrid and implicit capture curves of the test code or the MCNP implicit and analog capture curves in Figure 3.3.1.2. The author speculates that implicit capture transport reduces the variation in the neutron tracks through the problem, which offsets some of the increased variance from non-analog filling of the intermediate bank. The increase in single-cycle variances when using implicit capture compared with analog capture was also observed for the double peak slab problem described in Appendix D as one can see in Figure 3.3.1.3. The representative variances in Figure 3.3.1.3 were generated from 1000 simulations of 1000 cycles with 100 temporary bank repetitions of 1.0E5 histories in each temporary bank.

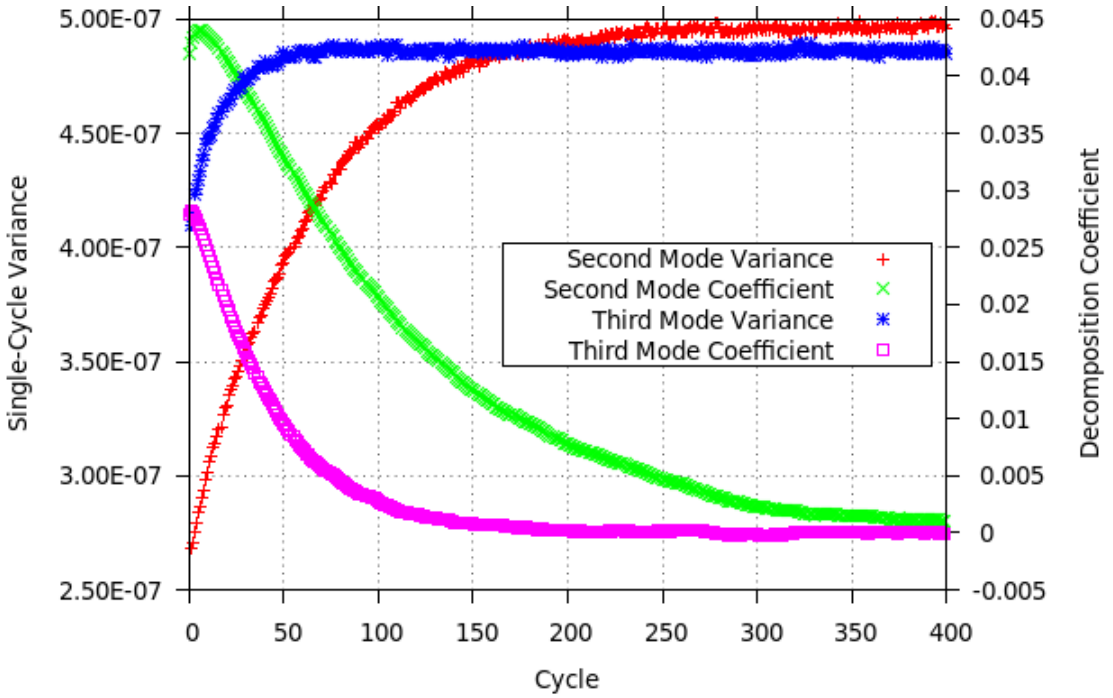

Figure 3.3.1.1 Uniform slab second and third mode expected SBDCs and their DFDC (single-cycle) variances versus cycle.

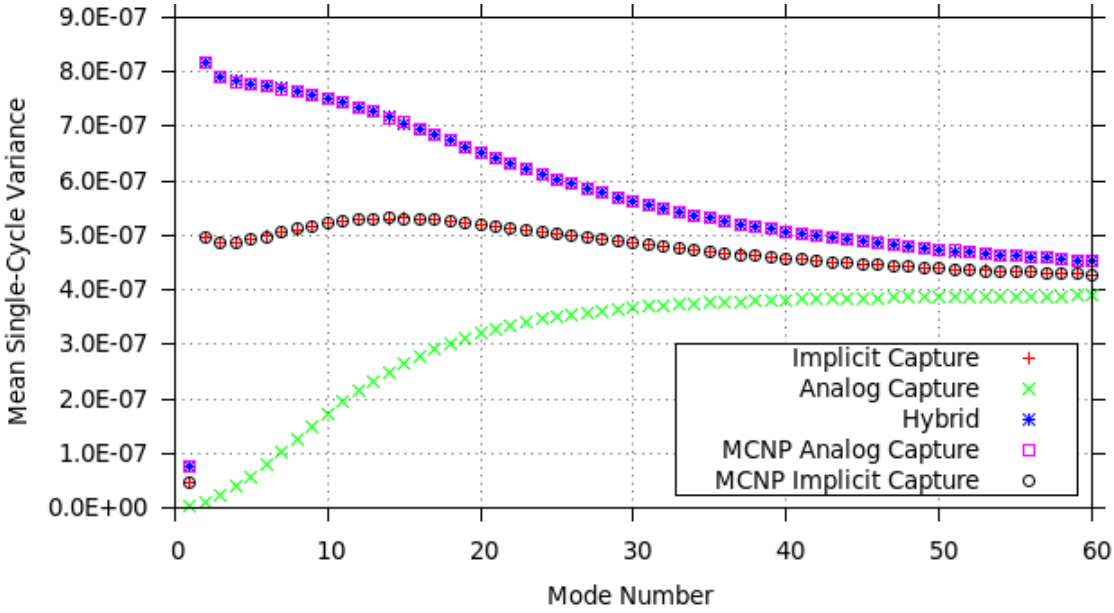

Figure 3.3.1.2 Representative single-cycle variances of uniform slab problem in Appendix A for 1.0E4 histories per cycle.

For the simplified 2-D reactor problem of Appendix B, the reference single-cycle variances were calculated for the first 50 modes from sample means of single-cycle variances from multiple simulations of 500 stationary cycles with 100 temporary bank repetitions of 1.0E5 histories, each. The representative variances from 118 MCNP analog capture simulations and 84 MCNP implicit capture simulations appear in Figure 3.3.1.4. The standard deviations of the mean single-cycle variances were all less than 0.1% of their respective mean single-cycle variance. The uncertainties are not plotted because they are too small to notice. From Figure 3.3.1.4, one can see that the use of implicit capture transport reduces the single-cycle variances and their spread when compared with the MCNP analog capture hybrid method. This matches the behavior observed for the uniform slab problem of Appendix A.

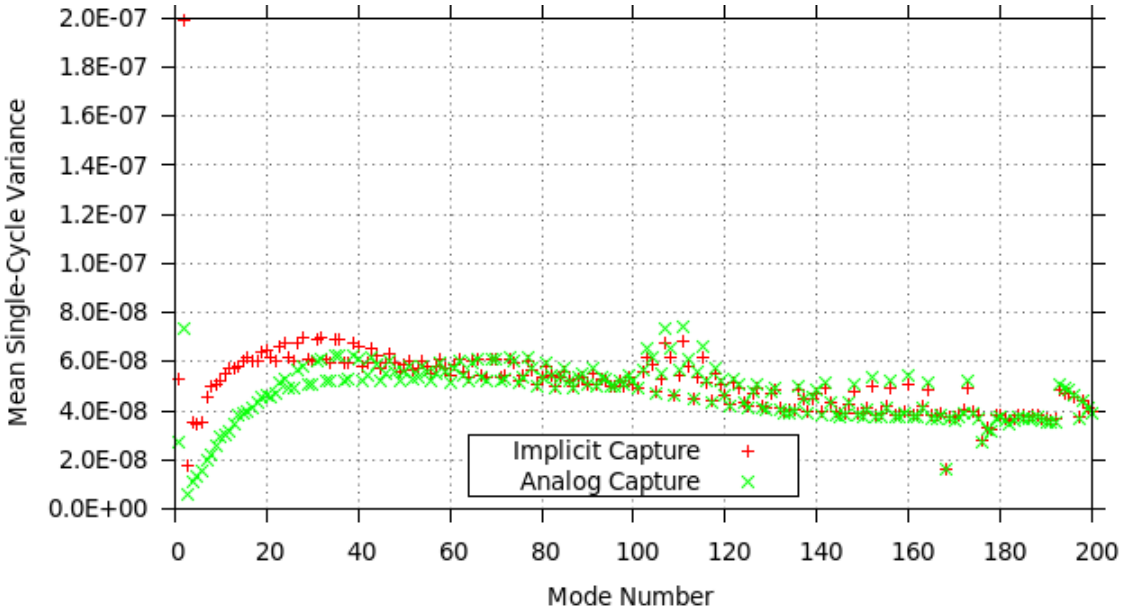

Figure 3.3.1.3 Representative single-cycle variances of double peak slab problem in Appendix D for 1.0E5 histories per cycle.

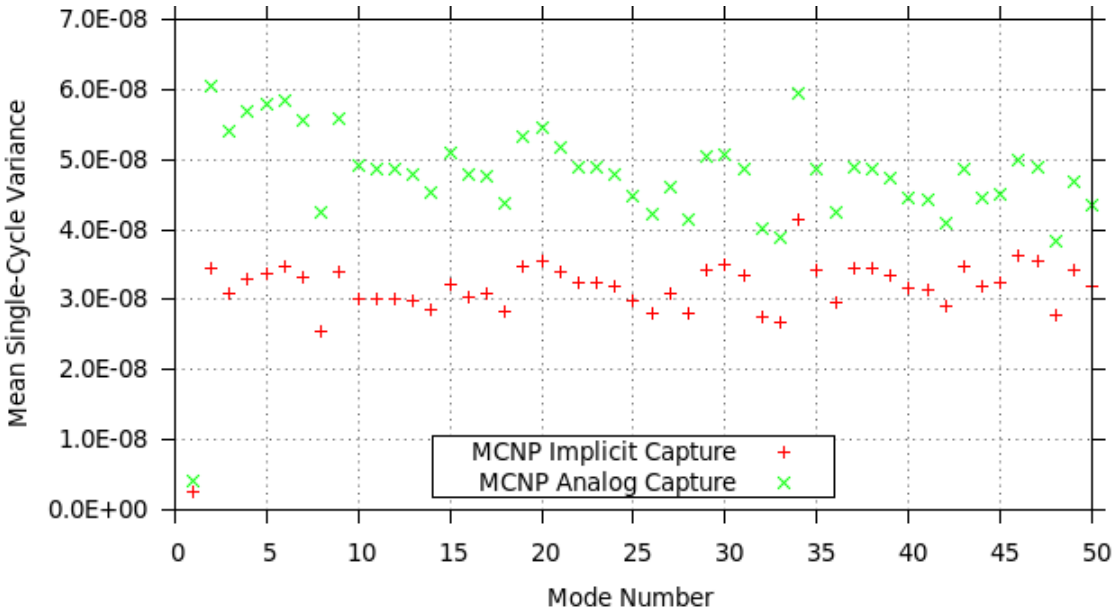

Figure 3.3.1.4 Representative single-cycle variances of simplified 2-D reactor problem in Appendix B for 1.0E5 histories per cycle.

In the subsections to follow, the observed sample variances of SBDCs are compared with variances from the constant multiplier model using the aforementioned reference values of σ_n^2 for the uniform slab problem of Appendix A and the simplified 2-D reactor problem of Appendix B using the standard power method in Section 3.3.2 and the extrapolated power method in Section 3.3.3.

3.3.2 Standard Power Method Converged Variances

Using the representative variances from the appropriate reference calculations in Section 3.3.1 as σ_n^2, the expected SBDC variances for the standard power method were calculated using (2.5.18),

$$Var\left[\widetilde{u}_n^{(m)}\right]=\sigma_n^2\frac{1-\left(\lambda_n/\lambda_1\right)^{2m}}{1-\left(\lambda_n/\lambda_1\right)^2}\quad \forall\, n>1\,. \tag{3.3.2.1}$$

As demonstrated in Section 3.2, the SBDCs may be approximated as normally distributed random variables. For a normally distributed random variable *X* with standard deviation σ, the expected variance of the unbiased sample variance from *N* samples is [45]

$$E\left[Var\left[s^2[X]\right]\right]=\frac{2\sigma^4}{N-1}, \tag{3.3.2.2}$$

and the distribution of the sample variance is proportional to the chi-square distribution with $N-1$ degrees of freedom, $\chi^2(N-1)$ [13]. The scaled standard deviation of the sample variance of a normally distributed random variable, τ, shall be defined as

$$\tau=\frac{\sqrt{E\left[Var\left[s^2[X]\right]\right]}}{Var[X]}=\sqrt{\frac{2}{N-1}}. \tag{3.3.2.3}$$

The percent difference, *PD*, between sample variances of SBDCs and the model for mode *n* at cycle *m* shall be defined as

$$PD_n^{(m)}=\left\{\frac{\left[s_n^{(m)}\right]^2}{Var\left[\widetilde{u}_n^{(m)}\right]}-1.0\right\}\times 100\,\%. \tag{3.3.2.4}$$

The expected variance of the percent difference is

$$E\left\{Var\left[PD_n^{(m)}\right]\right\}=100^2\frac{E\left\{Var\left[\left(s_n^{(m)}\right)^2\right]\right\}}{\left\{Var\left[\widetilde{u}_n^{(m)}\right]\right\}^2}=100^2\,\tau^{2,} \tag{3.3.2.5}$$

and the standard deviation is

$$\sigma\left[PD_n^{(m)}\right]=\sqrt{E\left\{Var\left[PD_n^{(m)}\right]\right\}}=100\,\tau. \tag{3.3.2.6}$$

For sample sizes greater than 50, the chi-square distribution may be approximated by the normal distribution. Therefore, if the percent differences between the sample variances of SBDCs and the model are attributable only to random fluctuations, then one may expect that the majority, approximately 99.7%, of observed percent differences in SBDC variances will lie within 3 standard deviations of the mean percent difference, which should be zero if the model is accurate.

For the uniform slab problem of Appendix A, Figures 3.3.2.1-3.3.2.3 contain the predictions from the constant multiplier approximation along with empirical sample variances of SBDCs obtained from 1E4 independent implicit capture simulations of the test code without any temporary repetitions for the second, third, and fourth modes, respectively. For the sample size of 1E4, 3 standard deviations from (3.3.2.6) equal 4.24%. All of the calculated percent differences in Figures 3.3.2.1-3.3.2.3 are within 3 standard deviations, and they do not appear biased in a positive or negative direction. Similar results were obtained from 9254 analog capture simulations of the test code, which Figures 3.3.2.4-3.3.2.6 contain for the second, third, and fourth modes, respectively. SBDC variances of modes 2 and 4 did not differ from the model by more than 3 standard deviations; however, mode 3 did show 1 cycle that differed from the model by more than 3 standard deviations, which is within expectations from 500 observations. These observations support the assumptions of the constant-multiplier model and support the use of the mean single-cycle variance as a reasonable value for the representative variance σ_n^2.

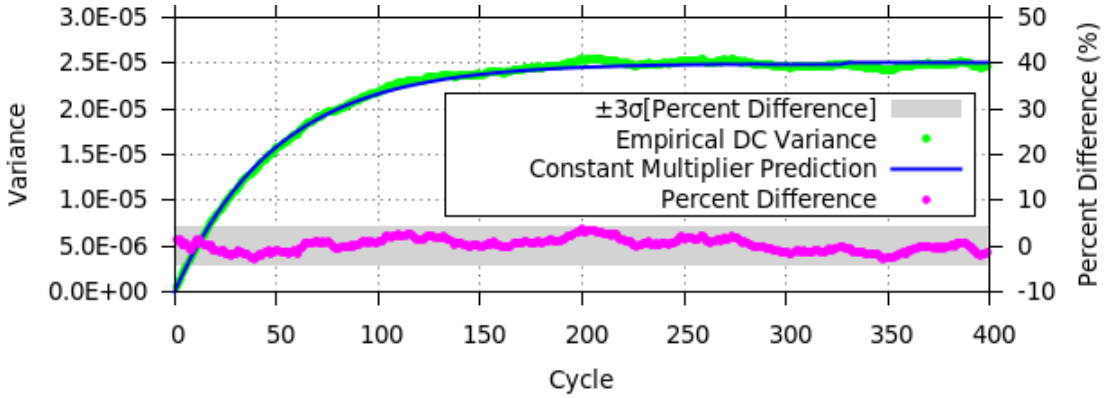

Figure 3.3.2.1 SBDC variances for the second mode of the uniform slab problem versus cycle for empirical observations and those predicted by the constant multiplier approximation using implicit capture.

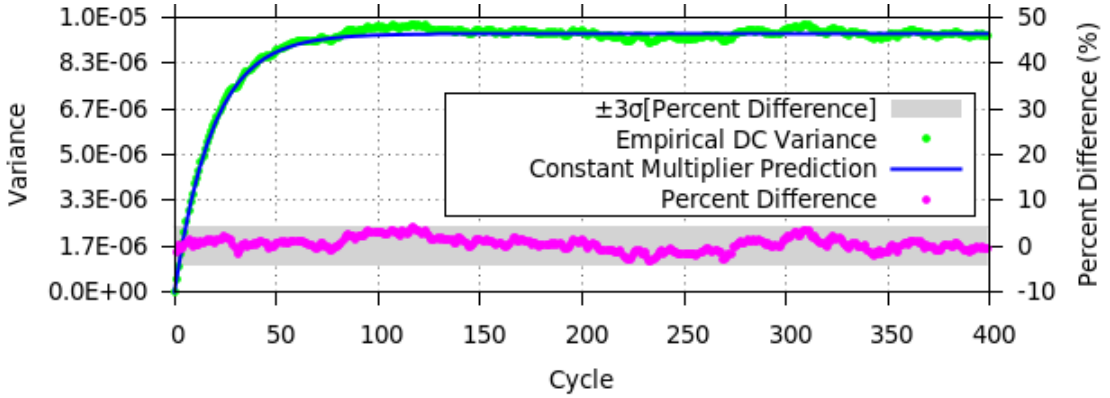

Figure 3.3.2.2 SBDC variances for the third mode of the uniform slab problem versus cycle for empirical observations and those predicted by the constant multiplier approximation using implicit capture.

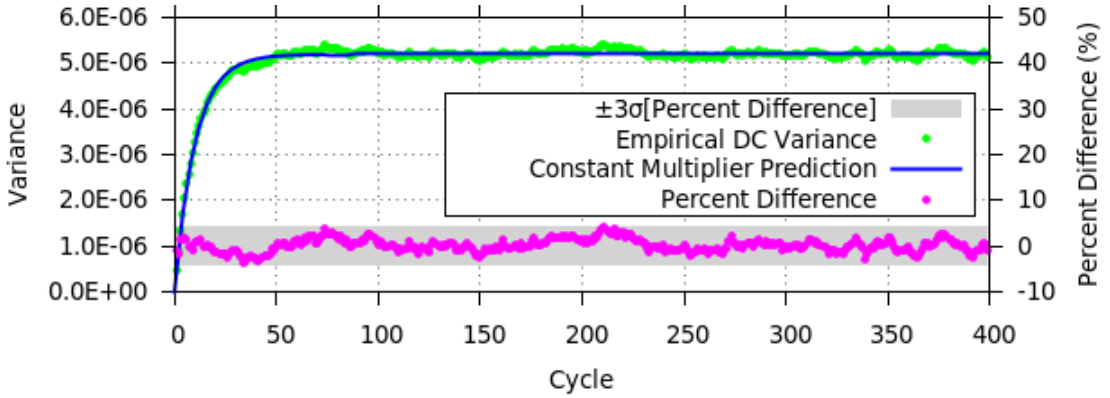

Figure 3.3.2.3 SBDC variances for the fourth mode of the uniform slab problem versus cycle for empirical observations and those predicted by the constant multiplier approximation using implicit capture.

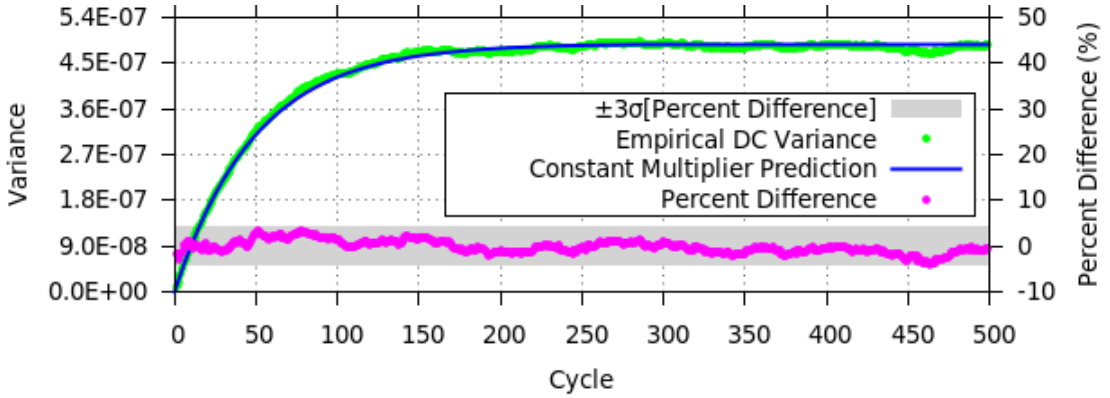

Figure 3.3.2.4 SBDC variances for the second mode of the uniform slab problem versus cycle for empirical observations and those predicted by the constant multiplier approximation using analog capture.

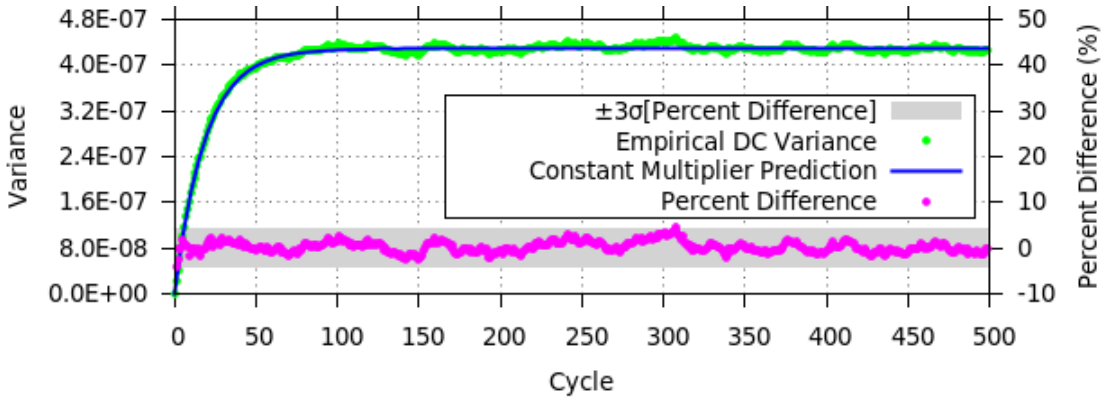

Figure 3.3.2.5 SBDC variances for the third mode of the uniform slab problem versus cycle for empirical observations and those predicted by the constant multiplier approximation using analog capture.

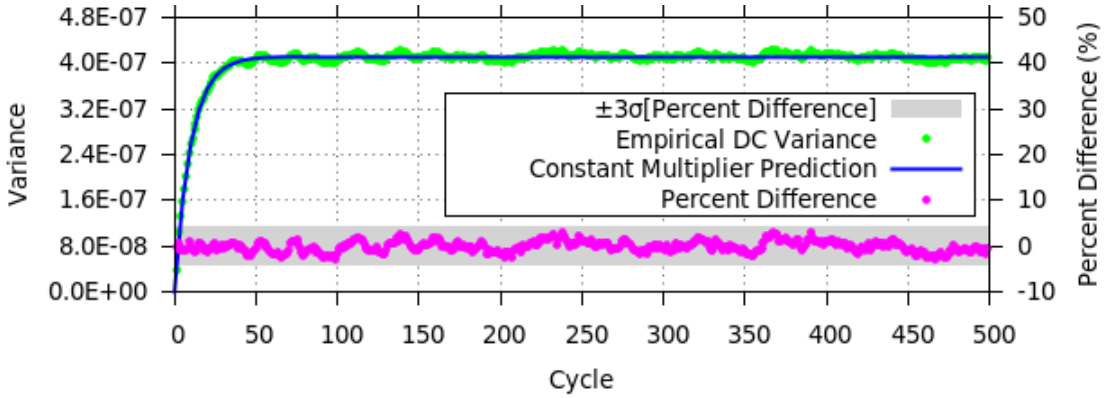

Figure 3.3.2.6 SBDC variances for the fourth mode of the uniform slab problem versus cycle for empirical observations and those predicted by the constant multiplier approximation using analog capture.

Observations for the simplified 2-D reactor of Appendix B using MCNP showed fair agreement between the model and observations; however, the differences are statistically significant and show under-prediction of the SBDC variances. Figures 3.3.2.7-3.3.2.9 display predictions with aggregated observations from 6254 independent simulations of 1E5 histories using the standard power method with MCNP implicit capture. As one can see in Figures 3.3.2.7-3.3.2.9, the model matched the observations within 10% for all cycles, which is likely sufficiently accurate to use for convergence detection purposes. However, the percent differences of many cycles were statistically significant because they exceeded the $3\sigma[PD]$ level of 5.36%, and those differences were clearly biased in the positive direction. Figures 3.3.2.10-3.3.2.12 display predictions with aggregated observations from 9724 independent simulations of 1E5 histories using the standard power method with MCNP analog capture. As one can see in Figures 3.3.2.10-3.3.2.12, the model also matched these observations within 10% for nearly all cycles. However, the percent differences of many cycles were statistically significant because they exceeded the $3\sigma[PD]$ level of 4.30%, and those differences were biased in the positive direction.

Possible sources for the difference are incorrect eigenvalue ratios from the fission matrix solution, correlations between cycle noise, and the assumption that the single-cycle variance is constant. For example, Figure 3.3.2.11 from MCNP analog capture, which showed the greatest percent difference, becomes Figure 3.3.2.13 if the eigenvalue ratio of the third mode is actually 3.6E-4 or 36 pcm larger than the reference eigenvalue ratio. For the increased eigenvalue ratio, the percent differences would not exceed $3\sigma[PD]$. Such a modification of the eigenvalue ratio would shift the MCNP implicit capture results from Figure 3.3.2.8 to Figure 3.3.2.14 where the percent differences also would not exceed $3\sigma[PD]$. A difference of 36 pcm between the actual eigenvalue ratio and the fission matrix estimated value is possible but unlikely given the trend in the eigenvalue ratios with grid refinement shown in Appendix B. The presence of some small correlations for lags up to approximately 10 can be seen in Figure 3.3.2.15 for the analog capture case. The trend is more visible when viewing the mean of correlation coefficients

from multiple modes as in Figure 3.3.2.16. From Figures 3.3.2.15 and 3.3.2.16, one can clearly see that the lag 1 correlation tends to be low and often negative, and the correlation coefficients for the next approximately 9 lags are positive and are larger in magnitude when compared with greater lags. Positive correlations cause the model to under-predict variances because they were ignored in the interest of simplification. The sources of error were not investigated further for this problem because the model was considered to be sufficiently accurate.

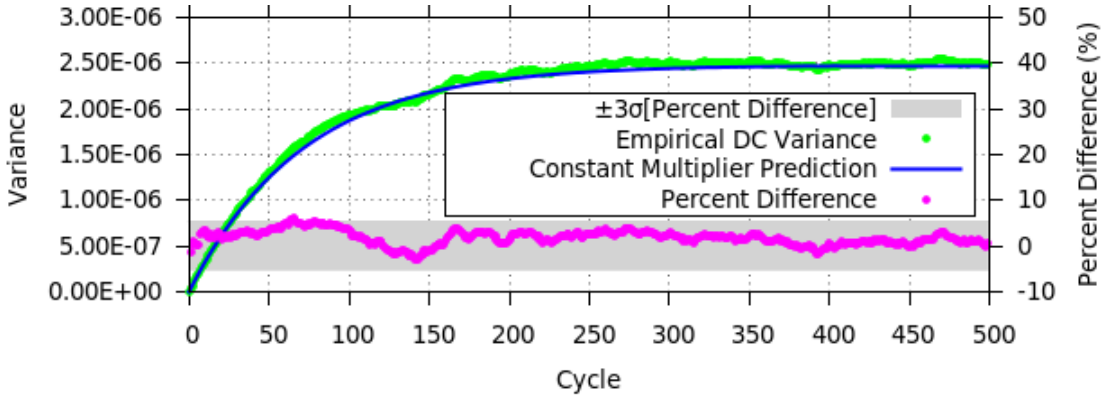

Figure 3.3.2.7 SBDC variances for the second mode of the simplified 2-D reactor problem versus cycle for standard power method MCNP implicit capture observations and those predicted by the constant multiplier approximation.

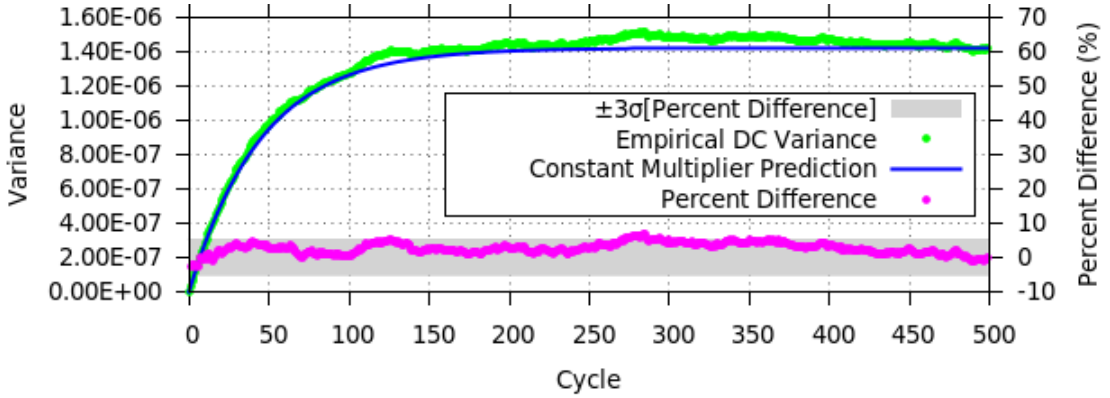

Figure 3.3.2.8 SBDC variances for the third mode of the simplified 2-D reactor problem versus cycle for standard power method MCNP implicit capture observations and those predicted by the constant multiplier approximation.

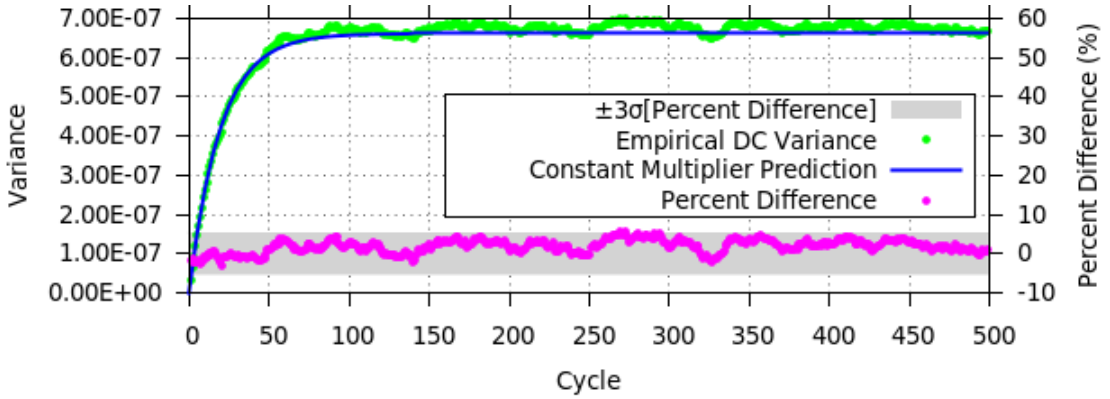

Figure 3.3.2.9 SBDC variances for the fourth mode of the simplified 2-D reactor problem versus cycle for standard power method MCNP implicit capture observations and those predicted by the constant multiplier approximation.

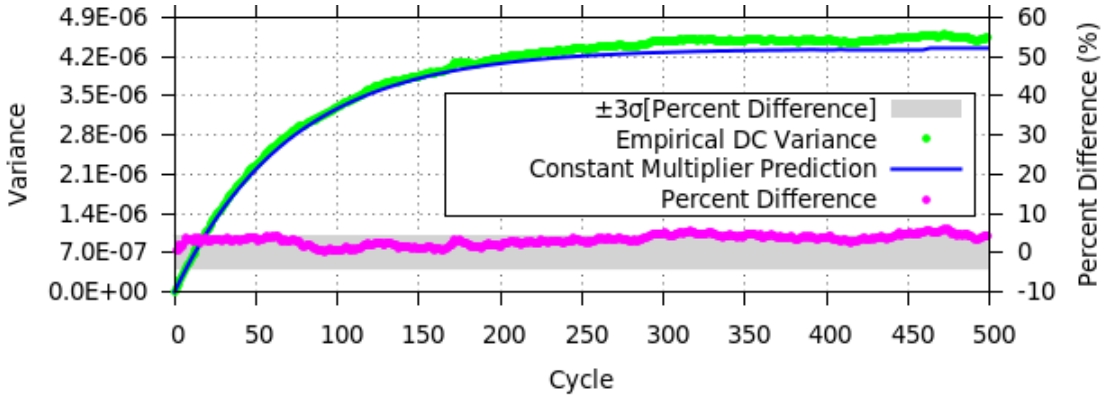

Figure 3.3.2.10 SBDC variances for the second mode of the simplified 2-D reactor problem versus cycle for standard power method MCNP analog capture observations and those predicted by the constant multiplier approximation.

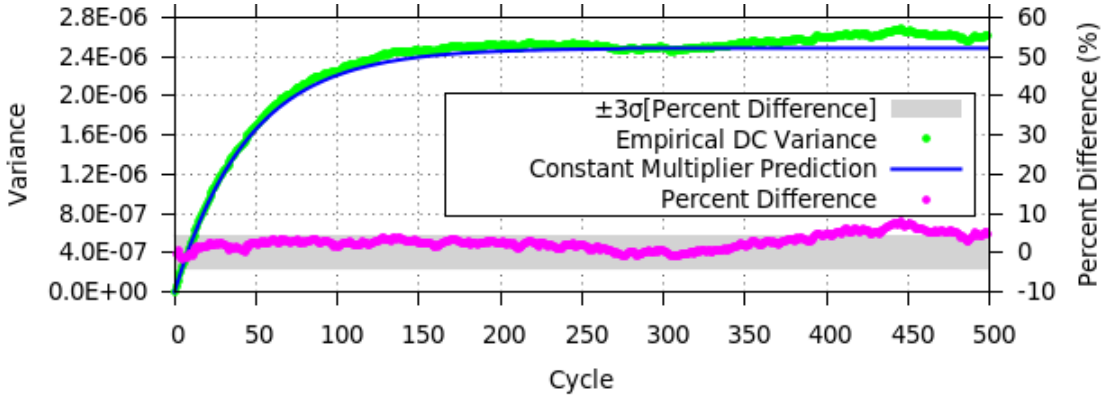

Figure 3.3.2.11 SBDC variances for the third mode of the simplified 2-D reactor problem versus cycle for standard power method MCNP analog capture observations and those predicted by the constant multiplier approximation.

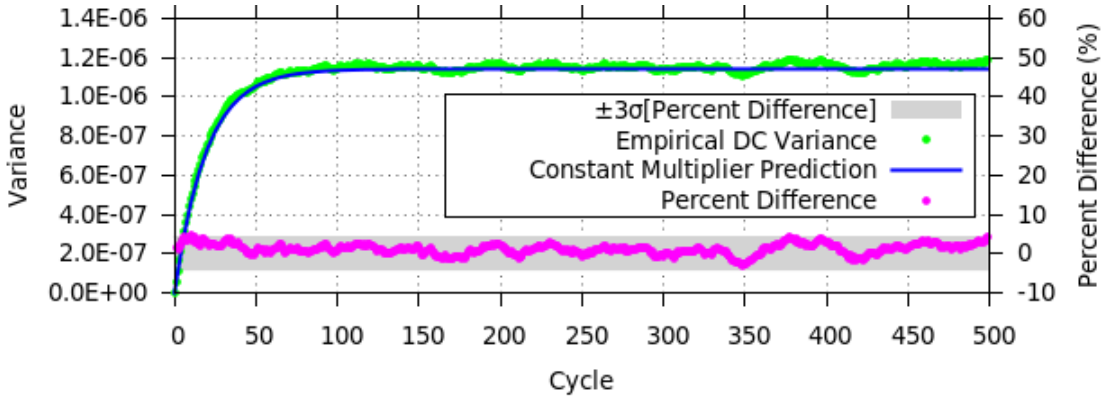

Figure 3.3.2.12 SBDC variances for the fourth mode of the simplified 2-D reactor problem versus cycle for standard power method MCNP analog capture observations and those predicted by the constant multiplier approximation.

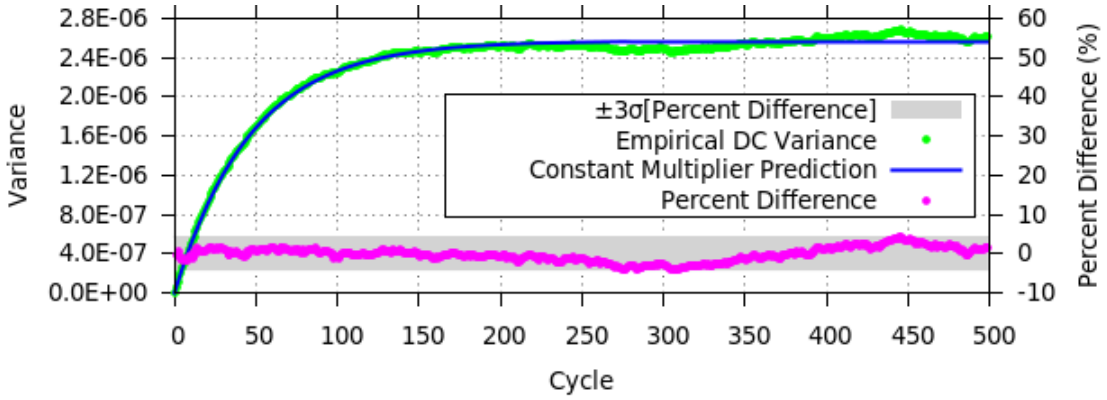

Figure 3.3.2.13 SBDC variances for the third mode of the simplified 2-D reactor problem versus cycle for standard power method MCNP analog capture observations and those predicted by the constant multiplier approximation with an adjusted eigenvalue ratio of 0.9893925.

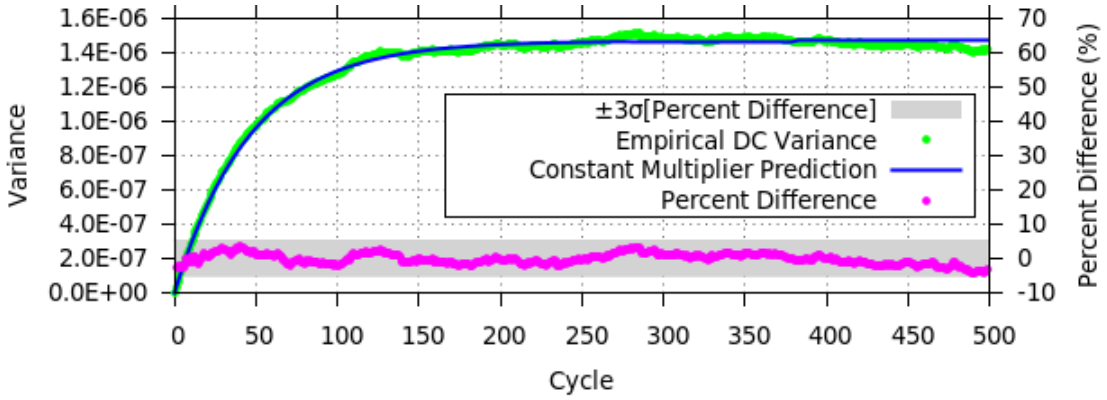

Figure 3.3.2.14 SBDC variances for the third mode of the simplified 2-D reactor problem versus cycle for standard power method MCNP implicit capture observations and those predicted by the constant multiplier approximation with an adjusted eigenvalue ratio of 0.9893925.

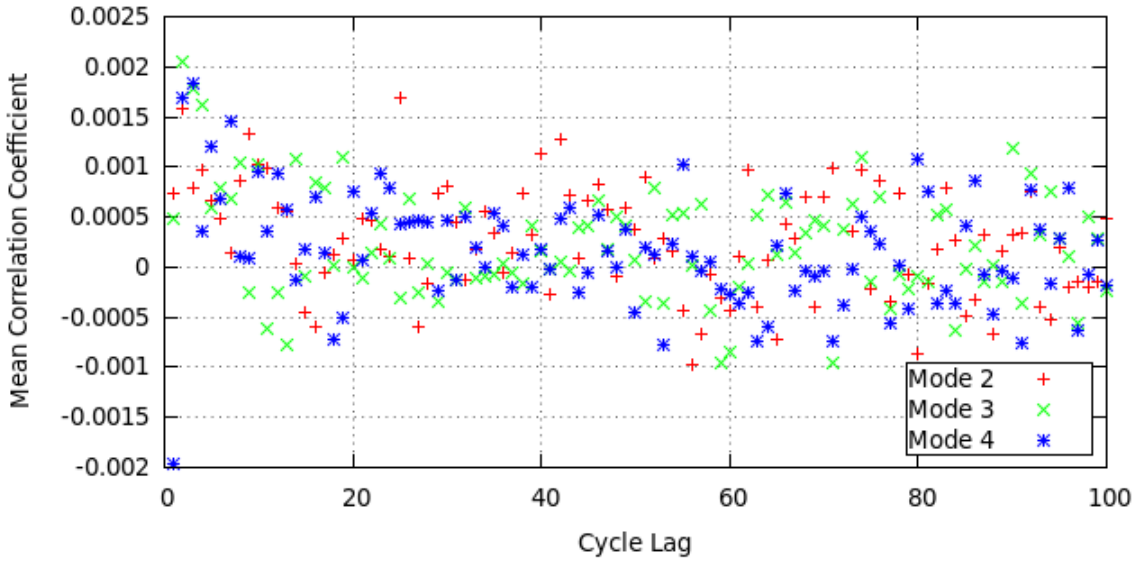

Figure 3.3.2.15 Ratio of mean covariance to mean single-cycle variance for several modes of the simplified 2D-reactor problem of Appendix B using analog MCNP.

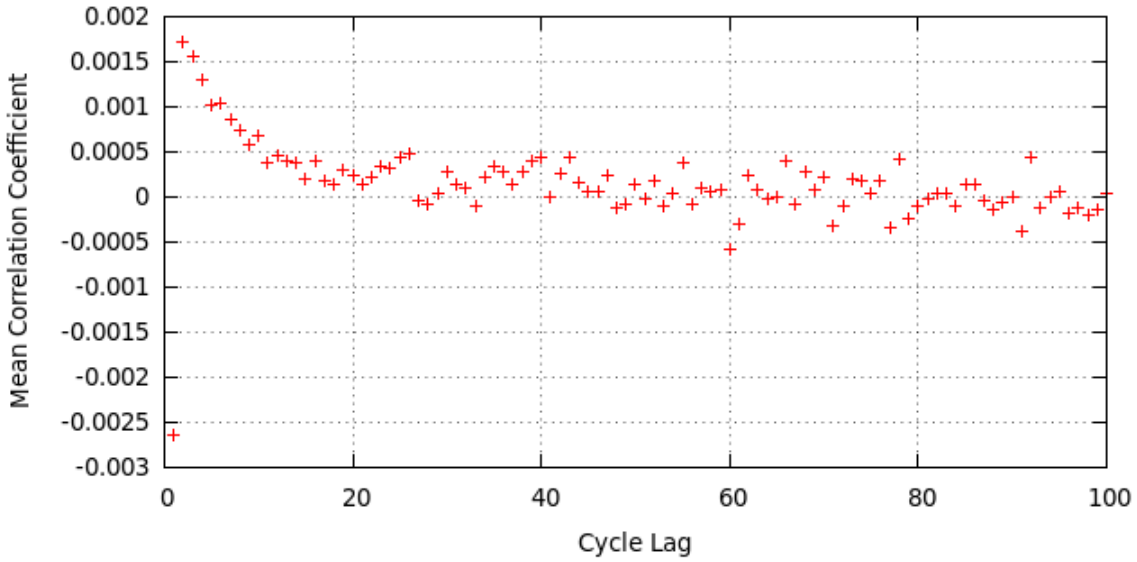

Figure 3.3.2.16 For modes 2 through 9, mean of ratios of mean covariance to mean single-cycle variance using analog MCNP for the simplified 2D-reactor problem of Appendix B.

3.3.3 Extrapolated Power Method Converged Variances

This section demonstrates that the constant multiplier model is reasonably accurate at predicting a reasonable maximum for the variance of SBDCs when using the extrapolated power method. The SBDC variances approach that maximum as the grid is refined with an appropriate increase in the number of histories. The SBDC variance estimates tended to be more accurate for the lower order modes than the higher order modes. Using the representative variances from the appropriate reference calculations in Section 3.3.1 as σ_n^2, the expected SBDC variances for the extrapolated power method were calculated using the constant multiplier model in (2.5.22),

$$Var\left[\tilde{v}_n^{(m)}\right] = \frac{1-\left[(1+\alpha)\lambda_n/\lambda_1-\alpha\right]^{2m}}{1-\left(\frac{\lambda_n}{\lambda_1}\right)^2-\frac{2\alpha}{1+\alpha}\left(1-\frac{\lambda_n}{\lambda_1}\right)}\sigma_n^2. \quad \forall n>1. \tag{3.3.3.1}$$

For the uniform slab problem in Appendix A, Figures 3.3.3.1, 3.3.3.2, and 3.3.3.3 contain the predictions from the constant multiplier approximation along with empirical SBDC variances for the second, third, and fourth modes, respectively. The empirical results were obtained from 1E4 independent implicit capture simulations of the test code using extrapolation with $\alpha=0.98$ on a uniform 16 bin mesh with 1E4 histories per per cycle. For the sample size of 1E4, 3 standard deviations from (3.3.2.6) equal 4.24%. All of the calculated percent differences in Figures 3.3.3.1-3.3.3.3 are within 10% of the model; however, they are biased in a negative direction and exceed the expected range, which indicates that the model overestimates the SBDC variances. For 6108 analog capture simulations of the test code, which Figures 3.3.3.4, 3.3.3.5, and 3.3.3.6 display for the second, third, and fourth modes, respectively, the bias was less noticeable. The second and third modes showed no bias for the analog simulations, but for the fourth mode and higher modes, which are not presented, the bias increased with increasing mode number similar to that reported in Figure 2.5.7. The results in Figure 2.5.7 were from an empirical fit of the stationary SBDC variances from the standard power method whereas the results of th model presented in this section use an empirically determined single-

cycle variance.

The biases in the variance estimates were reduced for the lower order modes by increasing the number of extrapolation mesh bins and the number of histories. For implicit capture, Figure 3.3.3.7 contains the ratios of the mean SBDC variances over implicit capture cycles 200-500 to those predicted by the constant-multiplier model in the limit of infinite cycles for the first 59 non-fundamental modes and for histories per cycle ranging from 1E4 to 1E6. The 3σ uncertainties for the ratios are all less than $\pm 1\%$. The results from 1E4 histories with 16 bins show the effect of aliasing on the coarse mesh as Section 2.5 discusses. In particular, the anomalies in modes 16 and 48, which correspond to multiples of the number of mesh bins, demonstrate the presence of aliasing. For the results from 1E4 histories per cycle with 256 bins, the extrapolation procedure breaks down and converges to erroneous non-zero expected SBDCs for non-fundamental modes, which explains the odd behavior of the variance ratios. For the 1E5 and 1E6 histories per cycle data using implicit capture, all of the displayed SBDC variances fall within 4% of that predicted by the model. Additionally, the empirical mean SBDC variances for the analog capture data from the test code was within 4% of the model for the 1E5 and 1E6 histories per cycle cases, which Figure 3.3.3.8 shows. The extrapolated algorithm with 1E4 histories per cycle and 256 extrapolation bins did not converge properly using analog capture, either, which explains the exceptionally high variance of the low order modes for that case in Figure 3.3.3.8. The effects of aliasing, which is discussed in Section 2.5, are observable in the analog capture results from 1E4 histories with 16 bins. The most notable example is the jump in accuracy of the model for mode 16 in Figure 3.3.3.8. The accuracy of the variance estimate for mode 48 is slightly improved relative to its neighboring modes but to a lesser extent than was observed with implicit capture.

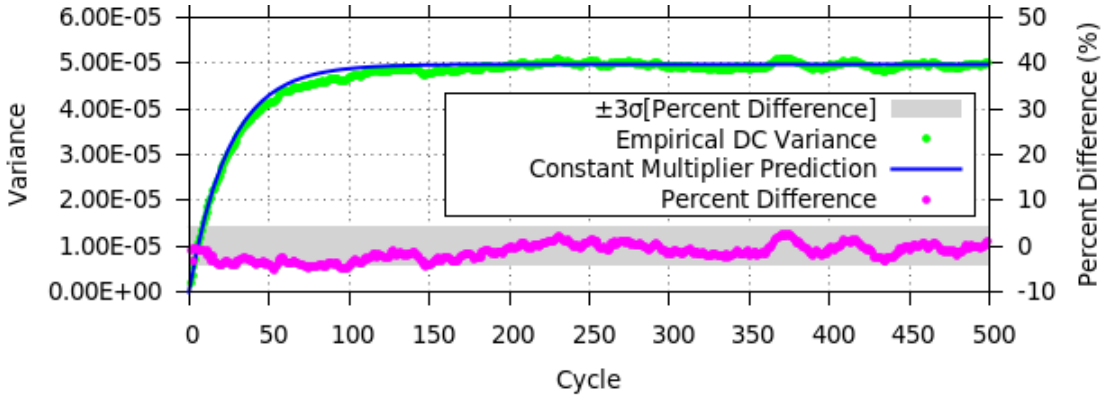

Figure 3.3.3.1 SBDC variances for the second mode of the uniform slab problem versus cycle from observations with the extrapolated power method using implicit capture and from predictions by the constant multiplier approximation.

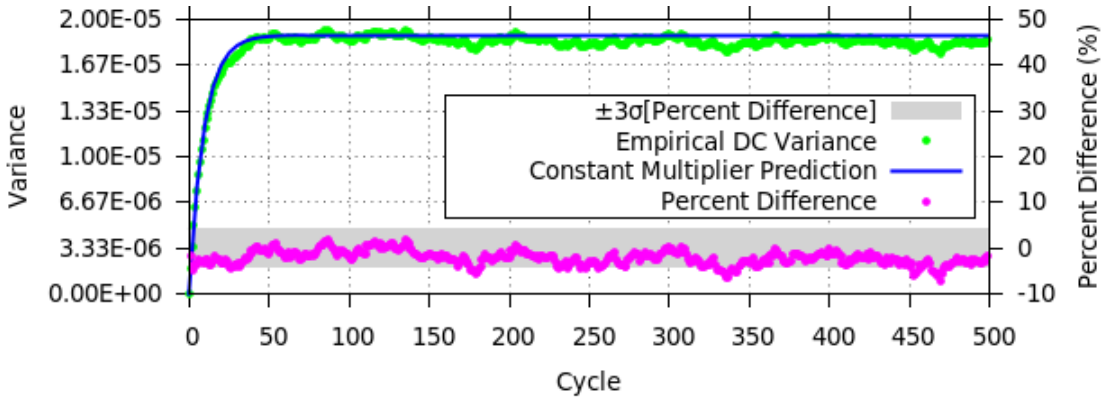

Figure 3.3.3.2 SBDC variances for the third mode of the uniform slab problem versus cycle from observations with the extrapolated power method using implicit capture and from predictions by the constant multiplier approximation.

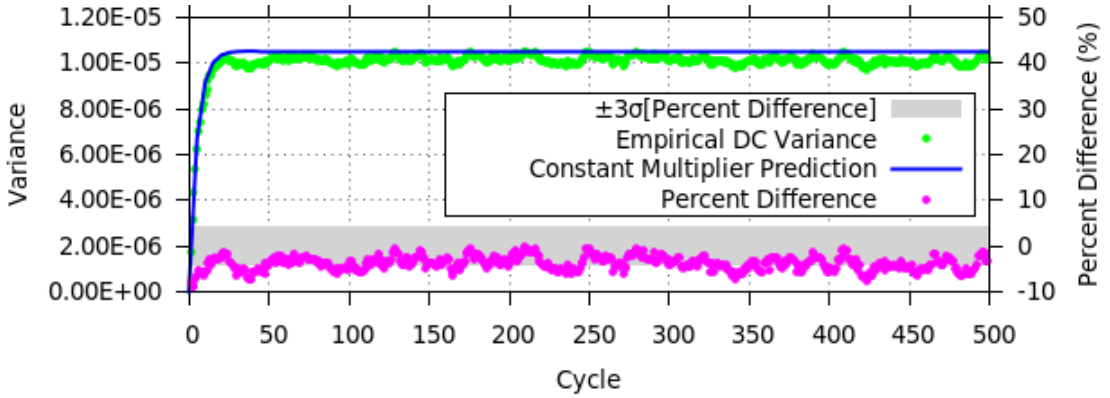

Figure 3.3.3.3 SBDC variances for the fourth mode of the uniform slab problem versus cycle from observations with the extrapolated power method using implicit capture and from predictions by the constant multiplier approximation.

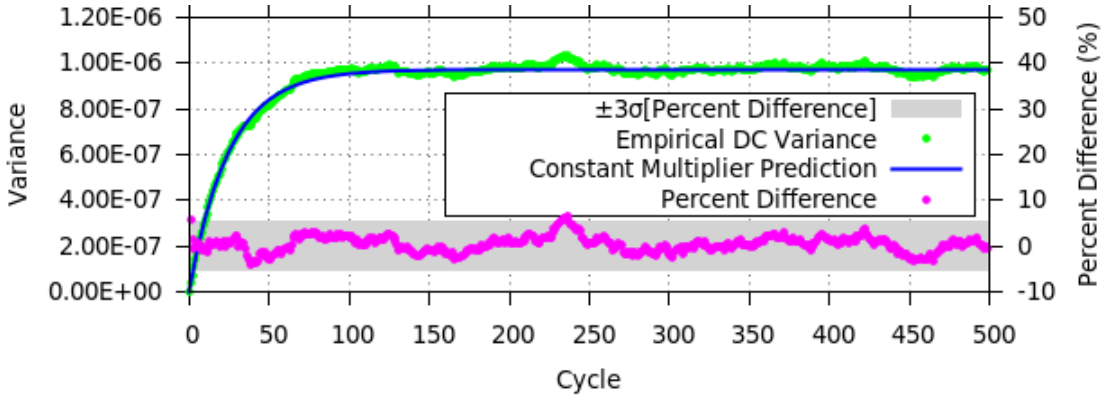

Figure 3.3.3.4 SBDC variances for the second mode of the uniform slab problem versus cycle from observations with the extrapolated power method using analog capture and from predictions by the constant multiplier approximation.

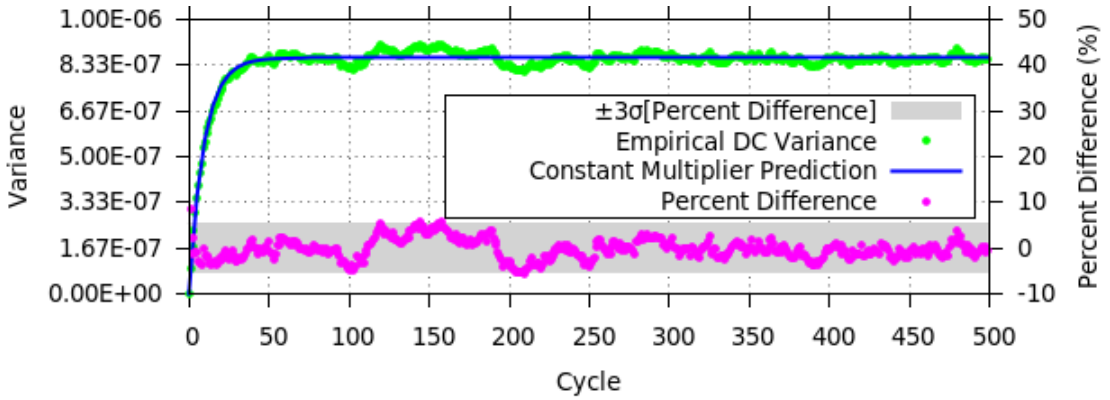

Figure 3.3.3.5 SBDC variances for the third mode of the uniform slab problem versus cycle from observations with the extrapolated power method using analog capture and from predictions by the constant multiplier approximation.

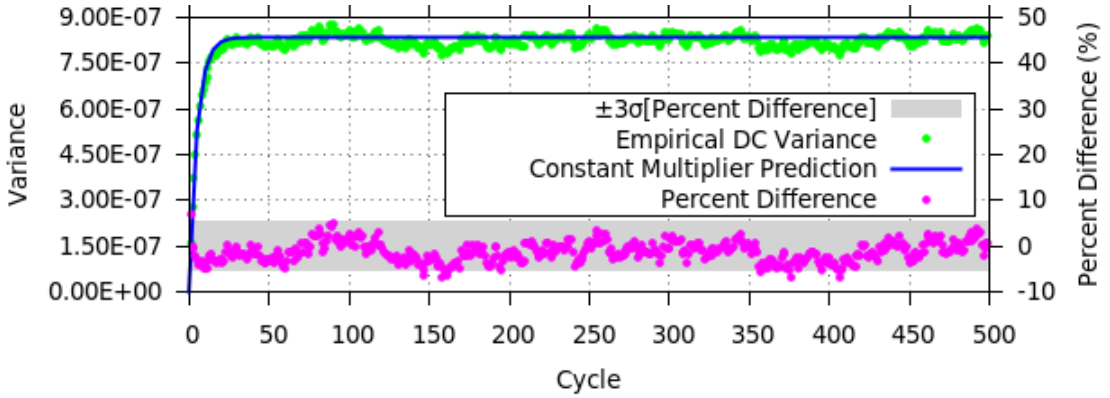

Figure 3.3.3.6 SBDC variances for the fourth mode of the uniform slab problem versus cycle from observations with the extrapolated power method using analog capture and from predictions by the constant multiplier approximation.

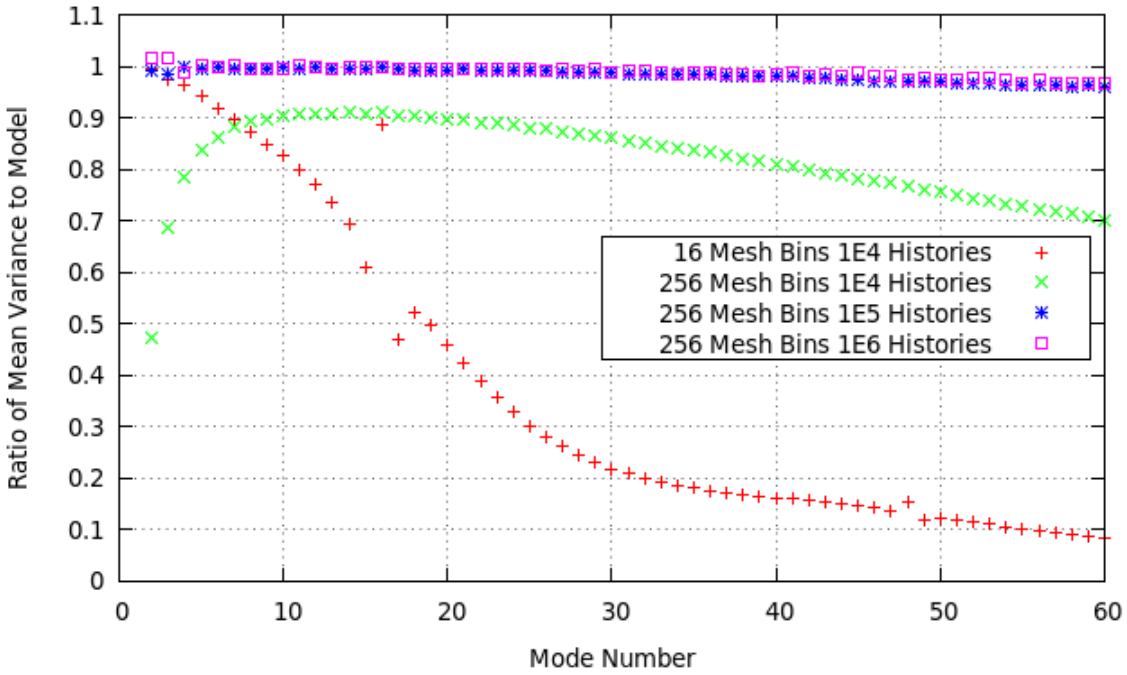

Figure 3.3.3.7 Ratio of empirical mean stationary SBDC variances to those expected from the constant multiplier model for the uniform slab problem in Appendix A using the test code with implicit capture.

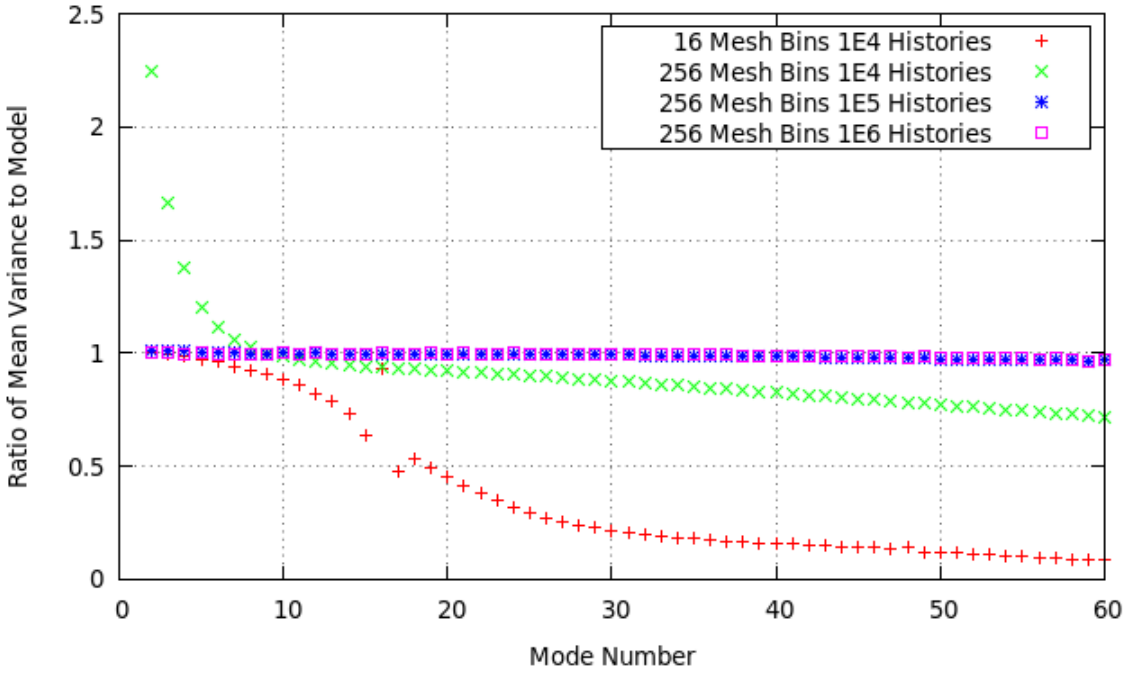

Figure 3.3.3.8 Ratio of empirical mean stationary SBDC variances to those expected from the constant multiplier model for the uniform slab problem in Appendix A using the test code with analog capture.

For the simplified 2D-reactor problem in Appendix B, results with extrapolation show a similar accuracy as those from the standard power method. For implicit capture, Figures 3.3.3.9, 3.3.3.10, and 3.3.3.11 contain the predictions from the constant multiplier model along with empirical SBDC variances for the second, third, and fourth modes, respectively. The empirical results in Figures 3.3.3.9-3.3.3.11 were obtained from 6445 independent implicit capture simulations of MCNP using extrapolation with $\alpha = 0.983$ on a uniform 21x21 bin mesh with 1E5 histories per cycle. For MCNP analog capture, Figures contain the predictions from the constant multiplier model along with empirical SBDC variances for the second, third, and fourth modes, respectively. The empirical results in Figures were obtained from 10010 independent implicit capture simulations of MCNP using extrapolation with $\alpha = 0.983$ on a uniform 21x21 bin mesh with 1E5 histories per cycle. The representative variances input to the model are from Figure 3.3.1.4. The constant multiplier model estimates for the SBDC variances are within 10% for all cycles and modes examined for both MCNP implicit capture and MCNP analog capture. The model underestimates the variances for the low order modes presented, which is attributable to the inter-cycle correlations that the model ignores. However, the model overestimates the SBDC variances for the majority of the modes as one can see in Figure 3.3.3.15, which contains the ratios of the mean SBDC variances over cycles 200-500 to those predicted by the constant-multiplier model in the limit of infinitely many cycles. Increasing the number of mesh bins with an increase in the number of histories per cycle eliminates the underestimation from observations as Figure 3.3.3.15 shows for an 84x84 bin mesh with 1E6 histories per cycle. Without an increase in the number of histories, the extrapolation leads to erroneous fission distribution estimates, which can be seen in Figure 3.3.3.15 for the 84x84 bin mesh case with 1E5 histories per cycle.

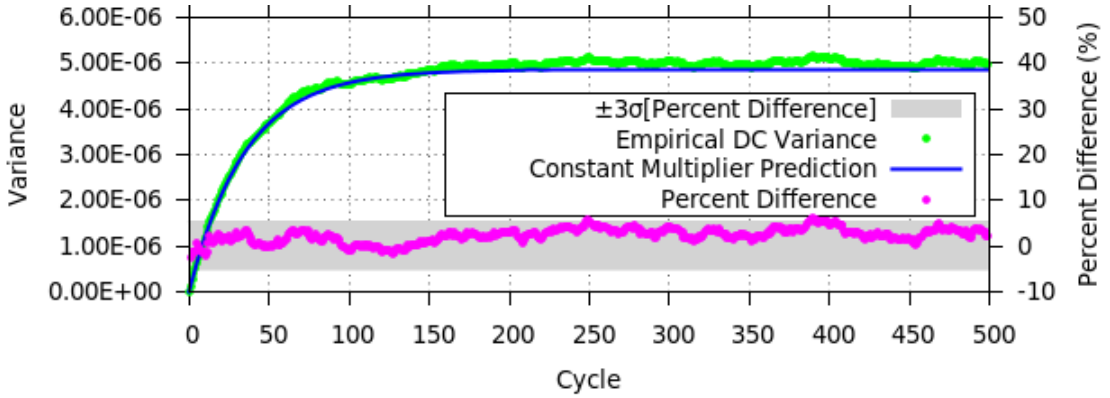

Figure 3.3.3.9 SBDC variances for the second mode of the simplified 2-D reactor in Appendix B versus cycle from observations with the extrapolated power method using MCNP implicit capture and from predictions by the constant multiplier model.

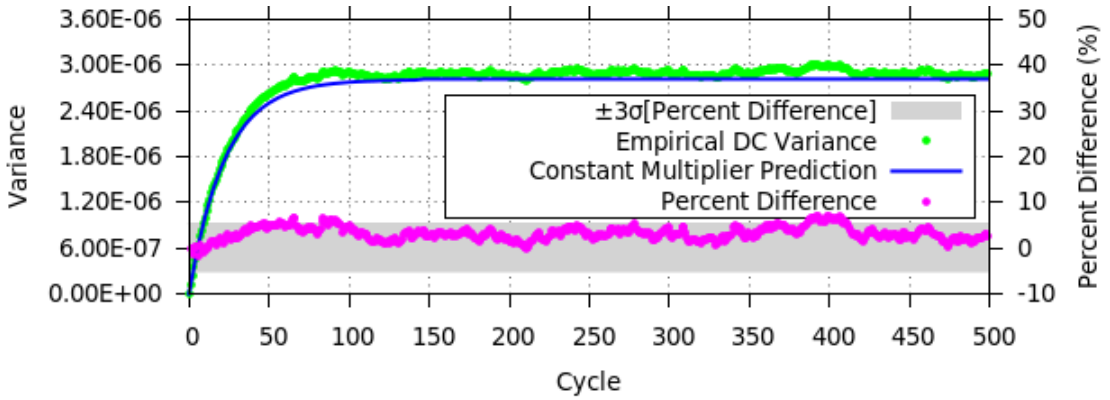

Figure 3.3.3.10 SBDC variances for the third mode of the simplified 2-D reactor in Appendix B versus cycle from observations with the extrapolated power method using MCNP implicit capture and from predictions by the constant multiplier model.

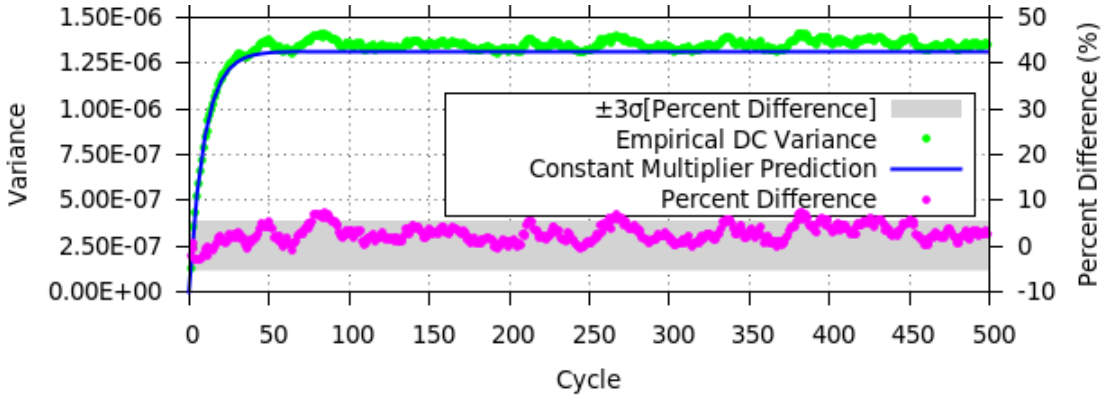

Figure 3.3.3.11 SBDC variances for the fourth mode of the simplified 2-D reactor in Appendix B versus cycle from observations with the extrapolated power method using MCNP implicit capture and from predictions by the constant multiplier model.

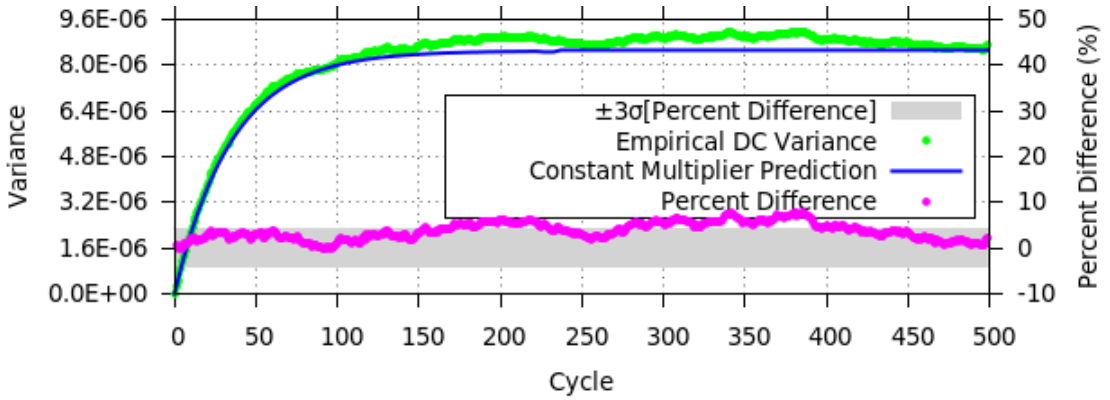

Figure 3.3.3.12 SBDC variances for the second mode of the simplified 2-D reactor in Appendix B versus cycle from observations with the extrapolated power method using MCNP analog capture and from predictions by the constant multiplier model.

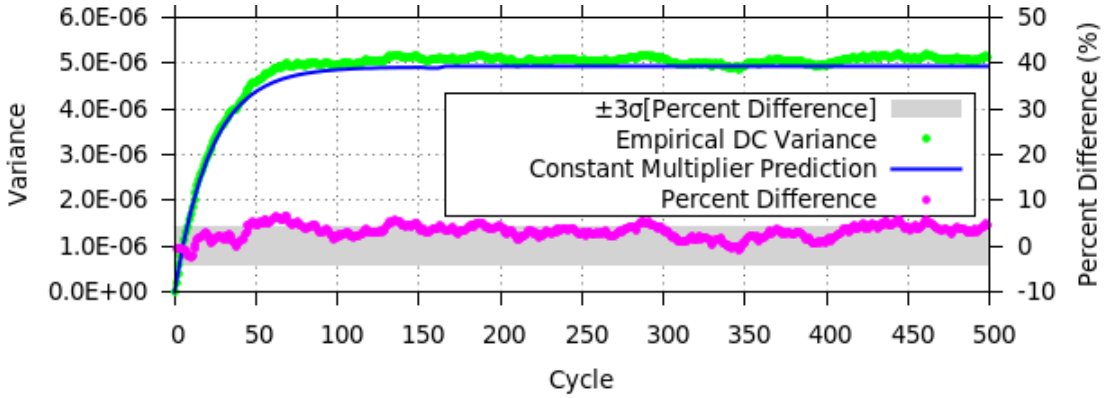

Figure 3.3.3.13 SBDC variances for the third mode of the simplified 2-D reactor in Appendix B versus cycle from observations with the extrapolated power method using MCNP analog capture and from predictions by the constant multiplier model.

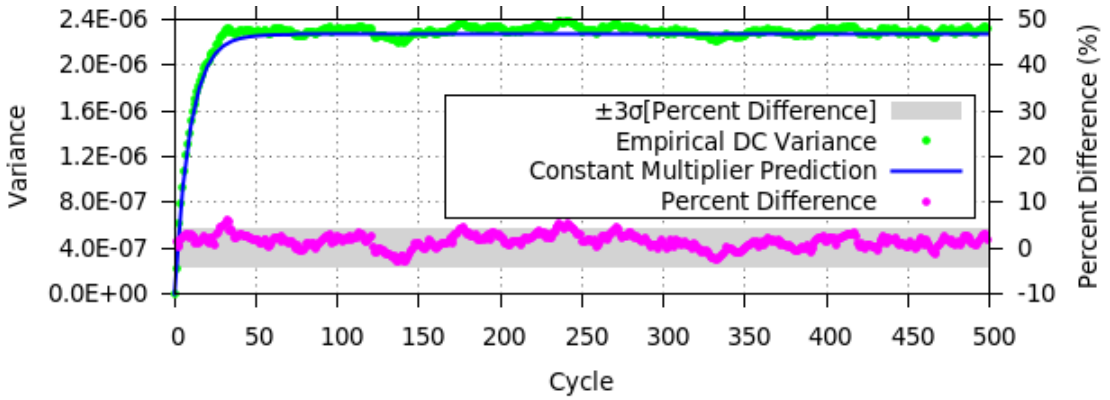

Figure 3.3.3.14 SBDC variances for the fourth mode of the simplified 2-D reactor in Appendix B versus cycle from observations with the extrapolated power method using MCNP analog capture and from predictions by the constant multiplier model.

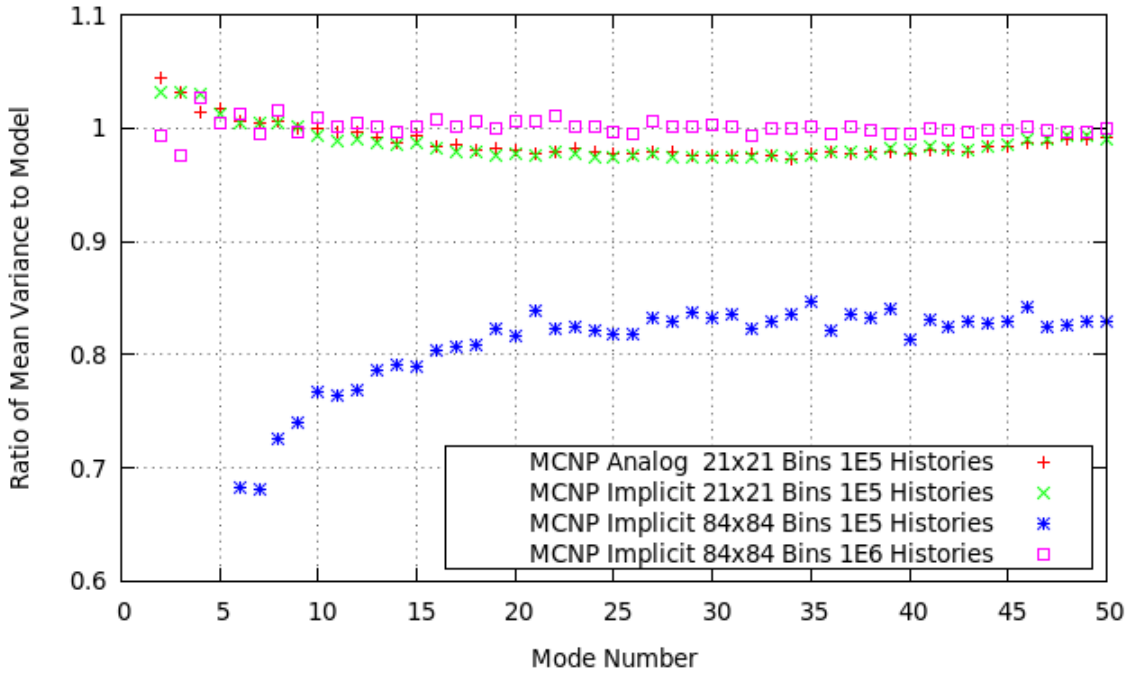

Figure 3.3.3.15 Ratio of empirical mean stationary SBDC variances to those expected from the constant multiplier model for the simplified 2-D reactor problem in Appendix B using MCNP.

3.4 Estimating Representative Variances

The evidence in Section 3.3 supports the use of representative values σ_n^2 for each mode *n* for the single-cycle variances in each cycle for approximating the accumulated variance in SBDCs. The procedure that Section 3.3 presents for calculating a representative variance is computationally expensive and wasteful because most of the collected fission sites are discarded. In this section, an alternate technique that uses spatially stratified subdivisions of the source bank to approximate the repetitions that are necessary for estimating $\sigma_n^{(m)}$ is proposed and assessed. The technique was implemented in two ways with one using eigenvectors that must be known or approximated and the other using no knowledge of eigenvectors.

In Section 3.3, the source bank from each cycle is transported, normalized, and decomposed multiple times with different random number streams to calculate single-cycle variances. This provides an accurate estimate for the single-cycle variances; however, this computer time is mostly wasted because the extra source sites are thrown away. That time could be better spent running more cycles to better converge the source distribution. As an alternative, one can apply a mesh to the problem space and subdivide the sites in the source bank into sub-banks in a spatially stratified way, such that each mesh-bin of each sub-bank contains approximately the same number of sites as the other sub-banks with a possible difference of only 1 site per bin between sub-banks. Then after transporting the source bank in the usual way, the resulting fission sites from source sites in a particular sub-bank are assigned to an intermediate sub-bank, which is then sampled without extrapolation to form a temporary source bank for which the temporary source bank decomposition coefficients (TSBDCs) are calculated. The TSBDCs are not identically distributed random variables because the sub-banks are not sampled with replacement; however, the spatial stratification used to sample the sub-banks makes the TSBDCs approximately identically distributed for a sufficiently large source bank. The SBDCs are approximately sample means of TSBDCs; therefore, for *P* sub-banks, an approximation for the single-cycle variance of a SBDC is the unbiased sample variance

of the TSBDCs divided by P, i.e.,

$$Var\left[\xi_n^{(m)}\right] \approx \frac{1}{P} s^2\left[\epsilon_n^{(m)}\right] \tag{3.4.1}$$

where $\epsilon_n^{(m)}$ are the TSBDCs of mode n at cycle m [13]. Sections 3.4.1 and 3.4.2 apply this methodology with and without using eigenvectors, respectively. A comparison of the two methods suggests that the method without eigenvectors may be most useful for early cycles while the other is preferable for later cycles. However, there is no barrier to using both simultaneously to produce input for a convergence diagnostic.

3.4.1 Estimating Representative Variances Using the Eigenvectors

This section assesses the precision and accuracy of estimating the representative variances for each mode using spatially stratified sub-banks, which are decomposed using eigenvectors from analytic or fission matrix solutions. Results from the uniform slab problem in Appendix A and the simplified 2-D reactor problem in Appendix B show that this approximation method is a reasonably accurate estimator for the representative variances, and a derivation is presented for the precision of the estimator, which shows a reasonable level of precision after a modest number of sufficiently converged cycles. An estimator for representative variance is considered sufficiently accurate and precise if the absolute value of the difference between the mean of the estimator and the reference representative variance plus three standard deviations of the estimator is less than 20%. This condition is consistent with accepting a 10% perturbation in the standard deviation of SBDCs. In addition, using extrapolation between transport cycles is shown to have a negligible effect on the estimated single-cycle variances.

The mean of estimated single-cycle variances over all sufficiently converged cycles will yield the most precise estimates for the representative variances. Some initial cycles may need to be discarded to avoid bias from the far-from-converged single-cycle variances like those shown in Figure 3.3.1.1. For the investigation here, the initial source bank was sampled from the fundamental mode distribution to avoid introducing a bias from far-from-converged source distributions.

To predict precision of the estimator, the variance of the single-cycle variance estimator is derived. As Section 3.2 shows, SBDCs are approximately normally distributed random variables; therefore, the variances of single-cycle sample variances from *P* sub-banks are determined by (3.3.2.2), which yields

$$E\left[Var\left\{\frac{s^2\left[\epsilon_n^{(m)}\right]}{P}\right\}\right]=\frac{1}{P^2}E\left[Var\left\{s^2\left[\epsilon_n^{(m)}\right]\right\}\right]=\frac{2}{P-1}\left(\frac{Var\left[\epsilon_n^{(m)}\right]}{P}\right)^2. \tag{3.4.1.1}$$

Assuming that the single-cycle variance estimates from each cycle are uncorrelated, then the variance of their sum is equal to the sum of their variances [13], which makes the expected variance of the mean of single-cycle sample variances simplify to

$$E\left\{Var\left[\frac{1}{M}\sum_{m=1}^{M}\frac{s^2\left[\epsilon_n^{(m)}\right]}{P}\right]\right\}=\frac{1}{M^2}\sum_{m=1}^{M}E\left\{Var\left[\frac{s^2\left[\epsilon_n^{(m)}\right]}{P}\right]\right\}. \tag{3.4.1.2}$$

Assuming that the single-cycle variances may be approximated by their representative variances σ_n^2, i.e.,

$$\frac{Var\left[\epsilon_n^{(m)}\right]}{P}\approx Var\left[\xi_n^{(m)}\right]\approx\sigma_n^2, \tag{3.4.1.3}$$

inserting (3.4.1.1) into (3.4.1.2) simplifies to

$$E\left\{Var\left[\frac{1}{M}\sum_{m=1}^{M}\frac{s^2\left[\epsilon_n^{(m)}\right]}{P}\right]\right\}=\frac{2\sigma_n^4}{M(P-1)}. \tag{3.4.1.4}$$

Using the definition in (3.3.2.3), the scaled standard deviations of the mean single-cycle variances at cycle *M*, $\tau_n^{(M)}$, are defined as

$$\tau_n^{(M)}=\frac{\sqrt{E\left\{Var\left[\frac{1}{M}\sum_{m=1}^{M}Var\left[\epsilon_n^{(m)}\right]\right]\right\}}}{\sigma_n^2}=\sqrt{\frac{2}{M(P-1)}}. \tag{3.4.1.5}$$

From (3.4.1.5), one can see that the scaled standard deviation of a single-cycle variance estimate, $\tau_n^{(M)}$, may be decreased by using more sub-banks *P*, or averaging over more cycles *M*. Decreasing $\tau_n^{(M)}$ indicates an improvement in the relative precision of the estimator.

To verify this derivation, the uniform slab problem in Appendix A was simulated with a variety of parameter choices, which generally show agreement with the model for the precision of the single-cycle variance estimator. The effect of the cycle number and the number of sub-banks on $\tau_n^{(M)}$ was examined by simulating the uniform slab many times using the standard power method for 400 cycles with 1E4 histories per cycle and a variety of numbers of sub-banks. The TSBDCs were calculated on a uniform 256-bin mesh. Figures 3.4.1.1-3.4.1.3 summarize the observed values of $\tau_n^{(M)}$ multiplied by $\sqrt{M}$ as a function of *P* for several different cycles with each figure corresponding to a different mode. The uncertainties in Figures 3.4.1.1-3.4.1.3 are not shown because they are all less than 1% of $\tau_n^{(M)}$. From Figures 3.4.1.1-3.4.1.3, one can see that the observed variances of the single-cycle variance estimator match the model up to some threshold value of *P*, which is mode dependent. The results from higher order modes match the model for higher thresholds than the lower order modes. For mode 2, the threshold is between 20 and 100; for mode 10, the threshold is between 500 and 1000, and for mode 60, the threshold is between 2000 and 10000. The variances of the estimator increased with more cycles for those cases with values of *P* that were greater than the threshold, which is best observed in Figure 3.4.1.1. As one may expect, increasing the number of histories increases the threshold value of *P*, which Figure 3.4.1.4 demonstrates for the same problem with the number of histories per cycle increased to 1E5. From Figure 3.4.1.4, one can see that the threshold value of *P* for mode 2 is between 200 and 500, which is an increase by approximately a factor of ten relative to the threshold in Figure 3.4.1.1. Similar results were observed for other modes, but they are not reported for brevity. This supports the conclusion that the threshold for a particular mode is related to a minimum number of source sites inside each sub-bank that is sufficient to represent the source distribution. The threshold size of a sub-bank will likely depend upon the problem geometry and be related to the bias in estimating the fundamental eigenvalue [3], [25]; the investigation is left for future research.

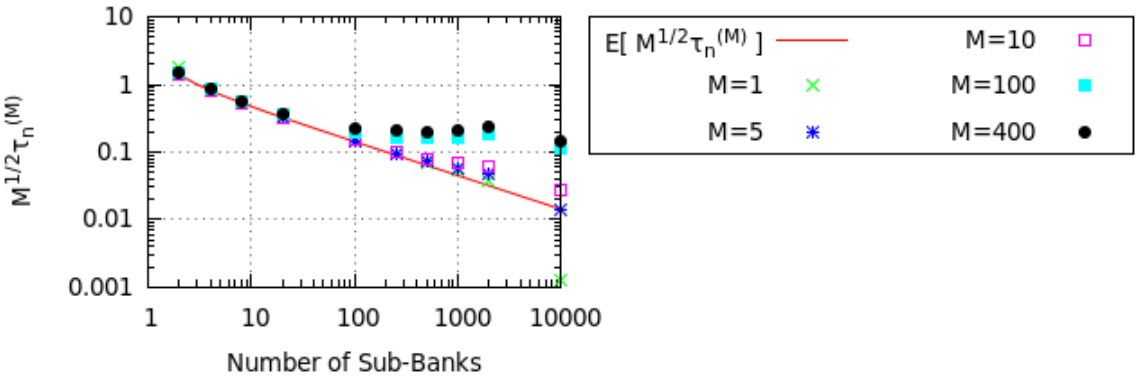

Figure 3.4.1.1 The scaled standard deviations as a function of *P*, the number of sub-banks, for the uniform slab in Appendix A with 1E4 histories per cycle for mode 2.

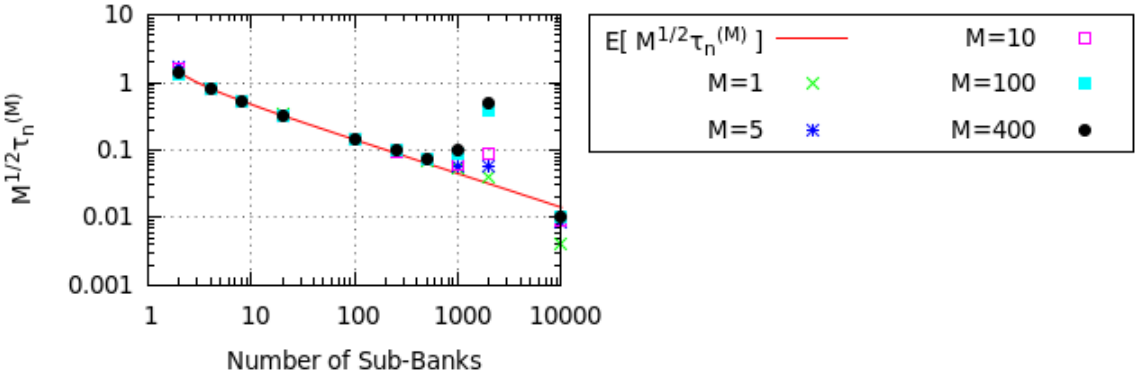

Figure 3.4.1.2 The scaled standard deviations as a function of *P*, the number of sub-banks, for the uniform slab in Appendix A with 1E4 histories per cycle for mode 10.

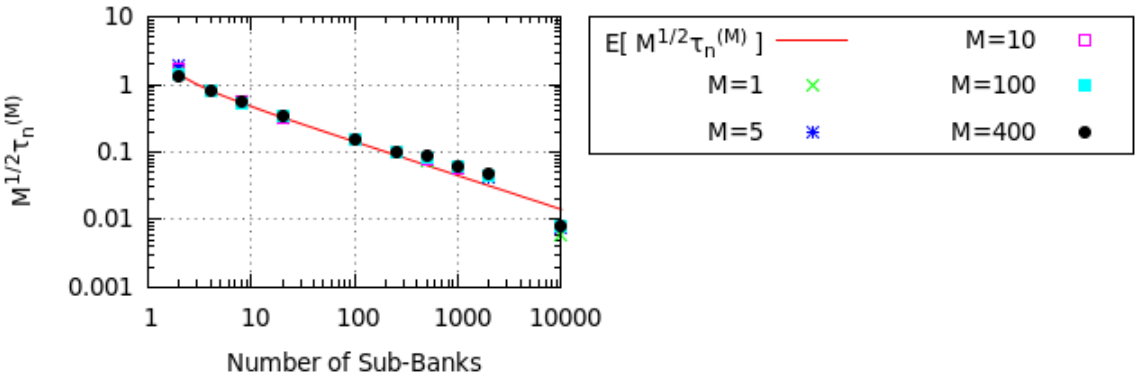

Figure 3.4.1.3 The scaled standard deviations as a function of *P*, the number of sub-banks, for the uniform slab in Appendix A with 1E4 histories per cycle for mode 60.

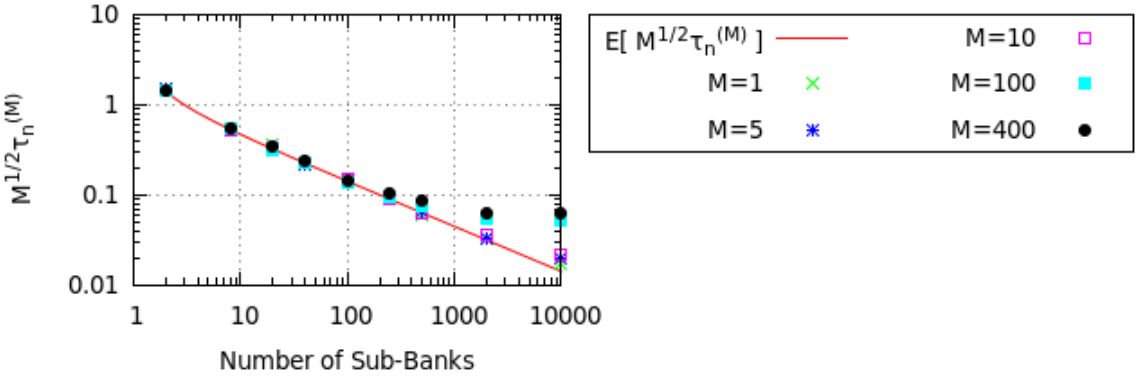

Figure 3.4.1.4 The scaled standard deviations as a function of *P*, the number of sub-banks, for the uniform slab in Appendix A with 1E5 histories per cycle for mode 2.

In addition to precision, the accuracy of the single-cycle variance estimator is also important. The accuracy of the estimator is measured by the expected percent difference with respect to the reference representative variance from Section 3.3.1. The expected percent differences are approximated by repeating simulations with different random number streams and accepting the means of the observed percent differences as the expectations. The estimator is expected to be positively biased because the TSBDCs are not independent and identically distributed.

Collected evidence shows that the estimator tends to become increasingly inaccurate as the number of sub-banks increases, which is expected. To observe this trend, the uniform slab problem from Appendix A was simulated for 400 cycles using the test code with the standard power method and a 256-bin uniform mesh for spatially stratifying the sub-banks. Figure 3.4.1.5 contains the expected percent differences with 1E4 histories per cycle. From Figure 3.4.1.5, one can see that accuracy of the estimator diminishes as the number of sub-banks increases except when the number of sub-banks equals the number of histories per cycle. The trend is nearly exponential. The variance estimate for the extreme case of one history per sub-bank is anomalous and lower than the true value because for the multitude of sub-banks which sample no fissions, the algorithm revives the process by selecting the source point as the temporary source for the next cycle. Increasing the number of histories per cycle to 1E5 yielded the expected percent differences in Figure 3.4.1.6, which shows a similar trend, but the expected percent differences are lower. This is expected because for more histories per cycle, the TSBDCs become more similarly distributed random variables and less correlated. A comparison between Figures 3.4.1.5 and 3.4.1.6 reveals that the accuracy is similar for estimators with the same number of histories per sub-bank. For example for mode 60, the expected percent difference is 26.6% for 1E3 sub-banks with 1E4 histories, and the expected percent difference is 28.2% for 1E4 sub-banks with 1E5 histories. As an additional example, modes 2 and 5 show a similar relationship for the results from 1E4 and 1E5 histories per cycle, which one can see in Figure 3.4.1.7. The points of variation between the two data sets in Figure 3.4.1.7 are mostly due to the differences in which numbers of

histories per sub-bank were simulated.

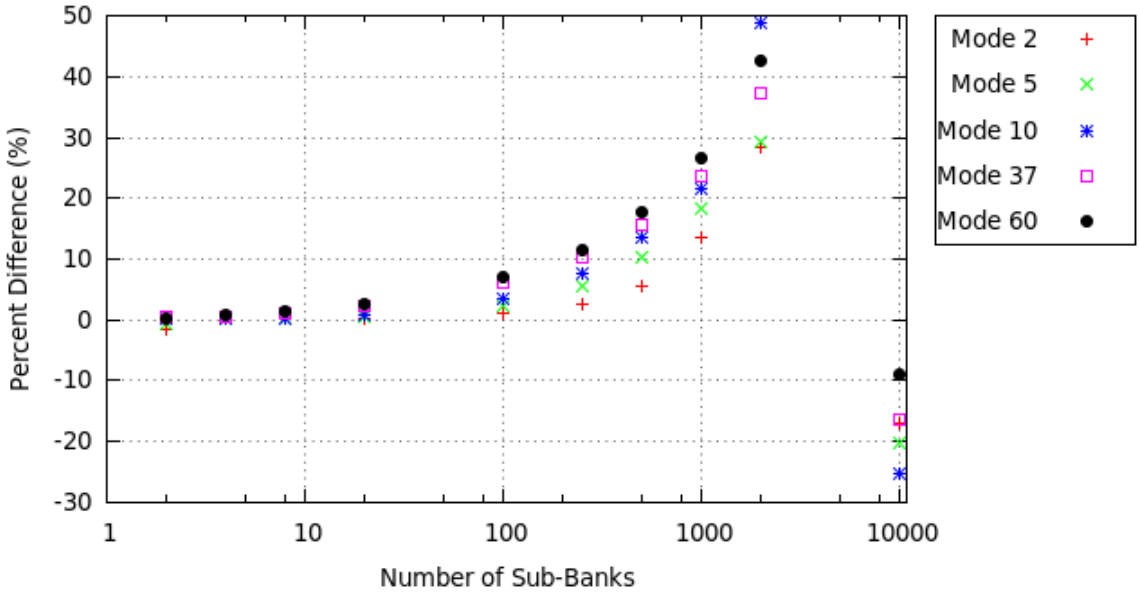

Figure 3.4.1.5 The accuracy of the single-cycle variance estimator as a function of *P*, the number of sub-banks, for the uniform slab in Appendix A after 400 cycles with 1E4 histories per cycle for several modes.

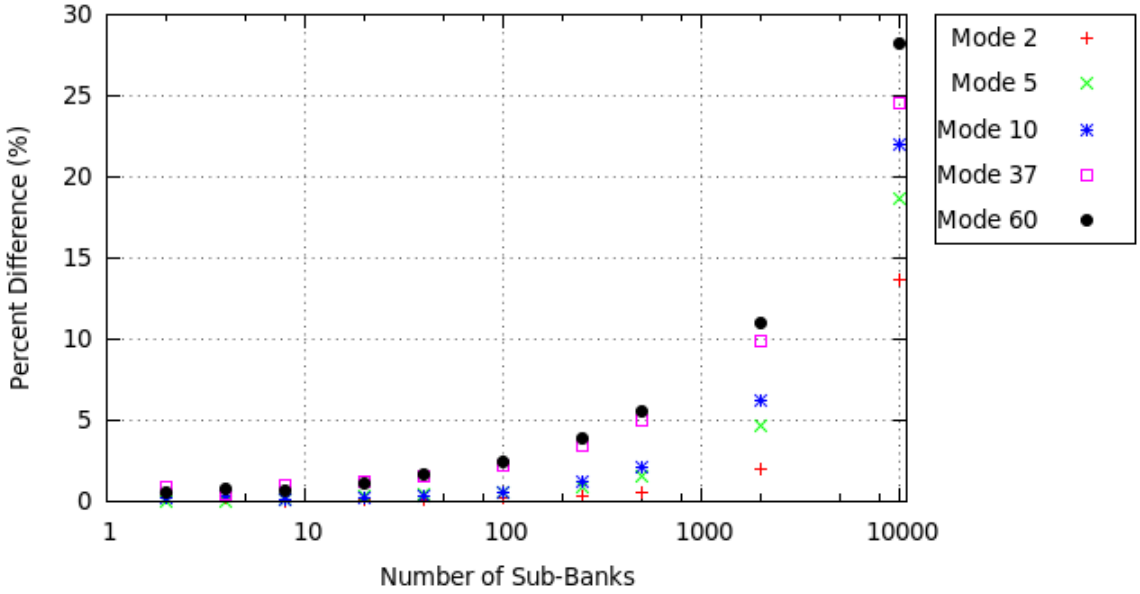

Figure 3.4.1.6 The accuracy of the single-cycle variance estimator as a function of *P*, the number of sub-banks, for the uniform slab in Appendix A after 400 cycle with 1E5 histories per cycle for several modes.

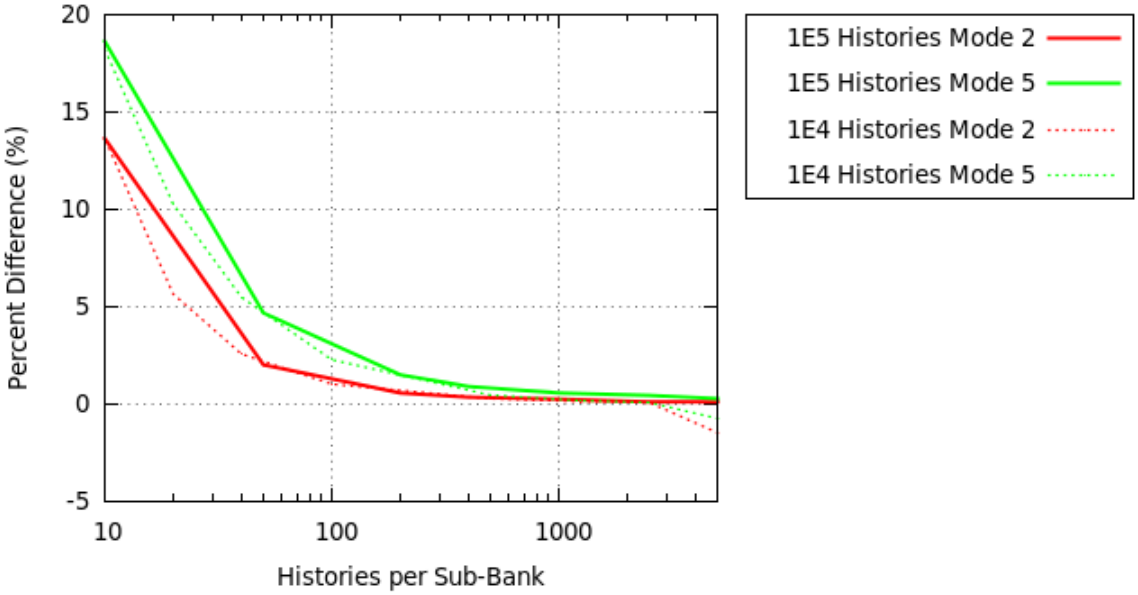

Figure 3.4.1.7 The accuracy of the single-cycle variance estimator as a function of number of histories per sub-bank for the uniform slab in Appendix A after 400 cycles for modes 2 and 5.

In addition to the number of histories per sub-bank, the cycle number also affects the accuracy, and the extent of the effect is diminished by increasing the number of sub-banks. For example, Figures 3.4.1.8 and 3.4.1.9 contain the bias in the single-cycle variance estimator for modes 2 and 31, respectively, for the uniform slab problem in Appendix A with a starting source bank of 1E4 sites. From Figures 3.4.1.8 and 3.4.1.9, one can see that the bias does not change significantly for most of the curves as more cycles are included in the estimate with a range in the biases of less than 3% over the 400 cycles run. An exception to that trend occurs for the variance estimator with 2 sub-banks, which showed a large bias for early cycles that rapidly decayed after approximately 5 cycles, and then, changed by less than 7% over the remaining 400 cycles. In Figure 3.4.1.10, results for mode 25 of the same slab problem with the number of histories increased to 1E5 showed reduced biases in the estimators and a similar gradually decreasing trend for some of the curves; however, results using up to 20 sub-banks showed some deviation from the trend. Results for other modes were similar in nature and are not included for brevity. This behavior indicates that as the number of histories increases, a corresponding increase in the number of sub-banks will sample the entirety

of the stationary SBDC PDFs with fewer cycles than using fewer sub-banks would.

The accuracy of the estimator may vary some across the eigenspectrum. To demonstrate this, the uniform slab problem from Appendix A was simulated with various parameter choices. Figure 3.4.1.11 contains the means of all single-cycle variance estimates for each of the first 60 modes using the standard power method and the extrapolated power method with $\alpha = 0.98$ and 16 extrapolation bins. For each transport scheme, 1E4 independent simulations were performed where each simulation consisted of 1E4 histories per cycle for 400 cycles using 20 sub-banks, which were spatially stratified on a 256-bin mesh. The estimator results were compared with the reference values from Figure 3.3.1.2 via a percent difference included in Figure 3.4.1.11. From Figure 3.4.1.11, one can see that the single-cycle variances are within 5% of their reference values with the majority within 3% for both the standard and extrapolated simulations. Mode 32 had the largest percent difference of 4.37% with the extrapolated power method. The percent difference for Mode 32 was an outlier from the rest, which is most likely due to the spatial stratification of extrapolation interacting with the periodicity of the eigenmodes as discussed in the context of aliasing in Section 2.5. Due to aliasing, a similar but less pronounced anomaly occurs in the extrapolated data for mode 16, which corresponds to the number of bins in the extrapolation mesh. Using analog capture with the test code, the maximum percent difference between the estimator and the reference was 3.16% as can be seen in Figure 3.4.1.12. The maximum difference between the estimator and the reference was reduced to 0.638% when the number of histories per cycle was increased from 1E4 to 1E5 and the number of extrapolation bins from 16 to 256 as can be seen in Figure 3.4.1.13 for implicit capture.

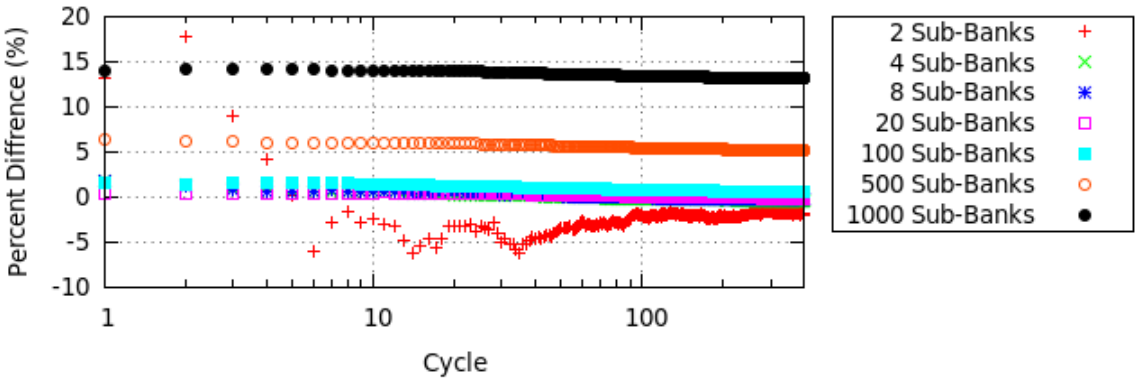

Figure 3.4.1.8 The percent difference between the estimated representative variance and the reference value for mode 2 as a function of cycle number for the uniform slab in Appendix A with 1E4 histories per cycle for several numbers of sub-banks.

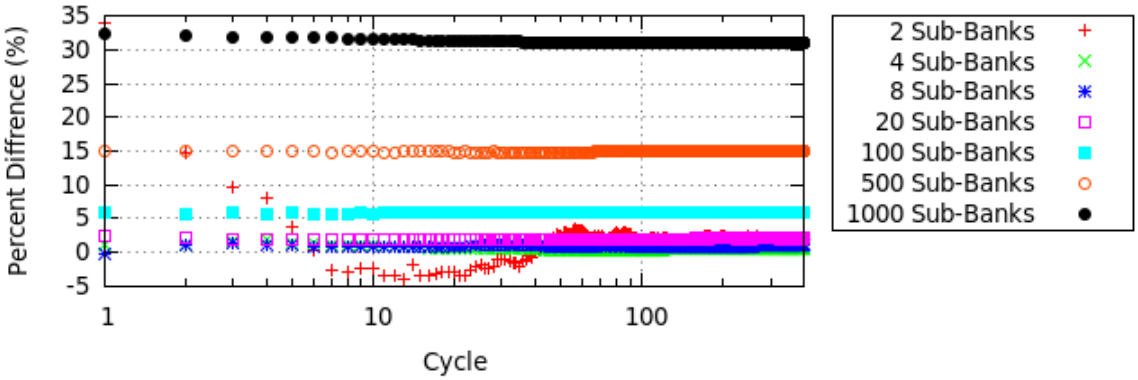

Figure 3.4.1.9 The percent difference between the estimated representative variance and the reference value for mode 31 as a function of cycle number for the uniform slab in Appendix A with 1E4 histories per cycle for several numbers of sub-banks.

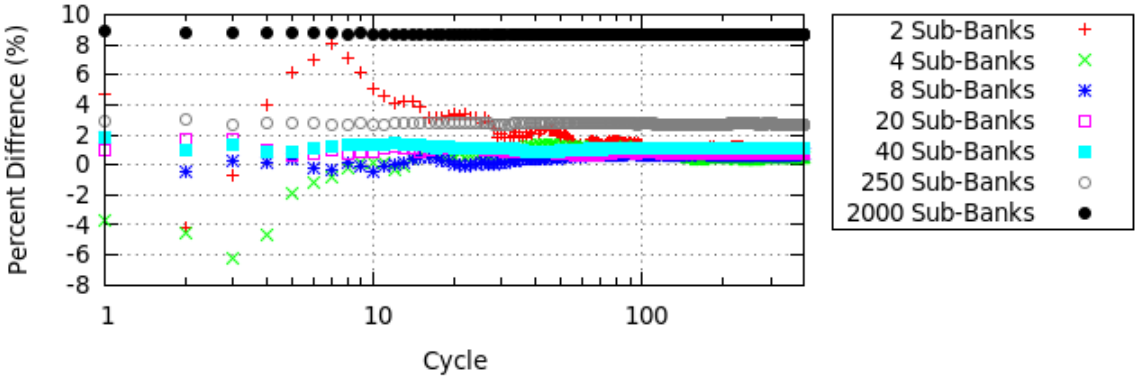

Figure 3.4.1.10 The percent difference between the estimated representative variance and the reference value for mode 25 as a function of cycle number for the uniform slab in Appendix A with 1E5 histories per cycle for several numbers of sub-banks.

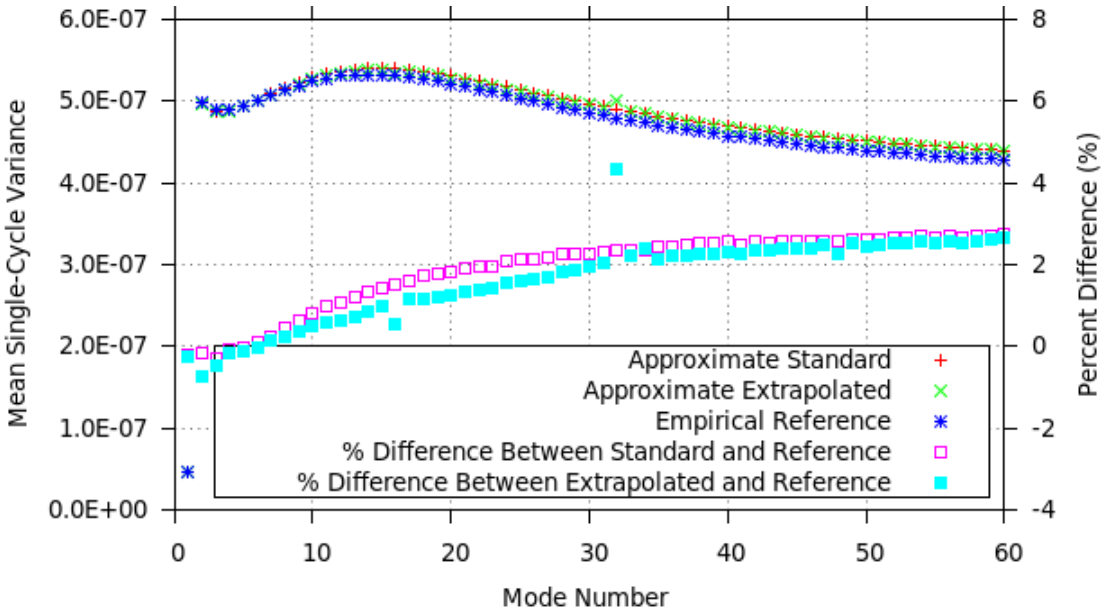

Figure 3.4.1.11 Mean of single-cycle variance estimates over 400 cycles of 1.0E4 histories using implicit capture with 20 sub-banks for the uniform slab from Appendix A compared with a reference empirical calculation.

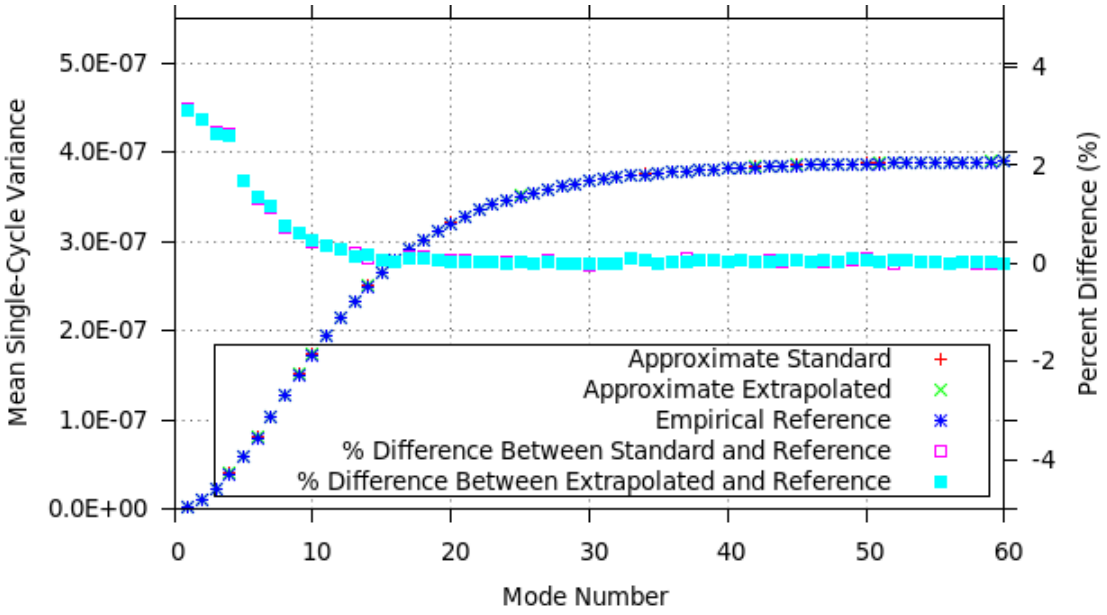

Figure 3.4.1.12 Mean of single-cycle variance estimates over 400 cycles of 1.0E4 histories using analog capture with 20 sub-banks for the uniform slab from Appendix A compared with a reference empirical calculation.

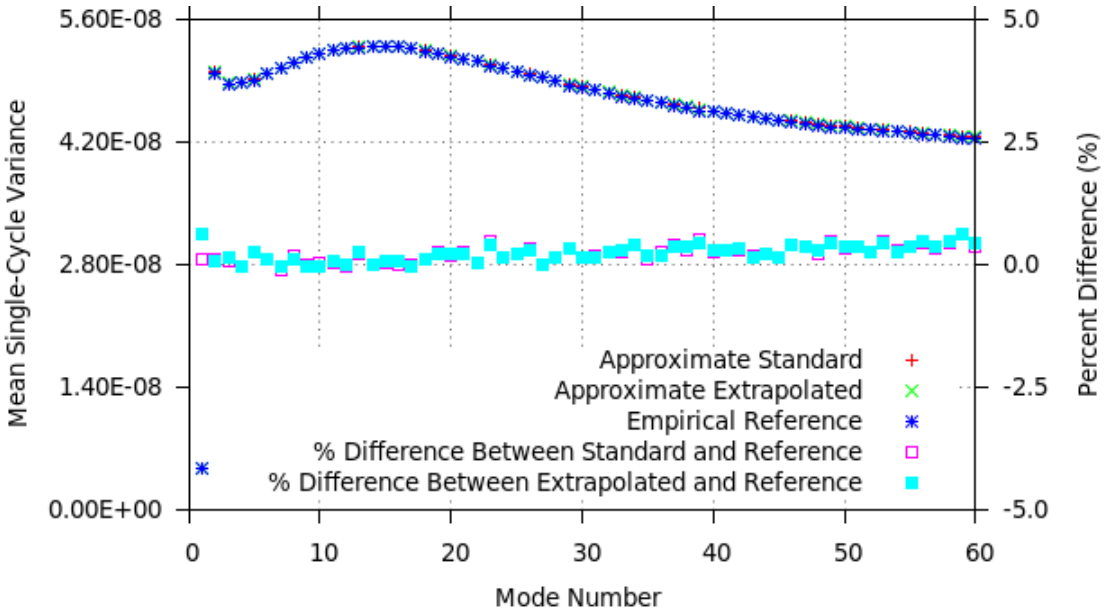

Figure 3.4.1.13 Mean of single-cycle variance estimates over 400 cycles of 1.0E5 histories using implicit capture with 20 sub-banks for the uniform slab from Appendix A compared with a reference empirical calculation.

The accuracy of the single-cycle variance estimator was also examined over the eigenspectrum for the simplified 2-D reactor problem in Appendix B. Figure 3.4.1.14 displays the mean of single-cycle variance estimates from 1E5 histories per cycle after 500 cycles using MCNP with implicit capture. The 3σ uncertainties in the estimates do not appear on the plot because they are less than 0.1% and would not be visible. The percent differences between the estimates and the reference gradually increase with mode number, which is similar to the trend in the single-cycle variance estimates for the uniform slab problem from Appendix A with implicit capture. Using MCNP with analog capture yielded the percent differences between the estimates and their reference values in Figure 3.4.1.15. Figure 3.4.1.15 shows a similar trend as Figure 3.4.1.14, but the accuracy of the MCNP analog capture data appears improved; however, this is only because MCNP analog capture raises the single-cycle variances. The differences between the estimates and reference values fall within the same range, which Figures 3.4.1.16 and 3.4.1.17 show along the right-hand axis. They only differ on a relative basis.

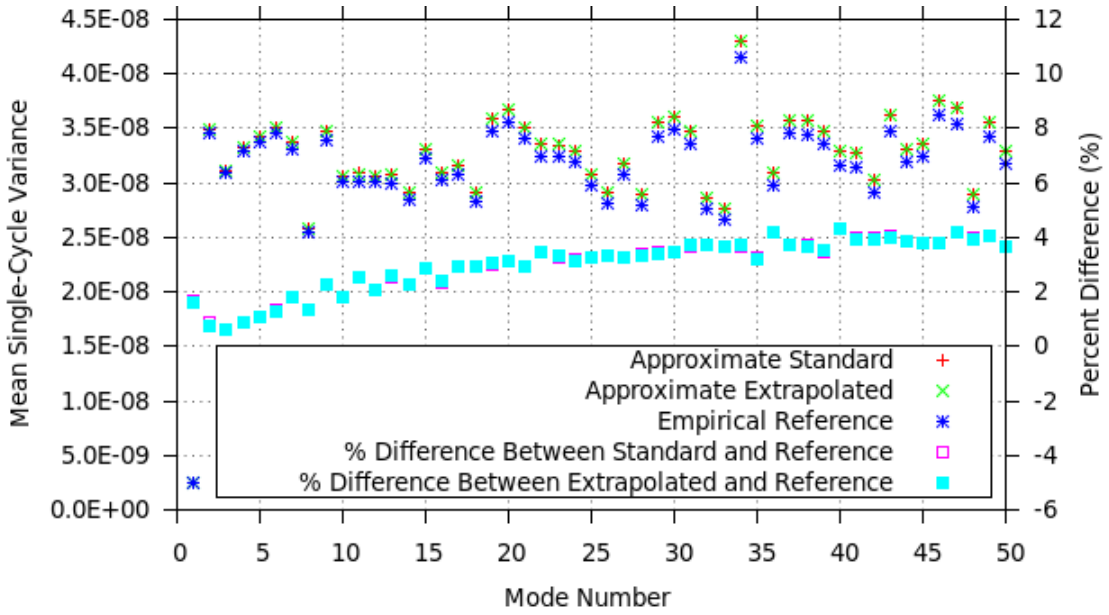

Figure 3.4.1.14 Mean of single-cycle variance estimates over 500 cycles of 1.0E5 histories using implicit capture with 20 sub-banks for the simplified 2-D reactor in Appendix B compared with a reference empirical calculation.

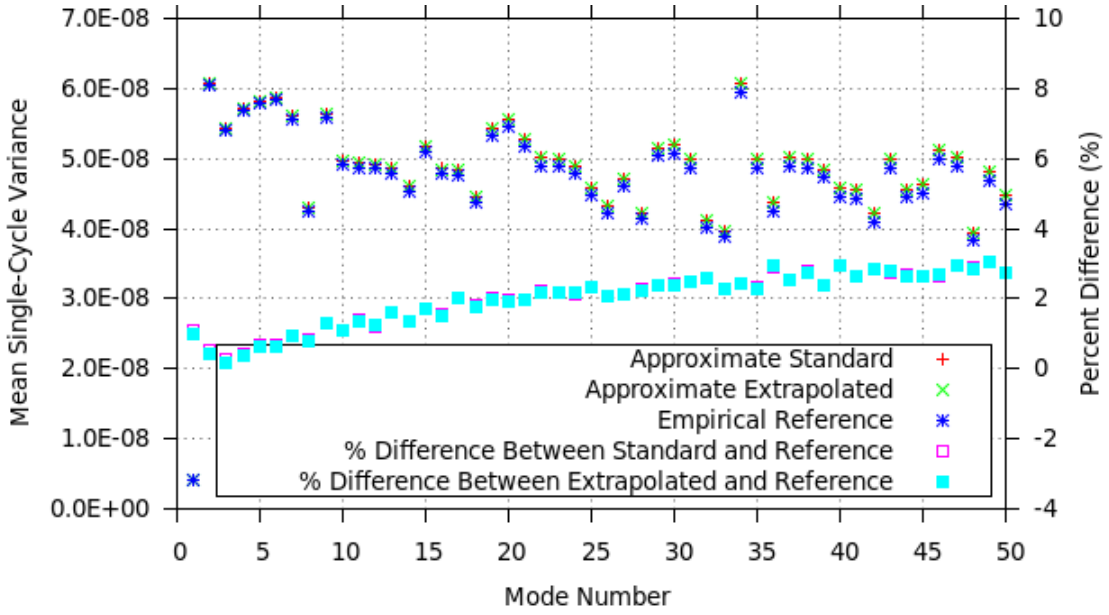

Figure 3.4.1.15 Mean of single-cycle variance estimates over 500 cycles of 1.0E5 histories using MCNP analog capture with 20 sub-banks for the simplified 2-D reactor in Appendix B compared with a reference empirical calculation.

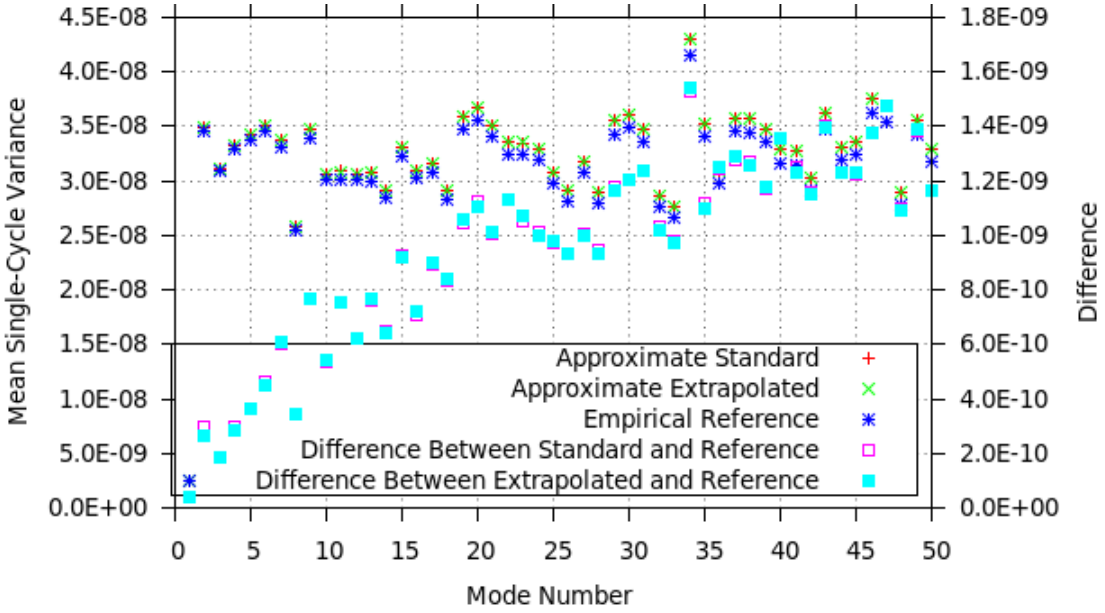

Figure 3.4.1.16 Mean of single-cycle variance estimates over 500 cycles of 1.0E5 histories using implicit capture with 20 sub-banks for the simplified 2-D reactor in Appendix B compared with a reference empirical calculation on an absolute basis.

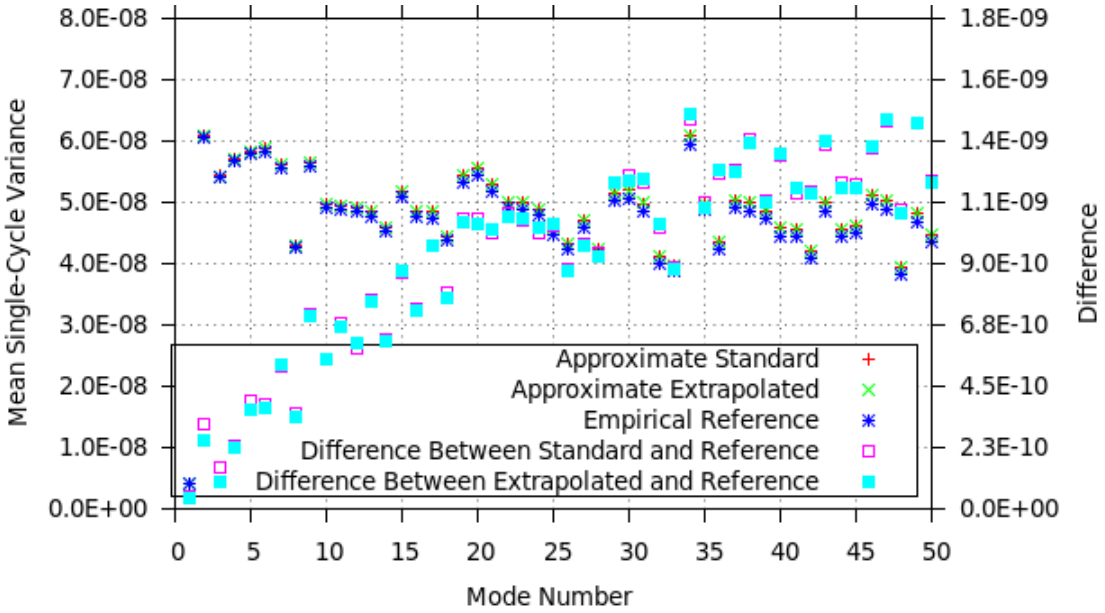

Figure 3.4.1.17 Mean of single-cycle variance estimates over 500 cycles of 1.0E5 histories using MCNP analog capture with 20 sub-banks for the simplified 2-D reactor in Appendix B compared with a reference empirical calculation on an absolute basis.

3.4.2 Estimating Representative Variances Without Eigenvectors

Because a user may not have a sufficiently accurate set of eigenvectors at the beginning of a calculation, an approximate method for obtaining rough estimates of the representative variances is presented. Evidence in Section 3.3.1 supports the assumption that the representative variances of non-fundamental modes have similar values within an order of magnitude under implicit capture. With similarity between representative variances of SBDCs, the mean of all representative variances over the eigenvector spectrum, which shall be referred to as the spectral mean variance, can be a reasonable approximation for the representative variances of non-fundamental modes. By computing the representative variances of SBDCs in an alternate orthonormal basis, the spectral mean variance can be readily estimated. From empirical evidence, the estimates for the spectral mean are within 30% of the empirical reference values. The spectral mean estimate is less sensitive to source bank distribution than the individual mode single-cycle variances; therefore, the spectral mean may be used very early in a simulation to estimate SBDC PDFs and set convergence criteria before approaching the stationary state.

The representative variances of non-fundamental mode SBDCs tend to have similar magnitudes under implicit capture, which makes their mean a reasonable approximation to their values. Table 3.4.2.1 summarizes the ranges and means of non-fundamental mode single-cycle variances from Section 3.3.1. From Table 3.4.2.1, one can see that for both, the uniform slab problem in Appendix A and the double peak slab problem in Appendix D, the extremes of the observed single-cycle variances had lower ratios to the spectral mean with implicit capture than analog capture. The spectral mean was 31.623 times greater than the minimum representative variance using analog capture with the uniform slab, which exceeds an order of magnitude. For the double peak slab, a relatively large ratio of 8.2817 was observed for the spectral mean compared to the minimum representative variance. Considering these observations, the spectral mean is not recommended as a reasonable approximation for representative variances under

analog capture. This was not verified with MCNP because it does not fill the fission bank in an analog manner. However, for the implicit capture results using MCNP and the test code, none of the ratios exceeded 4, which means that the standard deviation from the spectral mean variance is within a factor of 2 of the representative standard deviations, which is likely sufficiently accurate for setting convergence criteria as in Section 4.2.

Problem	Spectral Mean Variance	Minimum Observed Variance	Mean / Minimum	Maximum Observed Variance	Maximum / Mean
Slab Analog Capture 1E4 Histories	3.0692E-07	9.7056E-09	31.623	3.8900E-07	1.2674
Slab Implicit Capture 1E4 Histories	4.7278E-07	4.2766E-07	1.1055	5.3226E-07	1.1258
Slab Implicit Capture 1E5 Histories	4.6940E-08	4.2420E-08	1.1065	5.2943E-08	1.1279
Double Peak Implicit Capture 1E5 Histories	5.0250E-08	1.6491E-08	3.0922	1.9911E-07	3.9046
Double Peak Analog Capture 1E5 Histories	4.7096E-08	5.6867E-09	8.2817	7.4433E-08	1.5804
Simple 2-D Reactor MCNP Implicit 1E5 Histories	3.1418E-08	2.5477E-08	1.2332	4.1468E-08	1.3199
Simple 2-D Reactor MCNP Analog 1E5 Histories	4.7400E-08	3.8300E-08	1.2392	6.0500E-08	1.2746

Table 3.4.2.1: Representative variance ranges of non-fundamental modes from several test problems.

The spectral mean variance may be approximated by calculating the mean single-cycle variances of SBDCs in an alternate orthonormal basis. Any vector U in the span of the

eigenvectors of an *N*x*N* fission matrix *F* can be comprised of up to *M* linearly independent eigenvectors and up to *N* orthonormal vectors in another basis as follows

$$\sum_{i=1}^{N} a_i L_i = U = \sum_{i=1}^{M} u_i B_i \tag{3.4.2.1}$$

Where L_i is the i^{th} orthonormal basis vector, and a_i is the DC of the i^{th} orthonormal basis vector, and B_i is the i^{th} eigenvector, and u_i is the DC of the i^{th} eigenvector. From basic linear algebra, the number of linearly independent eigenvectors must be less than or equal to the rank of *F,* which is less than or equal to the dimension of the vector space; therefore, $M \le N$. The left and right-hand sides of Equation (3.4.2.1) can be expressed as matrix vector products, i.e.,

$$L\vec{a} = B\vec{u} \tag{3.4.2.2}$$

where the i^{th} column of L is the vector L_i, and the i^{th} column of B is the eigenvector B_i, and the elements in the i^{th} row of the vectors $\vec{a}$ and $\vec{u}$ are a_i and u_i, respectively. Since the vectors comprising *L* are orthonormal, *L* is an orthogonal matrix; therefore, multiplying by the hermitian conjugate L^* on the left of each side of (3.4.2.2) yields

$$\vec{a} = L^* B \vec{u}\,. \tag{3.4.2.3}$$

The covariance of a random vector $\vec{a}$ is defined as [13]

$$\mathrm{Cov}(\vec{a}) = E\left[\vec{a}\,\vec{a}^*\right] - E[\vec{a}]\,E\left[\vec{a}^*\right]. \tag{3.4.2.4}$$

Entries along the diagonal of the covariance matrix are the variances of the vector elements, and the trace of $\mathrm{Cov}(\vec{a})$ is the sum of the diagonal elements; therefore, the spectral mean variance is the trace of $\mathrm{Cov}(\vec{u})$ divided by *M*. The covariance of $\vec{a}$ can be expressed in terms of $\vec{u}$ as

$$\begin{aligned} \mathrm{Cov}(\vec{a}) &= E\left[L^* B\vec{u}\left(L^* B\vec{u}\right)^*\right] - E\left[L^* B\vec{u}\right]E\left[\left(L^* B\vec{u}\right)^*\right] \\ &= E\left[L^* B\vec{u}\,\vec{u}^* B^* L\right] - E\left[L^* B\vec{u}\right]E\left[\vec{u}^* B^* L\right]. \end{aligned} \tag{3.4.2.5}$$

The matrices are constant; therefore, the matrices can be pulled out of the expectations to yield

$$\begin{aligned} \mathrm{Cov}(\vec{a}) &= L^* B\,E\left[\vec{u}\,\vec{u}^*\right]B^* L - L^* B\,E[\vec{u}]\,E\left[\vec{u}^*\right]B^* L \\ &= L^* B\left(E\left[\vec{u}\,\vec{u}^*\right] - E[\vec{u}]\,E\left[\vec{u}^*\right]\right)B^* L \\ &= L^* B\,\mathrm{Cov}(\vec{u})\,B^* L\,. \end{aligned} \tag{3.4.2.6}$$

The trace of (3.4.2.6) is

$$TR\left(\mathrm{Cov}\left(\vec{a}\right)\right)=TR\left(L^{*}B\,\mathrm{Cov}\left(\vec{u}\right)B^{*}L\right), \tag{3.4.2.7}$$

which is invariant under cyclic permutations [46]; therefore,

$$TR\left(\mathrm{Cov}\left(\vec{a}\right)\right)=TR\left(B^{*}L\,L^{*}B\,\mathrm{Cov}\left(\vec{u}\right)\right). \tag{3.4.2.8}$$

Because L is an orthogonal matrix whose transpose is its own inverse, (3.4.2.8) reduces to

$$TR\left(\mathrm{Cov}\left(\vec{a}\right)\right)=TR\left(B^{*}B\,\mathrm{Cov}\left(\vec{u}\right)\right). \tag{3.4.2.9}$$

If the eigenvector basis is approximately orthogonal, then the traces of the covariance matrices will be approximately equal because $B^{*}B\approx I$ where I is the identity matrix, which empirical evidence supports [10].

In general, the eigenbasis may not be full rank. The spectral mean variance is the trace of the covariance matrix divided by the number of eigenvectors, which is *M* not *N*. If any mesh cells contain no fissionable material, then the operator *F* will not be full rank*;* therefore, an upper bound for the rank of *F* is the number of mesh bins that can have a fission event. That number of mesh bins can be readily approximated by accumulating the number of fission events in each mesh bin over an entire simulation, or a more accurate number of fissile mesh bins can be found with a scan of materials in each mesh cell. To save implementation time, the former technique was used in this dissertation. Selecting the standard vectors as the orthogonal basis is a natural choice because the decomposition in standard vectors makes the task of bounding the rank of *F* trivial, and the standard vector decomposition is most likely already being computed for use with an entropy diagnostic [47] or a fission matrix [6], [10], [34]. If the number of eigenvectors of the fission matrix is nearly equal to the number of fissionable cells, then the spectral mean variance will be well approximated by the mean of all SBDC variances in the orthogonal basis. Empirical evidence supports the assumption that the number of eigenvectors is approximately equal to the number of fissile cells [34].

Table 3.4.2.2 presents a summary of results from estimating the spectral mean using the orthogonal standard vector basis for various test cases, and those results show fair agreement with the empirically determined spectral means. From Table 3.4.2.2, one can

see that the spectral mean estimates from the implicit capture simulations were within 25.6% of the reference spectral mean. The spectral mean estimates of the analog capture simulations were somewhat worse with a maximum percent difference of approximately 31.1%. These differences are at least partially attributable to the fact that the reference spectral means were obtained from fewer modes than the estimator. As an example, the slab with analog capture yields a relatively high estimate for the spectral mean because the representative variances of approximately the first 20 modes in the reference calculation were notably lower than the apparent asymptotic representative variances that the second half of modes approach in Figure 3.3.1.2. The relative differences in the spectral mean estimates are less than the accepted error with respect to individual modes shown in Table 3.4.2.1; therefore, the spectral mean estimator using standard basis vectors may be considered sufficiently accurate. Additionally from Table 3.4.2.2, one can see that the errors from the spectral mean estimator for the extrapolated cases differed by less than 0.1% when compared to the errors in the spectral mean estimates from the standard power method; therefore, the use of extrapolation does not affect the estimator as expected because extrapolation was not performed when determining TSBDCs.

Problem	Spectral Mean Variance Estimate	Spectral Mean Variance Reference	Spectral Mean Difference (%)
Slab, Analog, 1E4 Histories, Standard	3.7255E-07	3.0692E-07	6.5628E-08 (21.38)
Slab, Analog, 1E4 Histories, Extrapolated	3.7170E-07	3.0692E-07	6.4781E-08 (21.11)
Slab, Implicit, 1E4 Histories, Standard	4.3139E-07	4.7278E-07	-4.1385E-08 (-8.75)
Slab, Implicit, 1E4 Histories, Extrapolated	4.3109E-07	4.7278E-07	-4.1691E-08 (-8.82)
Slab, Implicit, 1E5 Histories, Standard	4.1923E-08	4.6940E-08	-5.0171E-09 (-10.69)
Slab, Implicit, 1E5 Histories, Extrapolated	4.1926E-08	4.6940E-08	-5.0142E-09 (-10.68)
Double Peak, Implicit, 1E5 Histories, Standard	6.4029E-08	5.0995E-08	1.3034E-08 (25.56)
Double Peak, Analog, 1E5 Histories, Standard	6.1748E-08	4.7096E-08	1.4651E-08 (31.11)
Simple 2-D Reactor, MCNP Implicit, 1E5 Histories, Standard	3.3258E-08	3.1418E-08	1.8406E-09 (5.86)
Simple 2-D Reactor, MCNP Implicit, 1E5 Histories, Extrapolated	3.3259E-08	3.1418E-08	1.8411E-09 (5.86)
Simple 2-D Reactor, MCNP Analog, 1E5 Histories, Standard	4.0821E-08	4.7400E-08	-6.6278E-09 (-13.97)
Simple 2-D Reactor, MCNP Analog, 1E5 Histories, Extrapolated	4.0821E-08	4.7400E-08	-6.6277E-09 (-13.97)

Table 3.4.2.2: Estimated spectral mean variances of several test problems, which are compared with their empirically determined reference values.

One strength of the spectral mean estimator is that it has a lower variance than the representative variance estimator in Section 3.4.1 for the first cycle, and that advantage persists through all cycles. The sample variances are chi-distributed random variables, as previously stated in Section 3.3.2. Thus, the spectral mean variance estimate from a single cycle is approximately the mean of N chi-distributed random variables with the same number of degrees of freedom, which may be correlated. This is only an

approximate definition if *N* is greater than *M* but is exact if *N* equals *M*. If one assumes that the single-cycle variances are similar in magnitude and that the covariances are less than 1, then the variance of their mean is less than the variance of the variance of each SBDC from a single cycle [13]. If one assumes that the estimates for the spectral variance from each cycle are independent, then the variance of the mean of the spectral mean variance estimates will decrease by the factor 1/*m* where *m* is the number of cycles [13]. From Figures 3.4.2.1, 3.4.2.2, and 3.4.2.3, one can see that variance of the representative variance and spectral mean variance estimators for the uniform slab, double peak slab, and simplified 2-D reactor, respectively, are proportional to 1/*m* because when multiplied by *m*, they appear flat with respect to changes in cycle number. Also, from Figures 3.4.2.1, 3.4.2.2, and 3.4.2.3, one can see that the variance of the spectral mean variance estimator is generally one or more orders of magnitude less than the variance of the representative variance estimator. The variance of the spectral mean variance estimate may therefore be useful for setting convergence criteria in early cycles until the other estimator has a sufficient number of samples.

In addition to having a lower variance than the representative variance estimator, the spectral mean variance estimator is also less sensitive to the closeness of the source distribution to the fundamental mode. For example, the uniform slab problem in Appendix A had a notable trend in the empirically estimated expected single-cycle variances when starting with a far from converged source, which may be seen in Figure 3.3.1.1. The same problem was simulated 1000 times from the same initial source distribution using 4E5 histories per cycle with 20 temporary banks. Estimates for the representative variances were calculated using the procedure in Section 3.4.1, and the spectral mean variance was approximated using the standard vectors as this section describes. The 3σ uncertainty bands for those estimators are plotted in Figure 3.4.2.4. As one can see in Figure 3.4.2.4, the spectral mean estimator was more accurate and precise than the representative variance estimator for the second mode until approximately cycle 160 where the representative variance estimator became more accurate. For the third mode, the spectral mean estimator is not particularly

advantageous but may be regarded as a reasonable alternative until approximately cycle 70 where the spectral mean estimator range lies outside of the representative variance estimator range. This test used reference eigenvectors from diffusion theory to calculate representative variances. In a simulation where the eigenvectors must be calculated on-the-fly, then the spectral mean estimator may have additional utility because the representative variance estimator will likely have greater variance and a bias from changing estimates for the eigenvectors. Depending upon circumstances, both estimators may be used in tandem to produce better informed convergence criteria with the spectral mean estimator preferred in early cycles, and the representative variance estimator preferred for later cycles.

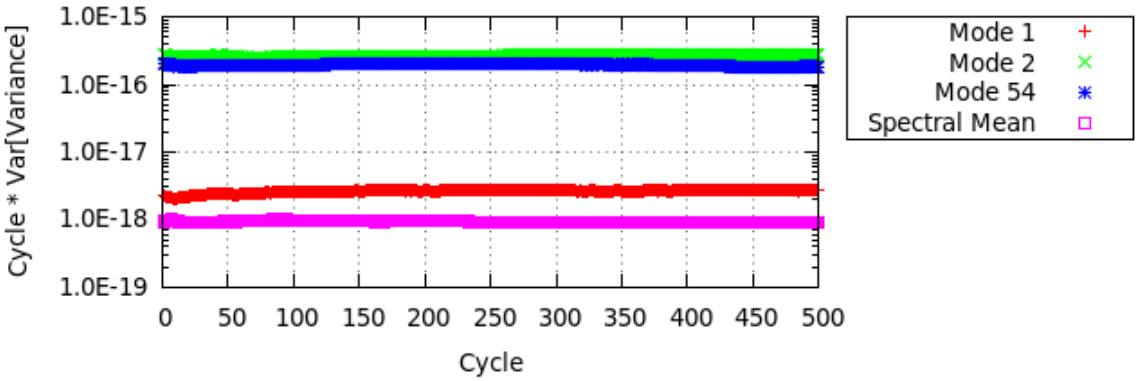

Figure 3.4.2.1 Variance of representative variance estimate scaled by cycle from 1.4E3 simulations of 1.0E5 histories using implicit capture with 20 sub-banks for the uniform slab in Appendix A.

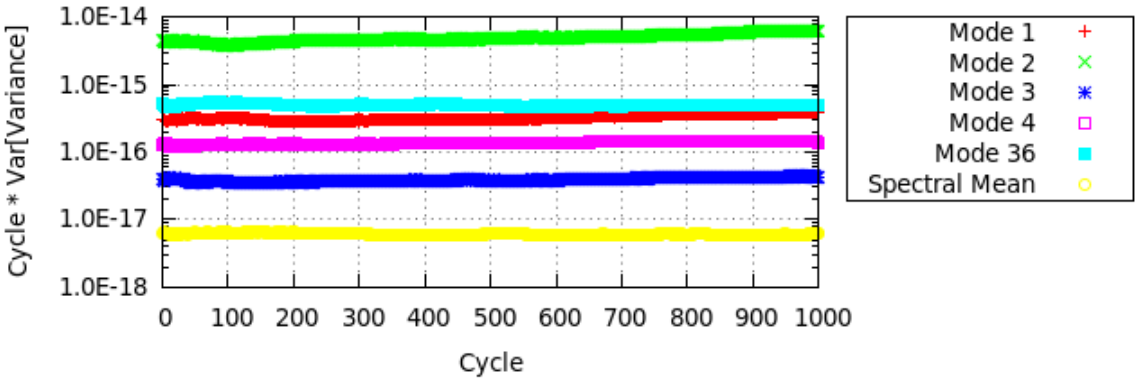

Figure 3.4.2.2 Variance of representative variance estimate scaled by cycle from 1.0E3 simulations of 1.0E5 histories using implicit capture with 20 sub-banks for the double peak slab in Appendix D.

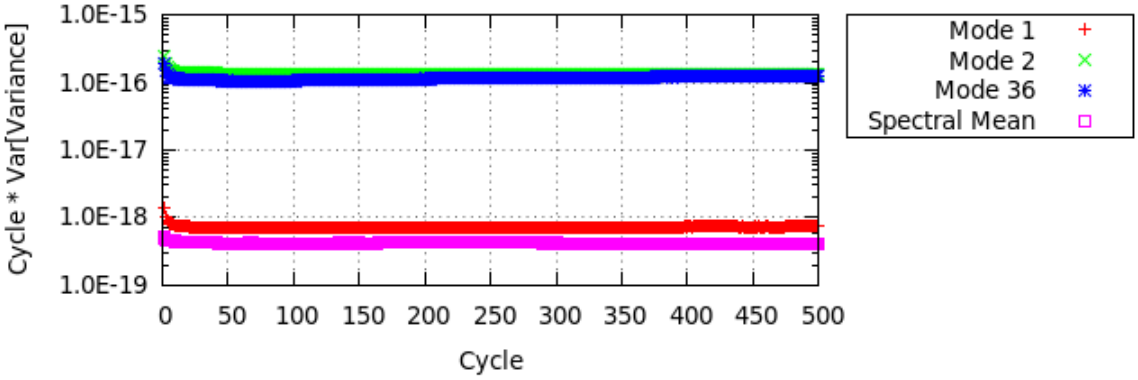

Figure 3.4.2.3 Variance of representative variance estimate scaled by cycle from 6.254E3 simulations of 1.0E5 histories using implicit capture with 20 sub-banks for the simplified 2-D reactor in Appendix B.

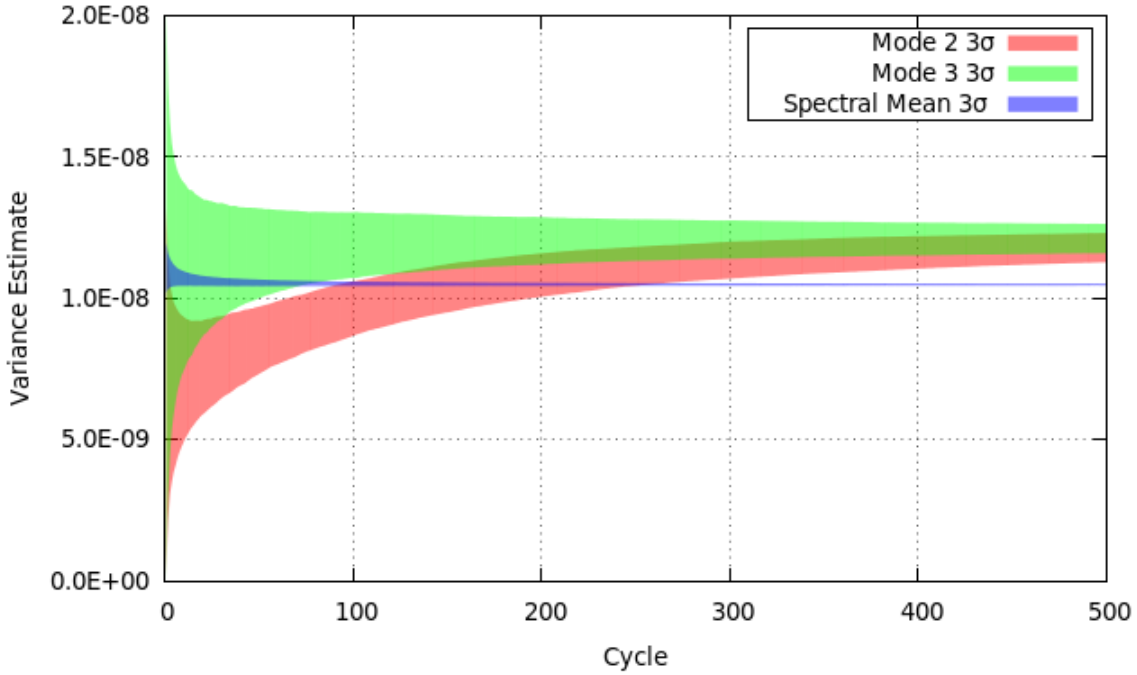

Figure 3.4.2.4 The 3σ uncertainty range of the cumulative mean of single-cycle variance and spectral mean variance estimates for the uniform slab in Appendix A with 1.0E5 histories per cycle using implicit capture with 20 sub-banks with a poor initial source.

Chapter 4. Identifying, Predicting, and Optimizing Convergence

Before active tallying of desired quantities may begin, the source distribution must be sufficiently converged toward its stationary distribution, which fluctuates about the fundamental mode. Detecting sufficient convergence of the MC source iteration is a difficult problem that has motivated volumes of research. A convergence criterion based on similarity of eigenvectors calculated from fission matrices of successive cycles was proposed [48], but the technique was not able to guarantee convergence [49]. The use of two separate simulations running in parallel with specially selected different initial sources such that the fundamental eigenvalue estimate is sandwiched by the two simulations has been suggested [50], [51] ; however, the fundamental eigenvalue estimate can converge much earlier than the source distribution for some problems [52]. Entropy diagnostics from information theory are the current standard used to assess convergence [1], [47], [53]–[55]. Some newer diagnostics focus on eliminating the need for specifying a mesh, such as nine-centers distance sums [56], and mean and standard deviation of particle positions [55]. These diagnostics do not provide the user with a tangible confidence interval for the accuracy of the source distribution or allow the user to specify a desired confidence. Also, these diagnostics are not readily applicable in a predictive manner to suggest the number of discarded cycles before simulating all discarded cycles. A new convergence diagnostic that investigates eigenvector components is developed in this chapter to address these shortcomings.

The new diagnostic seeks to measure convergence in distribution [13] of the SBDCs. Two measures of similarity between PDFs, the relative entropy [57] and Bhattacharrya coefficient (BC) [58], are examined for the specific case of normally distributed random variables. The adjusted constant multiplier model is used to approximate the PDFs.

When the PDFs of the non-stationary and stationary SBDCs are compared, the relative entropy is shown to be preferable over the BC. A convergence threshold value for the new diagnostic is specified by the user to impose a particular desired confidence in the proximity of SBDC PDFs to their stationary distributions. The threshold must be met for every mode to be considered sufficiently converged; however, in practice, only some eigenvectors need to be diagnosed for convergence because the others may safely be assumed to converge much faster. The diagnostic is applied to the problem of determining the optimal number of extrapolated and discarded cycles for a MC source iteration using linear extrapolation.

4.1 Defining Modal Convergence Measure

To assess convergence of SBDCs, their PDFs may be compared with their stationary PDFs. Two of the many potential measures of similarity between PDFs are the relative entropy and BC. From evidence in Section 3.2, the SBDC PDFs are assumed to be normally distributed for a sufficient number of histories per cycle. Equations for the relative entropy and BC between two normally distributed PDFs are derived. The equations are then cast in a form relative to the standard deviation of the second PDF, which is assumed to have a mean of zero like the stationary SBDCs of non-fundamental modes from the constant multiplier model. The contours of the relative entropy and BC show that the BC rewards increased uncertainty beyond the stationary amount. This is deemed undesirable; therefore, the relative entropy is selected as the preferred measure of SBDC convergence.

The relative entropy (Kullback-Leibler divergence) between two continuous probability density functions (PDFs), $p(r)$ and $q(r)$, is [57]

$$D(p(r)\|q(r)) = \int_{-\infty}^{\infty} p(r)\log\left(\frac{p(r)}{q(r)}\right)dr = \int_{-\infty}^{\infty} p(r)\left[\log(p(r)) - \log(q(r))\right]dr. \qquad (4.1.1)$$

The relative entropy between two PDFs has a lower bound of zero and no upper bound. The relative entropy is zero if and only if the two PDFs are identical almost everywhere. The entropy approaches infinity if the PDF $q(r)$ is ever zero in some region where

$p(r)$ is non-zero, which cannot occur if $q(r)$ is a normal distribution. If both PDFs, $p(r)$ and $q(r)$, are normally distributed with means μ_1 and μ_2 and standard deviations σ_1 and σ_2, respectively, then their relative entropy can be calculated from

$$D(p(r)\|q(r)) = \int_{-\infty}^{\infty} dr\, N_{\mu_1,\sigma_1}(r)\left[\log N_{\mu_1,\sigma_1}(r) - \log N_{\mu_2,\sigma_2}(r)\right] \tag{4.1.2}$$

where $N_{\mu,\sigma}(r)$ is the one-dimensional normal distribution, i.e.,

$$N_{\mu,\sigma}(r) = \frac{1}{\sigma\sqrt{2\pi}} e^{-\frac{(r-\mu)^2}{2\sigma^2}}. \tag{4.1.3}$$

Substituting (4.1.3) into the logarithms of (4.1.2) yields

$$D(p(r)\|q(r)) = \int_{-\infty}^{\infty} dr\, N_{\mu_1,\sigma_1}(r)\left[\left(\frac{r-\mu_2}{\sigma_2\sqrt{2}}\right)^2 - \left(\frac{r-\mu_1}{\sigma_1\sqrt{2}}\right)^2 - \log\frac{\sigma_1}{\sigma_2}\right]. \tag{4.1.4}$$

The first term in brackets can be manipulated to make use of the definition of variance such that (4.1.4) becomes

$$D(p(r)\|q(r)) = \int_{-\infty}^{\infty} dr\, N_{\mu_1,\sigma_1}(r)\left[\left(\frac{(r-\mu_1)+(\mu_1-\mu_2)}{\sigma_2\sqrt{2}}\right)^2 - \left(\frac{r-\mu_1}{\sigma_1\sqrt{2}}\right)^2 - \log\frac{\sigma_1}{\sigma_2}\right]. \tag{4.1.5}$$

Then a change of variable from *r* to *x*, such that $x = r - \mu_1$, produces

$$D(p(r)\|q(r)) = \int_{-\infty}^{\infty} dx\, N_{0,\sigma_1}(x)\left[\left(\frac{x+(\mu_1-\mu_2)}{\sigma_2\sqrt{2}}\right)^2 - \left(\frac{x}{\sigma_1\sqrt{2}}\right)^2 - \log\frac{\sigma_1}{\sigma_2}\right]. \tag{4.1.6}$$

The terms containing odd powers of *x* will integrate to zero leaving

$$D(p(r)\|q(r)) = \int_{-\infty}^{\infty} dx\, N_{0,\sigma_1}(x)\left[\left(\frac{x}{\sigma_2\sqrt{2}}\right)^2 + \left(\frac{\mu_1-\mu_2}{\sigma_2\sqrt{2}}\right)^2 - \left(\frac{x}{\sigma_1\sqrt{2}}\right)^2 - \log\frac{\sigma_1}{\sigma_2}\right]. \tag{4.1.7}$$

Isolating the *x* terms reveals

$$\begin{aligned} D(p(r)\|q(r)) = & \left(\frac{1}{2\sigma_2^2} - \frac{1}{2\sigma_1^2}\right)\int_{-\infty}^{\infty} x^2 N_{0,\sigma_1}(x)\,dx \\ & + \left[\left(\frac{\mu_1-\mu_2}{\sigma_2\sqrt{2}}\right)^2 - \log\frac{\sigma_1}{\sigma_2}\right]\int_{-\infty}^{\infty} N_{0,\sigma_1}(x)\,dx, \end{aligned} \tag{4.1.8}$$

which contains the definition of variance for a zero-centered and normally distributed random variable in the first integral. Therefore, both integrals in (4.1.8) can be evaluated, yielding

$$D(p(r)\|q(r)) = \frac{\sigma_1^2 - \sigma_2^2 + (\mu_1 - \mu_2)^2}{2\sigma_2^2} - \log\frac{\sigma_1}{\sigma_2}. \tag{4.1.9}$$

The Bhattacharyya coefficient (BC) is defined for two continuous PDFs, $p(r)$ and $q(\vec{r})$, as [58]

$$BC = \int \sqrt{p(r)q(r)}\,dr\,. \tag{4.1.10}$$

Because PDFs are normalized with a unity 1-norm, the BC can only have values between and including zero and one. The BC reaches its maximum value of one when the two PDFs are identical almost everywhere [58], and its minimum value of zero when the PDFs have no overlapping regions of positive probability. In this dissertation, the PDFs of concern are all Gaussian; therefore, an equation is derived for the BC of two Gaussian PDFs, $p(r)$ and $q(\vec{r})$, with means μ_1 and μ_2 and standard deviations σ_1 and σ_2, respectively. For two normally distributed random variables whose PDFs are described by (4.1.3), substituting the PDFs of the random variables into (4.1.10) yields the following equation for calculating the BC,

$$BC = \frac{1}{\sqrt{2\pi\sigma_1\sigma_2}} \int_{-\infty}^{\infty} \exp\left[-\frac{(r-\mu_1)^2}{4\sigma_1^2} - \frac{(r-\mu_2)^2}{4\sigma_2^2} \right] dr. \tag{4.1.11}$$

Where exp[] denotes the exponential function used for readability. Performing the squaring operations and organizing the terms according to powers of *r* produces

$$BC = \frac{1}{\sqrt{2\pi\sigma_1\sigma_2}} \int_{-\infty}^{\infty} \exp\left[-\frac{(\sigma_1^2+\sigma_2^2)r^2 - 2(\mu_1\sigma_2^2+\mu_2\sigma_1^2)r + \mu_1^2\sigma_2^2+\mu_2^2\sigma_1^2}{4\sigma_1^2\sigma_2^2} \right] dr. \tag{4.1.12}$$

Factoring out the coefficient of the r^2 term produces

$$BC = \frac{1}{\sqrt{2\pi\sigma_1\sigma_2}} \int_{-\infty}^{\infty} \exp\left\{ -\frac{\sigma_1^2+\sigma_2^2}{4\sigma_1^2\sigma_2^2} \left[r^2 - \frac{2(\mu_1\sigma_2^2+\mu_2\sigma_1^2)r}{(\sigma_1^2+\sigma_2^2)} \right] - \frac{\mu_1^2\sigma_2^2+\mu_2^2\sigma_1^2}{(\sigma_1^2+\sigma_2^2)} \right\} dr. \tag{4.1.13}$$

Completing the square for the bracketed terms yields

$$\begin{aligned} BC = & \frac{1}{\sqrt{2\pi\sigma_1\sigma_2}} \int_{-\infty}^{\infty} dr \\ & \times \exp\left\{ -\frac{\sigma_1^2+\sigma_2^2}{4\sigma_1^2\sigma_2^2} \left[r - \frac{(\mu_1\sigma_2^2+\mu_2\sigma_1^2)}{(\sigma_1^2+\sigma_2^2)} \right]^2 + \frac{(\mu_1\sigma_2^2+\mu_2\sigma_1^2)^2}{4\sigma_1^2\sigma_2^2(\sigma_1^2+\sigma_2^2)} - \frac{\mu_1^2\sigma_2^2+\mu_2^2\sigma_1^2}{(4\sigma_1^2\sigma_2^2)} \right\}. \end{aligned} \tag{4.1.14}$$

Pulling constant terms out of the integration shows that

$$BC = \frac{1}{\sqrt{2\pi\sigma_1\sigma_2}}\exp\left[\frac{\left(\mu_1\sigma_2^2+\mu_2\sigma_1^2\right)^2}{4\sigma_1^2\sigma_2^2\left(\sigma_1^2+\sigma_2^2\right)}-\frac{\mu_1^2\sigma_2^2+\mu_2^2\sigma_1^2}{\left(4\sigma_1^2\sigma_2^2\right)}\right] \times\int_{-\infty}^{\infty} dr\exp\left\{-\frac{\sigma_1^2+\sigma_2^2}{4\sigma_1^2\sigma_2^2}\left[r-\frac{\left(\mu_1\sigma_2^2+\mu_2\sigma_1^2\right)}{\left(\sigma_1^2+\sigma_2^2\right)}\right]^2\right\}. \tag{4.1.15}$$

The exponent of the first exponential function simplifies such that

$$\frac{\left(\mu_1\sigma_2^2+\mu_2\sigma_1^2\right)^2}{4\sigma_1^2\sigma_2^2\left(\sigma_1^2+\sigma_2^2\right)}-\frac{\mu_1^2\sigma_2^2+\mu_2^2\sigma_1^2}{\left(4\sigma_1^2\sigma_2^2\right)}=-\frac{\left(\mu_1-\mu_2\right)^2}{4\left(\sigma_1^2+\sigma_2^2\right)}. \tag{4.1.16}$$

Using (4.1.16), the substitution

$$s=\sqrt{\frac{\sigma_1^2+\sigma_2^2}{4\sigma_1^2\sigma_2^2}}\left(r-\frac{\mu_1\sigma_2^2+\mu_2\sigma_1^2}{\sigma_1^2+\sigma_2^2}\right), \tag{4.1.17}$$

and its derivative

$$ds=\sqrt{\frac{\sigma_1^2+\sigma_2^2}{4\sigma_1^2\sigma_2^2}}dr \tag{4.1.18}$$

simplifies the integral in (4.1.15) to

$$BC=\exp\left[-\frac{\left(\mu_1-\mu_2\right)^2}{4\left(\sigma_1^2+\sigma_2^2\right)}\right]\sqrt{\frac{2\sigma_1\sigma_2}{\sigma_1^2+\sigma_2^2}}\int_{-\infty}^{\infty}\frac{1}{\sqrt{\pi}}e^{-s^2}ds. \tag{4.1.19}$$

The PDF of a normally distributed random variable with zero mean and standard deviation of $\sqrt{2}/2$ is the integrand of (4.1.19); therefore, the integration over the entire domain evaluates to 1, and the BC evaluates to

$$BC=\sqrt{\frac{2\sigma_1\sigma_2}{\sigma_1^2+\sigma_2^2}}\exp\left[-\frac{\left(\mu_1-\mu_2\right)^2}{4\left(\sigma_1^2+\sigma_2^2\right)}\right]. \tag{4.1.20}$$

Both, the relative entropy and the BC, can be used to quantify how similar the PDF of a SBDC at a particular cycle is to the stationary PDF of the SBDC. Section 3.2 demonstrates that eigenmode SBDCs may be approximated as normally distributed random variables; therefore, the formulas derived earlier in this section for the relative entropy and BC may be applied to measure the similarity between a SBDC PDF at a particular cycle and its stationary PDF. The variables μ_1 and σ_1 represent the mean and

standard deviation, respectively, of a SBDC at a particular cycle, and the variables μ_2 and σ_2 represent the mean and standard deviation, respectively, of the stationary SBDC. To facilitate analysis, the relative entropy and BC will be examined using the relative variables μ_r and σ_r, where the relative mean μ_r is defined as μ_1/σ_2, and the relative standard deviation σ_r is defined to be σ_1/σ_2. In addition, this analysis will only apply to non-fundamental modes where the stationary mean μ_2 equals 0 with the assumption that the neutron transport scheme is unbiased. For the relative entropy, expressing (4.1.9) in terms of the relative parameters forms

$$D(p(r)\|q(r)) = \frac{\sigma_r^2 + \mu_r^2 - 1}{2} - \log \sigma_r. \tag{4.1.21}$$

The same transformation of variables for the BC in (4.1.20) produces

$$BC = \sqrt{\frac{2\sigma_r}{\sigma_r^2 + 1}} \exp\left[\frac{-\mu_r^2}{4\sigma_r^2 + 4}\right]. \tag{4.1.22}$$

From the contours of (4.1.21) and (4.1.22), one can observe the range of possibilities for the relative means and relative standard deviations of SBDCs that would have a particular relative entropy or BC value. Figure 4.1.1 displays some contour lines of the relative entropy calculated for relative means and relative standard deviations ranging between 0 and 5. Figure 4.1.2 displays contours of the BC for the same parameter ranges. Because (4.1.21) and (4.1.22) contain terms with the relative mean squared, Figures 4.1.1-4.1.2 could be displayed with reflections of the contours over the horizontal axis, but this is not displayed because it provides no additional insight.

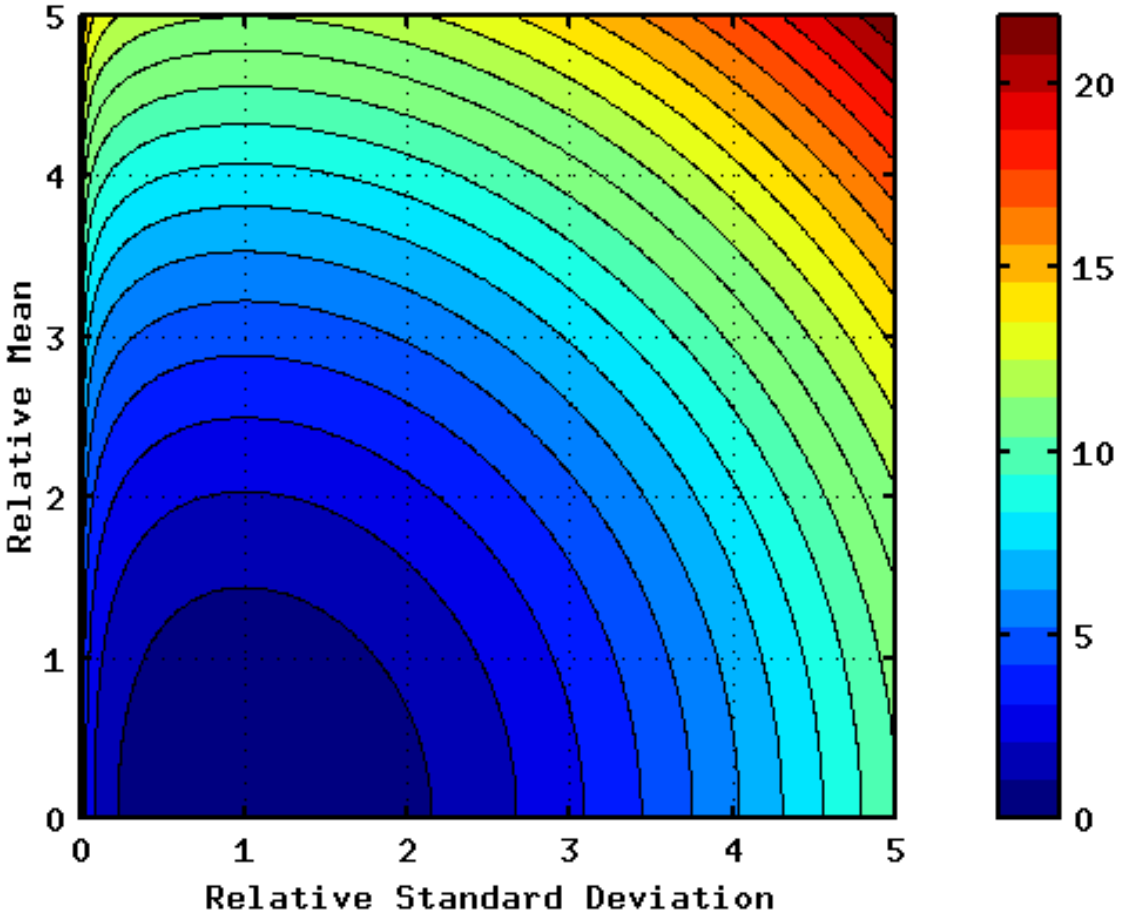

Figure 4.1.1 Contour lines of the relative entropy between a decomposition coefficient PDF and the stationary PDF of the coefficient.

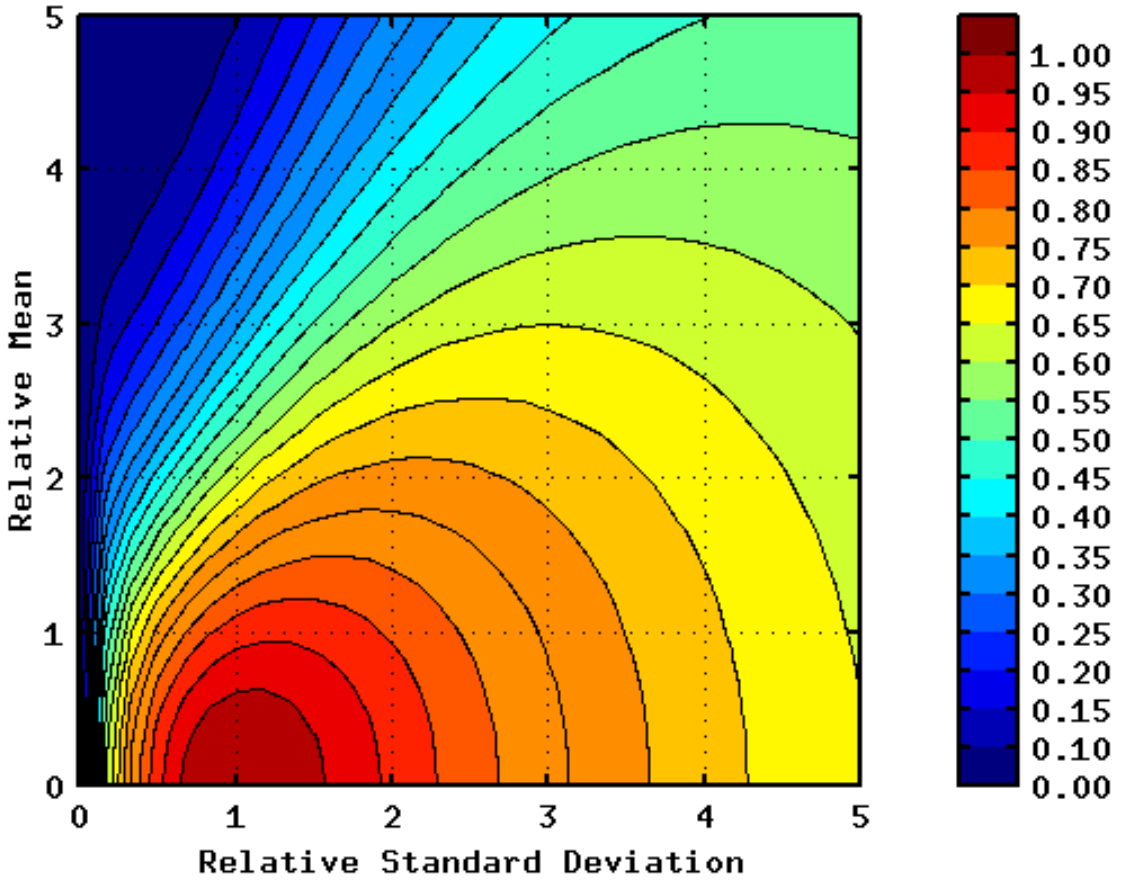

Figure 4.1.2 Contours of the BC calculated between a decomposition coefficient PDF and the stationary PDF of the coefficient.

The most noteworthy difference between the relative entropy and the BC contours is that when the relative standard deviation is 1, the BC can improve with an increase in only the relative standard deviation whereas the relative entropy always degrades if the relative standard deviation moves away from 1 for a fixed relative mean. Generally, increased uncertainty beyond the stationary level is undesirable; however, the BC rewards such an increase up to a point after which the BC degrades similar to the relative entropy. Because increasing the variance of a SBDC beyond the stationary variance without any improvement in the relative mean would not be beneficial; the BC is deemed less useful as a SBDC convergence metric than the relative entropy; thus, the BC will not be examined any further in this dissertation.

To apply the relative entropy measure as a diagnostic for convergence of a particular mode, one must select an appropriate condition on the measure, which in this case is a maximum value for the relative entropy because smaller values of the relative entropy indicate better agreement between the PDF at a particular cycle and the reference PDF than larger values of the relative entropy. Section 4.2 addresses making a choice for the maximum threshold of the modal relative entropy that indicates sufficient convergence.

4.2 Defining a Modal Convergence Diagnostic

With the relative entropy between a SBDC PDF and its stationary distribution as a measure of convergence, this section describes how to use that measure as a convergence diagnostic. To formulate a diagnostic, a maximum threshold value is derived for the modal relative entropy from a simple assumption about what level of bias is acceptable when attempting to estimate a parameter from a random variable. Implications of threshold selection are examined with an example that shows the effectiveness of two possible threshold choices. Utilizing the predictive equations for the mean and variance of SBDCs from Chapter 2 allows application of the modal relative entropy as a predictive convergence diagnostic, which can ultimately be used for turning on or off extrapolation or some other convergence acceleration technique for which the SBDC PDFs can be estimated.

In general, a user desires that the bias in obtained results is negligible when compared with the uncertainty of those results. In formulating this diagnostic, the expected values and variances of SBDCs and eigenvalues are assumed to be calculable. A discussion of how they are calculated appears elsewhere in this document. For a non-fundamental SBDC, one can quantify this desire by restricting the magnitude of the expected SBDC to be less than some multiple, *Z*, of the standard deviation of the SBDC, i.e.,

$$\left| E\left[v_n^{(m)} \right] \right| \le Z \sqrt{Var\left[v_n^{(m)} \right]} \tag{4.2.1}$$

where $v_n^{(m)}$ may be considered the SBDC of mode *n* at cycle *m* for any MC source iteration scheme, not specifically the extrapolated power method, which it denotes elsewhere in this document. In addition, when the results from *N* simulations or cycles

are combined, the bias in their mean will be considered negligible if it is less than the product of Z and the standard deviation of the mean, i.e.,

$$\left| E\left[\frac{1}{N} \sum_{i=0}^{N-1} v_n^{(m,i)} \right] \right| \le Z \sqrt{Var\left[\frac{1}{N} \sum_{i=0}^{N-1} v_n^{(m,i)} \right]}, \tag{4.2.2}$$

where $v_n^{(m,i)}$ is the SBDC of the i^{th} simulation or i^{th} tallied cycle. For independent simulations, the SBDCs are uncorrelated and identically distributed; therefore, (4.2.2) simplifies to

$$\left| E\left[v_n^{(m)} \right] \right| \le \frac{Z}{\sqrt{N}} \sqrt{Var\left[v_n^{(m)} \right]}. \tag{4.2.3}$$

This is a useful starting point for a modal convergence criterion; however, if a noise amplifying acceleration technique like extrapolation is in use, the variance may be unnecessarily large. To account for modifications to the uncertainty, the stationary variance may be used; thus, the convergence criterion becomes

$$\left| E\left[v_n^{(m)} \right] \right| \le \frac{Z}{\sqrt{N}} \sqrt{\lim_{m \to \infty} Var\left[u_n^{(m)} \right]} \tag{4.2.4}$$

where $u_n^{(m)}$ is the SBDC of mode n at cycle m for all m greater than some cycle M where the acceleration technique is switched off, which is the SBDC from standard power method in this dissertation. However, for the limit in (4.2.4) to be an acceptable bound, the variance of the SBDC at cycle M must be greater than or equal to the stationary variance; otherwise, (4.2.3) may not be satisfied. This will be shown to be satisfied by a condition on the modal relative entropy.

For multiple tallied cycles from a single simulation, the expected value of the summation in (4.2.2) is

$$\begin{aligned} \left| E\left[\frac{1}{N} \sum_{i=0}^{N-1} v_n^{(m,i)} \right] \right| &= \frac{1}{N} \left| E\left[v_n^{(m)} + v_n^{(m+1)} + \ldots + v_n^{(m+N-1)} \right] \right| \\ &= \frac{1}{N} \left| E\left[v_n^{(m)} \right] + E\left[v_n^{(m+1)} \right] + \ldots + E\left[v_n^{(m+N-1)} \right] \right|. \end{aligned} \tag{4.2.5}$$

With the assumption that the standard power method would be used for any actively tallied cycles, the expected SBDCs of later cycles can be expressed as multiples of the first tallied cycle using the adjusted constant multiplier approximation in (2.2.24), which

transforms (4.2.5) to

$$\left|E\left[\frac{1}{N}\sum_{i=0}^{N-1} v_n^{(m,i)}\right]\right| \quad = \quad \frac{1}{N}\left|E\left[v_n^{(m)}\right]+E\left[v_n^{(m)}\right]\eta_n+\ldots+E\left[v_n^{(m)}\right]\eta_n^{N-1}\right|. \tag{4.2.6}$$

Equation (4.2.6) contains a geometric series with common ratio $\eta_n=\lambda_n/\lambda_1$; therefore, the expectation evaluates to

$$\left|E\left[\frac{1}{N}\sum_{i=0}^{N-1} v_n^{(m,i)}\right]\right|=\frac{1}{N}\left|E\left[v_n^{(m)}\right]\right|\left|\frac{1-\eta_n^N}{1-\eta_n}\right| \quad \forall\, n>1. \tag{4.2.7}$$

Continuing with multiple tallied cycles from a single simulation, the variance of the summation in (4.2.2) is

$$Var\left[\frac{1}{N}\sum_{i=0}^{N-1} v_n^{(m,i)}\right]=\frac{1}{N^2}\sum_{i=0}^{N-1}\sum_{j=0}^{N-1} Cov\left[v_n^{(m+i)}, v_n^{(m+j)}\right] \tag{4.2.8}$$

Where *Cov[x,y]* indicates the covariance of *x* and *y*. Considering the evidence in Section 3.3.2, the sum of off-diagonal covariances shall be assumed positive for the standard power method, which is assumed to be used for tallied cycles. As a result of this assumption, the variance of the sum has a lower bound that is the sum of the variances, i.e.,

$$Var\left[\frac{1}{N}\sum_{i=0}^{N-1} v_n^{(m,i)}\right]\geq\frac{1}{N^2}\sum_{i=0}^{N-1} Var\left[v_n^{(m+i)}\right]. \tag{4.2.9}$$

For ease of computation, the more restrictive condition on the right-hand side of (4.2.9) was required; therefore, the bias criteria in (4.2.2) becomes

$$\left|E\left[v_n^{(m)}\right]\right|\left|\frac{1-\eta_n^N}{1-\eta_n}\right|\leq Z\sqrt{\sum_{i=0}^{N-1} Var\left[v_n^{(m+i)}\right]} \quad \forall\, n>1. \tag{4.2.10}$$

Rather than conditioning convergence on the possibly elevated noise level from an acceleration technique, such as extrapolation, the stationary variance of the SBDC from the standard power method was used for the criterion, which similar to (4.2.4), yields

$$\left|E\left[v_n^{(m)}\right]\right|\left|\frac{1-\eta_n^N}{1-\eta_n}\right|\leq Z\sqrt{N\lim_{i\to\infty} Var\left[u_n^{(m+i)}\right]} \quad \forall\, n>1. \tag{4.2.11}$$

The relationship in (4.2.11) demonstrates the expected result that in the limit of infinitely many tallied cycles, the magnitude of the SBDC for the first tallied cycle is insignificant and may tend toward infinity without affecting the tallied summation of SBDCs. Since

the decay coefficient for the power method is greater than or equal to zero and less than one, then the multiplicative factor on the left-hand side of (4.2.11) follows the relation,

$$\frac{1}{\sqrt{N+1}}\left|\frac{1-\eta_n^{N+1}}{1-\eta_n}\right| < \frac{1}{\sqrt{N}}\left|\frac{1-\eta_n^{N}}{1-\eta_n}\right| < 1 \quad \forall\, n > 1, \tag{4.2.12}$$

which ensures that if (4.2.11) holds for some value of $N \geq 1$, then

$$\left|E\left[v_n^{(m)}\right]\right|\left|\frac{1-\eta_n^{N+1}}{1-\eta_n}\right| \leq Z\sqrt{(N+1)\lim_{i\to\infty} Var\left[u_n^{(m+i)}\right]} \quad \forall\, n > 1. \tag{4.2.13}$$

Therefore, if an expected value of a SBDC PDF is sufficiently converged after *m* transport cycles when using *N* active cycles, then adding more active cycles to a calculation necessitates no additional discarded cycles because (4.2.12) may be applied recursively to show that the convergence condition holds for any number of tallied cycles greater than *N*. This is in direct contrast with the condition for combining independent simulations in (4.2.4), which requires that the bias in the SBDC of the first tallied cycle must decrease when the number of simulations increases. Dividing both sides of (4.2.11) by the terms containing η_n yields the following sufficient convergence condition for the expected value of a SBDC PDF,

$$\left|E\left[v_n^{(m)}\right]\right| \leq Z\left|\frac{1-\eta_n}{1-\eta_n^{N}}\right|\sqrt{N\lim_{i\to\infty} Var\left[u_n^{(m+i)}\right]} \quad \forall\, n > 1. \tag{4.2.14}$$

Determining an adequate number of actively tallied cycles is outside the scope of this dissertation; therefore, the simpler and more conservative condition if Z does not change is to diagnose convergence based on only a single tallied cycle, which will be used in the examples to follow, i.e.,

$$\left|E\left[v_n^{(m)}\right]\right| \leq Z\sqrt{\lim_{i\to\infty} Var\left[u_n^{(m+i)}\right]} \quad \forall\, n > 1. \tag{4.2.15}$$

Thus, the convergence condition on the SBDC mean for multiple independent simulations in (4.2.4) and the convergence condition on the SBDC mean for multiple cycles from a single simulation in (4.2.15) are identical if *N* is used only to represent the number of independent simulations, which is the convention for the remainder of this document.

For the sufficient convergence condition in (4.2.4) to satisfy the desired condition in

(4.2.2), the variances of the SBDCs must be reasonably close to their stationary variances. Otherwise, the bias may satisfy the criterion of (4.2.4) but not the desired condition of (4.2.2). As an example, if one were to start tallying after a single discarded cycle when using a well-converged source from a prior simulation with the same number of histories, the standard deviation of the SBDC after one cycle would be approximately 1/7 of the stationary standard deviation for an eigenvalue ratio of 0.99 from (2.5.19),

$$\lim_{m\to\infty} Var\left[\tilde{u}_n^{(m)}\right]=\sigma_n^2\frac{1}{1-\left(\lambda_n/\lambda_1\right)^2} \quad \forall\, n>1. \tag{4.2.16}$$

From the normal cumulative distribution function, the mean would be less than the stationary standard deviation but greater than the standard deviation of the current cycle for 57.4% of initial sources sampled from the stationary cycles of the prior simulation. If (4.2.4) were used as a criterion without sufficiently converged variance, then an unacceptable amount of bias on tallies could result from the choice for the initial source.

Setting an upper bound for the modal relative entropy as an indicator of convergence enforces a condition on the variance in addition to the mean. The maximum modal entropy threshold was determined using the condition on the expected values of SBDCs in (4.2.4). In the notation of modal relative entropy from Section 4.1,

$$\mu_1=E\left[v_n^{(m)}\right], \tag{4.2.17}$$

$$\sigma_1=\sqrt{Var\left[v_n^{(m)}\right]}, \tag{4.2.18}$$

and

$$\sigma_2=\sqrt{\lim_{m\to\infty} Var\left[u_n^{(m)}\right]}=\frac{\sigma_n}{\sqrt{1-\left(\lambda_n/\lambda_1\right)^2}}\,. \tag{4.2.19}$$

Therefore, the sufficient convergence condition on the expected value of SBDCs in (4.2.4) may be expressed as

$$|\mu_r|\le Z/\sqrt{N}\,. \tag{4.2.20}$$

The modal relative entropy has an associated maximum threshold value where this convergence condition on the relative mean is always satisfied. The maximum modal relative entropy threshold for a condition on the relative mean can be found by examining the partial derivatives of (4.1.21) to find a local maximum. The first and second partial

derivatives of (4.1.21) with respect to the relative standard deviation,

$$\frac{\partial}{\partial \sigma_r} D(p(r)\|q(r)) = \sigma_r - \frac{1}{\sigma_r} \forall \sigma_r > 0 \tag{4.2.21}$$

and

$$\frac{\partial^2}{\partial \sigma_r^2} D(p(r)\|q(r)) = 1 + \frac{1}{\sigma_r^2} \forall \sigma_r > 0, \tag{4.2.22}$$

reveal that for a particular relative mean, the modal relative entropy is minimized when $\sigma_r = 1$ because the first derivative, (4.2.21), is zero, and the second derivative, (4.2.22), is always positive. Therefore, the greatest modal relative entropy that always satisfies the relative mean convergence criterion in (4.2.20), which shall be referred to as D_{max}, is

$$D_{max} = \frac{Z^2}{2N} \tag{4.2.23}$$

as calculated from (4.1.21) with $\sigma_r = 1$ and $\mu_r = Z/\sqrt{N}$.

Secondly, the extremes of the converged relative standard deviation for a modal relative entropy threshold of D_{max} are found by setting $\mu_r = 0$ in (4.1.21) yielding

$$\begin{aligned} D_{max} &= \frac{\sigma_r^2 + \mu_r^2 - 1}{2} - \log \sigma_r \Big|_{\mu_r = 0} \\ D_{max} &= \frac{\sigma_r^2 - 1}{2} - \log \sigma_r, \end{aligned} \tag{4.2.24}$$

which can be solved for σ_r numerically by the Newton-Raphson method for example. For all positive values of D_{max}, (4.2.24) has two positive roots. The symbols σ_{min} and σ_{max} shall refer to the lesser and greater of the two roots of (4.2.24), respectively. As an example, for a maximum relative mean of 0.1, the bounds on the relative standard deviation for a sufficiently converged SBDC are [0.93175, 1.07325]. Thus when using modal relative entropy to diagnose convergence, the SBDC PDFs must be close to the stationary distribution in both mean and variance.

The choice for *Z* depends on the error tolerance of a user. For this dissertation, convergence was investigated with two reasonable choices for *Z*, and those are 0.1 and $\sqrt{2/\pi}$. The first option, $Z = 0.1$, is equivalent to stating that the bias in a random

variable should be an order of magnitude less than the standard deviation of that variable. The second option, $Z=\sqrt{2/\pi}$, arises from conditioning convergence on the expected value of a SBDC being less than the stationary expected absolute value of the SBDC from (2.5.30), which is

$$E\left[v_n^{(m)}\right] \le \lim_{m\to\infty} E\left[\left|u_n^{(m)}\right|\right] = \sqrt{\lim_{m\to\infty} Var\left[u_n^{(m)}\right]}\sqrt{\frac{2}{\pi}}. \tag{4.2.25}$$

As a demonstration, applying the condition on the modal relative entropy in (4.2.23) for 1000 repetitions of a single simulation yielded the expected number of discarded cycles in Table 4.2.1 for the uniform slab in Appendix A with 4.0E5 histories starting from a far-from-converged source using 256 bins and an extrapolation parameter of 0.98 applied for 500 cycles.

Transport Scheme	$D_{max}=1/\pi$	$D_{max}=0.005$
	Discard Cycles	**Discard Cycles**
Standard	410	660
Coarse Extrapolation	215	572
Fine Extrapolation	214	572

Table 4.2.1: Minimum number of discarded cycles for different modal relative entropy convergence criteria applied to the second mode of the uniform slab in Appendix A.

As can be seen in Table 4.2.1, the more restrictive modal entropy condition of $D_{max}=0.005$ suggests far more discarded cycles than $D_{max}=1/\pi$ for the extrapolated transport schemes. This notable increase occurs because the sufficient convergence level of $D_{max}=0.005$ does not include the stationary relative standard deviation with extrapolation enabled while $D_{max}=1/\pi$ does, which Figure 4.2.1 shows. The flat region of the modal relative entropy in Figure 4.2.1 between approximately cycles 300 and 500, indicates that too many cycles were extrapolated. This observed behavior is not necessarily characteristic of all modes. For example, mode 31 of the uniform slab converges slower under extrapolation than the standard power method as Figure 4.2.2 shows. Additionally, under fine-mesh extrapolation, mode 31 is not sufficiently converged until after extrapolation ceases for both modal relative entropy threshold

choices.

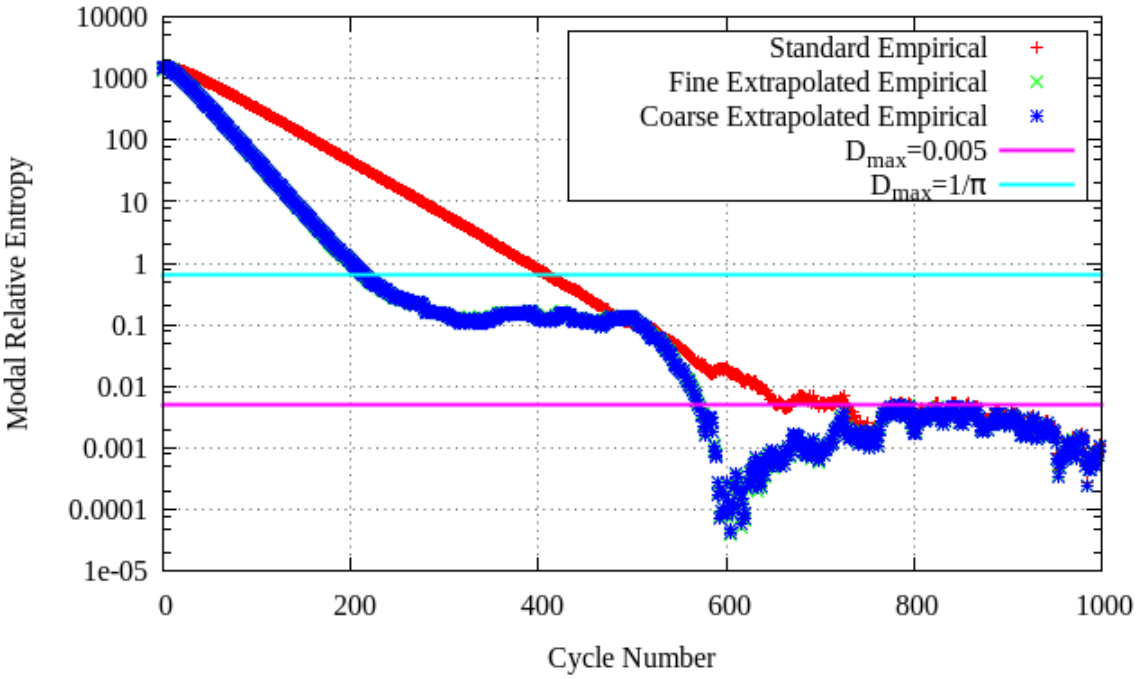

Figure 4.2.1 Modal relative entropy of second mode for the uniform slab problem with 4E5 histories per cycle.

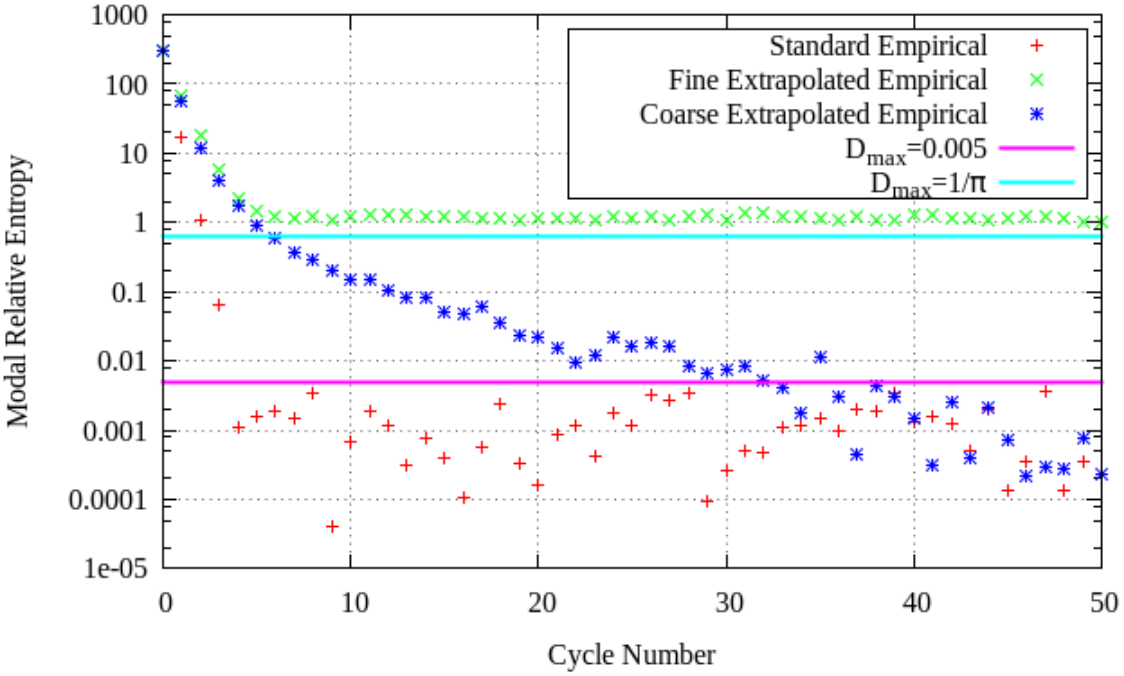

Figure 4.2.2 Modal relative entropy of mode 31 for the uniform slab problem with 4E5 histories per cycle.

Use of the equations for the mean and variance from the adjusted constant multiplier approximation from Chapter 2 can predict most of the observed behaviors. To better explain the observed behaviors in the modal relative entropy diagnostic, the modal relative entropy definition from (4.1.21) can be split into two components D_μ and D_σ where D_μ is the component of the modal entropy related to the relative mean, such that

$$D_\mu = \frac{\mu_r^2}{2}, \tag{4.2.26}$$

And D_σ is the component of the modal entropy related to the spread of the SBDC PDF, the relative standard deviation, which is defined as

$$D_\sigma = \frac{\sigma_r^2 - 1}{2} - \log \sigma_r. \tag{4.2.27}$$

The modal entropies are related by

$$D\left(p(r)\|q(r)\right) = D_\mu + D_\sigma. \tag{4.2.28}$$

In the limit of infinitely many standard power method cycles, both modal entropy components approach zero. Figure 4.2.3 displays these modal relative entropy components for the fine-mesh extrapolated simulations and the standard power method simulations of the diffuse uniform slab. From Figure 4.2.3, one can see that the relative mean dictated the modal entropy of the standard power method because the D_σ component was roughly a factor of 1E3 smaller than D_μ or less for each cycle. For the extrapolated simulations, D_μ dominated the convergence behavior until approximately cycle 245 where D_σ became greater than D_μ and stayed that way throughout the 1000 simulated cycles. The variance component D_σ plateaued in the vicinity of cycle 100 and stayed at that level throughout the remaining 400 extrapolated cycles, then proceeded to fall at a rate faster than the relative mean under the standard power method. That faster decay of D_σ versus D_μ is the reason that the number of discarded cycles for the $D_{max} = 0.005$ threshold was fewer with extrapolation than the standard power method despite extrapolation being executed for too many cycles. The empirical data deviates from the constant normalization theory at the lower modal entropy value because the data was collected from a finite sample size of 1000 simulations for each iterative scheme. The statistical uncertainty in calculating the mean and variance from a finite sample

ensures that the empirical data must diverge from the theory at some point when the entropy components should approach zero in theory. The theory breaks down for mode 31 under coarse-mesh extrapolation because the mode is not well-represented by the extrapolation grid, which gives rise to an inconsistent impact from extrapolation. This divergence is evident in Figure 4.2.2 because the modal relative entropy of the coarse-mesh extrapolation scheme transitioned from the path of the empirical modal entropy from the fine-mesh extrapolation scheme to the stationary empirical modal entropy of the standard power method scheme during extrapolated cycles. Therefore, the adjusted constant multiplier approximation may be combined with the modal entropy diagnostic, which includes a chosen threshold, to predict a minimum number of cycles that should be discarded to sufficiently converge the source distribution with respect to a particular mode if that mode is adequately represented by the applied mesh. To construct the adjusted constant multiplier approximation equations for the mean and variance, the user must have knowledge of or reasonable approximations for all of the following variables: β_n, Y/β_1, α, λ_n/λ_1, σ_n, and the number of extrapolated cycles. Assuming that the user has some knowledge of at least the largest eigenvalue ratio and that an estimate for σ_n can be obtained from the method in Section 3.4, the user must determine or estimate the parameters relating to the initial SBDCs, β_n and Y/β_1, which the next section addresses.

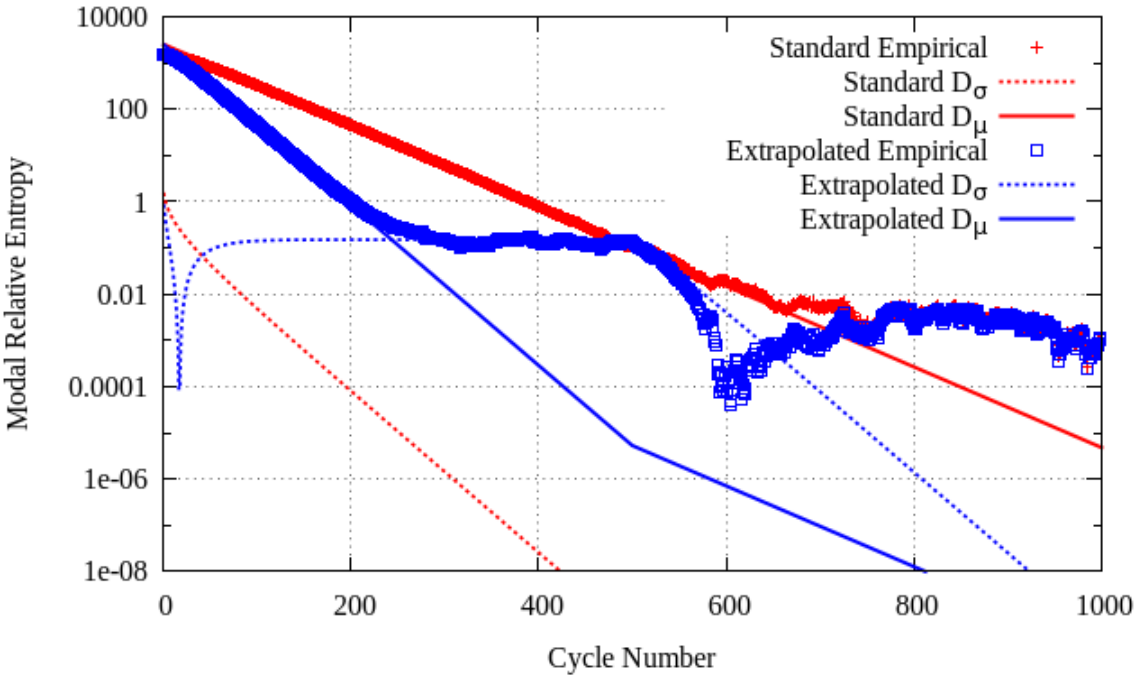

Figure 4.2.3 Modal relative entropy components of second mode for the uniform slab problem with 4E5 histories per cycle.

4.3 Selecting the Extrapolation Cutoff Cycle

Finding an optimum number of extrapolated cycles to converge a particular mode requires that one have a measure of convergence over which the accelerated algorithm can be optimized and a termination condition. The modal relative entropy in Section 4.2 provides such a measure of convergence for the PDF of a SBDC and a sufficient convergence condition for that PDF. Using the adjusted multiplier equations from Section 2.3, which describe the evolution of the PDF of an extrapolated SBDC, the number of discarded cycles that are needed to sufficiently converge a SBDC PDF under the modal entropy diagnostic can be estimated. The technique also works for determining the number of cycles that should be discarded for standard power method schemes. This section contains the details of a numerical iteration to determine how many cycles should be extrapolated and discarded for a particular extrapolation parameter, such that the total number of cycles that should be discarded to sufficiently converge a single mode is minimized. Using this numerical iteration, the affects of variations in relevant variables on the efficacy of extrapolation are examined.

The primary reason for applying extrapolation is to hasten convergence by reducing the magnitude of decay coefficients of non-fundamental modes, which appear in (1.3.10) as

$$\eta_n = (1+\alpha)\frac{\lambda_n}{\lambda_1} - \alpha \quad \forall n \geq 1 \,. \tag{4.3.1}$$

However, the extrapolation induces higher stationary variances in the SBDCs as discussed in Section 2.5. As a result of the increased stationary variance, the extrapolation should be turned off at a particular cycle, $m_{n,cut}$, which may differ for each mode; the subscript *n* indicates mode number. To satisfy the modal entropy convergence criterion of Section 4.2, more discarded cycles beyond $m_{n,cut}$ may be required to sufficiently converge the mode; the total number of discarded cycles shall be denoted by $m_{n,discard}$. For compactness of display in equations, the subscript *n*, which indicates the mode number, is dropped, and the descriptors shortened to one letter, e.g., $m_{n,cut} \equiv m_c$; however, in sentences, the full variable names will always be displayed. For the purpose

of this predictive analysis, extrapolation is assumed to have been used for enough cycles such that the adjusted constant multiplier approximation from Section 2.3 applies at or before the cutoff cycle. Thus, at the cutoff cycle, the expected values of extrapolated SBDCs from (2.3.17) are

$$E\left[\widetilde{\nu}_n^{(m_c)}\right]=\beta_n\frac{Y}{\beta_1}\eta_n^{m_c}, \tag{4.3.2}$$

and the variances of extrapolated SBDCs from (2.5.22) are

$$Var\left[\widetilde{\nu}_n^{(m_c)}\right]=\frac{1-\eta_n^{2m_c}}{1-\eta_n^2}(1+\alpha)^2\sigma_n^2 \quad \forall |\eta_n|\neq 1. \tag{4.3.3}$$

After turning off extrapolation, the SBDC diminishes by the decay coefficient of the standard power method λ_n/λ_1, and noise is introduced in subsequent cycles without amplification as in (2.2.9),

$$\widetilde{\nu}_n^{(m+1)}=\frac{\lambda_n}{\lambda_1}\widetilde{\nu}_n^{(m)}+\xi_n^{(m+1)} \forall\, m>m_c, \tag{4.3.4}$$

such that the SBDCs of the extrapolated algorithm after the cutoff cycle are described by their expected values,

$$E\left[\widetilde{\nu}_n^{(m)}\right]=\beta_n\frac{Y}{\beta_1}\eta_n^{m_c}\left(\frac{\lambda_n}{\lambda_1}\right)^{m-m_c} \forall\, m>m_c, \tag{4.3.5}$$

and variances,

$$Var\left[\widetilde{\nu}_n^{(m)}\right]=(1+\alpha)^2\frac{1-\eta_n^{2m_c}}{1-\eta_n^2}\sigma_n^2\left(\frac{\lambda_n}{\lambda_1}\right)^{2(m-m_c)}+\frac{1-(\lambda_n/\lambda_1)^{2(m-m_c)}}{1-(\lambda_n/\lambda_1)^2}\sigma_n^2 \quad \forall\, m>m_c, |\eta_n|\neq 1. \tag{4.3.6}$$

The variance in (4.3.6) and the mean in (4.3.5) fully describe the PDFs of extrapolated non-fundamental mode SBDCs because they are normally distributed when using a sufficient number of histories per cycle. In running simulations, these PDF-defining equations may be better approximated in cycles that are far from converged by including actual normalization factors as Section 2.5 describes.

With an estimate for the PDF of a non-fundamental SBDC, the modal relative entropy can be evaluated to find an optimal value of $m_{n,cut}$ that minimizes $m_{n,discard}$. A simple search algorithm was used to find the optimal value of $m_{n,cut}$ that started with $m_{n,cut}=0$, and thus, $m_{n,discard}$ started with the number of discard cycles associated with the standard

power method. Then the algorithm repeatedly incremented $m_{n,cut}$ by 1 and calculated the modal relative entropy. If the increase in $m_{n,cut}$ reduced the modal relative entropy, then the lowest possible value of $m_{n,discard}$ that kept the modal relative entropy under D_{max} was found and the search continued; otherwise, the search terminated. After termination, the selected value of $m_{n,cut}$ was the smallest value of $m_{n,cut}$ that minimized $m_{n,discard}$. This choice avoids any computational expense of extrapolation that does not result in a reduction of the number of discarded cycles. Also, a MC code may be implemented in such a way that a user can adjust the number of discarded cycles after running a simulation [1]; therefore, this choice avoids unnecessary extrapolated cycles that would likely not be used for tallies because of the potential bias in the source distribution from extrapolation as explained in Section 2.4.

For any selected number of extrapolated cycles, the number of discard cycles was calculated by first calculating the modal relative entropy at the cutoff cycle. If the modal entropy after $m_{n,cut}$ cycles was less than or equal to D_{max}, then $m_{n,discard}=m_{n,cut}$; otherwise, the number of discard cycles was calculated by finding the larger of the minimum number of cycles needed to converge the relative mean and the minimum number of cycles needed to converge the relative standard deviation; then if necessary, additional discard cycles were added until the modal entropy condition was satisfied. Using the relative mean condition in (4.2.20), the number of discard cycles for a non-fundamental mode must satisfy

$$\frac{\left|E\left[\tilde{\nu}_n^{(m_d)}\right]\right|}{\lim\limits_{m\to\infty}\sqrt{Var\left[\tilde{u}^{(m)}\right]}}=\frac{\left|\beta_n\right|\frac{Y}{\beta_1}\eta_n^{m_c}\left(\frac{\lambda_n}{\lambda_1}\right)^{m_d-m_c}}{\sigma_n\left[1-\left(\lambda_n/\lambda_1\right)^2\right]^{-1/2}}\le\frac{Z}{\sqrt{N}}\quad\forall\frac{\lambda_n}{\lambda_1}\neq 1$$

$$\left(m_d-m_c\right)\log\frac{\lambda_n}{\lambda_1}\le\log\left\{\frac{Z\sigma_n\left[1-\left(\lambda_n/\lambda_1\right)^2\right]^{-1/2}}{\sqrt{N}\left|\beta_n\right|\frac{Y}{\beta_1}\eta_n^{m_c}}\right\}\quad\forall\,\eta_n\neq 0,\frac{\lambda_n}{\lambda_1}\neq 0\text{ or }1 \tag{4.3.7}$$

$$m_d-m_c\ge\frac{1}{\log\frac{\lambda_n}{\lambda_1}}\log\left\{\frac{Z\sigma_n\left[1-\left(\lambda_n/\lambda_1\right)^2\right]^{-1/2}}{\sqrt{N}\left|\beta_n\right|\frac{Y}{\beta_1}\eta_n^{m_c}}\right\}\quad\forall\,\eta_n\neq 0,\frac{\lambda_n}{\lambda_1}\neq 0\text{ or }1$$

Considering the practical limitations that $m_{n,discard}$ is an integer and must be greater than or equal to $m_{n,cut}$, the condition in (4.3.7) refines to

$$m_d \geq m_c + \max\left[0, \text{ceil}\left(\frac{1}{\log\frac{\lambda_n}{\lambda_1}}\log\left\{\frac{Z\sigma_n\left[1-\left(\lambda_n/\lambda_1\right)^2\right]^{-1/2}}{\sqrt{N}\left|\beta_n\right|\frac{Y}{\beta_1}\eta_n^{m_c}}\right\}\right)\right] \quad \forall\, \eta_n \neq 0, \frac{\lambda_n}{\lambda_1} \neq 0 \text{ or } 1 \tag{4.3.8}$$

Where ceil[] is the ceiling function, which rounds rational numbers up to the nearest most positive integer, and max[] is a function that returns the most positive argument. For the special case of $\eta_n = 0$ with $m_{n,cut} \geq 1$, the minimum number of discards to satisfy the relative mean condition is equal to $m_{n,cut}$, and for the other special case of $\lambda_n = 0$ and $\eta_n \neq 0$, $m_{n,discard} = m_{n,cut} + 1$ if the relative entropy at cycle $m_{n,cut}$ is greater than D_{max} according to the first step in the procedure.

Additionally, the number of cycles needed to sufficiently converge the relative standard deviation depends on how the relative standard deviation at the cutoff cycle relates to σ_{min} and σ_{max}, the roots of (4.2.24). If the relative standard deviation is between σ_{min} and σ_{max}, then the minimum number of discard cycles is greater than or equal to $m_{n,cut}$. However, if the relative standard deviation at the cutoff cycle is less than σ_{min}, then the variance from (4.3.6) is sufficiently converged after $m_{n,discard}$ cycles when

$$\begin{aligned}
\sigma_{min}^2\sigma_\infty^2 &\leq Var\left[\tilde{v}_n^{(m_d)}\right] \quad \forall\, m_d > m_c, |\eta_n| \neq 1, \lambda_n \neq \lambda_1 \\
\sigma_{min}^2\sigma_\infty^2 &\leq Var\left[\tilde{v}_n^{(m_c)}\right]\left(\frac{\lambda_n}{\lambda_1}\right)^{2(m_d-m_c)} + \left[1-\left(\frac{\lambda_n}{\lambda_1}\right)^{2(m_d-m_c)}\right]\sigma_\infty^2 \\
\left(\sigma_{min}^2-1\right)\sigma_\infty^2 &\leq \left\{Var\left[\tilde{v}_n^{(m_c)}\right]-\sigma_\infty^2\right\}\left(\frac{\lambda_n}{\lambda_1}\right)^{2(m_d-m_c)}
\end{aligned} \tag{4.3.9}$$

where the definition of the stationary standard deviation σ_∞ from (2.5.19) is

$$\sigma_\infty^2 = \lim_{m\to\infty} Var\left[\tilde{u}_n^{(m)}\right] = \frac{\sigma_n^2}{1-\left(\lambda_n/\lambda_1\right)^2}. \tag{4.3.10}$$

Since the relative standard deviation at the cutoff cycle is less than σ_{min} for the condition in (4.3.9), the variance at the cutoff cycle is less than the stationary variance, which necessitates a reversal of the conditional relationship in (4.3.9) when dividing by their

difference, i.e.,

$$\frac{\left(\sigma_{min}^2-1\right)\sigma_\infty^2}{\left\{Var\left[\widetilde{v}_n^{(m_c)}\right]-\sigma_\infty^2\right\}}\geq\left(\frac{\lambda_n}{\lambda_1}\right)^{2(m_d-m_c)}. \tag{4.3.11}$$

For the special case of $\lambda_n=0$, (4.3.11) yields $m_{n,discard}\geq m_{n,cut}+1$; otherwise, taking the logarithm of both sides of (4.3.11) and observing that the square of the eigenvalue ratio is a positive number less than one yields

$$\frac{\log\left\{\frac{\left(\sigma_{min}^2-1\right)\sigma_\infty^2}{\left\{Var\left[\widetilde{v}_n^{(m_c)}\right]-\sigma_\infty^2\right\}}\right\}}{2\log\left|\lambda_n/\lambda_1\right|}+m_c\leq m_d. \tag{4.3.12}$$

Since only an integer number of cycles may be discarded, the ceiling function corrects (4.3.12) to

$$\text{ceil}\left[\frac{\log\left\{\frac{\left(\sigma_{min}^2-1\right)\sigma_\infty^2}{\left\{Var\left[\widetilde{v}_n^{(m_c)}\right]-\sigma_\infty^2\right\}}\right\}}{2\log\left|\lambda_n/\lambda_1\right|}\right]+m_c\leq m_d. \tag{4.3.13}$$

Conversely, if the relative standard deviation at the cutoff cycle is greater than σ_{max}, then the variance from (4.3.6) is sufficiently converged after $m_{n,discard}$ cycles when

$$\begin{aligned}
\sigma_{max}^2\sigma_\infty^2 &\geq Var\left[\widetilde{v}_n^{(m_d)}\right] \quad \forall\, m_d>m_c, |\eta_n|\neq 1, \lambda_n\neq\lambda_1 \\
\sigma_{max}^2\sigma_\infty^2 &\geq Var\left[\widetilde{v}_n^{(m_c)}\right]\left(\frac{\lambda_n}{\lambda_1}\right)^{2(m_d-m_c)}+\left[1-\left(\frac{\lambda_n}{\lambda_1}\right)^{2(m_d-m_c)}\right]\sigma_\infty^2 \\
\left(\sigma_{max}^2-1\right)\sigma_\infty^2 &\geq\left\{Var\left[\widetilde{v}_n^{(m_c)}\right]-\sigma_\infty^2\right\}\left(\frac{\lambda_n}{\lambda_1}\right)^{2(m_d-m_c)}.
\end{aligned} \tag{4.3.14}$$

Since the relative standard deviation at the cutoff cycle is greater than σ_{max} for the condition in (4.3.14), the variance at the cutoff cycle is greater than the stationary variance, which does not necessitate a reversal of the conditional relationship in (4.3.14) when dividing by their difference, i.e.,

$$\frac{\left(\sigma_{max}^2-1\right)\sigma_\infty^2}{\left\{Var\left[\widetilde{v}_n^{(m_c)}\right]-\sigma_\infty^2\right\}}\geq\left(\frac{\lambda_n}{\lambda_1}\right)^{2(m_d-m_c)}, \tag{4.3.15}$$

which is in contrast with the sign change in (4.3.11). For the special case of $\lambda_n=0$, (4.3.15) yields $m_{n,discard}\geq m_{n,cut}+1$; otherwise, taking the logarithm of both sides of

(4.3.15) and observing that the square of the eigenvalue ratio is a positive number less than one yields

$$\frac{\log\left\{\frac{\left(\sigma_{max}^2-1\right)\sigma_\infty^2}{Var\left[\widetilde{v}_n^{(m_c)}\right]-\sigma_\infty^2}\right\}}{2\log\left|\lambda_n/\lambda_1\right|}+m_c\le m_d. \tag{4.3.16}$$

Since only an integer number of cycles may be discarded, the ceiling function corrects (4.3.16) to

$$\text{ceil}\left[\frac{\log\left\{\frac{\left(\sigma_{max}^2-1\right)\sigma_\infty^2}{Var\left[\widetilde{v}_n^{(m_c)}\right]-\sigma_\infty^2}\right\}}{2\log\left|\lambda_n/\lambda_1\right|}\right]+m_c\le m_d. \tag{4.3.17}$$

The equations (4.3.13) and (4.3.17) for the minimum number of discarded cycles needed to sufficiently converge the relative standard deviation of a SBDC PDF are identical in form with the only difference being the bounding relative variance term. Solving (4.3.8) and (4.3.13) or (4.3.17), as appropriate, and using the larger of the two values for $m_{n,discard}$ yields the minimum number of cycles that are required to enter a rectangular region of a plot similar to Figure 4.1.1 that tightly bounds the modal entropy convergence region associated with D_{max}, which is semi-circular in shape. Therefore, after determining a value for $m_{n,discard}$ from the aforementioned equations, the value of the modal entropy was checked against D_{max}, and if the modal entropy was too large, an additional discard cycle was added and the modal entropy was checked again. The process was repeated until the modal entropy was less than or equal to D_{max}. This process could potentially be optimized further, but that was left as potential future work if the algorithm is to be implemented into a production level code.

As an example calculation, the uniform slab problem in Appendix A with 4E+3 histories per cycle and the 33-mode starting source has the relevant parameters that Table 4.3.1 specifies. Using (4.3.8) and (4.3.17), the minimum number of discarded cycles that are sufficient to converge the relative means and relative standard deviations for two different modal entropy convergence levels were calculated. Tables 4.3.2 and 4.3.3 summarize

those results for maximum entropy levels of $1/\pi$ and 0.005, respectively. In the column headers of Tables 4.3.2 and 4.3.3, $\mu_r^{(m_d)}$, $\sigma_r^{(m_d)}$, and $D^{(m_d)}$ indicate the relative mean, relative standard deviation, and modal relative entropy, respectively, of a SBDC PDF at the first cycle that is greater than or equal to the number of extrapolated cycles with a sufficiently converged modal entropy that is below the specified threshold value. For the less stringent convergence criterion derived from using $Z=\sqrt{2/\pi}$, which necessitates $\sigma_{max}=1.61$, only mode number 2 required additional cycles beyond the extrapolation cutoff to sufficiently converge, which was 133 cycles. Mode 2 required more discarded cycles than was indicated to converge both the relative mean, which was 125, and the relative standard deviation, which was 100, because the modal relative entropy at cycle 125 fell in the region outside of the convergence contour but inside the enclosing rectangle of the discard search algorithm. The relative standard deviation of all four modes in Table 4.3.2 were sufficiently converged without needing any standard power method cycles because the choice for the extrapolation parameter was small enough to keep the converged relative standard deviations below the $\sigma_{max}=1.61$ threshold. For the more restrictive convergence criterion derived from using $Z=0.1$, which requires $\sigma_{max}=1.07$, all four of the modes in Table 4.3.3 required some cycles beyond the extrapolation cutoff to be sufficiently converged. Mode 2 required 331 cycles to sufficiently converge the relative mean and modal entropy, which was greater than 100, the number of extrapolated cycles; however, only 193 cycles were needed to sufficiently converge the relative standard deviation, which was a difference of 138. Such a large difference indicates that more cycles should have been extrapolated to converge the relative mean faster. For the higher numbered modes, the relative standard deviations required more cycles to converge than the relative means, which indicates that fewer cycles could have been extrapolated to sufficiently converge those modes with fewer cycles.

Mode	1	2	3	4	5
λ_n/λ_1	1.00E+0	9.90E-1	9.74E-1	9.52E-1	9.25E-1
σ_∞	1.53E-3	7.80E-3	4.85E-3	3.62E-3	2.93E-3
β_n	5.06E-2	4.28E-2	2.92E-2	2.14E-2	1.68E-2
Y	6.92E-2	6.92E-2	6.92E-2	6.92E-2	6.92E-2
Y/β_1	1.37E+0	1.37E+0	1.37E+0	1.37E+0	1.37E+0
α	9.80E-1	9.80E-1	9.80E-1	9.80E-1	9.80E-1
η_n	1.00E+0	9.80E-1	9.48E-1	9.05E-1	8.52E-1
m_c	100	100	100	100	100
$\mu_r^{(m_c)}$	NA	1.02E+0	3.99E-2	3.66E-4	8.64E-7
$\sigma_r^{(m_c)}$	NA	1.40E+0	1.42E+0	1.42E+0	1.43E+0
$D^{(m_c)}$	NA	8.48E-1	3.53E-1	3.61E-1	3.72E-1

Table 4.3.1: Parameters of uniform slab problem with 33-mode starting source that are used to predict the number of discarded cycles.

	$m_{n,discard}$ **To Converge**			**DC PDF Properties When First Converged**		
Mode	μ_r	σ_r	D	$\mu_r^{(m_d)}$	$\sigma_r^{(m_d)}$	$D^{(m_d)}$
2	125	100	133	7.30E-1	1.22	3.12E-1
3	100	100	100	3.99E-2	1.42	1.56E-1
4	100	100	100	3.66E-4	1.42	1.61E-1
5	100	100	100	8.64E-7	1.43	1.68E-1

Table 4.3.2: Number of discard cycles, $m_{n,discard}$, required to converge various modes of the uniform slab problem for D_{max}=3.18E-1 with $m_{n,cutoff}$=100 along with relevant properties of the SBDC PDFs after their first sufficiently converged cycles.

	$m_{n,discard}$ To Converge			DC PDF Properties When First Converged		
Mode	μ_r	σ_r	D	$\mu_r^{(m_d)}$	$\sigma_r^{(m_d)}$	$D^{(m_d)}$
2	331	193	331	9.97E-2	1.00	5.00E-3
3	100	137	137	1.49E-2	1.07	4.64E-3
4	100	120	120	1.37E-4	1.07	4.70E-3
5	100	113	113	3.15E-7	1.07	4.51E-3

Table 4.3.3: Number of discard cycles, $m_{n,discard}$, required to converge various modes of the uniform slab problem for D_{max}=5.0E-3 with $m_{n,cutoff}$=100 along with relevant properties of the DC PDFs after their first sufficiently converged cycles.

By inputing different parameters into the cutoff and discard cycle search algorithm, one can observe how each parameter affects the output of the algorithm. Inspecting the equations governing the SBDC PDFs reveals which parameters affect convergence. Dividing the SBDC variance from (4.3.6) by the stationary standard power method SBDC variance from (4.3.10) yields

$$\sigma_r^2=(1+\alpha)^2\frac{1-\eta_n^{2m_c}}{1-\eta_n^2}\left[1-\left(\frac{\lambda_n}{\lambda_1}\right)^2\right]\left(\frac{\lambda_n}{\lambda_1}\right)^{2(m-m_c)}+1-\left(\frac{\lambda_n}{\lambda_1}\right)^{2(m-m_c)}\quad \forall\, m>m_c, |\eta_n|\neq 1. \tag{4.3.18}$$

From (4.3.18), one can see that the relative variance and relative standard deviation of a mode depend on the extrapolation parameter, the eigenvalue ratio, the number of extrapolated cycles, and the total number of cycles run. The relative mean from (4.3.7) is

$$\mu_r=\frac{\left|E\left[\tilde{v}_n^{(m)}\right]\right|}{\sigma_\infty}=\frac{|\beta_n|}{\sigma_n}\frac{Y}{\beta_1}\eta_n^{m_c}\left(\frac{\lambda_n}{\lambda_1}\right)^{m-m_c}\sqrt{1-(\lambda_n/\lambda_1)^2}\quad \forall\,\frac{\lambda_n}{\lambda_1}\neq 1. \tag{4.3.19}$$

In (4.3.19), the same parameters as for the variance compose the relative mean with one additional parameter, the grouped coefficient, which is defined as

$$T\equiv\frac{|\beta_n|}{\sigma_n}\frac{Y}{\beta_1}. \tag{4.3.20}$$

Substituting the definition for the grouped coefficient into (4.3.19) simplifies the expression for the relative mean to

$$\mu_r=T\,\eta_n^{m_c}\left(\frac{\lambda_n}{\lambda_1}\right)^{m-m_c}\sqrt{1-(\lambda_n/\lambda_1)^2}\quad \forall\,\frac{\lambda_n}{\lambda_1}\neq 1. \tag{4.3.21}$$

Figure 4.3.1 shows an example of how varying the grouped coefficient affects the minimum number of cycles that are required to sufficiently converge the modal relative entropy for a mode with $\lambda_n/\lambda_1=0.99$ and $\alpha=1.0$ to the more restrictive condition of $D_{max}=5.00\text{E-}3$. From Figure 4.3.1, one can see the relatively flat region for values of *T* that are less than or equal to 1, which corresponds to convergence conditioned primarily on the relative variance. As the grouped coefficient increases beyond 1, the number of discards associated with extrapolation increases sharply because adding additional extrapolated cycles is prohibitive because the relative variance would reach beyond the convergence limits. Eventually, the lines displaying the number of discarded cycles with extrapolation and the number of extrapolated cycles approach being parallel. The vertical distance between them is equal to the number of standard power method cycles that are required to sufficiently converge the stationary relative variance to σ^2_{max}. Because extrapolation essentially reduces the eigenvalue ratio of the mode, the number of discards associated with the standard power method increases at a faster rate than that associated with the extrapolated power method.

The line representing the number of extrapolated cycles in Figure 4.3.1 appears wider and more jagged than the others because of the chosen algorithm for selecting the optimal number of extrapolated cycles. A zoomed view of a narrow range of *T* values in the asymptotic parallel region of Figure 4.3.1 reveals a regular alternating pattern in the number of extrapolated cycles, which Figure 4.3.2 displays. In Figure 4.3.2, one can see that for every increase in the number of discarded cycles, there is initially a decrease in the number of extrapolated cycles. This is a direct consequence of my choice to use the fewest extrapolated cycles that will sufficiently converge the modal relative entropy. The number of discarded cycles is a step function that only allows integer increments. When an additional discarded cycle is necessitated by an infinitesimal increase in *T*, then the modal relative entropy may drop below the convergence threshold far enough that some extrapolated cycles may be removed while keeping the modal entropy below the threshold. If one continues to increase *T*, then those extrapolated cycles may be added back to the simulation incrementally until reaching one more than the maximum reached

before the drop because of the additional discarded cycle. Adding any more extrapolated cycles necessitates an increase in the number of discarded cycles to keep the relative variance within the convergence bounds. This pattern repeats in perpetuity for increasing values of *T*. If the algorithm had been designed to minimize the modal relative entropy, then the number of extrapolated cycles would increase with each increment of the number of discarded cycles when at their asymptotic parallel behavior.

As (4.3.18) and (4.3.21) show, the eigenvalue ratio affects the relative variances and means at different cycles, which in turn affects the minimum number of discarded cycles that are needed to sufficiently converge the modal relative entropy. As an example, Figure 4.3.3 displays the minimum numbers of discarded cycles associated with various eigenvalue ratios for a mode that has a relatively large grouped coefficient of $T=10^5$ and an extrapolation factor of $\alpha=0.5$. The number of discarded and extrapolated cycles associated with the extrapolated power method in Figure 4.3.3 has a notable dip in the vicinity of $\lambda_n/\lambda_1=0.33$. The dip in the curves corresponds to the modes whose decay coefficients approach zero as a result of extrapolation. Increasing α would shift the dip toward greater eigenvalue ratios, and the opposite is true when reducing α. Some of the jaggedness in the number of extrapolated cycles that can be seen in Figure 4.3.2 is visible in Figure 4.3.3 with the same reasoning as the previous paragraph mentions; however, the pattern is reflected for eigenvalue ratios less than 0.33 because those modes have negative decay coefficients, which get worse as the eigenvalue ratio decreases. For the lowest range of eigenvalue ratios, extrapolation does not offer any benefit as Figure 4.3.3 shows for eigenvalue ratios below approximately 0.22. At the opposite end of the spectrum, the number of discarded cycles grows faster than an exponential curve, and the difference between the number of discarded cycles under the standard power method and under the extrapolated power method also grows as the eigenvalue ratio increases.

The relationship between the eigenvalue ratio and the number of discarded cycles differs somewhat when the relative mean is well converged. Figure 4.3.4 shows an example where $T=0.0$ and $\alpha=0.5$. The dip in the number of discarded cycles from

extrapolation occurs at a greater value for the eigenvalue ratio than in the previous example.

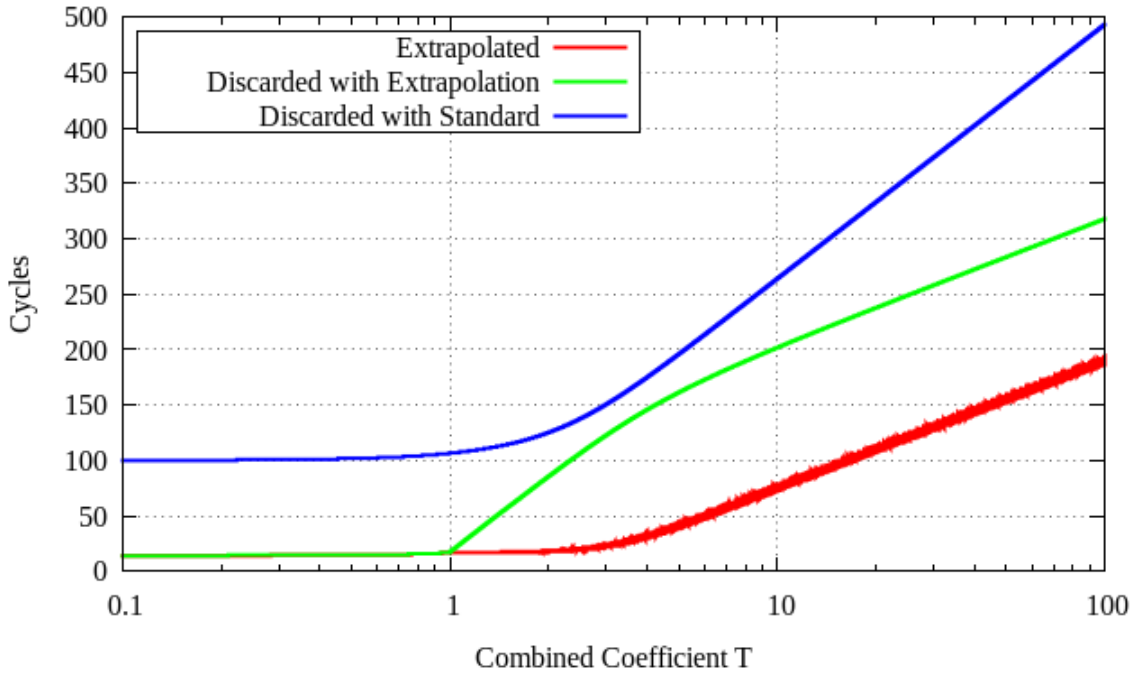

Figure 4.3.1 Optimal number of cycles by type that are required to sufficiently converge a problem with $\lambda_n/\lambda_1 = 0.99$ and $\alpha=1.0$ for a range of grouped coefficient T values.

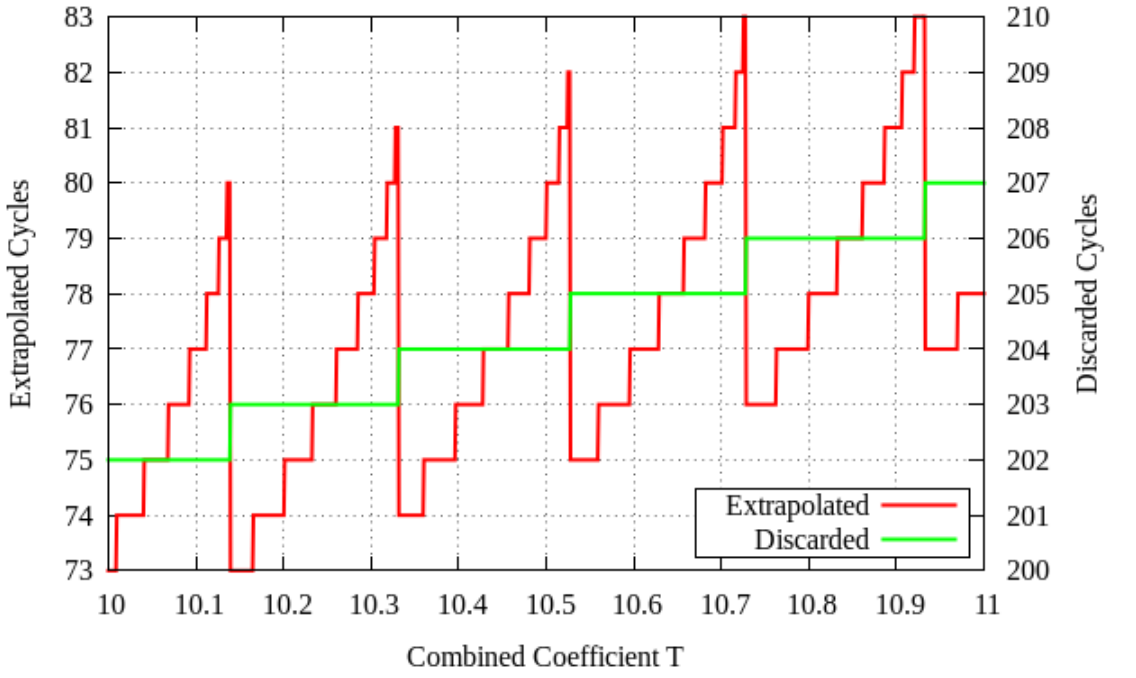

Figure 4.3.2 Optimal numbers of extrapolated and discarded cycles to sufficiently converge a problem with $\lambda_n/\lambda_1 = 0.99$ and $\alpha=1.0$ for a narrow range of T values.

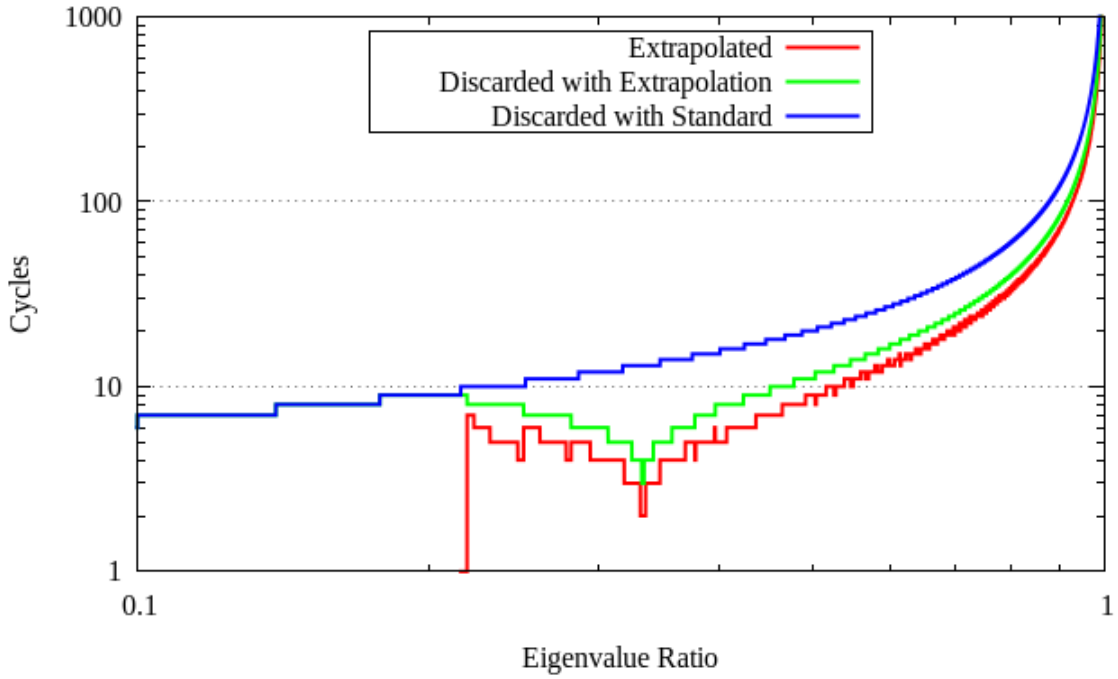

Figure 4.3.3 Plot of expected numbers of cycles that are required to sufficiently converge modes with T=1E5, α=0.5, and various eigenvalue ratios.

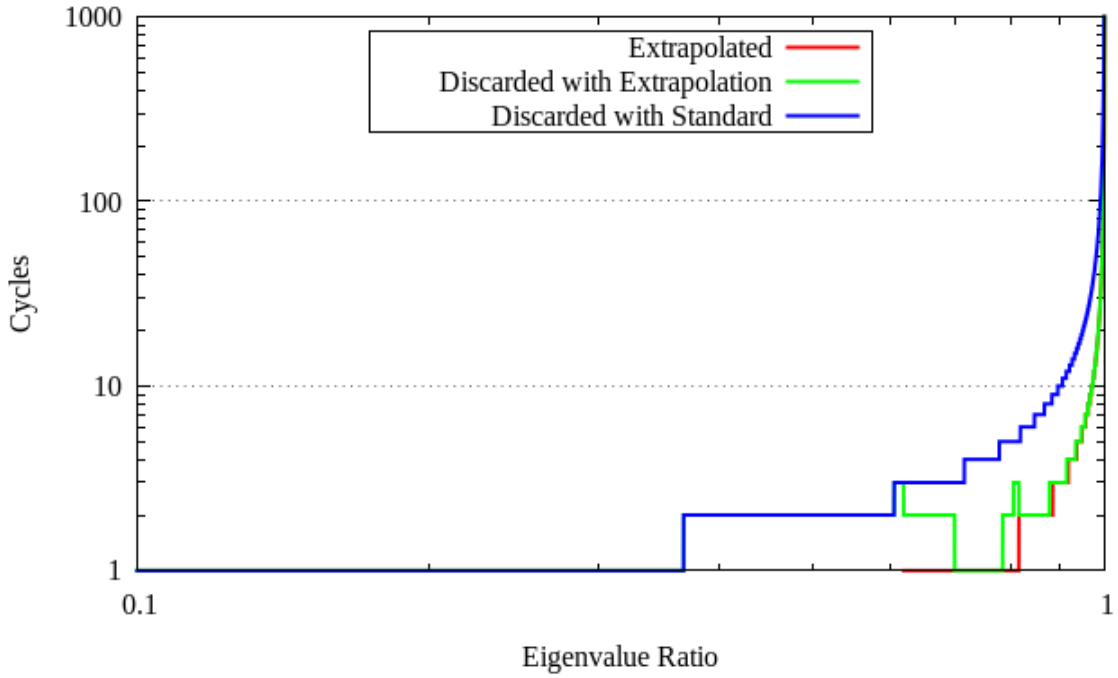

Figure 4.3.4 Plot of expected numbers of cycles that are required to sufficiently converge modes with T=0.0, α=0.5, and various eigenvalue ratios.

λ_n/λ_1	Extrapolation		Standard	Reduction in # of Cycles to Discard	Percentage of Reduction (%)
	$m_{n,cut}$	$m_{n,discard}$	# to Discard		
0.918	26	43	70	27	38.6
0.927	30	48	79	31	39.2
0.936	33	55	89	34	38.2
0.945	41	63	103	40	38.8
0.954	48	75	122	47	38.5
0.963	57	93	149	56	37.6
0.972	74	121	193	72	37.3
0.981	104	175	275	100	36.4
0.990	187	318	493	175	35.5
0.999	1364	2618	3799	1181	31.1

Table 4.3.4: While holding constant T=100 and α=1.0 the number of discard cycles were calculated for various eigenvalue ratios satisfying D_{max}=5.0E-3.

λ_n/λ_1	Extrapolation		Standard	Reduction in # of Cycles to Discard	Percentage of Reduction (%)
	$m_{n,cut}$	$m_{n,discard}$	# to Discard		
0.918	2	2	12	10	83.3
0.927	2	2	14	12	85.7
0.936	2	2	16	14	87.5
0.945	3	3	18	15	83.3
0.954	3	3	22	19	86.4
0.963	4	4	27	23	85.2
0.972	5	5	36	31	86.1
0.981	8	8	53	45	84.9
0.990	14	14	100	86	86.0
0.999	142	142	1002	860	85.8

Table 4.3.5: While holding constant T=0.0 and α=1.0, the number of discard cycles were calculated for various eigenvalue ratios satisfying D_{max}=5.0E-3.

T	Extrapolation		Standard	Reduction in # of Cycles to Discard	Percentage of Reduction (%)
	$m_{n,cut}$	$m_{n,discard}$	# to Discard		
1.00E-2	14	14	100	86	86.0
1.00E-1	14	14	100	86	86.0
1.00E+0	17	18	107	89	83.2
1.00E+1	73	202	264	62	23.5
1.00E+2	187	318	493	175	35.5
1.00E+3	301	432	722	290	40.2
1.00E+4	415	546	951	405	42.6
1.00E+5	529	660	1180	520	44.1
1.00E+6	643	774	1409	635	45.1
1.00E+7	757	888	1638	750	45.8

Table 4.3.6: While holding constant λ_n/λ_1 = 0.99 and α=1.0, the number of discard cycles were calculated for various values of the grouped coefficient satisfying D_{max}=5.0E-3.

α	Extrapolation		Standard	Reduction in # of Cycles to Discard	Percentage of Reduction (%)
	$m_{n,cut}$	$m_{n,discard}$	# to Discard		
0.125	365	448	493	45	9.1
0.25	325	415	493	78	15.8
0.5	257	370	493	123	24.9
1	187	318	493	175	35.5
2	120	274	493	219	44.4
4	71	249	493	244	49.5
8	38	246	493	247	50.1
16	19	260	493	233	47.3
32	9	287	493	206	41.8
64	3	326	493	167	33.9

Table 4.3.7: While holding constant T=100 and λ_n/λ_1 = 0.99, the number of discarded cycles were calculated for various extrapolation parameters satisfying D_{max}=5.0E-3.

For the purpose of determining *a priori* when active cycles should begin, a conservative estimate should overestimate the number of discard cycles to avoid including biased results. For determining when to stop extrapolating, a conservative number of cycles is too low because extrapolation introduces a bias in the variance and requires more computational work. With conservatism in mind, a high estimate for β_n should be assumed for predicting convergence. However, for determining when to stop extrapolation, a low estimate for β_n is preferable. A low estimate for λ_n/λ_1 is preferable for predicting a cutoff for acceleration, and the converse is true for choosing when to start active cycles. Additionally, a high estimate for σ_n will predict an earlier cutoff cycle than a low estimate would; therefore, a conservative use for turning off extrapolation would be to assume higher variance, and a low variance estimate would be preferred for calculating the first active cycle. The appropriate choice for α will depend on the estimates for the other parameters and a numerical search that is left for potential future research.

Chapter 5. Summary and Conclusions

With a few assumptions, equations, referred to as the constant multiplier model, were derived that govern the PDFs of eigenfunction DCs of fission source estimates from MC neutron transport simulations. The PDFs generated from collected evidence follow the model equations with a reasonable degree of accuracy, which supports the reasonableness of the assumptions used to generate the model equations. A new diagnostic for fission source convergence is defined by setting a criterion for the difference between the PDFs at each cycle and their stationary PDFs. The new diagnostic highlights how the extrapolated power method with an appropriate cutoff cycle can be an improvement over the standard power method, which contradicts prior published work addressing linear extrapolation. Using the PDF equations, a prescription for the optimal number of extrapolated and standard cycles is generated for two specified levels of convergence. After a specified level of convergence is reached, the user has a reasonable estimate for the potential bias from the initial source and an estimate for the variance in each eigenmode component of the fission source estimate. This information is useful for determining when to begin tallying; however, the task of determining how the bias and variance in SBDCs translates to bias and variance of desired quantities, such as neutron flux in a fuel element, is left as potential future research.

There are 4 primary assumptions that are needed to generate the model and one additional assumption that enables obtaining useful inferences from the model. The first assumption is that the normalized transport operator is unbiased, which is known from prior research to be approximately true for sufficiently many histories. The second assumption is that normalizations are uncorrelated with noise introduced in prior cycles, which is a corollary of the unbiased nature of the operator. The third assumption is that the covariance of noise components is zero between different cycles, which was shown to be reasonable

because it leads to conservative estimates for the variance of SBDCs for the purpose of diagnosing convergence. The fourth assumption is that the normalizations and single-cycle variances of SBDCs approach steady state distributions that may be approximately represented by constants. Empirical evidence from simulations starting with well converged source distributions supports the validity of this fourth assumption. For inference purposes, an additional assumption is made that the SBDC PDFs are normally distributed because without knowledge of the distribution, confidence intervals cannot be known. The unnormalized IBDCs are shown to be normally distributed by rigorous application of the central limit theorem, which may be extended to the normalized SBDCs under the assumption of approximately constant normalization. Empirical evidence supports the normality assumption for sufficiently converged source distributions and sufficient numbers of histories.

The new convergence diagnostic measures the relative entropy between the PDFs predicted by the constant multiplier model at each cycle and their stationary PDFs, which are also predicted by the constant multiplier model. The diagnostic prevents users from introducing non-negligible bias into their tallies attributable to the initial source estimate. The user may set a convergence criterion based on what bias relative to uncertainty they are willing to accept in the first tallied source bank. To generate the PDFs for modes of interest, the diagnostic requires estimates for the eigenvalue ratios, the ratio of the converged SBDC to the initial cycle SBDC of the fundamental mode, and the single-cycle variance or standard deviation. These are most likely to be obtained with the help of a fission matrix calculation or some prior knowledge. With a fission matrix solution, the first 2 requirements are trivial to obtain. An algorithm for calculating the single-cycle variance using an eigenvector and spatially stratified subdivisions of the source bank is presented and shown to yield reasonable estimates for the representative constant single-cycle variance in the constant multiplier model. For cycles or simulations without an available fission matrix solution, an alternate method is presented to calculate the mean of single-cycle variances over all modes. The alternative is less accurate than using an eigenvector but can still be useful in part because the alternative has lower variance and

is less sensitive to the source distribution, which may be particularly valuable in early cycles. A technique for estimating the ratio of the converged SBDC to the initial cycle SBDC of the fundamental mode without any knowledge of the fundamental mode is presented, but it suffers from exponentially increasing variance and is sensitive to undersampling bias from using too few histories. For future work, these estimators and their resultant PDFs should be validated for additional configurations. A difficulty in performing such validations is obtaining sufficiently accurate eigenvalues and eigenvectors, which may require a high resolution fission matrix that results in concerns regarding hard disk storage and computer memory.

Appendices

Appendix A. Uniform Slab

The uniform slab problem used in this work was a sub-critical homogeneous slab with infinite extent in all but one dimension, the *x* direction. The width of the slab was 310.64 cm, which was surrounded by vacuum. The macroscopic cross sections were energy independent or one-group with values 0.05 cm^{-1}, 0.1 cm^{-1}, and 0.1 cm^{-1} for fission Σ_f, absorption Σ_a, and scattering Σ_s, and a fixed number of neutrons emitted per fission, ν, equal to 2.0. Scattering was isotropic in the laboratory frame with the average cosine of the scattering angle, $\bar{\mu}_0$, equal to 0.0.

The slab was considered highly-scattering because $\Sigma_a \ll \Sigma_t$; therefore, the eigenvalues and eigenfunctions are well approximated by analytic diffusion theory [9]. The approximate eigenfunctions of a diffuse uniform slab have the form

$$b_n(x) = \hat{c}_n \sin\left(\frac{n\pi(x+\hat{a})}{\hat{L}}\right) \quad \forall 0 \le x \le L\,,\ n = 1,2,3,... \tag{A.1}$$

with corresponding eigenvalues

$$\lambda_n = \frac{\nu\Sigma_f/\Sigma_a}{1+\frac{1}{3\Sigma_{tr}\Sigma_a}\left(\frac{n\pi}{\hat{L}}\right)^2} \tag{A.2}$$

where *L* is the slab width, $\hat{a}$ is the extrapolation length, $\hat{L}$ is the width plus twice the extrapolation length, and $\hat{c}_n$ is a constant chosen to satisfy the normalization condition. The extrapolation length for plane geometries is given by [9]

$$\hat{a} = 0.7104\lambda_{tr} \tag{A.3}$$

where

$$\lambda_{tr} = \Sigma_{tr}^{-1} = \left(\Sigma_t - \bar{\mu}_0\Sigma_s\right)^{-1}. \tag{A.4}$$

The transport operator for the slab is self-adjoint because it is a mono-energetic problem [9]; however, the eigenfunctions from the diffusion approximation with extrapolation are not orthogonal inside the problem domain $0 \le x \le L$, but they are orthogonal over the

extrapolated domain $-\hat{a} \le x \le L + \hat{a}$. The eigenvalues of the first five modes, which were calculated using (A.2), are presented in Table A.1. The slab width was chosen to yield a relatively high dominance ratio of 0.99, which allows one to observe convergence over multiple cycles. However, this dominance ratio is low enough to allow numerous repetitions of calculations on a single processor.

Mode Number	Eigenvalue	Eigenvalue Ratio
1	9.9663306025E-01	1.0000000000E+00
2	9.8666691607E-01	9.9000018705E-01
3	9.7049234618E-01	9.7377097438E-01
4	9.4871887105E-01	9.5192394161E-01
5	9.2211974153E-01	9.2523495187E-01

Table A.1: Eigenvalues and eigenvalue ratios of the uniform slab.

Many of the simulations in this dissertation use a far-from-converged source. For the uniform slab problem, the far-from-converged source distribution was generated by combining the first 32 non-fundamental modes according to the inverse of their mode number and then adding the fundamental mode to keep the source non-negative yielding the distribution in Figure A.1.

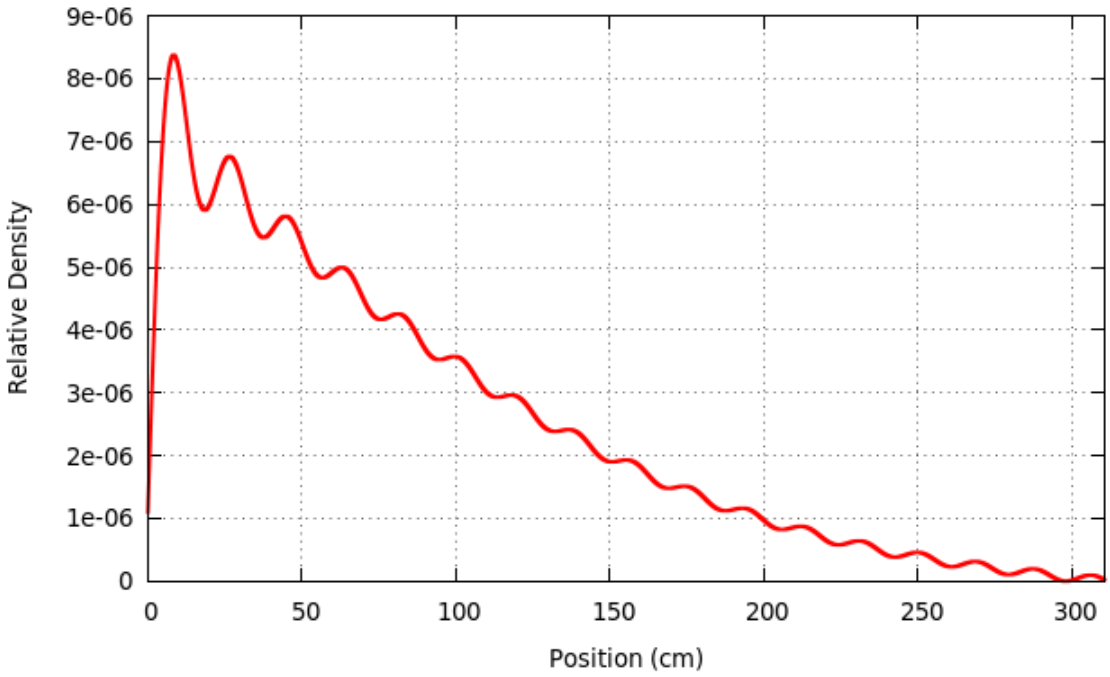

Figure A.1. Far-from-converged source containing the first 33 modes of the uniform slab problem.

Appendix B. Simplified 2-D Reactor

The simplified 2-D reactor problem models the radial dimension of a fictitious reactor with an asymmetric arrangement of homogenized assemblies and one-energy-group. The reactor materials consist of 3 assembly types and a moderator with macroscopic cross sections listed in Table B.1

Material	$\nu\Sigma_f$ **(cm^{-1})**	Σ_s **(cm^{-1})**	Σ_a **(cm^{-1})**
Moderator	0.0	1.98E-01	2.00E-03
High Enrichment	1.20E-02	1.80E-01	8.00E-03
Med Enrichment	1.12E-02	1.80E-01	8.80E-03
Low Enrichment	1.04E-02	1.80E-01	9.60E-03

Table B.1: Macroscopic cross sections of the uniform slab.

The arrangement of assemblies is shown in Figure B.1. Each assembly is 46 cm by 46 cm with infinite extent in the other dimension. Each assembly has a 0.1 cm thick border of moderator; therefore, the fissile region measures 45.8 cm x 45.8 cm. Reference fission matrix calculations were performed with bin resolutions of 21x21, 42x42, 84x84, and 168x168. The eigenvalue ratios for the first 3 non-fundamental modes are plotted in Figure B.2 for each resolution. The eigenvalue spectrum convergence was monotonic as expected from observations in other work [34]. The observed pattern in convergence of eigenvalue ratios does not indicate that an increase of 3.6E-4 or 36 pcm is warranted to correct the data as explored in Section 3.3.2.

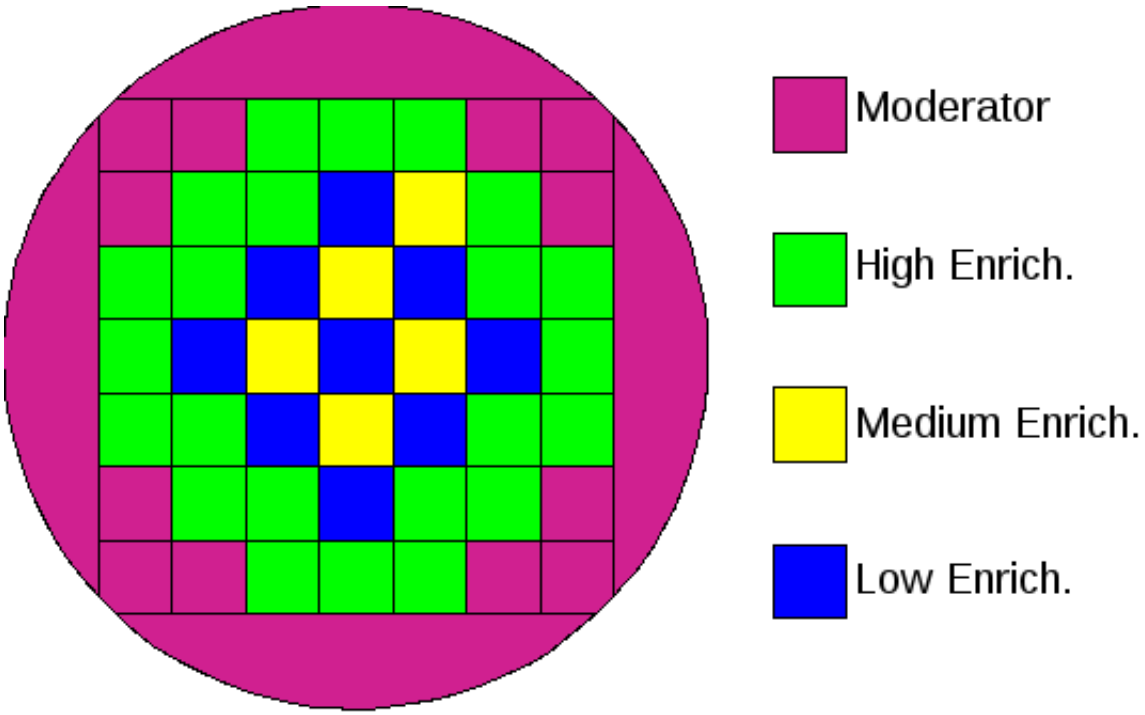

Figure B.1. Simplified 2-D reactor geometry.

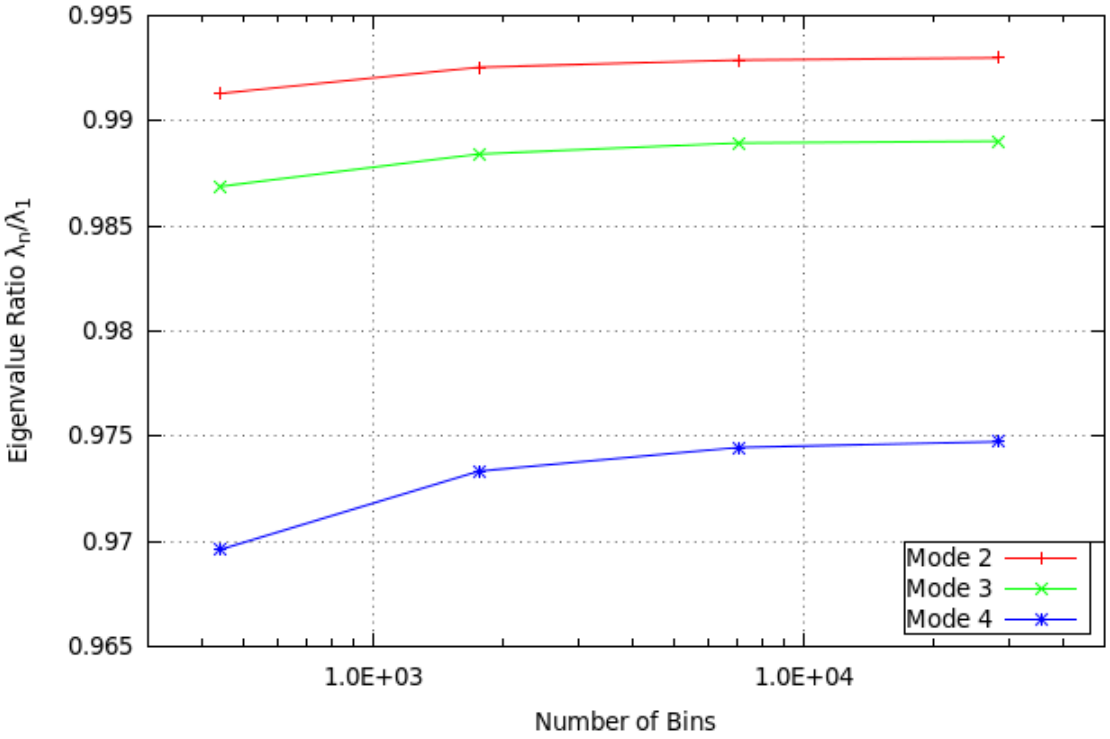

Figure B.2. Simplified 2-D reactor eigenvalue ratios for several fission matrix bin resolutions.

Appendix C. Continuous Energy 2-D Reactor

This is the pressurized water reactor (PWR) problem specified by Nakagawa and Mori [59] with no control rods inserted using continuous energy cross sections. A reasonably coarse 20x20 grid was applied for estimating the eigenvectors for calculating DCs for testing normality in Section 3.2. The cross-sections used were from the ENDF/B-VI evaluations at 293.6 Kelvin, which included S(α,β) data for the light water [60], which had been processed into libraries by NJOY 99 [61]. Figure B.1 displays the pin arrangement in an assembly and the baffle configuration, which is reproduced from Nakagawa and Mori [59]. Figure B.2 displays the full core with assembly indicators, which is reproduced from Nakagawa and Mori [59]; however, control rods indicated in Figure B.2 were not present in the simulations of this dissertation.

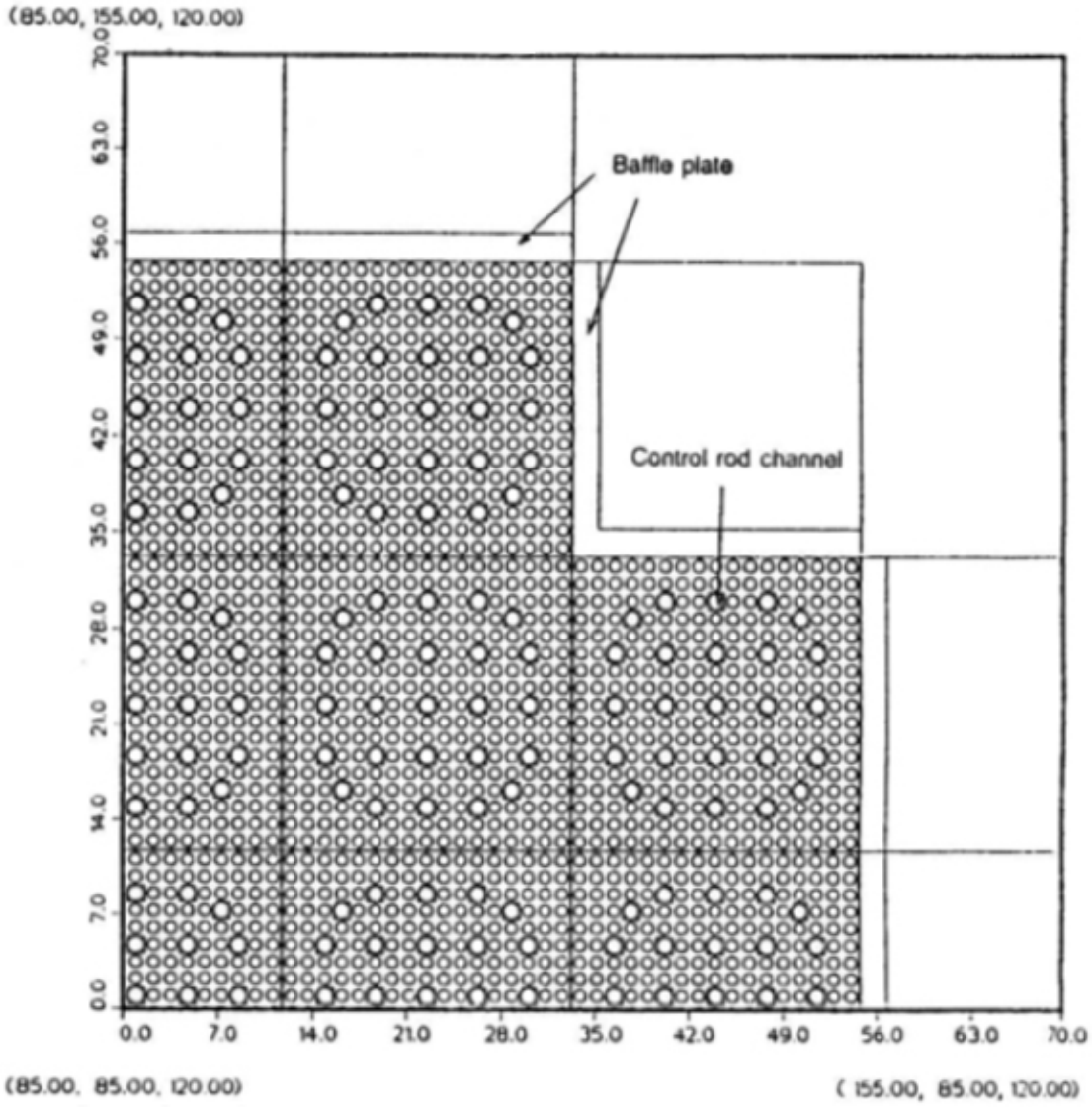

Figure C.1 Pin and baffle configuration of continuous energy 2-D reactor.

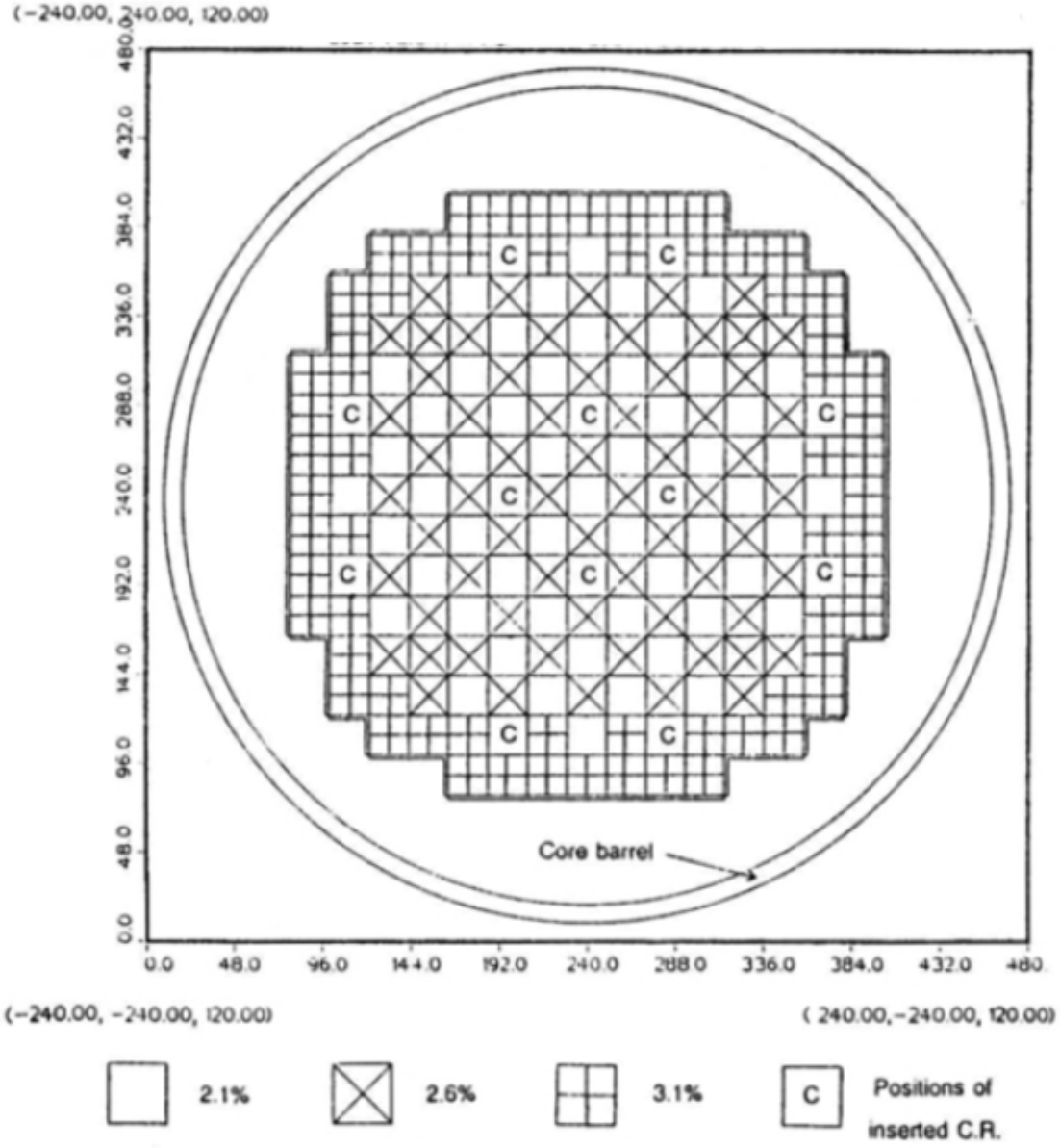

Figure C.2 Assembly configuration of continuous energy 2-D reactor.

Appendix D. Double Peak Slab

The double peak slab problem is a one-dimensional slab that consists primarily of low reactivity regions with two thin highly reactive slabs inserted on either side in asymmetric locations with dimensions shown in Figure D.1. The low reactivity regions have macroscopic cross sections equal to 0.24 cm^{-1}, 0.3 cm^{-1}, and 0.7 cm^{-1} for fission production $\nu\Sigma_f$, absorption Σ_a, and scattering Σ_s, respectively. The highly reactive slabs have identical cross sections except that $\nu\Sigma_f = 0.39\,\mathrm{cm}^{-1}$. The eigenvalues and eigenvectors were calculated for a 200-bin uniform mesh. The first five eigenvalues are shown in Table D.1.

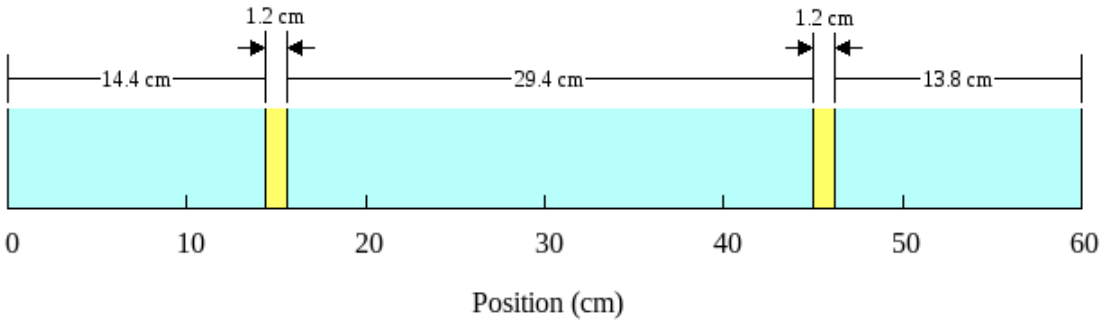

Figure D.1 Diagram of double peak slab dimensions with the highly reactive regions shaded with yellow and the less reactive regions shaded with cyan.

Mode Number	Eigenvalue	Eigenvalue Ratio
1	0.88368235	1.00000000
2	0.88362945	0.99994014
3	0.78816450	0.89190929
4	0.76496562	0.86565678
5	0.76000920	0.86004796

Table D.1: Eigenvalues and eigenvalue ratios of the double peak slab.

Bibliography

[1] X-5 Monte Carlo Team, *MCNP – A General Monte Carlo N-Particle Transport Code*, 5th ed., vol. 1, 3 vols. 2005.

[2] R. Sanchez and N. J. McCormick, “A Review of Neutron Transport Approximations,” *Nucl. Sci. Eng.*, vol. 80, pp. 481–535, 1982.

[3] G. E. Whitesides, “Difficulty in Computing the k-effective of the World,” *Trans. Am. Nucl. Soc.*, vol. 14, no. 2, p. 680, Oct. 1971.

[4] J. Lieberoth, “A Monte Carlo technique to solve the static eigenvalue problem of the Boltzmann transport equation,” *Nukleonik*, vol. 11, no. 5, pp. 213–19, Sep. 1968.

[5] G. H. Golub and C. F. Van Loan, *Matrix Computations*, 3rd ed. Baltimore: Johns Hopkins University Press, 1996.

[6] T. J. Urbatsch, “Iterative acceleration methods for Monte Carlo and deterministic criticality calculations,” University of Michigan, 1995.

[7] R. E. Swaja, “Application of Stochastic Optimal Estimation Principles to Monte Carlo Eigenfunction Convergence,” Ph.D., Carnegie Mellon University, United States -- Pennsylvania, 1973.

[8] R. C. Gast and N. R. Candelore, “Monte Carlo Eigenfunction Strategies and Uncertainties,” in *Proceedings of the NEACRP Meeting of a Monte Carlo Study Group*, 1974, p. 162.

[9] J. J. Duderstadt and L. J. Hamilton, *Nuclear Reactor Analysis*, 1 edition. New York: Wiley, 1976.

[10] F. B. Brown, S. E. Carney, B. C. Kiedrowski, and W. R. Martin, “Fission Matrix Capability for MCNP, Part I - Theory,” in *Proceedings of International Conference on Mathematics and Computational Methods Applied to Nuclear Science & Engineering*, Sun Valley, Idaho, USA, 2013.

[11] O. Perron, “Zur Theorie der Matrices,” *Math. Ann.*, vol. 64, no. 2, pp. 248–263, Jun. 1907.

[12] G. Frobenius, *Über Matrizen aus nicht negativen Elementen*. De Gruyter, 1912.

[13] A. Papoulis and S. U. Pillai, *Probability, random variables, and stochastic processes*, 4. ed., internat. ed., Nachdr. Boston, Mass.: McGraw-Hill, 2009.

[14] K. W. Morton and E. Atomic Energy Research Establishment (Harwell, *Criticality Calculations by Monte Carlo Methods*. Atomic Energy Research Establishment, 1956.

[15] L. N. Trefethen and D. B. III, *Numerical Linear Algebra*, 1 edition. Philadelphia: SIAM: Society for Industrial and Applied Mathematics, 1997.

[16] Y. Saad, *Numerical methods for large eigenvalue problems*. Manchester, UK : New York: Manchester University Press ; Halsted Press, 1992.

[17] Y. Saad, *Iterative Methods for Sparse Linear Systems*. PWS Publishing Company, 1996.

[18] D. P. Griesheimer and B. E. Toth, “A Novel Source Convergence Acceleration Scheme for Monte Carlo Criticality Calculations, Part I: Theory,” presented at the Joint International Topical Meeting on Mathematics & Computation and Supercomputing in Nuclear Applications (M&C + SNA 2007), Monterey, California, 2007.
[19] B. E. Toth and W. R. Martin, “Noise analysis of Smoothed Residual Acceleration, a Monte Carlo Neutron Source Convergence Algorithm,” presented at the International Conference on Mathematics, Computational Methods & Reactor Physics (M&C 2009), Saratoga Springs, New York, 2009.
[20] J. Spanier and E. M. Gelbard, *Monte Carlo principles and neutron transport problems*. Reading, Mass.: Addison-Wesley Pub. Co., 1969.
[21] I. Lux and L. Koblinger, *Monte Carlo Particle Transport Methods: Neutron and Photon Calculations*. Boca Raton: CRC Press, 1991.
[22] L. L. Carter and E. D. Cashwell, *Particle-Transport Simulation with the Monte Carlo Method*. Washington, D.C. : Oak Ridge, Tenn.: United States. Dept. of Energy ; distributed by the Office of Scientific and Technical Information, U.S. Dept. of Energy, 1975.
[23] G. I. Bell and S. Glasstone, *Nuclear Reactor Theory*. New York, NY: Van Nostrand Reinhold Co, 1970.
[24] E. M. Gelbard and R. E. Prael, “Monte Carlo Work at Argonne National Laboratory,” in *Proceedings of the NEACRP Meeting of a Monte Carlo Study Group*, 1974, p. 202.
[25] R. J. Brissenden and A. R. Garlick, “Biases in the Estimation of k_eff and its Error by Monte Carlo Methods,” *Ann. Nucl. Energy*, vol. 13, no. 2, pp. 63–83, 1986.
[26] R. C. Gast, “Monte Carlo eigenfunction iteration strategies that are and are not fair games (LWBR Development Program),” United States, Technical Report WAPD-TM-878, Sep. 1969.
[27] T. E. Booth, “A simple eigenfunction convergence acceleration method for Monte Carlo,” in *International Conference on Mathematics and Computational Methods Applied to Nuclear Science and Engineering (M&C2011)*, Saratoga Springs, New York, 2011, pp. 8–12.
[28] B. E. Toth and D. P. Griesheimer, “A Novel Source Convergence Acceleration Scheme for Monte Carlo Criticality Calculations, Part II: Implemntation & Results,” presented at the Joint International Topical Meeting on Mathematics & Computation and Supercomputing in Nuclear Applications (M&C + SNA 2007), Monterey, California, 2007.
[29] T. Ueki, “Information theory and undersampling diagnostics for Monte Carlo simulation of nuclear criticality,” *Nucl. Sci. Eng.*, vol. 151, no. 3, pp. 283–292, 2005.
[30] D. P. Griesheimer *et al.*, “MC21 v.6.0 – A continuous-energy Monte Carlo particle transport code with integrated reactor feedback capabilities,” *Jt. Int. Conf. Supercomput. Nucl. Appl. Monte Carlo 2013 SNA MC 2013 Pluri- Trans-Discip. New Model. Numer. Simul. Paradig.*, vol. 82, pp. 29–40, Aug. 2015.
[31] W. L. Briggs, *Multigrid Tutorial*. Philadelphia, Pa: Society for Industrial & Applied, 1987.
[32] H. Kadotani, Y. Hariyama, M. Shiota, and T. Takada, “Acceleration of fission

distribution convergence using eigen-vectors from matrix K calculations in the KENO code,” *ICNC 91 Int. Conf. Nucl. Crit. Saf.*, 1991.
[33] L. L. Carter and N. J. McCormick, “Source convergence in Monte Carlo calculations,” *Nucl. Sci. Eng.*, vol. 36, no. 3, pp. 438–441, 1969.
[34] S. Carney, F. Brown, B. Kiedrowski, and W. Martin, “Theory and applications of the fission matrix method for continuous-energy Monte Carlo,” *Ann. Nucl. Energy*, vol. 73, pp. 423–431, Nov. 2014.
[35] Paul K Romano, “Application of the Stochastic Oscillator to Assess Source Convergence in Monte Carlo Criticality Calculations,” in *2009 International conference on mathematics, computational methods & reactor physics*, Saratoga Springs, New York, 2009.
[36] A. Dubi and T. Elperin, “On the Markov Chain Analysis of Source Iteration Monte Carlo Procedures for Criticality Problems: II,” *Nucl. Sci. Eng.*, vol. 91, no. 1, pp. 77–83, Sep. 1985.
[37] T. Elperin and A. Dubi, “On the Markov Chain Analysis of Source Iteration Monte Carlo Procedures for Criticality Problems: I,” *Nucl. Sci. Eng.*, vol. 91, no. 1, pp. 59–76, Sep. 1985.
[38] G. Rempala and J. Wesolowski, “Asymptotics for Products of Sums and U-statistics,” *Electron. Commun. Probab.*, vol. 7, no. 0, pp. 47–54, 2002.
[39] D. P. Griesheimer and B. R. Nease, “Spectral Analysis of Stochastic Noise in Fission Source Distributions from Monte Carlo Eigenvalue Calculations,” *Prog. Nucl. Sciene Technol.*, vol. 2, pp. 706–715, 2011.
[40] S. Lang, *Complex analysis*, 4th ed. New York: Springer, 1999.
[41] J. J. Filliben, “The Probability Plot Correlation Coefficient Test for Normality,” *Technometrics*, vol. 17, no. 1, pp. 111–117, Feb. 1975.
[42] “NIST/SEMATECH e-Handbook of Statistical Methods.” [Online]. Available: http://www.itl.nist.gov/div898/handbook/index.htm. [Accessed: 12-Jun-2017].
[43] E. Jones, T. Oliphant, P. Peterson, and others, *SciPy: Open source scientific tools for Python*. 2001.
[44] J. Devaney, “Equation Discovery Through Global Self-Referenced Geometric Intervals and Machine Learning,” George Mason University, Fairfax, VA, 1997.
[45] E. W. Weisstein, “Sample Variance Distribution.” [Online]. Available: http://mathworld.wolfram.com/SampleVarianceDistribution.html. [Accessed: 16-Jun-2017].
[46] E. W. Weisstein, “Matrix Trace.” [Online]. Available: http://mathworld.wolfram.com/MatrixTrace.html. [Accessed: 19-Dec-2017].
[47] T. Ueki and F. B. Brown, “Stationarity diagnostics using Shannon entropy in monte carlo criticality calculation I: F test,” *Trans Am Nucl Soc*, vol. 87, p. 156, 2002.
[48] T. KITADA and T. TAKEDA, “Effective Convergence of Fission Source Distribution in Monte Carlo Simulation,” *J. Nucl. Sci. Technol.*, vol. 38, no. 5, pp. 324–329, May 2001.
[49] H. J. Shim and C. H. Kim, “Convergence Criterion of Fundamental Mode Fission Source Distribution in Monte Carlo Calculations,” in *Proc. Monte Carlo 2005 Topical Meeting*, Chattanooga, TN USA, 2005.

[50] Y. Naito and J. Yang, “The Sandwich Method for Determining Source Convergence in Monte Carlo Calculation,” *J. Nucl. Sci. Technol.*, vol. 41, no. 5, pp. 559–568, May 2004.
[51] M. NAMEKAWA and Y. NAITO, “Development of a Method to Calculate keff Satisfying a Convergence Criterion of Source Iteration in Monte Carlo Calculation,” *J. Nucl. Sci. Technol.*, vol. 47, no. 10, pp. 884–893, Oct. 2010.
[52] T. Ueki, F. B. Brown, D. K. Parsons, and D. E. Kornreich, “Autocorrelation and dominance ratio in Monte Carlo criticality calculations,” *Nucl. Sci. Eng.*, vol. 145, no. 3, pp. 279–290, 2003.
[53] T. Ueki and F. B. Brown, “Stationarity modeling and informatics-based diagnostics in Monte Carlo criticality calculations,” *Nucl. Sci. Eng.*, vol. 149, pp. 38–50, 2005.
[54] H. J. Shim and C. H. Kim, “Stopping criteria of inactive cycle Monte Carlo calculations,” *Nucl. Sci. Eng.*, vol. 157, no. 2, pp. 132–141, 2007.
[55] S. Hyun Kim, D. Hyun Kim, J. Kyung Kim, and J. Man Noh, “A New Approach to Check and Diagnose the Fission Source Convergence in Monte Carlo Criticality Calculations,” *Nucl. Sci. Eng.*, vol. 178, no. 1, pp. 29–41, Sep. 2014.
[56] T. Ueki and B. S. Chapman, “A Mesh-Input-Free On-The-Fly Source Convergence Indicator in Monte Carlo Power Method,” *J. Nucl. Sci. Technol.*, vol. 48, no. 5, pp. 805–815, May 2011.
[57] T. M. Cover and J. A. Thomas, *Elements of Information Theory*, 99 edition. New York: Wiley-Interscience, 1991.
[58] A. Bhattacharyya, “On a Measure of Divergence Between Two Statistical Populations Defined by Their Probability Distributions,” *Bull. Calcutta Math. Soc.*, vol. 35, pp. 99–109, 1943.
[59] M. Nakagawa and T. Mori, “Whole Core Calculations of Power Reactors by Use of Monte Carlo Method,” *J. Nucl. Sci. Technol.*, vol. 30, no. 7, pp. 692–701, Jul. 1993.
[60] P. F. Rose, “ENDF/B-VI Summary Documentation,” National Nuclear Data Center, Brookhaven National Laboratory, Upton, NY, BNL-NCS-17541 (ENDF-201), 1991.
[61] *NJOY 99: New Capabilities in Data Processing*. United States. Department of Defense, 2002.